Synthesis and Applications of Group 4 and 13 Metal-Organic Frameworks

Claire Housley

School of Chemistry, University of Nottingham

A thesis presented to the University of Nottingham in fulfilment of the requirement for the degree of Doctor of Philosophy

February 2022

Declaration

I hereby declare that the work presented in this thesis is my own investigation except otherwise state and acknowledged by explicit reference. This thesis has not previously been accepted for any academic degree or qualification and is not being currently submitted in candidature for any degree or qualification.

Claire Housley

11 January 2022

Abstract

Metal-organic frameworks (MOFs) are a class of crystalline porous materials that have received growing interest due to their highly tuneable properties and ability to form from a wide variety of components. By altering the metal centres and organic ligands used in their synthesis a vast number of structures have been developed, finding applications in gas storage, catalysis, and chemical separations. In order to be applied to these real-world challenges MOFs must possess mechanical, thermal and chemical stability. Due to the high stability associated with MOFs containing high-valent metals, this thesis focuses on the synthesis of MOFs containing Al(III), Ti(IV), Zr(IV), and Hf(IV). Throughout this thesis, reaction conditions were tailored carefully to produce new phases, increase yields, and improve crystallinity.

Chapter 3 focuses on the synthesis of MOFs that could be used to remove Cu(II) ions from aqueous environments. As MOFs containing Lewis basic groups often provide good uptake of heavy metals, a series of MOFs was chosen where pendant Lewis basic groups could be added to the linker with the aim that this would increase Cu(II) uptake. MIL-53(Al), MIL-53(Al)-NH_2 and MIL-121 were all synthesised using microwave heating which significantly reduced the reaction time required. Investigations into the reaction conditions used to produce MIL-53(Al)-NH_2 meant that improvements on previously reported methods were made; using a mixed solvent system of DMF and H_2O produced a material with no linker trapped in the pores before activation had been carried out. To the best of my knowledge, the microwave synthesis of MIL-121 was carried out for the first time. The activation of MIL-121, on the other hand, presented some challenges, with neither calcination nor Soxhlet extraction successfully removing the linker from the pores.

As the stability of these materials is extremely important for their successful application as Cu(II) sorbents, the three MOFs were submerged in a range of aqueous solution at different pHs and changes in their structure were observed *via* PXRD analysis. MIL-53(Al) and MIL-53(Al)-NH_2 were very susceptible to phase change, bringing into question their ability to act as sorbents in real world scenarios. Indeed, when Cu(II) sorption experiments were carried out, MIL-53(Al) and MIL-53(Al)-NH_2 adsorbed little Cu(II). Although MIL-121 was comparatively more stable over a range of pH, it also exhibited very poor Cu(II) uptake, but

this was likely due its activation being unsuccessful, resulting in the MIL-121 having a low internal surface area.

The focus in Chapter 4 shifts to focus on the synthesis of Group 4 naphthalene diimide (NDI) MOFs. NDIs are a class of aromatic compounds that possess an electron deficient and redox-active core. They have a rigid, linear structure and chemical robustness that makes them ideal candidates as linkers in MOFs. There are limited examples of Group IV NDI MOFs in the literature and those that have been reported often lack crystallinity and structure solution is often performed using PXRD studies, rather than analysis of single crystals. By performing carrying out a large number of experiments where conditions such as solvent, reaction temperature, reactant ratios and the use of modulators were varied, four new frameworks were produced.

Two MOFs (Zr-SA-NDI-α and Zr-SA-NDI-β) containing Zr(IV) and salicylic naphthalene diimide (SA-NDI) were produced by employing different ratios of $ZrCl_4$ to SA-NDI and different modulators; Zr-SA-NDI-α was produced when a 1:4 metal salt to linker ratio and trifluoroacetic acid was used, whilst Zr-SA-NDI-β was produced when a 1:6 metal salt to linker ratio and benzoic acid was used. The structure of Zr-SA-NDI-α was found using single crystal X-ray diffraction, whilst the structure of Zr-SA-NDI-β remains unknown as single crystals could not be produced. Whilst different reaction conditions were being investigated in attempts to make Zr SA-NDI MOFs, a hydrogen-bonded organic framework (HOF) was also synthesised. Using a DEF/MeCN solvent mixture led to the production of single crystals of SA-NDI HOF. Single crystal X-ray diffraction revealed that the structure is held together through hydrogen bonding of adjacent SA-NDI moieties and that MeCN molecules are present in the pores of the HOF.

Acknowledgements

I think it is fair to say that my PhD experience had been quite far from normal. As such, there are quite a few people that must be mentioned here.

First, let me say thank you to my two supervisors Professor Neil Champness and Dr. Matt Cliffe. You have both known me for an unusually short period of my PhD but nevertheless the guidance that you have given me in that time is truly appreciated.

I am very grateful to Dr. Stephen Argent, Dr. Rosemary Young and Dr. Georgia Orton for their help with all things crystallography. This work would also not have been possible without technical support from staff at nmRC, the Khlobystov group, Dr. Andreas Weilhard and innumerable people across both the Chemistry and Engineering departments at Nottingham.

Next, I come to thank all the research groups that I have been part of over the past four years…

A big thanks to Cohort 4 of Sustainable Chemistry CDT (which now goes by another name). We had some extremely rememberable times with the CDT and I hold some very treasured memories from our times in the CDT office and at many CDT events.

Second, we come to the Microwave Engineering Group (which now goes by another name). Ieuan, your guidance in the first year of my MOF research journey was phenomenal and never-ending. Special thanks also go to Caleb Marsh and Ben Weare who both contributed to start of my work on MILs. SEM isn't quite the same without someone to read you the BBL score. To the rest of you, thank you for the many trips to Sanchans, for eating my many bakes and for keeping my spirits up when I hit one the most challenging parts of my PhD journey.

Third, a big thank you goes to the Champness group (the name hasn't changed, but the location has). I had obviously never imagined turning up to a new research group halfway through my PhD, but you all made the transition a lot less painful and a lot more enjoyable. Special thanks to Sarah, for listening to my many questions, all along the lines of "how on earth will I ever grow a single crystal?" Extra thanks go to Rosie, who leant her eyes and brain to this thesis and who also encouraged me with a smile, even when smiling was the last thing on my mind. I also owe Georgia an immeasurable amount of thanks. Without her I would not have got through some very difficult times or written this thesis. It is an absolute honour to

be your friend and have shared in your passion for research. Here's to you never leaving Beeston (please).

Fourth and finally, thanks the Cliffe group for supporting me through the last year of my PhD. A big thanks goes to Jem, for allowing me to a bit too rude to him, to Martin for keeping me company as I slowly went insane in my last few months in the lab and Alex for taking on some cluster chemistry.

To Marysia, thank you for all you have done for me, including some nifty work in blender. From day one, you have always been someone I can lean on and your ability to turn up on my doorstep with chocolate at the exact right moment is phenomenal. I have treasured our friendship, and I hope it will last for many years to come.

I also must give a special mention to Elizabeth, from the House of Commons Library, for helping me to understand where my true strengths lie and for emailing about a job when it was far too early for me to apply (but I did anyway). To my new boss Danielle, thanks for kick-starting me career and for the constant positive feedback. I hope one day that academia might take a leaf out of your book.

To my family, in the UK and further afield, thank you for all the love and support you've given me. Thanks especially to my parents, who made sure I never gave up and provided some essential holidays and therapy over the phone across the past fourth years.

Finally, an absolute never-ending amount of thanks goes to my husband, Kieran. The sacrifices you have made to support me on this journey are countless. You supported me through some very dark moments and never once doubted that I could finish this thing. I could not have done this without you by my side and I will never be able to thank you enough.

Contents

Abbreviations

AA	Acetic acid
abz	Aminobenzoate
BA	Benzoic acid
BDC	1,4-benzenedicarboxylate
BET	Brunauer-Emmett-Teller
BTC	1,3,5-benzenedicarboxylate
BPDC	biphenyl-4,4'-dicarboxylate
BTEC	1,2,4,5-benzenetetracarboxylate
CHN	Carbon Hydrogen Nitrogen Analysis
DEF	N,N-Diethyl formamide
DGIST	Daegu Gyeongbuk Institute of Science and Technology
DI	Deionised
DLS	Diamond Light Source
DEF	Diethyl formamide
DM	Dimethyl
DMF	N,N-Dimethyl formamide
DMSO	Dimethyl sulfoxide
EDTA	Ethylenediaminetetraacetic acid
EDX	Electron Dispersive X-Ray
ESI MS	Electrospray Ionisation Mass Spectrometry
et al.	And others
EtOH	Ethanol
FA	Formic acid
FT-IR	Fourier-Transform Infrared spectroscopy
FTO	Fluorine-doped tin oxide
GOF	Goodness of Fit
HCl	Hydrochloric acid
HNO_3	Nitric acid
HOF	Hydrogen-bonded Organic Framework
ICP	Inductively Coupled Plasma

MeCN	Acetonitrile
MeOH	Methanol
MIL	Matériaux de l'Institut Lavoisier
MOF	Metal-Organic Framework
MW	Microwave
MW	Molecular Weight
NaOH	Sodium hydroxide
NDI	Naphthalene diimide
NMR	Nuclear Magnetic Resonance
NTCA	1,4,5,8-naphthalenetetracarboxylic dianhydride
PCN	Porous Coordination Network
PXRD	Powder X-Ray Diffraction
SA	Salicylic acid
SBU	Secondary Building Unit
SCXRD	Single Crystal X-Ray Diffraction
SEM	Scanning Electron Microscopy
TFA	Trifluoroacetic acid
TGA	Thermogravimetric Analysis
THF	Tetrahydrofuran
UiO	Universitetet i Oslo
UV-Vis	Ultraviolet-Visible

1 Chapter One: Introduction

1.1 Metal-Organic Frameworks

1.1.1 An introduction to Metal-Organic Frameworks

Metal-organic frameworks (MOFs) are a class of crystalline materials constructed from metal-based metal nodes (ions or clusters) connected through multidentate organic linkers to give extended frameworks.[1] MOFs can be formed from a vast array of components, giving rise to an extraordinary number of structures with different topologies.[2] These frameworks often exhibit permanent porosity upon removal of guest solvent, with surface areas up to 7000 m^2 g^{-1} being reported.[3] Although they are a relatively new class of compounds, their large surface areas and high structural tunability has led to much interest, with the past thirty years seeing an exponential growth in the number of papers published in this area of chemistry.[4] The unique properties of MOFs allow them to find application in areas such as gas storage and separation,[5–7] metal remediation,[8] catalysis,[9,10] and drug delivery.[11]

The birth of MOF chemistry dates back to the late 1980s when Hoskins and Robson reported the first examples of porous coordination polymers, materials that linked together metal centres to organic linkers and exhibited large range crystalline order.[12,13] The term MOF was coined later by Yaghi *et al.* in 1995, when they synthesised a Co-trimesate MOF.[14] The field continued to expand throughout the rest of the decade, when some of the now most well-studied MOFs, including MOF-5[15] and HKUST-1,[16] were originally reported (Figure 1.1).

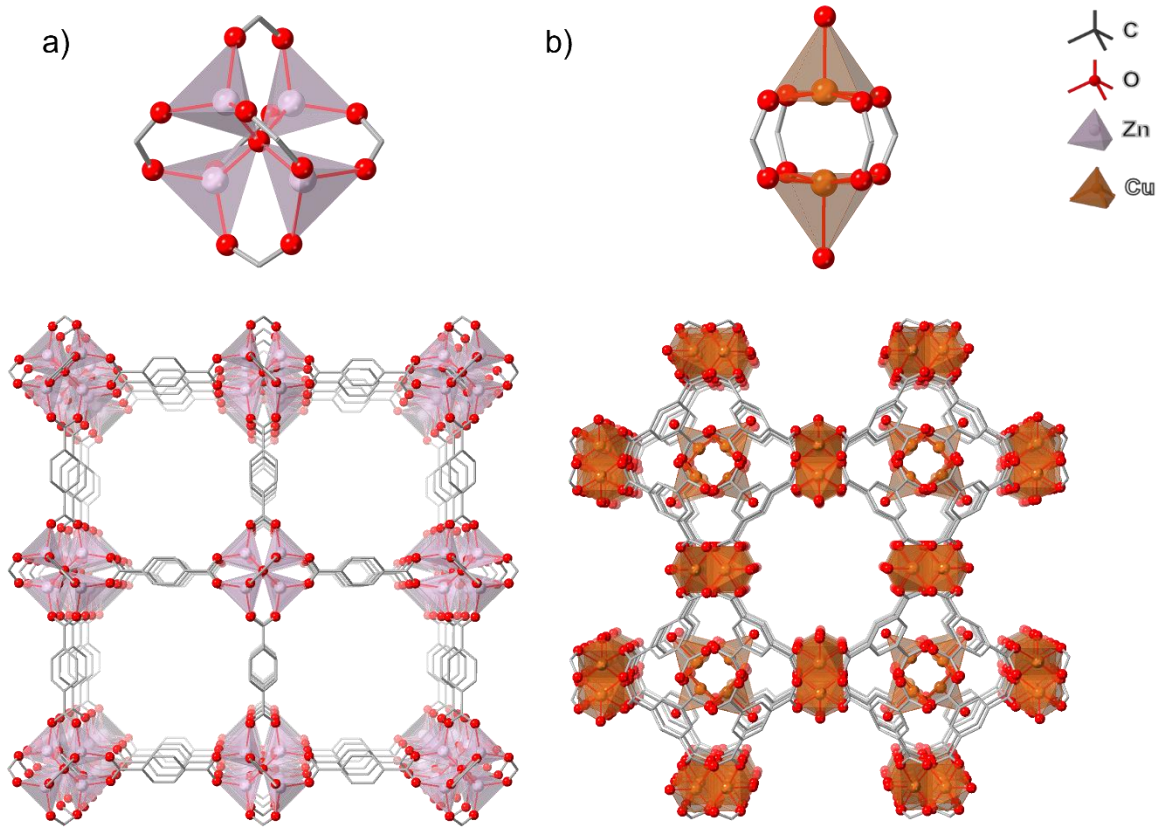

Figure 1.1 – a) Zinc tetrahedral SBUs (top) that, along with 1,4-benzenedicarboxylate (BDC), make up the crystal structure of MOF-5 (bottom, CSD code = SAHYIK).[15] b) Copper paddlewheel SBUs (top) that, with 1,3,5-benzenetricarboxylate (BTC), make up the crystal structure of HKUST-1 (bottom, CSD code = FIQCEN).[16] Hydrogens omitted for clarity.

As there are a vast array of metals and linkers that can be used to synthesise MOFs, there are theoretically an almost infinite amount of MOF structures that could be formed. For the metal centre, metals from across the periodic table have been used in MOFs, including s, p and f block elements.[17] Having said this, transition metals are used most frequently in MOF synthesis, with some of the commonly reported being Cu(II), Zn(II), Fe(III), and Zr(IV).[18–22]

In comparison to the metal centre, the choice of linker is even more varied. As long as the linker contains two or more Lewis basic groups that are able to coordinate to a metal, the length, composition and shape of the linker can all be changed, delivering MOFs with varying connectivity, topology and functionality.[23] Linkers containing phenyl groups with carboxylate or nitrogen-containing donor groups are most commonly used. A linker as simple as terephthalic acid (H_2BDC) is used to make prototypical MOFs such as MOF-5,[15] UiO-66,[24] and MIL-53,[25] however much more complicated linkers can be used, such as tetrakis(4-carboxyphenyl)porphyrin.[26] Figure 1.2 shows a range of linkers commonly found in MOF

structures. For the most part, readily synthesised and/or commercially available linkers are used. However, it is possible to create more highly functional MOFs by the design and synthesis of new linkers that possess desired properties and functionality, such as chirality, additional binding sites or pendant groups, for example.

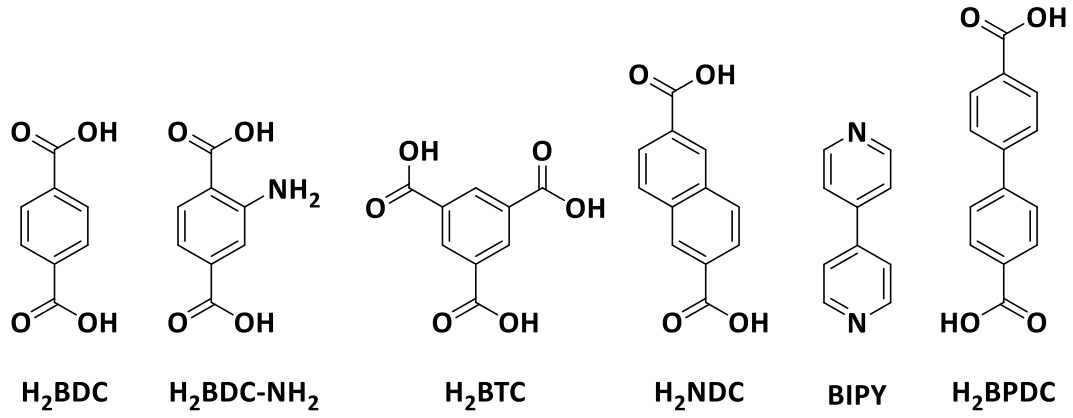

Figure 1.2 – A selection of the most commonly used linkers in the synthesis of MOFs.[15,16,24,25,27–31]

The description of a MOF structure can be considered on four levels (Figure 1.3).[32] The first is the chemical building blocks, the metal node and organic linker, as described above. The second level is the secondary building unit (SBU). SBUs are the simplest repeated unit of the MOF structure and consist of several ligands coordinated to a metal ion or cluster in a relatively rigid and directional geometry. The SBUs link together to form the extended lattice of the MOF (the third level of the MOF structure), which can be described by its topology and presence of open pores and channels. The fourth and last level of the MOF structure is the morphology of the MOF particles, which can have varied shapes and sizes on the macro- or micro- scopic scales.

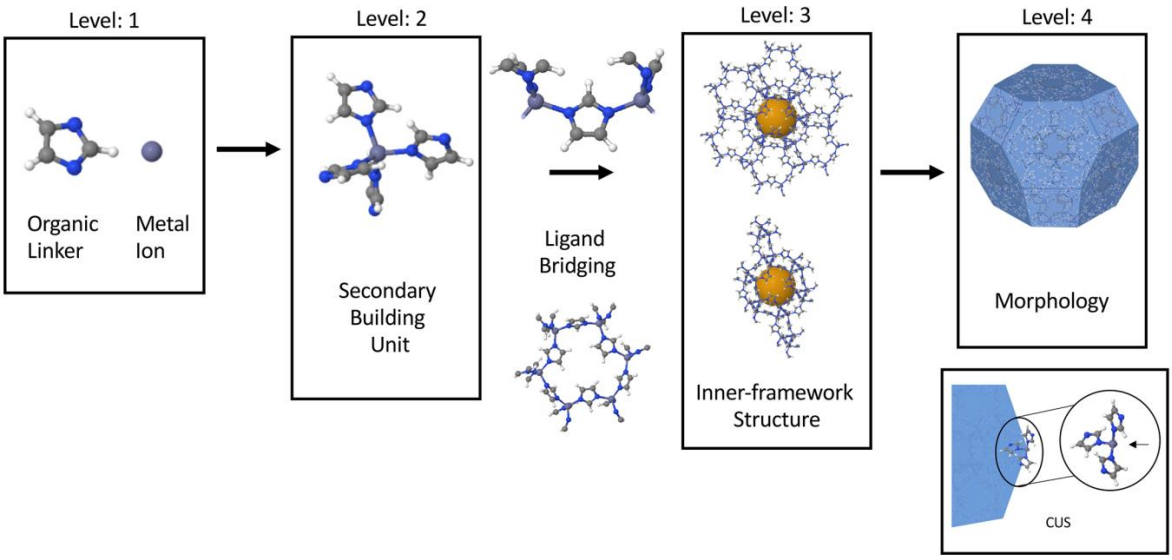

Figure 1.3 - Levels of structure and composition for MOFs: Level 1 - node and linker; Level 2 - secondary building unit (SBU) and coordinatively unsaturated site (CUS); Level 3 - inner-framework structure; and Level 4 - morphology. Reprinted with permission from *ACS Appl. Mater. Interfaces,* 2021, 13, 7004−7020. Copyright 2021 American Chemical Society.[32]

1.1.1.1 Isoreticular MOFs

As the geometry of the SBU defines the overall framework connectivity, reticular chemistry can be applied to MOF synthesis. Series of MOFs may be synthesised which exhibit the same topology but consist of different organic linkers with varying length and functionality. One of the first sets of isoreticular MOFs to be reported, the IRMOFs, demonstrated that an increase in length of the linker, from terephthalic acid in MOF-5 (or IRMOF-1) to 4,4''-terphenyldicarboxylate in IRMOF-16 (Figure 1.4), results in an increase in pore size.[27] Nevertheless, increased linker length can produce interpenetrated networks, resulting in decreased pore volume compared to the original MOF. Interpenetration of MOFs can be described as the growth of additional frameworks within the pore space of other frameworks. Careful control of synthetic conditions, such as reactant concentration and temperature, allowed IRMOF-16 to be produced with an increase in pore volume by a factor of eight compared to MOF-5, whilst the unit cell edge was doubled.[27]

Functionalised linkers can enhance the properties of a MOF beyond pore volume. For example, if terephthalic acid is replaced with 2-aminoterephthalic acid in MOF-5, IRMOF-3 is formed (Figure 1.4), which has the same structure as MOF-5 but contains an extra amino group.[27] The presence of this extra functionality allows IRMOF-3 (and amino functionalised

MIL-53) to be used as a solid-phase basic catalyst, in the Knoevenagel condensation of an acetate with benzaldehyde, for example.[33] The pK_a of the amino group in 2-aminoterephthalic acid is increased when it is incorporated into the MOF structure, resulting in the MOF providing an increase in catalytic activity, compared to the equivalent solution phase catalyst.

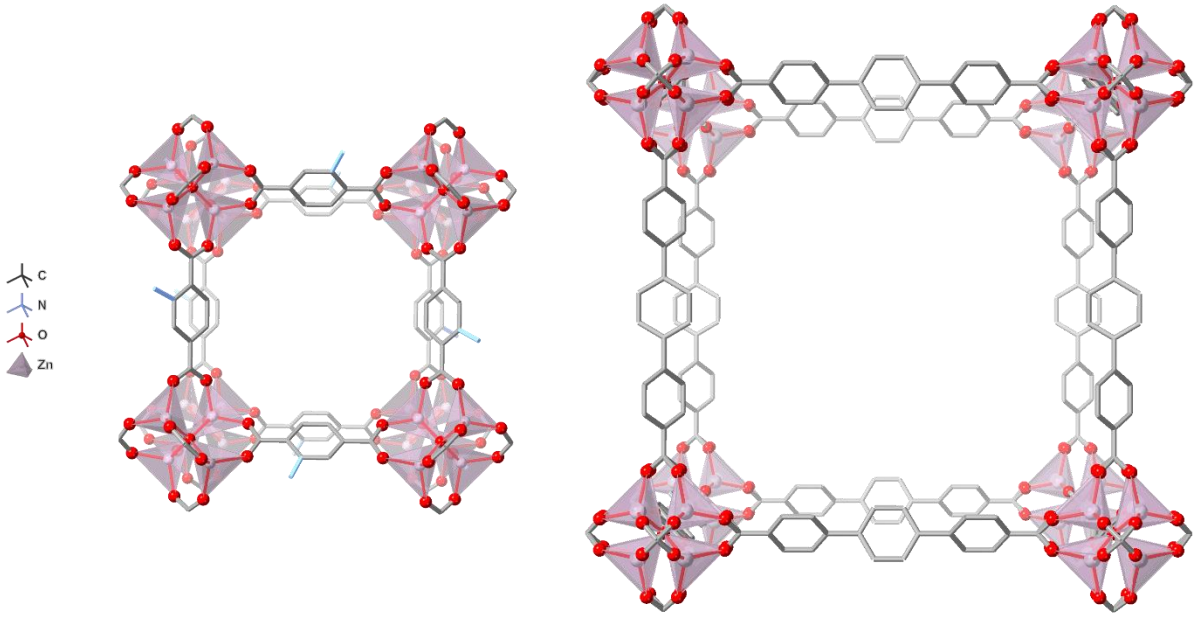

Figure 1.4 – Crystal structure of IRMOF-3 (left, CSD code = EDUSUR) and IRMOF-16 (right, CSD code = EDUWAB).[27] Hydrogens omitted for clarity.

Isoreticular MOFs can also be formed by the replacement of the metal ions in the inorganic SBUs, for example the replacement of Cu(II) in HKUST-1 with Zn(II), Fe(II), Mo(II), Cr(II) or Ru(II).[34–38] Changing the metal can lead to changes in physical and chemical characteristics, for example the Ru analogue of HKUST-1 gives rise to higher CO_2 adsorption than other analogues, which is attributed to the increased charge of the di-metal secondary building unit.[39] Furthermore, the analogue of UiO-66 that is made with Ce(IV) (the first report of the material was with Zr(IV)),[24] has significantly enhanced catalytic properties when compared to UiO-66(Zr), due to Ce(IV)'s oxidative properties.[40]

1.1.1.2 MOF nomenclature

The naming regime used for MOFs in the literature is inconsistent and does not follow any IUPAC standards. MOFs are often named by the combination of a three or four lettered abbreviation, that references the research institute where the MOF was first synthesised and reported, and a number. For example, UiO-66 refers to the Universitetet i Oslo,[24] and MIL-53

to the (Matériaux de l') Institut Lavoisier.[41] The numbers associated with the codes do not follow any rules but in isoreticular MOFs containing different metals these codes are often followed by an element in brackets to indicate which metal is present in the MOF structure. For example, MIL-53 can be MIL-53(Fe),[42] MIL-53(Cr),[43] and MIL-53(Al)[25] and UiO-66 can be UiO-66(Zr)[24] or UiO-66(Hf),[44] amongst others.

1.1.2 Synthesis of MOFs

A wide breadth of synthetic methods are used to make MOFs, including solvothermal (and hydrothermal),[45] mechanochemical,[46] by extrusion,[47] electrochemical,[48,49] and microwave assisted heating methods (Figure 1.5).[45,50]

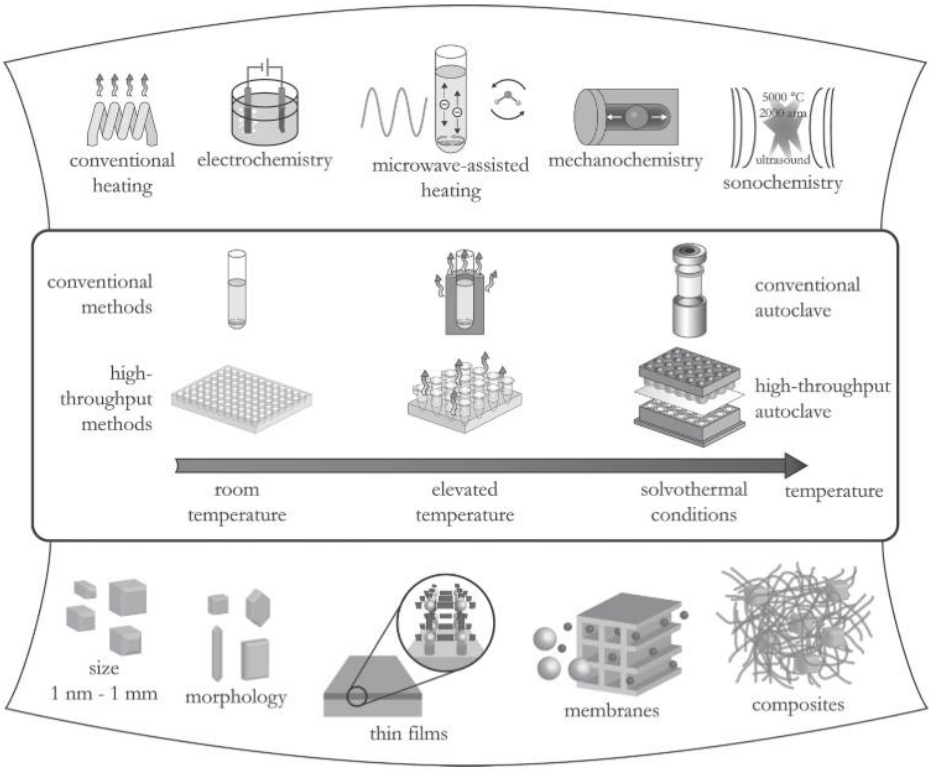

Figure 1.5 – Overview of synthesis methods, possible reaction temperatures, and final reaction products in MOF synthesis. Reprinted with permission from *Chem. Rev.*, 2012, 112, 933–969. Copyright 2012 American Chemical Society.[45]

The conditions used in MOF synthesis should provide the required energy to allow for formation of the inorganic building blocks without linker decomposition, whilst controlling the kinetics of the crystallisation to allow nucleation and growth of the desired phase of MOF.[45] For the successful synthesis of MOFs, the rigidity and directionality of bonding towards the SBU is important, as is the lability of the metal-linker bonds formed during self-

assembly. These bonds must be able to dissociate if the linker does not coordinate in correct orientation. As such, the production of robust frameworks is limited by an inverse relationship between metal-organic bond strength and the reversible formation of this bond.[2] The reaction conditions are also key to controlling and directing MOF formation. Conditions such as concentration and ratio of reactants, temperature, reaction time, solvent and pH can all have an impact on the MOF phase obtained and effect factors such as crystallinity and morphology.[51,52]

Although some prototypical MOFs have been synthesised at room temperature,[53–55] hydrothermal and solvothermal synthesis are the most commonly used methods for MOF synthesis, where metal salts and organic ligands are combined in water or organic solvents, respectively. Reaction mixtures are placed and heated in closed vials, or autoclaves, under autogenous pressure at elevated temperature, which are often above the boiling point of the solvent.[56] During successful syntheses, single crystals or crystalline powder will precipitate out of the solution as self-assembly occurs.

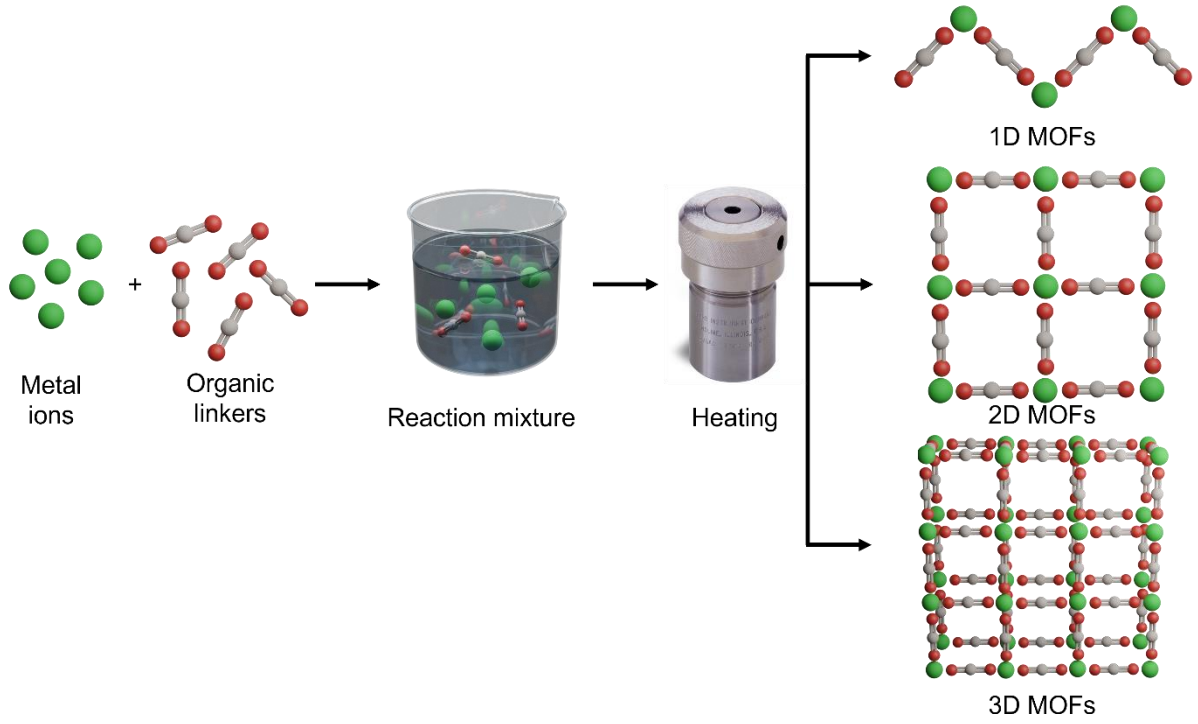

Figure 1.6 – Metal ions and organic linkers are combined in a solvent and heated in a sealed vessel to form MOFs with various topologies.

The use of higher temperatures and pressures increases both solubility of the reactants and enhances diffusion rates, increasing the reaction rate and providing the energy to produce a thermodynamic favoured phase.[45] The temperature of the MOF synthesis can have a strong impact on the product formed, potentially changing the morphology of crystals obtained.[57] Higher temperatures can also lead to denser phases.[57,58] For example, the phase density and connectivity of Co(II) in cobalt succinate MOFs is increased with increasing temperature (Figure 1.7).[59] At higher temperatures, there are fewer molecules of water coordinated to each Co(II) and more carboxylate or hydroxide groups coordinated to each Co(II) instead. This is attributed to the increased entropic contribution of releasing more H_2O molecules at higher temperatures.

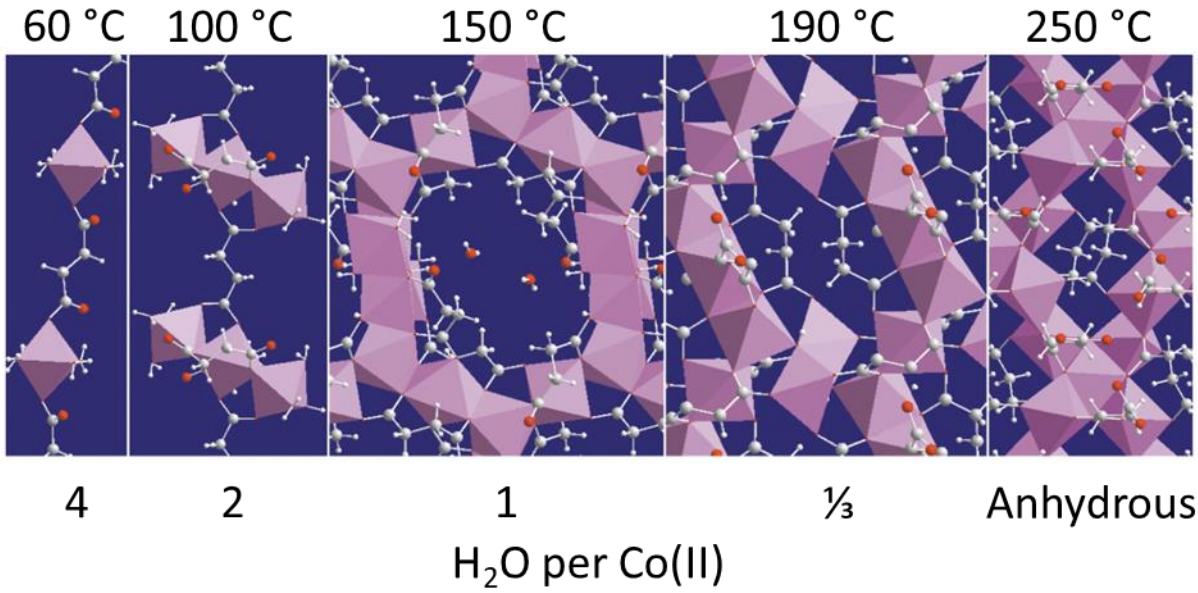

Figure 1.7 – Structures of five cobalt succinates, showing greater connectivity and less hydration as formation temperature increases. Grey = carbon, red = oxygen, white = hydrogen, pink = CoO_6 octahedra. Figure adapted with permission from *Chem. Commun.*, 2004, 368–369. Copyright (2004) Royal Society of Chemistry.[59]

In addition to the five phases achieved by varying the reaction temperature, a high throughput study (a process in which many parameters are varied slightly) found that increasing the pH can favour the formation of extended structures.[58] This effect has been shown elsewhere, where increasing the pH gave rise to the deprotonation of coordinating groups such as carboxylates and phosphonates, leading to the formation of 2 or 3D structures with high connectivity, rather than 1D structures which are formed when the pH of the

reaction mixture is lower (and the coordination groups in the linker remain partially protonated).[60]

As well as adjusting the pH of the reaction mixture by changing the ratio of linker to metal (acid to base) or adding acid or bases to the reaction mixture, the choice of solvent can give rise to changes in pH. DMF, which is one of the most commonly used solvents in MOF synthesis, decomposes at high temperatures to give dimethylamine. Dimethylamine can then act as base and deprotonate the linkers, enhancing the formation of metal to linker bonds. In addition to its ability to increase the pH of the reaction, DMF is highly polar, allowing many starting materials to readily dissolve, and has a high boiling point (153 °C), allowing high temperatures to be reached in the MOF-forming reactions.

The properties of the solvent used play a significant role in MOF synthesis, due to their ability to directly or indirectly influence the coordination behaviour of the metal and ligand. For example, Parise and co-workers managed to isolate four different 3D magnesium-based MOFs (and one 2D polymer) using pyridinedicarboxylate as the linker, by simply changing the solvent mixture used.[61] The different topologies are produced due the varied ability of the solvents (DMF, H_2O, MeOH and EtOH) to coordinate to Mg(II).

Microwave-assisted heating was first applied to the production of MOFs in 2005 for the synthesis of MIL-100(Cr)[62] and has since become an increasingly popular method for MOF synthesis.[50,63] Microwave (MW) heating relies on the interaction of electromagnetic waves with mobile electric charges. In solution, polar molecules align themselves to the applied electromagnetic field (which is applied by the MWs). As the applied field is an oscillatiing field, the molecules constantly change orientation, causing molecule collisions and leading to an increase in the kinetic energy and temperature of the system.[45]

As the MWs interact directly with the reagents (or solvent), this heating method is very efficient and can enhance heating rates and reduce reaction times.[64,65] Due to the increased heating efficiency, the kinetics of crystal nucleation are usually significantly increased and often microcrystalline materials are produced.[50] To avoid over-heating and over-pressurisation of the reaction vessel, the reagents and solvents must be chosen with particular care and an understanding of how they will interact with MW radiation.[45]

In addition to reducing the reaction time required to produce MOFs, MW heating can also be used to produce small crystallites,[66,67] change particle morphology,[68,69] carry out phase-selective syntheses,[70,71] perform PSM of MOFs,[72–74] and create hybrid materials.[75–77]

In summary, many methods of MOF synthesis have been reported, and each system requires detailed studies to optimise yield, phase purity and sample morphology.

1.2 Chemically and thermally stable MOFs

Stability can be defined as the resistance of a structure to degradation.[78] For MOFs, mechanical, thermal and chemical stability are required if the MOF is to be used for industrial applications, such as catalysis or water purification (see section 1.3). Chemical stability can be defined as the MOFs ability to maintain its structure when exposed to a range of different chemical environments, such as solvents, aqueous solutions (including acids and bases), gases, electrophiles, and nucleophiles.[79] Most commonly, the stability of MOFs in water is studied, as water is present in most environments and as a vast amount of MOF applications involve exposure to water.[80,81] Thermal stability (the MOF maintaining its structure at elevated temperature) is also important, as many catalytic applications of MOFs involve the use of high temperatures.[82] Mechanical stability (the MOF maintaining its structure on exposure to pressure or handling) is also of interest, as some applications require MOFs to be compacted into pellets.[83]

A MOF's stability can be determined through a few different methods. Firstly, thermogravimetric analysis (TGA) can be used to examine the thermal stability of a MOF, by identifying the temperature at which the MOF decomposes. Chemical stability can be studied through exposing a MOF to different chemical environments and then observing any changes in structure *via* techniques such Powder X-Ray Diffraction (PXRD), TGA and gas sorption. Mechanical stability can be studied in the same way as described for chemical stability, but pressure is applied to the sample instead of exposure to different chemicals. Alternatively, high pressure single XRD experiments can be carried out.

1.2.1 Properties of stable MOFs

The stability of a MOF is primarily determined by the strength of the metal-organic coordination bond; these are usually the first bonds to break on exposure to heat or an attack by a guest molecule, resulting in the collapse of the MOF framework.[78,84]

The use of high oxidation state metal ions, that possess high charge densities, leads to the formation of stronger coordination bonds than those formed with lower oxidation state metal ions, and therefore often lead to highly stable frameworks. Combining this with Pearson's hard/soft acid/base (HSAB) theory,[85] where highly charged metal ions are hard acids, leads us to the conclusion that MOFs formed from Al(III), Cr(III), Fe (III), Hf(IV), Ti(IV), and Zr(IV), and hard base carboxylate-containing linkers will be highly stable.[78,84,86,87] This has been seen in the MIL series of MOFs that contain Al(III), Fe(III) and Cr(III) and BDC (MIL-53,[41] and MIL-101[88]) or BTC (MIL-100[89]) and also in the UiO family of MOFs (UiO-66, UiO-67 and UiO-68) that contain di-carboxylate linkers of increasing lengths and the $[Zr_6(\mu_3\text{-}O)_4(\mu_3\text{-}OH)_4(COO)_{12}]$ cluster.[24]

In addition to using a high oxidation state metal, a few other factors are important in the design of stable MOFs:

- High connectivity of the metal nodes and ligands so that structural defects can repair themselves at a higher rate than ligand dissociation can occur.[90]
- Rigid ligands, as if a rigid (or short) ligand is used then it must be bent a significant amount for it to dissociate. This process of bending requires a larger activation energy for smaller, more rigid ligands, making dissociation of the ligand less favourable.[84,90]
- Hydrophobic groups, because introducing these groups onto the ligands can help to exclude water. This prevents water from attacking and displacing the metal-ligand bonds that are holding the framework together.[91,92]

1.2.2 Synthesis of stable MOFs

The synthesis of materials that exhibit both high crystallinity and high stability requires judicious choice of reaction conditions and MOF components. The successful synthesis of highly crystalline materials relies on the reversible bond association and dissociation of the

metal ions and ligands.[93,94] If the M-O bond is suitably labile, it is able to associate and dissociate, allowing larger crystals to grow.[84] The strong M-O bonds required for stable MOF synthesis are often poorly labile, leading to MOFs that possess poor crystallinity and small particle sizes. In order to circumvent this issue, modifications to synthetic strategies have been developed such as modulation, pre-formation of clusters, and even the use of covalent chemistry in place of coordination chemistry.

To obtain large single crystals, a process called modulation is often employed in the synthesis.[95] Modulators are species that compete with the ligand during synthesis, binding reversibly to the metal node. This competition reduces the rate of nucleation and slows down the crystallisation process, allowing larger crystals to grow (see Figure 1.8).[96] Modulating agents are often simple monocarboxylic acids, such as acetic acid, benzoic acid and trifluoroacetic acid.[97–99]

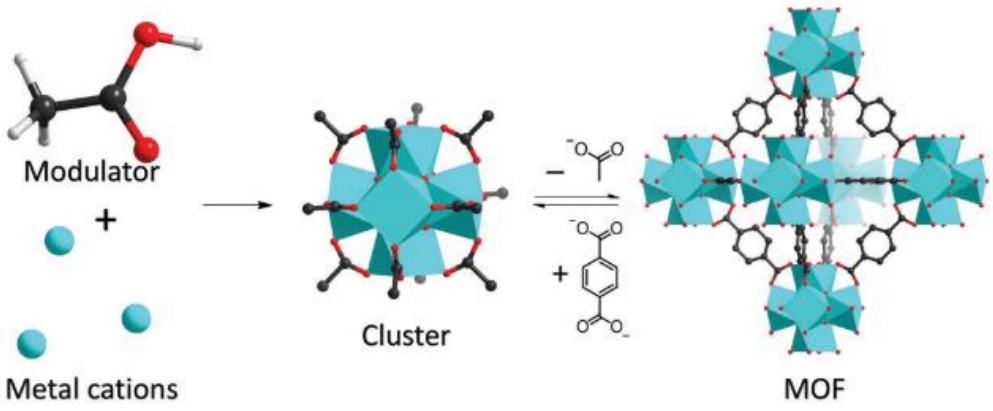

Figure 1.8 – Representative modulated synthesis of UiO-66. Reproduce with permission from *Adv. Mater.* 2018, **30**, 1704303. Copyright 2018 John Wiley and Sons.[84]

Modulation has been used widely in the synthesis of the UiO family of MOFs. The structure of the archetypical MOF, UiO-66, was originally solved by Rietveld refinement of PXRD data when the MOF was first reported in 2008.[24] UiO-66 contains a zirconium oxide ($Zr_6O_4(OH)_4$) cuboctahedral SBU which is connected by 12 bridging BDC linkers. The strong Zr-O bonds give rise to the thermodynamic stability of the MOF (the thermal degradation temperature is 540 °C), with the carbon-carbon bonds in the linker breaking down before the Zr-O coordination bonds are broken.[24] The strength of these bonds also prevents the growth of single crystals, as the process of dissociation and association, which allows crystal growth, is limited. The crystal structure possesses *Fm*-3*m* symmetry with **fcu** topology.[100]

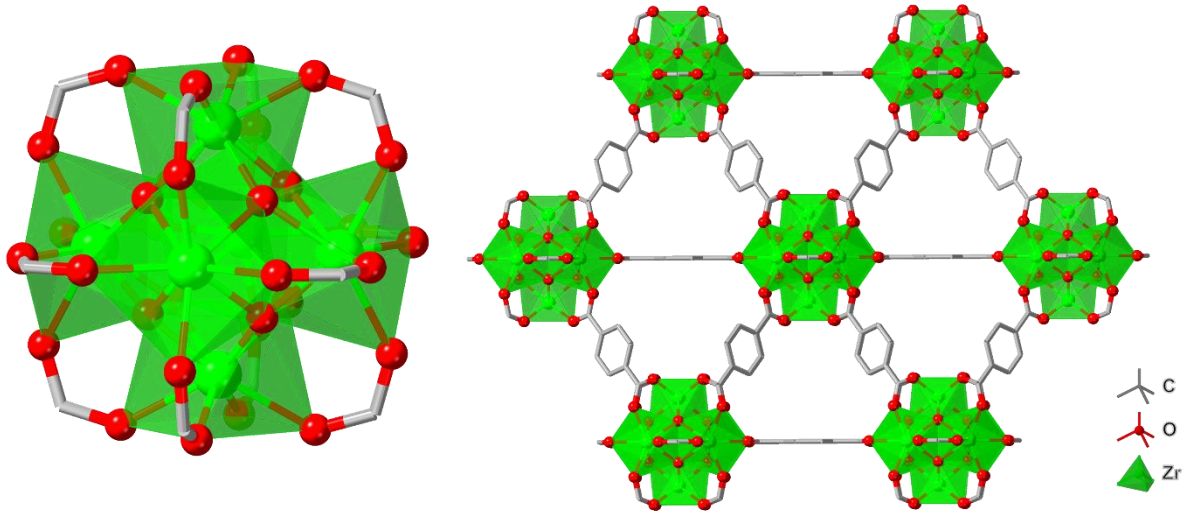

Figure 1.9 –The $Zr_6O_4(OH)_4$ SBU of the UiO family of MOFs (left) and the structure of UiO-66(Zr) (CSD code = RUBTAK).[24] Hydrogens omitted for clarity.

In 2011, Schaate *et al.* showed that the use of a modulating agent can improve the crystallinity of the UiO-66 formed.[97] The size of crystals obtained was tuned by altering the amount of the monocarboxylic acid added as a modulating agent; higher equivalents (30 equivs.) of benzoic acid or acetic acid led to an increase in particle size, as shown by SEM, and a decrease in the width of reflections in the PXRD pattern. The authors suggested that the increase in particle size with increasing equivalents of modulator is due to the *in situ* formation of intermediate complexes containing Zr(IV) and benzoic acid. Self-assembly of the framework then proceeds through exchange of the benzoic acid with BDC until the 12-coordinate SBU is built. As the equivalents of modulator increases, the possibility of the SBU containing 12 BDC ligands is reduced, slowing down the nucleation rate and encouraging the growth of fewer, larger crystals. The authors also found that the synthesis of UiO-67 (where BPDC is the linker) was affected in the same way by the addition of modulators. Although they were not yet able to achieve a large enough UiO-66 or UiO-67 crystal to carry out SCXRD, a single crystal of amino-functionalised UiO-68 (where TPDC-NH_2 is the linker) was formed using benzoic acid (30 equivalents) and H_2O (3 equivalents), with the amino group enhancing the solubility of the linker.

The single crystal structures of UiO-66 and UiO-67 were eventually reported in 2014, with both HCl and benzoic acid used as modulators. In addition to the use of two modulators, the reaction vessels had been submerged in 2.0 M KOH overnight to prevent seeding of crystals on the vessel walls.[98] The synthesis of single crystals of UiO-68 was recently reported after

high throughput synthesis was carried out.[101] The optimum conditions were found to be: the use of DMF as a solvent, and using a 1:1 ratio of metal to linker with 40 equivalents of trifluoroacetic acid (TFA) at 100 °C for 72 hours.

As with other Group IV MOFs, the synthesis of crystalline Ti-MOFs is difficult due to the formation of strong Ti(IV)-oxygen bonds during MOF synthesis limiting the growth of crystals. In fact, synthesis of crystalline Ti-MOFs is even more challenging that Zr(IV), Hf(IV) and Ce(IV) MOFs, due Ti(IV)'s even higher charge density. As such, there are a relatively limited number of reports of Ti-MOFs and most Ti-MOFs are synthesised as powders, sols or gels and very few reports have been made of the synthesis of single crystal Ti(IV)-MOFs.[102,103]

In 2016, Zhou *et al.* reported a strategy that they called High Valence Metathesis and Oxidation (HVMO) as a method for accessing more Ti-MOFs. Group III MOFs were converted to Ti(III)-MOFs by metathesis and then oxidised to create Ti(IV)-MOFs (Figure 1.10).

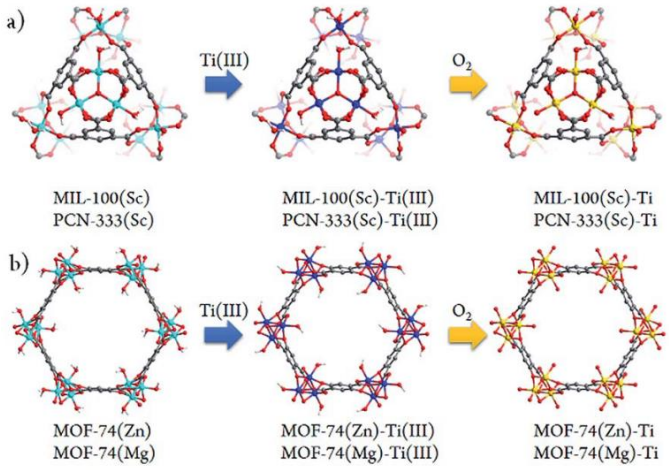

Figure 1.10 - Schematic illustration of the stepwise HVMO procedure for the design of Ti-MOFs from the template MOFs: (a) MIL-100(Sc) and PCN- 333(Sc) metal metathesis with Ti(III), followed by metal node oxidation in the air (PCN-333(Sc) and MIL-100(Sc) have same topology but different structures); (b) similar process for MOF-74(Zn) and MOF- 74(Mg). Reprinted from *Chem. Sci*., 2016, **7**, 1063 with permission from the Royal Society of Chemistry.[104]

In 2015 the first ever single crystal Ti MOF, PCN-222, was synthesised.[103] A pre-formed titanium aminobenzoate cluster ($Ti_6O_6(O^iPr)_6(abz)_6$)[105] was used as the starting source of titanium, overcoming the issue of irreversible bond formation between the densely charged Ti(IV) ion with carboxylate groups. The MOF contains a novel Ti_7O_6 cluster, which consists of a pair of Ti_3O_3 sub-units bridged by a Ti atom. Each Ti_3O_3 unit is connected to six tetrakis(4-

carboxyphenyl)porphyrin) (TCPP) linkers, forming a 2D layer. The bridging Ti atoms connect these layers to form a 3D framework (Figure 1.11).[103]

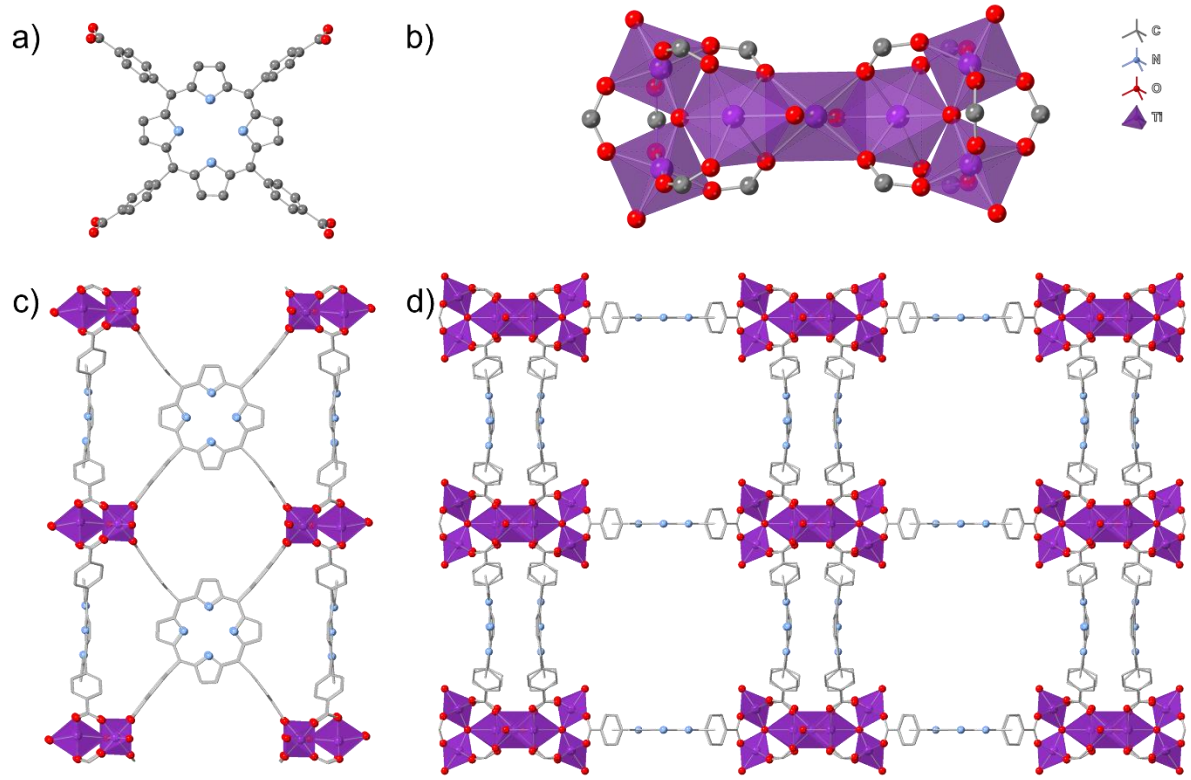

Figure 1.11 – a) TCPP linker, b) Ti_7O_6 cluster, c) view of PCN-22 along *b*-axis and d) *a*-axis. H atoms omitted for clarity.[103]

Later, Park *et al.* used a similar method to obtain a single crystal structure of a new Ti-MOF, DGIST-1.[106] Three different clusters: $Ti_6O_6(O^iPr)_6(abz)_6$, $Ti_6O_6(O^iPr)_6(t\text{-}BA)_6$, and $Ti_8O_{10}(O^iPr)_6(abz)_{12}(acetonitrile)_{0.5}$, could be employed as Ti sources in the synthesis of DGIST-1. In each case, the cluster rearranges to give a Ti(IV) chain where each Ti(IV) is coordinated to four oxygens from four TCPP linkers and two μ_2-O atoms and is connected to neighbouring Ti(IV) atoms by one μ_2-O bridge and two carboxylate groups.[106]

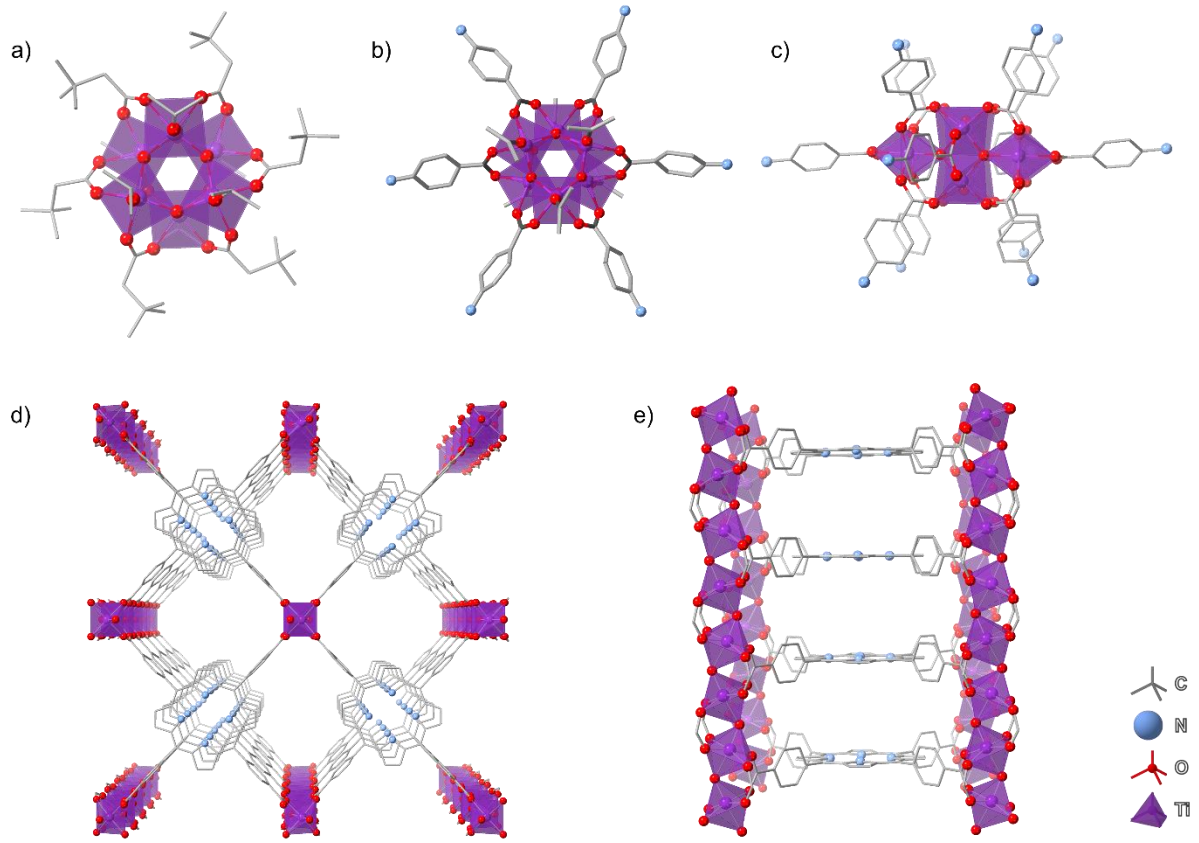

Figure 1.12 – a) $Ti_6O_6(O^iPr)_6(t\text{-BA})_6$ (O^iPr = isopropoxide, *t*-BA = t-butylacetate), b) $Ti_6O_6(O^iPr)_6(abz)_6$ (abz = 4-aminobenzoic acid), c) $Ti_8O_{10}(O^iPr)_6(abz)_{12}(acetonitrile)_{0.5}$, d) DGIST-1 along the *b*-axis and e) the *c*-axis.[105,106] Hydrogens omitted for clarity.

The use of pre-formed clusters in the synthesis of Group IV MOFs is a relatively well-studied topic within the literature, as it seen as a way of "self-modulating" the MOF synthesis. Most commonly, pre-formed Zr clusters have been used to aid the formation of large single crystals of Zr MOFs. In 2010, the first example of this was published by Férey *et al.*, where a Zr MOF with the UiO-66 architecture was synthesised from a zirconium methacrylate oxocluster.[107]

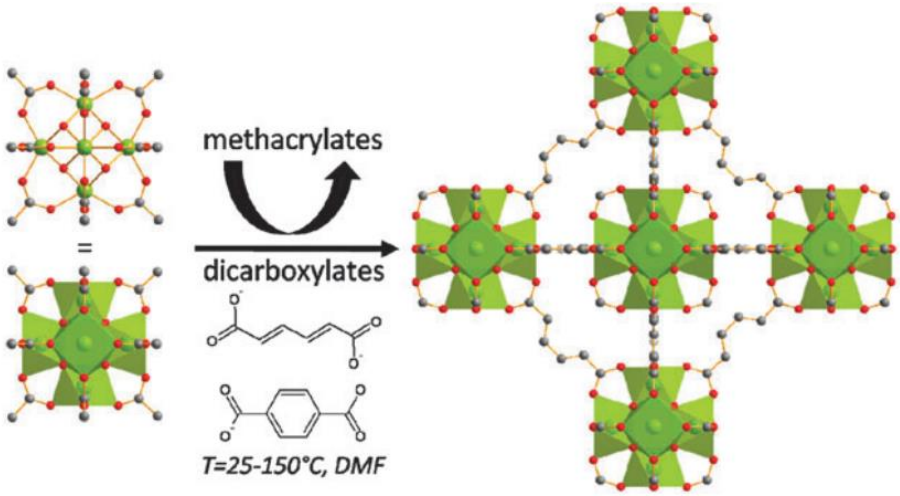

Figure 1.13 – Synthesis of UiO-66 type MOF (with either trans, trans muconic acid and terephthalic acid) starting from Zr_6 methacrylate oxoclusters. Reprinted from *Chem. Commun*., 2010, **46**, 767–769 with permission from the Royal Society of Chemistry.[107]

A Zr_{12} acetate cluster was used to synthesise a new phosphine-containing MOF.[108] A solvent mixture of acetic acid and DMF was required to isolate $[Zr_{12}O_8(OH)_8(CH_3COO)_{18}(TPP)_2].4CH_3COOH.n$solvent (TPP = tris(4-carboxyphenyl)-phosphine), which is rare example of a Zr MOF containing a phosphine group.[108]

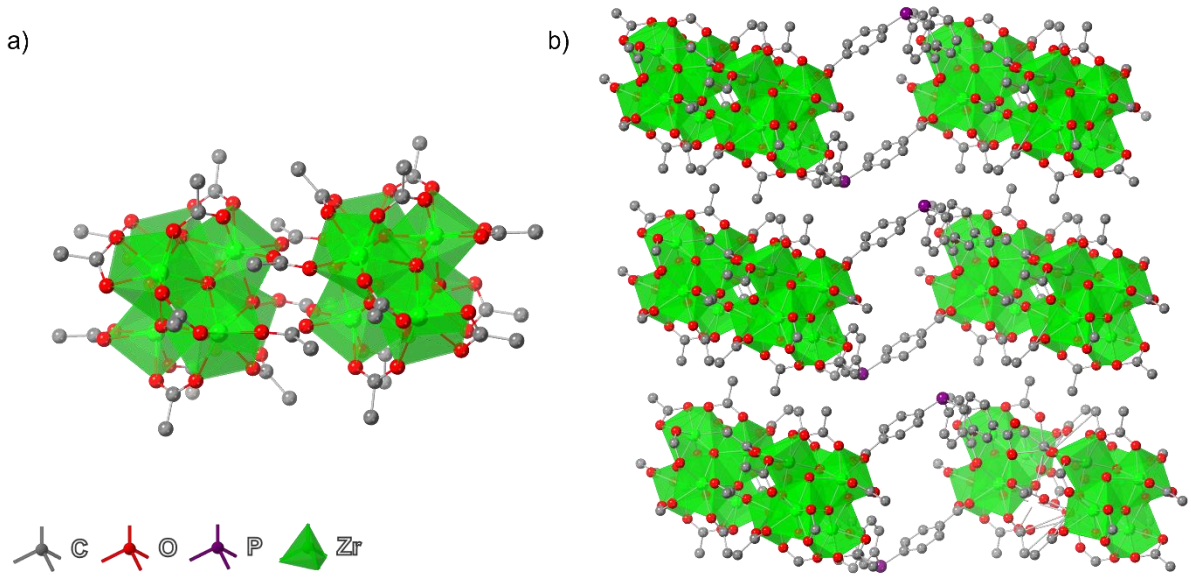

Figure 1.14 – a) Zr_{12} acetate cluster and b) phosphine containing Zr MOF ($[Zr_{12}O_8(OH)_8(CH_3COO)_{18}(TPP)_2]$) along *b*-axis. Hydrogens omitted for clarity.

Another strategy that is becoming increasing popular in the synthesis of stable MOFs, is to utilise covalent chemistry, instead of coordination chemistry, as the framework is built. The resulting materials are known as metal-covalent organic frameworks (MCOFs).[109] In a recent

example, a Cu_3-pyrazolate complex was converted into a framework by a Schiff base reaction that was carried out by grinding and heating.[110]

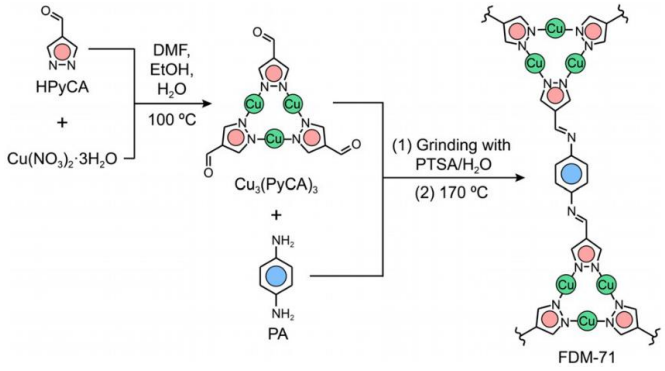

Figure 1.15 – Synthesis of $Cu_3(PyCA)_3$ by coordinating HPyCA with Cu^I, and its subsequent imine condensation with PA to obtain FDM-71. Reprinted with permission from *Angew. Chem. Int. Ed*., 2021, **60**, 2534 –2540. Copyright John Wiley and Sons.[110]

This section has demonstrated that the synthesis of highly crystalline stable MOFs is often challenging, but that several methods can be employed to combat the issues associated with the formation of these materials. As a result, it is possible to access thermally and chemically stable MOFs that can be used in important industrial applications.

1.3 Applications of MOFs

Since MOFs consist of well-defined molecular building blocks, their structure, functionality, and pore size can be controlled at the molecular level via a reticular chemistry approach. This tunability, along with their large surface area and high permanent porosity, has led to extensive research in a diverse array of potential applications such as gas sorption and separation, metal uptake and catalysis.

1.3.1 MOFs as adsorbents

Due to their high porosity and available internal surface area, MOFs are promising adsorbents for many types of compounds, such as small gas molecules (H_2, N_2, O_2, CO_2, and CH_4), fuels, dyes, pharmaceuticals, personal care products, heavy metals, and volatile organic compounds from various waste streams.[111–114] MOFs can be further utilised for the sensing of contaminants in different environments due to the luminescent properties of some MOFs.

Luminescence can be triggered when the MOF selectively adsorbs certain contaminants, allowing these pollutants to be effectively detected.[115–117]

MOFs can be tailored in a number of different ways to enhance their uptake of different types of molecules.[118] For example, when the linker used to form NOTT-101 is replaced with a linker containing an additional pyrimidine group to give UTSA-76a (Scheme 1.1), the additional nitrogens gives rise to interactions with CH_4 molecules, therefore enhancing volumetric uptake from 237 cm^3 (STP) cm^{-3} to 257 cm^3 (STP) cm^{-3}.[119] This an example of the use of additional functional groups in the linker giving rise to favourable interactions with guest molecules and enhancing adsorption capacities.

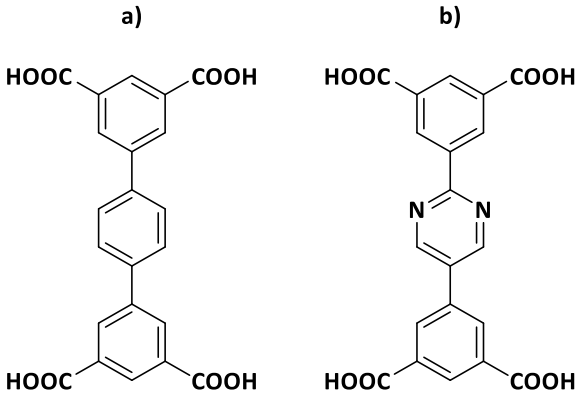

Scheme 1.1 – Structure of the organic ligands used to construct a) NOTT-101 and b) UTSA-76.[119]

In addition to incorporating extra functionality in the MOF structures, the size of the channels inside a MOF can be utilised in size exclusion separations.[120] For example PCN-17 exhibits selective adsorption of H_2 and O_2 over N_2 and CO due to the size-based exclusion of N_2 and CO (kinetic diameters: H_2 = 2.89 Å, O_2 = 3.46 Å, N_2 = 3.64 Å, CO = 3.76 Å).[121] This size exclusion occurs due to the pore window of the MOF being reduced to 3.5 Å by sulfate bridges, creating a doubly interpenetrated network.[122] This type of separation can find use in the separation of H_2 from CO in fuel-cell applications and H_2 enrichment from gas mixtures.

Some MOFs can possess flexibility due to some parts of their framework being supported by weak interactions such H-bonding, π-π stacking and van der Waals forces.[123] Sometimes these flexible characteristics gives rise to enhanced gas adsorption.[120] For example, $Cu_2(pzdc)_2(dpyg)$ (pzdc = pyrazine-2,3-dicarboxylate and dpyg = 1,2-dipyridylglycol), which

contains pendant -OH groups, exhibits a pore opening effect when exposed to guests that are capable of forming H-bonds with the -OH groups.[124]

The presence of coordinatively unsaturated sites (CUSs) can lead to interactions with guest species and increases in the MOFs adsorption capacity. CUSs exist where there are vacant Lewis acidic sites on the metal ions or clusters that are available for coordination. This was seen when MIL-100(Fe) was used for the adsorption of malachite green (a dye) from aqueous solutions. Malachite green possesses tertiary amine groups (Lewis bases) that can replace the water molecules that are bound to the Fe sites (Lewis acids). This was evidenced through zeta potential measurements and XPS data.[125]

MOFs can also be used to remove heavy metals from wastestreams.[118,126–132] As heavy metal removal is a key focus across this thesis, this topic is covered in detail below, with particular focus on Cu(II) and Zn(II) removal.

1.3.2 Metal remediation

1.3.2.1 Anthropogenic heavy metal contamination

Heavy metals are most commonly defined as those with densities exceeding 5 g cm^{-3}.[133,134] Regular concentrations of these metals in the environment are less than < 1000 mg kg^{-1}, and are generally not harmful.[134] However, human activity has led to the accumulation of heavy metals in rural and urban environments, which can lead to interference with plants, animals and ecosystems, and potential harm to human health.[134] Metals such as cadmium (Cd), chromium (Cr), nickel (Ni), arsenic (As, a semi-metal), lead (Pb), zinc (Zn) and copper (Cu) are amongst the most hazardous metals emitted by industry and agriculture due to their high solubility and resulting adsorption by living organisms.[133,135]

A number of heavy metals are vital for human life as they are required for specific bodily functions; for example, copper is required for the production of haemoglobin. However, when the safe concentrations in the body are exceeded, these metals can harm human health, increasing the risk of reduced growth and development of children, organ damage, cancer, nervous system damage and autoimmunity (Table 1.1).[133,136,137]

Table 1.1– Toxicities of heavy metal ion pollutants.

Heavy metal	Health issues arising from toxic levels of heavy metals[137,133,136]
Arsenic	Skin damage, visceral cancers, vascular disease, liver/kidney damage
Cadmium	Lung and kidney damage, fragile bones, anaemia
Chromium	Headache, diarrhoea, nausea, vomiting, cancer
Copper	Anaemia, kidney and liver damage, stomach irritation, insomnia
Lead	Foetal brain damage and kidney, circulatory, and nervous system diseases
Mercury	Rheumatoid arthritis and kidney, circulatory, and nervous system diseases
Nickel	Nausea, chronic asthma, lung damage, cancer in humans
Zinc	Lethargy, increased thirst, digestion problems, depression

There are many different routes in which heavy metals are released into wastewater and agricultural land, including metal mining and milling (Pb and Zn), wood processing (As), petroleum refining (Ni, V, Cr), fertilisers (Cd, Pb and Hg) and pesticides (Cu, Cr, As, Hg, Mn, Pb and Zn), manure (Cu, Zn), coal combustion (Pb, Hg) and petrochemical spillage (Cr, Pb, and Zn).[133,136] The concentrations of these metals found on agricultural land differs greatly from region to region due to the variation in local industries and geology.[138]

Unlike many organic contaminants, metals do not undergo chemical or microbial degradation and therefore their release can result in their accumulation and long-term presence in soil.[136] Excessive levels of heavy metals can be toxic to plant life, inhibiting growth and reducing crop yield.[139] Not only does the presence of heavy metals in agricultural land reduce crop yields, but they also bioaccumulate in plants,[138] which leads to transfer up the food chain through the ingestion of contaminated plants and animals.[136]

1.3.2.2 Digital dermatitis and footbath treatment in dairy cattle

Digital dermatitis (DD) is one of the most common contagious diseases in herds of housed dairy cattle in many countries, including the United States, United Kingdom, Japan and New Zealand.[142] It is a bacterial disease which usually affects the skin on the heel or between the digits of cattle, causing inflammation which can progress into large and painful ulcerative lesions.[143,144,145] Serious cases of DD may lead to lameness, or in the worst cases, death. This can have an economic impact on the farm due to the resulting decrease in milk

production.[142,144] There is also much concern over animal welfare in cattle herds where DD is prevalent.[144]

Commonly, disinfecting footbaths containing antimicrobial compounds are used to try to prevent DD. The cattle walk through the footbath after milking in order to harden the hoof, improve hoof hygiene and reduce the microbial population present on the hoof.[142] A variety of antimicrobials are used worldwide, including copper sulfate, zinc sulfate, formaldehyde and antibiotics such as lincomycin and oxytetracycline.[142,146,147] A survey undertaken by Cook *et al.* reported that across 65 dairy herds located in United States, United Kingdom, Spain, Japan, and New Zealand, the most commonly used agent for preventing DD was copper sulfate, with 63% of the farms using it.[148]

After the footbaths have been used by the cattle, the used solutions must be disposed of.[147] Current reported procedures suggest that the used footbath solution is transferred to a waste slurry tank, which is intermittently transferred with manure onto surrounding areas of the farm, leading to the concentrations of Cu and Zn in soil building up (Figure 1.16).[142] Studies in Oregon have shown that a large proportion of soil samples (75%) taken on dairy farms contained high Cu concentrations (> 2 ppm).[147] As well as previously mentioned concerns over polluting the environment with metals, there is risk that these metals may encounter antibiotics that are used within dairy farming (partially metabolised antibiotics are excreted by the cows). When metals and antibiotics interact they can act as co-selectors for antimicrobial resistance.[149] This could be detrimental as it may lead to the development and spread of AMR in the dairy farming environment.

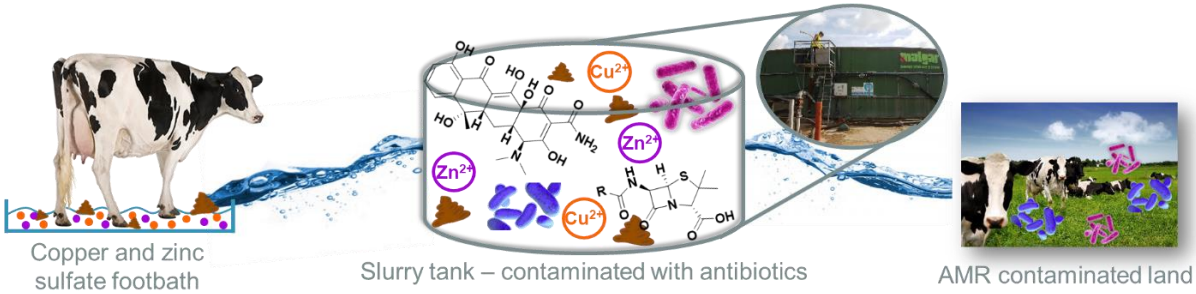

Figure 1.16 – Cattle walk through footbath solutions containing copper and zinc sulfate (left). The waste footbath solutions and placed into slurry tanks that also contain antibiotics from other waste on the farm (middle). This slurry tank mixture is spread onto land and the environment become contaminated with heavy metals, antibiotics and antimicrobial resistant bacteria (right).

Throughout this thesis, an emphasis will be placed on the application of MOFs for metal removal from waste cattle footbath solutions. For this reason, the following sections focus on reviewing the prospect of MOFs for removing Cu(II) and Zn(II) from wastewater streams.

1.3.2.3 Removing heavy metals from wastewater

Many techniques exist for the removal of heavy metals from wastewater.[133,150,151,152] Table 1.2 gives brief explanations and shows some of the advantages and disadvantages of the most commonly used techniques. In practice, often several methods will be used to increase the efficacy of the removal.

Table 1.2 - Heavy metal removal techniques

Technique	Description	Advantages	Disadvantages
Adsorption[153]	Highly porous materials are used to sequester metals by means of a chemical or physical interaction to an active site	Cheap, simple operating conditions, wide pH range, high uptake	Low selectivity, waste products formed if desorption is not possible
Chemical precipitation[154]	Chemicals are added to initiate the formation of precipitates that are insoluble, these solids are then separated by filtration	Simple operation	Use of reagents, production of solid wastes
Coagulation[155]	Colloids are destabilised by the addition of a coagulant, larger particles form which are more easily separated from the water *via* sedimentation	Cost effective	Must be used alongside other treatment techniques
Electrochemical treatment[156]	An electropotential is applied, inducing reactions that remove pollutants	High selectivity	High costs due to high energy use and electrode replacement
Ion exchange[157]	Ions in the wastewater are substituted for other ions by using a resin	High uptake	Low selectivity, production of waste if recycling is not possible
Membrane filtration[154]	A porous material separates the particles based on size, concentration, pH and applied pressure	High selectivity, low pressure, little space needed	High costs due to membrane replacement, complex process

Out of these techniques, adsorption has been hailed as the most effective way to treat water owing to its low cost, high efficiency and operational simplicity.[151,158,159] Other removal

techniques rely on sensitive operating conditions or result in costly disposal of waste materials.[158] Effective adsorbents typically have high surface areas and high densities of functional groups. Moreover, desorption of the bound ions is possible, making some adsorbents recyclable.[151]

The adsorption process is either chemical or physical, depending on the types of interaction that occur between the porous material and the adsorbate. Physical adsorption occurs when weak van der Waals forces hold the adsorbate in place. Chemical adsorption occurs when a chemical bond is formed between the adsorbate and adsorbent. Regeneration of a chemical adsorbent usually requires chemical treatment.[111] Some key adsorption mechanisms are defined as follows: [111]

- Adsorption onto a coordinatively unsaturated site.
- Adsorption *via* an acid-base mechanism.
- Adsorption *via* π-complex formation.
- Adsorption through hydrogen bonding formation.
- Adsorption due to electrostatic interaction.

Adsorption efficiency is determined by the capacity, selectivity, and the stability of the adsorbent and how well they can be regenerated.[111] Currently, the most used widely used adsorbents for contaminants from wastewater are activated carbons (ACs),[160–165] carbon nanotubes,[160,166,167] clays,[168–170] zeolites,[171–173] porous silicas[174] and graphene oxides.[160,175] However, most of these materials suffer from significant drawbacks, such as relatively low surface areas or a lack of tailorability.[129] MOFs, on the other hand, can possess extremely high surface areas (up to 7,000 $m^2\ g^{-1}$)[3] and easily tailorable pore sizes and functionalities.[176] In addition to this, MOF synthesis conditions tend to be milder (100-200 °C, for the MOFs discussed below) than other common adsorbents, such as ACs (800-900 °C), thus reducing the energy requirements of synthesis.[86]

A wide range of MOFs have been shown to remove heavy metals from aqueous solutions.[111,118,127–129,131,177,178] Below, some of the main themes concerning MOFs for metal removal are addressed, focusing primarily on Cu(II) and Zn(II), alongside some key examples that are relevant to the work carried out in this thesis.

MOFs can contain Lewis basic groups (either in the linkers or in molecules added through PSM) which give rise to heavy metal adsorption through acid-base interactions.[8] Lewis acids and bases can be defined as hard or soft in character, as defined in Table 1.3.[179,85] According to HSAB theory, 'hard acids prefer to bind to hard bases and soft acids prefer to bind to soft bases'.[85] Both Cu(II) and Zn(II) are borderline Lewis acids (see Table 1.3),[179,85] which means that they have no strong thermodynamic preference between binding to hard or soft Lewis bases. Widely used groups for the coordination of these heavy metals are carboxylates, hydroxyls, thiols, azines and amino groups.[180–182] Figure 1.17 gives some examples of the compounds that have been used in MOF synthesis to promote heavy metal adsorption.

Table 1.3 - A selection of Lewis acid and bases classified by HSAB theory

Hard (high electronegativity and oxidation states, low polarizability)	**Borderline**	**Soft** (low electronegativity and oxidation states, high polarizability)
Acids		
H^+, Na^+, Mg^{2+}, Ca^{2+}, Al^{3+}, As^{3+}, Zr^{4+}, Cr^{3+}, Co^{3+}, Fe^{3+}	Fe^{2+}, Co^{2+}, Ni^{2+}, Cu^{2+}, Zn^{2+}, Pb^{2+}	Cu^+, Ag^+, Au^+, Hg^{2+}, Cd^{2+}
Bases		
H_2O, ^-OH, COO^-, NH_3, F^-, Cl^-	$C_6H_5NH_2$, C_5H_5N, Br^-	R_2S, RSH, RS^-, I^-, CN^-, RNC, CO, C_6H_6

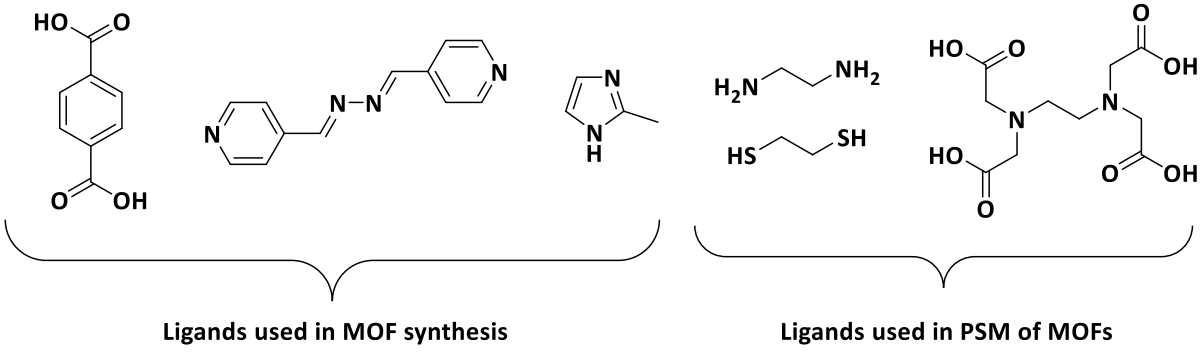

Figure 1.17 – (From left to right): Terephthalic acid, 1,4-bis(4-pyridyl)-2,3-diaza-1,3-butadiene, 2-methylimidazole, ethylenediamine, 1,2-ethanedithiol, ethylenediaminetetraacetic acid (EDTA).

Copper terephthalate has a promising adsorption capacity for both Cu(II) (210 mg g^{-1}) and Zn(II) (140 mg g^{-1}), including achieving reasonable removal efficiencies from real acid rock drainage samples (88% for Cu(II) and 53% for Zn(II)).[180] In addition, functionalisation of UiO-66(Zr) with Lewis basic groups such as NH_2 and COOH achieved higher Cu(II) uptake; 6 mg g^{-1} for UiO-66(Zr)-NH_2 and 20 mg g^{-1} for UiO-66(Zr)-2COOH, compared to 4 mg g^{-1} for the original UiO-66(Zr).[181] It was suggested that the difference in adsorption capacity occurs due to the

presence of uncoordinated carboxylate groups (Lewis bases) on adjacent organic ligands in UiO-66(Zr)-2COOH, which are able to chelate the Cu(II) ions.[181]

1.3.2.4 Using post-synthetic modification to enhance heavy metal uptake

Post synthetic modification (PSM) can be an effective way to add Lewis basic functionality to MOFs. MIL-101, which contains tri-nuclear chromium clusters that possess coordinatively unsaturated sites, was grafted with ethylenediamine (ED) to give a material functionalised with amine groups (Figure 1.18).[182]

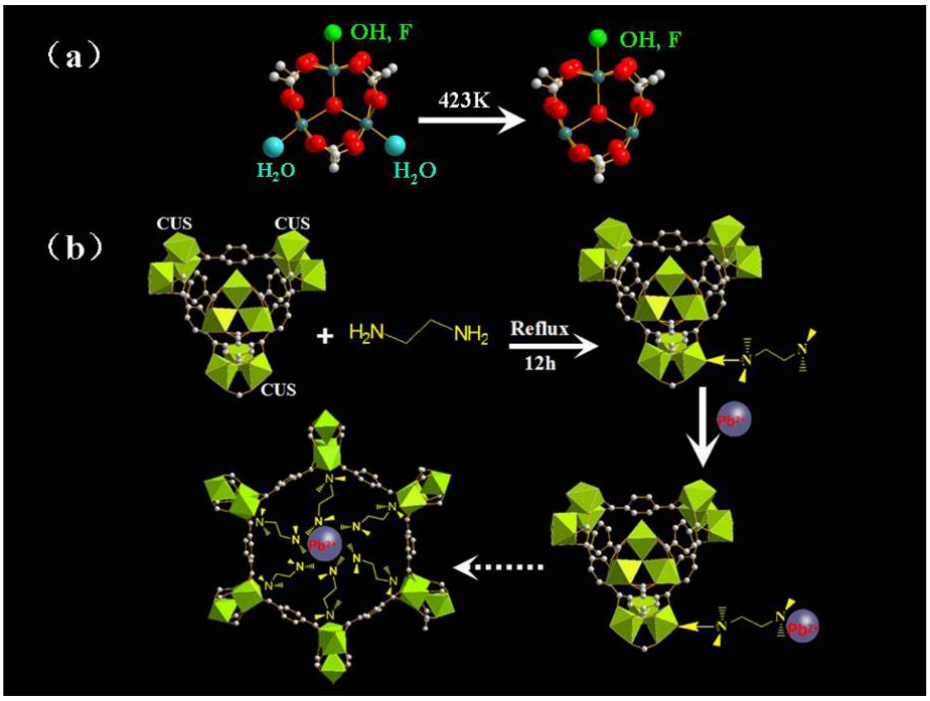

Figure 1.18 - (a) Generation of coordinatively unsaturated sites from chromium tri-nuclear clusters in MIL-101 after vacuum treatment at 423 K for 12 h; (b) Adsorption principle of amino-functionalized MIL-101 for Pb(II) ions. Reprinted with permission from *J. Chem. Eng. Data,* 2015, 60, 1732−1743. Copyright 2015 American Chemical Society.

Compared to unfunctionalised MIL-101, ED-MIL-101 possesses a much higher adsorption capacity for Pb(II) due to the presence of amino groups, suggesting that nitrogen atoms in the grafted ED are involved in the Pb(II) uptake process.[182] The adsorption of Cu(II), Ni(II), Co(II) and Zn(II) was also tested and ED-MIL-101 had a much stronger affinity for Cu(II) and Ni(II), than Co(II) and Zn(II). This result can be explained by examining EDTA complexation constants for these metals—they are higher for Pb(II), Cu(II) and Ni(II), confirming that the nitrogen donor atoms match these metals well as intermediate Lewis acids and bases. The authors also

suggested that Pb(II) is absorbed much more strongly than the other metals because the pore structure of the MOF matches the size of Pb.[182] The adsorption of metals from environmental water samples (lake water and river water) was also analysed, giving good results (Pb(II) levels in solution were reduced to 0.49 mg L^{-1} and 0.28 mg L^{-1}, respectively from 10 mg L^{-1}).[182]

More recently, a "versatile trap" for heavy metal ions was reported.[8] PSM was carried out on MOF-808 to graft EDTA into the pores of the MOF (see Figure 1.19).[8] EDTA was chosen as it contains six binding sites, four hard-base carboxyl and two softer-base amine groups that can bind to a large range of heavy metal species. MOF-808-EDTA removed 22 different heavy metals (including soft, hard and borderline acids) from aqueous solutions with >99% removal efficiency.[8] This efficiency was maintained when the MOF was exposed to multiple metals at a time. Furthermore, the material was regenerated by washing with EDTA-2Na solution and greater than 90% removal was still retained over further cycles.

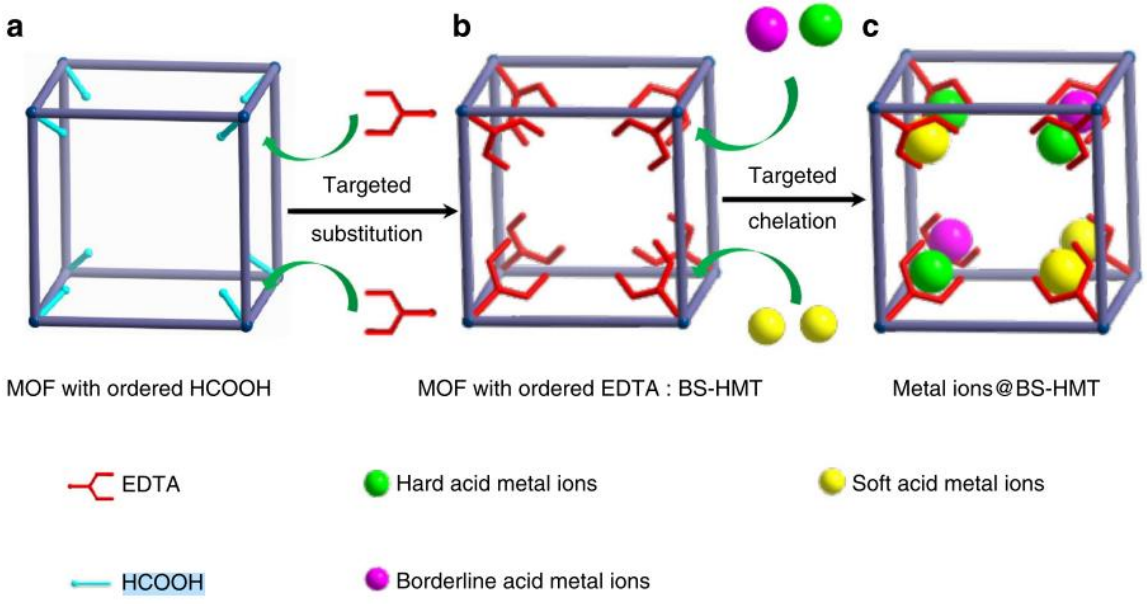

Figure 1.19 – Scheme showing the broad-spectrum heavy metal trap concept. a) The ordered HCOOH in MOF-808 can be substituted by EDTA to form, b) MOF-808 with ordered EDTA, which can be used as c) a trap for metal ion capture. Reprinted with permission from *Nature Comms.*, 2018, 9:187.[8]

Another important example of a material that exhibits very high uptake for Cu(II) (up to 800 mg g^{-1}) is ZIF-8.[183] Despite this high value for uptake, post-experiment ICP-OES analysis on the metal-containing aqueous solution showed that exchange of Cu(II) with framework Zn(II) was occurring. This ion exchange effect was further evidenced by TEM (change in particle morphology), FTIR (presence of Cu-N stretching) and PXRD (disappearance of long range ZIF-

8 structure) analyses. ZIF-8 is therefore undergoing ion exchange, rather than sorption, which means the MOF structure has been altered.[183]

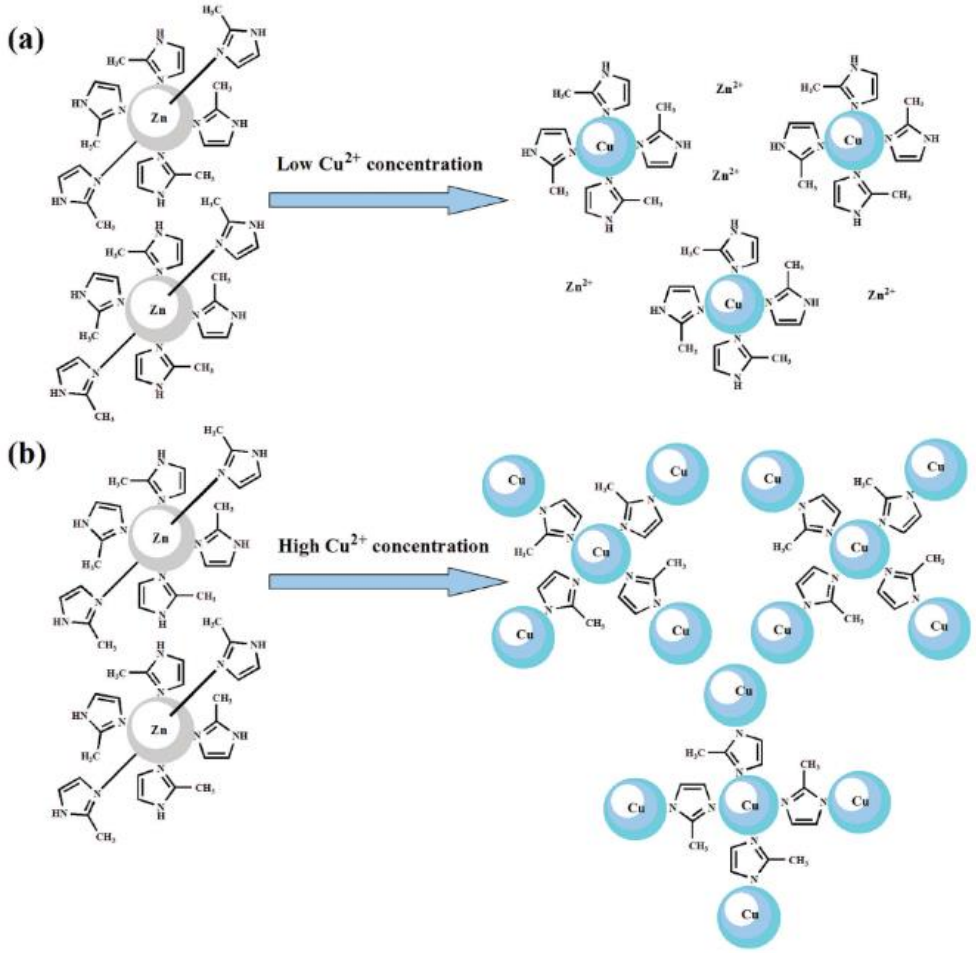

Figure 1.20 - The schematic showing the adsorption mechanism of Cu(II) in aqueous solutions by using ZIF-8 nanocrystals. (a) Ion exchange reaction at a low concentration of Cu(II); (b) coordination reaction between Cu(II) and the nitrogen atom on 2-methylimidazole at a high concentration of Cu(II).[183] Reprinted with permission from *Dalton Trans.*, 2016, **45**, 12653–12660. Copyright (2016) Royal Society of Chemistry.[183]

Overall, ion exchange by MOFs (or other adsorbents) is not an attractive way to remove metals from wastewater as it results in contamination of the water with another, although potentially less harmful, metal. It also results in the MOF being non-reusable. In an ideal world, the heavy metal will adsorb and desorb from the MOF, and the original framework will stay intact.

1.3.3 Catalysis

The key properties (permanent porosity, varied topologies, tunability of components) that MOFs possess have led to a broad interest in their use as heterogeneous catalysts.[184,185]

Specifically, MOFs have distinct characteristics that give rise to their catalytic activity. Firstly, Lewis acidic sites on coordinatively unsaturated metal sites (CUS) can be made available by removing solvent or through introducing defects into the MOFs structure.[186,187] For example, Kaskel *et al.* showed that the copper-bound water molecules in $Cu_3(BTC)_2(H_2O)_3$ can be removed to give coordinatively unsaturated copper sites that can catalyse the cyanosilylation of benzaldehyde by TMSCN.[188]

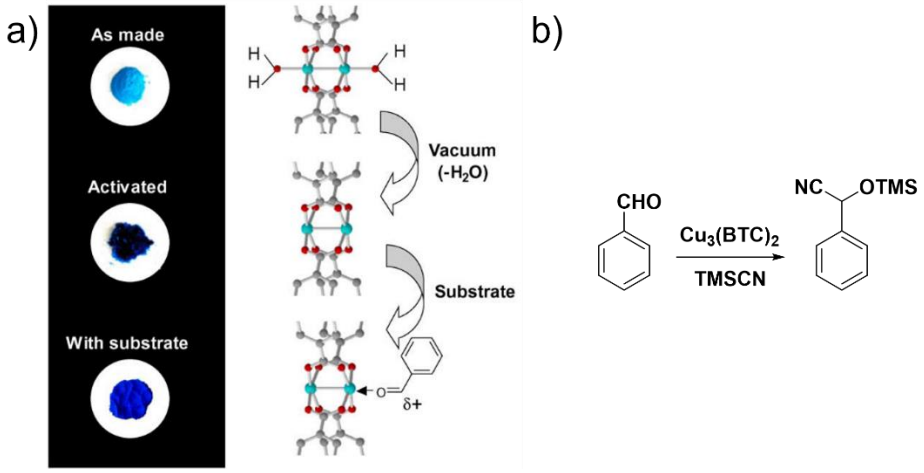

Figure 1.21 – a) Colour and structural changes during the dehydration of $Cu_3(BTC)_2(H_2O)_3$ and absorption of an aldehyde. b) Cyanosilylation of benzaldehyde with TMSCN, using $Cu_3(BTC)_2$ as a catalyst. Adapted with permission from *Microporous and Mesoporous Materials,* 2004, **73**, 81–88. Copyright 2004 Elsevier.[188]

Brønsted acid[189] and base sites[190] can be incorporated either *via* the linker itself, through PSM of the linker to add a catalytic site, or through incorporation of a guest molecule into the pores of the MOF.[191,192] An interesting example of this was carried out by Cao *et al.* where LIFM-80 was modified with secondary or ternary ligands, as well as copper metalation to create catalysts for a range of reactions.

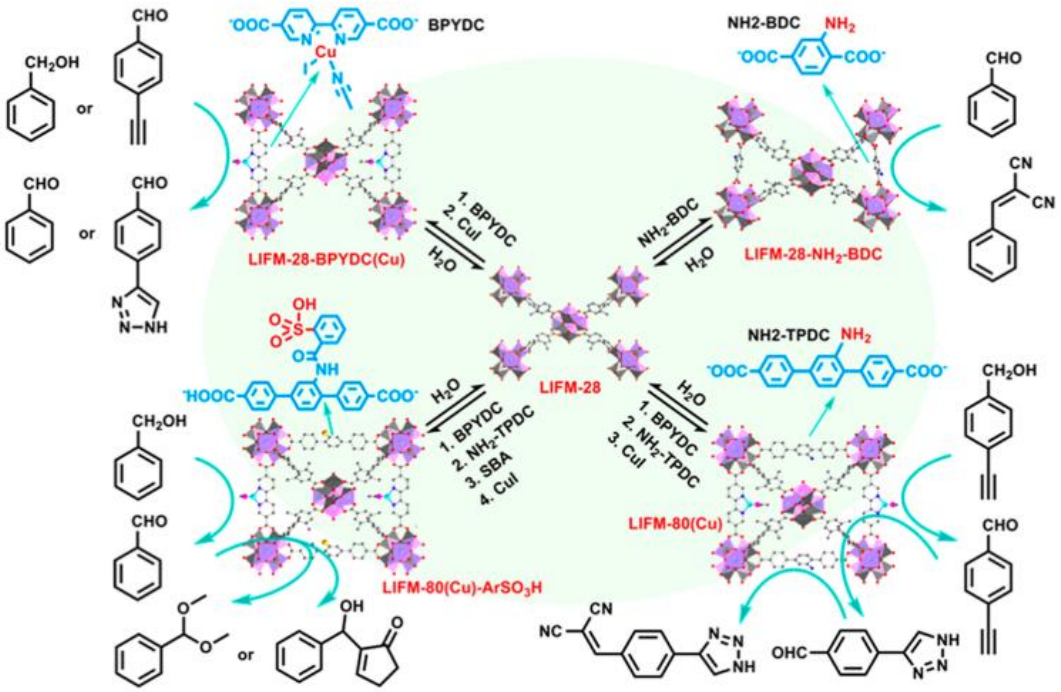

Figure 1.22 - Generation of multivariate MOF catalysts via the dynamic spacer installation approach using proto-LIFM-28 and the resultant interconversions for different catalytic purposes. The molecular structures of the inserted functional spacers are illustrated for the crystal structures, in which the −$ArSO_3H$ group is simplified as an orange ball and Zr_6-clusters are shown as purple polyhedrons. H and F are omitted for clarity. Reproduced with permission from *J. Am. Chem. Soc*., 2019, **141**, 2589−2593. Copyright 2019 American Chemical Society.[193]

Also, metal nanoparticles (MNPs) can be occluded in the MOF pores.[194–196] Ni@UiO-66, synthesised *via* solution impregnation of $Ni(NO_3)_2$ and subsequent reduction to Ni NPs inside the UiO-66, has been used as a catalyst for the reduction of CO_2 to CH_4. The catalyst showed superior performance compared to more widely used systems, such as Ni/ZrO_2 and Ni/SiO_2.[197]

The use of MOFs containing MNPs is becoming a popular choice for catalysing cross-coupling reactions.[198] Pd/MIL-101(Cr) has been used to catalyse the Suzuki-Miyaura cross-coupling reaction, showing greater catalytic activity than Pd^{2+}/MIL-101(Cr), Pd/C and Pd/ZIF-8.[199] Elsewhere, Pd/MIL-101(Cr) has also been used to catalyse the Sonogashira cross-coupling reaction.[200]

Finally, photoactive materials can be incorporated into MOFs (see next section).[9]

1.3.3.1 Photocatalysis

Due to the ever-increasing global energy demand, there is the need to development materials that harness solar energy to carry out important transformations. Thus, an alternative and potentially sustainable approach to catalysis is the use of photocatalysis. Photocatalysis allows solar energy to be converted into chemical energy. An early example of this was reported in 1972, when hydrogen was produced through UV-light driven water splitting by semiconducting TiO_2.[201] Recently, MOFs have emerged as a new type of photocatalytic material. Through their modular structure, inorganic semiconductors and photoactive molecular organic materials can be incorporated into their structure, *via* the metal node and organic linker, respectively. The ability to tune the distance and orientation between these photoactive components (and at the same time prevent chromophore aggregation)[202] is also key to designing materials where energy transfer processes can be controlled and understood.[203] In addition, their high surface area and porosity of MOFs allows for efficient mass transport and ion conductivity.[204]

MOF-5 was one of the first MOFs to be applied in photocatalysis, when it was shown to photocatalytically degrade phenol in aqueous environments.[205] Later this prototypical MOF was shown to be structurally unstable in aqueous solution,[206] and MOFs with proven structural stability came to the forefront of research in this area. Garcia and co-workers investigated the use of UiO-66, the high stability of which has been discussed previously (see Section 1.2), for the production of hydrogen from methanol under UV-vis irradiation.[207] In this investigation it was shown that functionalisation of the linker with an amino group led to a bathochromic shift in the optical spectrum of the MOF, suggesting that the linker can be tuned to shift the wavelength of light required to produce the excited state, into the visible region. This tuning of adsorption wavelength is important because photocatalysts rely on the excitation by light to produce charge carriers, so expanding the adsorption range, or moving into the visible region, can increase a photocatalysts' efficiency.[208]

In addition to their stability, Ti-MOFs have been shown to possess excellent photocatalytic activity.[209,210] For example, Ti-MOFs have been applied to CO_2 reduction,[211,212] water splitting,[213,214] and p-type semiconductors.[215] Serre and co-workers reported an early use of a Ti-MOF as a catalyst when they synthesised MIL-125(Ti) and showed it can be employed in

the oxidation of an alcohol with concomitant reduction of the Ti metal centre under UV-vis irradiation.[216] Later, an amino-functionalised version of MIL-125(Ti) was reported, with the extra amino group giving rise to an extra adsorption band, at around 550 nm, in the visible light region of the UV-vis spectra. This enhanced adsorption was utilised in the photocatalytic reduction of CO_2 under visible light irradiation (the non-functionalised MIL-125(Ti) material is inactive under the same conditions), in the presence of a sacrificial agent (triethanolamine - TEOA).[211] Further studies were conducted to elucidate the reaction mechanism. When the reaction mixture (NH_2-MIL-125(Ti) and triethanolamine in MeCN) was exposed to visible light and N_2, the suspension turned from yellow to green. In the presence of CO_2 and O_2, the suspension slowly changed back to bright yellow. This photochromic phenomenon is ascribed to intervalence charge transfer between Ti(III) and Ti(IV), which is supported by electron spin resonance (ESR) indicating the presence of Ti(III) when the suspension is green in colour.[211] The Ti(III) is formed through a process known as Ligand to Metal Charge Transfer (LMCT), which occurs through the excitation of the organic ligand through visible light adsorption, and then an electron transfer from the organic ligand to the Ti(IV) centres (Figure 1.23).[211]

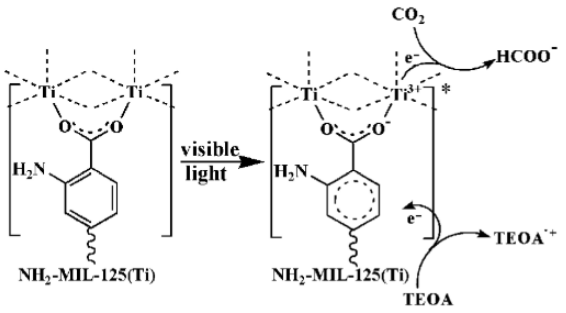

Figure 1.23 - Proposed mechanism for the photocatalytic CO_2 reduction over NH_2-MIL-125(Ti) under visible light irradiation. Reprinted with permission from *Angew. Chem. Int. Ed.*, 2012, **51**, 3364 –3367. Copyright (2012) John Wiley & Sons.[211]

In addition to the LMCT reaction, iron(III)-based MOFs can be directly excited, with electron transfer occurring between the O^{2-} in the Fe(III)-O cluster to form Fe(II). As such, both MIL-101(Fe) and MIL-88(Fe) have been shown to photodegrade Rhodamine 6G in aqueous solution.[217]

As well as expanding the light adsorption range through amino-functionalisation of common MOF ligands, more specialised linkers containing conjugated systems can be used to improve photo efficiency even further.[218] An example of this is the use of porphyrins, which are

strongly coloured ligands that adsorb light across the whole visible region. PCN-222, a MOF containing tetrakis(4-carboxyphenyl)-porphyrin (H_2TCPP) coordinated to Zr_6 clusters, exhibits high CO_2 uptake and absorbs light in the region of 200-800 nm.[219] It can be employed as a photocatalyst for the reduction of CO_2, in the presence of TEOA and MeCN as the solvent. The mechanism is similar to that described for NH_2-MIL-125(Ti) above, where the H_2TCPP absorbs visible light, becoming excited, and then transfers electrons to the Zr oxo clusters (ESR confirmed presence of Zr(III) ions).[219]

Naphthalene diimides (NDIs) are another type of compound that can be used in MOFs to produce photocatalytic materials.[204] When reduced to their electrochemically stable radical anion ($NDI^{\bullet-}$), they adsorb light from 400-800 nm and have a strong reducing potential.[220] As Chapter 4 covers the synthesis of MOFs containing NDIs, the synthesis, characterisation and applications of these types of materials will be covered in detail at the start of Chapter 4.

1.4 Research Directions

This thesis explores the synthesis and applications of stable MOFs. Group III and IV metals are used to ensure the formation of strong metal to oxygen bonds, which should enhance the stability of the resulting materials. Exploring the synthesis conditions to form these MOFs is a key focus of this thesis and the influence of temperature, solvents, modulator, and reactant ratio is explored.

Chapter 2 summarises the techniques that were used throughout this work to characterise the materials that were synthesised. Powder X-Ray diffraction (PXRD) features heavily in this thesis as it used to analyse the phases present in the synthesised materials. It is also used to analyse the stability of the materials after they are subjected to different conditions that may be present if the materials are used in real-world applications. Thermogravimetric analysis (TGA) is also used frequently, primarily to identify the thermal stability of the synthesised MOFs and to determine if activation procedures have been successful. It is also used to calculate the ratio of metal to organic material in some new and unknown products.

Chapter 3 is centred on the synthesis of MOFs for Cu(II) uptake. The MIL-53(Al) family of MOFs was explored, as the review of the literature showed that MOFs that contain Lewis basic functional groups frequently exhibit higher levels of heavy metal uptake and that MOFs

containing high valence metals are often highly stable. Microwave heating was used to form these MOFs quickly and efficiently. Investigations into improving the yield and purity of the materials obtained by adjusting the reaction conditions were carried out. The stability of the synthesised materials was examined, and metal uptake experiments were carried out to determine if the MOFs were suitable for use as industrial sorbents.

Chapter 4 turns to look at the synthesis of stable Group IV naphthalene diimide (NDI) MOFs, in the hope of making use of the interesting electrochemical properties of the NDIs. NDIs containing carboxyl and hydroxyl groups for coordination were synthesised and employed in MOF synthesis. Once again, it was hoped that employing a high valence metal and an oxygen-containing coordination group would enhance the stability of the resulting framework materials. Combining the difficulties of working with barely soluble NDIs and synthesising MOFs containing Group IV metals meant that particular attention was paid to varying the reaction conditions used to improve the crystallinity of the materials obtained. The use of Ti(IV) clusters was also investigated, with attempts to use covalent chemistry to form extended frameworks.

Chapter 5 concludes this thesis, providing a summary of key findings and suggesting future directions of study.

1.5 References

1 H. Furukawa, K. E. Cordova, M. O'Keeffe and O. M. Yaghi, Science, 2013, **341**, 1230444.
2 J. L. C. Rowsell and O. M. Yaghi, *Microporous Mesoporous Mater.*, 2004, **73**, 3–14.
3 O. K. Farha, I. Eryazici, N. C. Jeong, B. G. Hauser, C. E. Wilmer, A. A. Sarjeant, R. Q. Snurr, S. T. Nguyen, A. Ö. Yazaydin and J. T. Hupp, *J. Am. Chem. Soc.*, 2012, **134**, 15016–15021.
4 P. Falcaro, R. Ricco, C. M. Doherty, K. Liang, A. J. Hill and M. J. Styles, *Chem. Soc. Rev.*, 2014, **43**, 5513–5560.
5 J. R. Li, J. Sculley and H. C. Zhou, *Chem. Rev.*, 2012, **112**, 869–932.
6 M. P. Suh, H. J. Park, T. K. Prasad and D. W. Lim, *Chem. Rev.*, 2012, **112**, 782–835.
7 J. Long, O. Yaghi, A. U. Czaja, N. Trukhan and U. Muïler, *Chem. Soc. Rev.*, 2009, **38**, 1289–1293.
8 Y. Peng, H. Huang, Y. Zhang, C. Kang, S. Chen, L. Song, D. Liu and C. Zhong, *Nat. Commun.*, 2018, **9**, 187.
9 S. A. Dhakshinamoorthy, Z. Li, H. Garcia and A. Dhakshinamoorthy, *Chem. Soc. Rev*, 2018, **47**, 8134.
10 J. Liu, L. Chen, H. Cui, J. Zhang, L. Zhang and C.-Y. Su, *Chem. Soc. Rev*, 2014, **43**, 6011.
11 P. Horcajada, R. Gref, T. Baati, P. K. Allan, G. Maurin, P. Couvreur, G. Férey, R. E. Morris and C. Serre, *Chem. Rev.*, 2012, **112**, 1232–1268.
12 B. F. Hoskins and R. Robson, *J. Am. Chem. Soc.*, 1989, **111**, 5962–5964.
13 B. F. Hoskins and R. Robson, *J. Am. Chem. Soc.*, 1990, **112**, 59.
14 O. M. Yaghi, G. Li and H. Li, *Nature*, 1995, **378**, 703–706.
15 H. Li, M. Eddaoudi, M. O'Keeffe and O. M. Yaghi, *Nature*, 1999, **402**, 276.
16 S. S-Y Chui, S. M-F Lo, J. P. H Charmant, A. Guy Orpen and I. D. Williams, *Science,* 1999, **283**, 1148–1150.
17 S. L. Griffin and N. R. Champness, *Coord. Chem. Rev.*, 2020, **414**, 213295.
18 Y. Yan, S. Yang, A. J. Blake and M. Schroder, *Acc. Chem. Res.*, 2013, **47**, 296–307.
19 B. Chen, Z. Yang, Y. Zhu and Y. Xia, *J. Mater. Chem. A.*, 2014, **2**, 16811–16831.
20 X. Liu, Y. Zhou, J. Zhang, L. Tang, L. Luo and G. Zeng, *ACS Appl. Mater. Interfaces*, 2017, **9**, 20275.
21 M. Gaab, N. Trukhan, S. Maurer, R. Gummaraju and U. Müller, *Microporous Mesoporous Mater.*, 2012, **157**, 131–136.
22 V. Bon, I. Senkovska, I. A. Baburin and S. Kaskel, *Cryst. Growth Des.*, 2013, **13**, 1231–1237.
23 F. A. Almeida Paz, J. Klinowski, S. M. F Vilela, J. P. C Tomé, J. A. S Cavaleiro, J. Rocha, rgio M. F Vilela, ac P. Joaõ C Tome, A. S. Cavaleiro and J. Rocha, *Chem. Soc. Rev.*, 2012, **41**, 1088–1110.
24 J. H. Cavka, C. Lamberti, N. Guillou, S. Bordiga, S. Jakobsen, U. Olsbye, N. Guillou, S. Bordiga and K. P. Lillerud, *J. Am. Chem. Soc.*, 2008, **130**, 13850–13851.
25 T. Loiseau, C. Serre, C. Huguenard, G. Fink, F. Taulelle, M. Henry, T. Bataille and G. Férey, *Chem. Eur. J.*, 2004, **10**, 1373–1382.
26 W.-Y. Gao, M. Chrzanowski and S. Ma, *Chem. Soc. Rev.*, 2014, **43**, 5841.
27 M. Eddaoudi, J. Kim, N. Rosi, D. Vodak, J. Wachter, M. O'Keeffe and O. M. Yaghi, *Science*, 2002, **295**, 469.
28 B. Q. Ma, K. L. Mulfort and J. T. Hupp, *Inorg. Chem.*, 2005, **44**, 4912–4914.
29 H. Furukawa, J. Kim, N. W. Ockwig, M. O'Keeffe and O. M. Yaghi, *J. Am. Chem. Soc.*, 2008, **130**, 11650–11661.
30 W. Lu, Z. Wei, Z. Y. Gu, T. F. Liu, J. Park, J. Park, J. Tian, M. Zhang, Q. Zhang, T. Gentle, M. Bosch and H. C. Zhou, *Chem. Soc. Rev.*, 2014, **43**, 5561–5593.
31 S. Surblé, C. Serre, C. Mellot-Draznieks, F. Millange and G. Férey, *Chem. Commun.*, 2006, 284–286.
32 H. D. Lawson, S. P. Walton and C. Chan, *ACS Appl. Mater. Interfaces*, 2021, **13**, 7004–7020.
33 J. Gascon, U. Aktay, M. D. Hernandez-Alonso, G. P. M. van Klink and F. Kapteijn, *J. Catal.*, 2009, **261**, 75–87.
34 J. Lu, A. Mondal, B. Moulton and M. J. Zaworotko, *Angew. Chem. Int. Ed.*, 2001, **40**, 2113–2116.
35 L. Xie, S. Liu, C. Gao, R. Cao, J. Cao, C. Sun and Z. Su, *Inorg. Chem.*, 2007, **46**, 7782.
36 M. Kramer, U. Schwarz and S. Kaskel, *J. Mater. Chem.*, 2006, **16**, 2245–2248.
37 L. J. Murray, M. Dinca, J. Yano, S. Chavan, S. Bordiga, C. M. Brown and J. R. Long, *J. Am. Chem. Soc.*, 2010, **132**, 7856–7857.
38 O. Kozachuk, K. Yusenko, H. Noei, Y. Wang, S. Walleck, T. Glaser and R. A. Fischer, *Chem. Commun*, 2011, **47**, 8509–8511.
39 C. R. Wade and M. Dincă, *Dalton Trans.*, 2012, **41**, 7782–7791.
40 M. Lammert, M. T. Wharmby, S. Smolders, B. Bueken, A. Lieb, K. A. Lomachenko, D. De Vos and N. Stock, *Chem. Commun.*, 2015, **51**, 12578–12581.

41 C. Serre, F. Millange, C. Thouvenot, M. Noguès, G. Marsolier, D. Louër and G. Férey, *J. Am. Chem. Soc.*, 2002, **124**, 13519–13526.
42 F. Millange, N. Guillou, R. I. Walton, J. M. Grenèche, I. Margiolaki and G. Férey, *Chem. Commun.*, 2008, 4732–4734.
43 G. F. Franck Millange, Christian Serre, *Chem. Commun.*, 2002, 822–823.
44 Z. Hu, A. Nalaparaju, Y. Peng, J. Jiang and D. Zhao, *Inorg. Chem*, 2016, **55**, 1134−1141.
45 N. Stock and S. Biswas, *Chem. Rev.*, 2012, **112**, 933–969.
46 T. Friscic, *J. Mater. Chem. A*, 2010, **20**, 7599–7605.
47 D. Crawford, J. Casaban, R. Haydon, N. Giri, T. McNally and S. L. James, *Chem. Sci.*, 2015, **6**, 1645–1649.
48 V. M. V. and G. Nageswaran, *J. Electrochem. Soc.*, 2020, **167**, 155527.
49 H. Al-Kutubi, J. Gascon, E. J. R. Sudhölter and L. Rassaei, *ChemElectroChem*, 2015, **2**, 462–474.
50 J. Klinowski, F. A. Almeida Paz, P. Silva and J. Rocha, *Dalton Trans.*, 2011, **40**, 321-330.
51 G. X. Liu, H. Xu, H. Zhou, S. Nishihara and X. M. Ren, *CrystEngComm*, 2012, **14**, 1856–1864.
52 A. K. Cheetham, C. N. R. Rao and R. K. Feller, *Chem. Commun.*, 2006, 4780–4795.
53 L. Huang, H. Wang, J. Chen, Z. Wang, J. Sun, D. Zhao and Y. Yan, *Microporous Mesoporous Mater.*, 2003, **58**, 105–114.
54 D. J. Tranchemontagne, J. R. Hunt and O. M. Yaghi, *Tetrahedron*, 2008, **64**, 8553–8557.
55 J. Cravillon, S. Münzer, S. J. Lohmeier, A. Feldhoff, K. Huber and M. Wiebcke, *Chem. Mater.*, 2009, **21**, 1410–1412.
56 A. Rabenau, *Angew. Chemie Int. Ed*, 1985, **24**, 1026–1040.
57 E. Biemmi, S. Christian, N. Stock and T. Bein, *Microporous Mesoporous Mater.*, 2009, **117**, 111–117.
58 P. M. Forster, N. Stock and A. K. Cheetham, *Angew. Chem. Int. Ed.*, 2005, **44**, 7608–7611.
59 P. M. Forster, A. R. Burbank, C. Livage, G. Férey and A. K. Cheetham, *Chem. Commun.*, 2004, **4**, 368–369.
60 N. Stock and T. Bein, *J. Mater. Chem.*, 2005, **15**, 1384–1391.
61 D. Banerjee, J. Finkelstein, A. Smirnov, P. M. Forster, L. A. Borkowski, S. J. Teat and J. B. Parise, *Cryst. Growth Des.*, 2011, **11**, 2572–2579.
62 H. J. Sung, J. H. Lee and J. S. Chang, *Bull. Korean Chem. Soc.*, 2005, **26**, 880–881.
63 I. Thomas-Hillman, A. Laybourn, C. Dodds and S. W. Kingman, *J. Mater. Chem. A*, 2018, **6**, 11564–11581.
64 N. A. Khan and S. H. Jhung, *Bull. Korean Chem. Soc.*, 2009, **30**, 2921–2926.
65 M. Taddei, P. V Dau, S. M. Cohen, M. Ranocchiari, J. A. Van Bokhoven, F. Costantino, S. Sabatini and R. Vivani, *Dalton Trans.*, 2015, **44**, 14019.
66 J. S. Choi, W. J. Son, J. Kim and W. S. Ahn, *Microporous Mesoporous Mater.*, 2008, **116**, 727–731.
67 L. Bromberg, Y. Diao, H. Wu, S. A. Speakman and T. A. Hatton, *Chem. Mater.*, 2012, **24**, 1664–1675.
68 K. M. L. Taylor, W. J. Rieter and W. Lin, *J. Am. Chem. Soc.*, 2008, **130**, 14358–14359.
69 Y. Sakata, S. Furukawa, C. Kim and S. Kitagawa, *Chem. Lett.*, 2012, **41**, 1436–1438.
70 N. A. Khan and S. H. Jhung, *Cryst. Growth Des.*, 2010, **10**, 1860–1865.
71 N. A. Khan, J. S. Lee, J. Jeon, C. H. Jun and S. H. Jhung, *Microporous Mesoporous Mater.*, 2012, **152**, 235–239.
72 M. S. El-Shall, V. Abdelsayed, A. E. R. S. Khder, H. M. A. Hassan, H. M. El-Kaderi and T. E. Reich, *J. Mater. Chem.*, 2009, **19**, 7625–7631.
73 H. Y. Huang, C. L. Lin, C. Y. Wu, Y. J. Cheng and C. H. Lin, *Anal. Chim. Acta*, 2013, **779**, 96–103.
74 M. Kim, J. Sergio, Garibay and S. M. Cohen, *Inorg. Chem.*, 2011, **50**, 729–731.
75 J. Górka, P. F. Fulvio, S. Pikus and M. Jaroniec, *Chem. Commun.*, 2010, **46**, 6798–6800.
76 H. Depauw, I. Nevjestić, J. De Winne, G. Wang, K. Haustraete, K. Leus, A. Verberckmoes, C. Detavernier, F. Callens, E. De Canck, H. Vrielinck and P. Van Der Voort, *Chem. Commun.*, 2017, **53**, 8478–8481.
77 D. Li, X. Dai, X. Zhang, H. Zhuo, Y. Jiang, Y. B. Yu, P. Zhang, X. Huang and H. Wang, *J. Catal.*, 2017, **348**, 276–281.
78 A. J. Howarth, Y. Liu, P. Li, Z. Li, T. C. Wang, J. T. Hupp and O. K. Farha, *Nat. Rev. Mater.*, 2016, **1**, 1–15.
79 Z. Wang, A. Bilegsaikhan, R. T. Jerozal, T. A. Pitt and P. J. Milner, *ACS Appl. Mater. Interfaces*, 2021, **13**, 17517–17531.
80 B. S. Gelfand and G. K. H. Shimizu, *Dalton Trans.*, 2016, **45**, 3668–3678.
81 N. C. Burtch, H. Jasuja and K. S. Walton, *Chem. Rev.*, 2014, **114**, 10575–10612.
82 J. Long, O. Yaghi, J. Lee, O. K. Farha, J. Roberts, K. A. Scheidt, S. T. Nguyen and J. T. Hupp, *Chem. Soc. Rev.*, 2009, **38**, 1450–1459.
83 H. Wu, T. Yildirim and W. Zhou, *J. Phys. Chem. Lett.*, 2013, **4**, 925–930.

84 S. Yuan, L. Feng, K. Wang, J. Pang, M. Bosch, C. Lollar, Y. Sun, J. Qin, X. Yang, P. Zhang, Q. Wang, L. Zou, Y. Zhang, L. Zhang, Y. Fang, J. Li and H. C. Zhou, *Adv. Mater.*, 2018, **30**, 1–35.
85 R. G. Pearson, *J. Am. Chem. Soc.*, 1963, **85**, 3533–3539.
86 C. Wang, X. Liu, N. Keser Demir, J. P. Chen and K. Li, *Chem. Soc. Rev.*, 2016, **45**, 5107–5134.
87 M. Ding, X. Cai and H. L. Jiang, *Chem. Sci.*, 2019, **10**, 10209–10230.
88 G. Férey, C. Serre, F. Millange, J. Dutour, S. Surblé, G. Férey, C. Serre, F. Millange and J. Dutour, *Science*, 2005, **309**, 2040–2042.
89 G. Férey, C. Serre, C. Mellot-Draznieks, F. Millange, S. Surblé, J. Dutour and I. Margiolaki, *Angew. Chemie Int. Ed.*, 2004, **43**, 6296–6301.
90 K. Wang, X. L. Lv, D. Feng, J. Li, S. Chen, J. Sun, L. Song, Y. Xie, J. R. Li and H. C. Zhou, *J. Am. Chem. Soc.*, 2016, **138**, 914–919.
91 K. S. Park, Z. Ni, A. P. Côté, J. Y. Choi, R. Huang, F. J. Uribe-Romo, H. K. Chae, M. O'Keeffe and O. M. Yaghi, *Proc. Natl. Acad. Sci. U. S. A.*, 2006, **103**, 10186–10191.
92 L. H. Xie, M. M. Xu, X. M. Liu, M. J. Zhao and J. R. Li, *Adv. Sci.*, 2020, **7**, 1901758.
93 S. Yuan, T.-F. Liu, D. Feng, J. Tian, K. Wang, J. Qin, Q. Zhang, Y.-P. Chen, M. Bosch, L. Zou, S. J. Teat, S. J. Dalgarno and H.-C. Zhou, *Chem. Sci.*, 2015, **6**, 3926-3930.
94 S. Yuan, J.-S. Qin, H.-Q. Xu, J. Su, D. Rossi, Y. Chen, L. Zhang, C. Lollar, Q. Wang, H.-L. Jiang, D. Hee Son, H. Xu, Z. Huang, X. Zou and H.-C. Zhou, *ACS Cent. Sci.*, 2018, **4**, 105–111.
95 R. S. Forgan, *Chem. Sci.*, 2020, **11**, 4546–4562.
96 J. Winarta, B. Shan, S. M. McIntyre, L. Ye, C. Wang, J. Liu and B. Mu, *Cryst. Growth Des.*, 2020, **20**, 1347–1362.
97 A. Schaate, P. Roy, A. Godt, J. Lippke, F. Waltz, M. Wiebcke and P. Behrens, *Chem. A Eur. J.*, 2011, **17**, 6643–6651.
98 S. Øien, D. Wragg, H. Reinsch, S. Svelle, S. Bordiga, C. Lamberti and K. P. Lillerud, *Cryst. Growth Des.*, 2014, **14**, 5370–5372.
99 F. Vermoortele, B. Bueken, L. Le Bars, B. Van de Voorde, M. Vandichel, K. Houthoofd, A. Vimont, M. Daturi, M. Waroquier, V. Van Speybroeck, C. Kirschhock and D. E. De Vos, *J. Am. Chem. Soc*, 2013, **135**, 11465–11468.
100 L. Valenzano, B. Civalleri, S. Chavan, S. Bordiga, M. H. Nilsen, S. Jakobsen, K. P. Lillerud and C. Lamberti, *Chem. Mater*, 2011, **23**, 1700–1718.
101 B. Lerma-Berlanga, C. R. Ganivet, N. Almora-Barrios, S. Tatay, Y. Peng, J. Albero, O. Fabelo, J. González-Platas, H. García, N. M. Padial and C. Martí-Gastaldo, *J. Am. Chem. Soc.*, 2021, **143**, 1798–1806.
102 J. Gao, J. Miao, P.-Z. Li, W. Y. Teng, L. Yang, Y. Zhao, B. Liu and Q. Zhang, *Chem. Commun.*, 2014, **50**, 3786.
103 S. Yuan, T.-F. Liu, D. Feng, J. Tian, K. Wang, J. Qin, Q. Zhang, Y.-P. Chen, M. Bosch, L. Zou, S. J. Teat, S. J. Dalgarno and H.-C. Zhou, *Chem. Sci.*, 2015, **6**, 3926–3930.
104 L. Zou, D. Feng, T. F. Liu, Y. P. Chen, S. Yuan, K. Wang, X. Wang, S. Fordham and H. C. Zhou, *Chem. Sci.*, 2016, **7**, 1063–1069.
105 K. Hong and H. Chun, *Inorg. Chem.*, 2013, **52**, 9705–9707.
106 Y. Keum, S. Park, Y.-P. Chen and J. Park, *Angew. Chem.*, 2018, **130**, 15068–15072.
107 V. Guillerm, S. Gross, C. Serre, T. Devic, M. Bauer and G. Férey, *Chem. Commun.*, 2010, **46**, 767–769.
108 A. A. Bezrukov, K. W. Törnroos, E. Le Roux and P. D. C. Dietzel, *Chem. Commun.*, 2018, **54**, 2735–2738.
109 J. Dong, X. Han, Y. Liu, H. Li and Y. Cui, *Angew. Chemie - Int. Ed.*, 2020, **59**, 13722–13733.
110 X. Li, J. Wang, F. Xue, Y. Wu, H. Xu, T. Yi and Q. Li, *Angew. Chem.*, 2021, **60**, 2534–2540.
111 N. A. Khan, Z. Hasan and S. H. Jhung, *J. Hazard. Mater.*, 2013, **244**–**245**, 444–456.
112 Y. Pi, X. Li, Q. Xia, J. Wu, Y. Li, J. Xiao and Z. Li, *Chem. Eng. J.*, 2018, **337**, 351–371.
113 M. Mon, R. Bruno, J. Ferrando-Soria, D. Armentano and E. Pardo, *J. Mater. Chem. A*, 2018, **6**, 4912–4947.
114 P. W. Seo, B. N. Bhadra, I. Ahmed, N. A. Khan and S. H. Jhung, *Sci. Rep.*, 2016, **6**, 34462.
115 X. X. Jia, R. X. Yao, F. Q. Zhang and X. M. Zhang, *Inorg. Chem.*, 2017, **56**, 2690–2696.
116 J. C. Jin, R. L. Guo, W. Y. Zhang, C. Jiang and Y. Y. Wang, *J. Solid State Chem.*, 2016, **243**, 253–258.
117 X. Wang, T. Qin, S.-S. Bao, Y.-C. Zhang, X. Shen, L.-M. Zheng and D. Zhu, *J. Mater. Chem. A*, 2016, **4**, 16484–16489.
118 J. Li, X. Wang, G. Zhao, C. Chen, Z. Chai, A. Alsaedi, T. Hayat and X. Wang, *Chem. Soc. Rev.*, 2018, **47**, 2322–2356.
119 B. Li, H. M. Wen, H. Wang, H. Wu, M. Tyagi, T. Yildirim, W. Zhou and B. Chen, *J. Am. Chem. Soc.*, 2014, **136**, 6207–6210.

120 J. R. Li, R. J. Kuppler and H. C. Zhou, *Chem. Soc. Rev.*, 2009, **38**, 1477–1504.
121 D. W. Breck, Zeolite Molecular Sieves: structure, chemistry and use, *John Wiley & Sons Inc.*, 1973.
122 S. Ma, X. Sen Wang, D. Yuan and H. C. Zhou, *Angew. Chem. Int. Ed.*, 2008, **47**, 4130–4133.
123 S. Kitagawa and K. Uemura, *Chem. Soc. Rev.*, 2005, **34**, 109–119.
124 R. Kitaura, K. Fujimoto, S. Noro, M. Kondo and S. Kitagawa, *Angew. Chemie Int. Ed.*, 2002, **41**, 133–135.
125 S. H. Huo and X. P. Yan, *J. Mater. Chem.*, 2012, **22**, 7449–7455.
126 J. Wen, Y. Fang and G. Zeng, *Chemosphere*, 2018, **201**, 627–643.
127 M. Feng, P. Zhang, H. C. Zhou and V. K. Sharma, *Chemosphere*, 2018, **209**, 783–800.
128 M. Gao, G. Liu, Y. Gao, G. Chen, X. Huang, X. Xu, J. Wang, X. Yang and D. Xu, *Trends Anal. Chem.*, 2021, **137**, 116226.
129 Q. Gao, J. Xu and X. H. Bu, *Coord. Chem. Rev.*, 2019, **378**, 17–31.
130 Y. Wu, H. Pang, Y. Liu, X. Wang, S. Yu, D. Fu, J. Chen and X. Wang, *Environ. Pollut.*, 2019, **246**, 608–620.
131 P. A. Kobielska, A. J. Howarth, O. K. Farha and S. Nayak, *Coord. Chem. Rev.*, 2018, **358**, 92–107.
132 G. R. Xu, Z. H. An, K. Xu, Q. Liu, R. Das and H. L. Zhao, *Coord. Chem. Rev.*, 2021, **427**, 213554.
133 M. A. Barakat, *Arab. J. Chem.*, 2011, **4**, 361–377.
134 M. Kumar, A. Gogoi, D. Kumari, R. Borah, P. Das, P. Mazumder and V. K. Tyagi, *J. Hazardous, Toxic, Radioact. Waste*, 2017, **21**, 1–16.
135 P. Cantinho, M. Matos, M. A. Trancoso and M. M. C. dos Santos, *Int. J. Environ. Sci. Technol.*, 2016, **13**, 359–386.
136 R. A. Wuana and F. E. Okieimen, *ISRN Ecol.*, 2011, **2011**, 1–20.
137 I. Thornton, D. Butler, P. Docx, M. Hession, C. K. Makropoulos, M. McMullen, M. Nieuwenhuijsen, A. Pitman, R. Rautiu, R. Sawyer, S. Smith, D. White, P. Wilderer, S. Paris, D. Marani, C. Braguglia, J. Palerm and IICON, Pollutants in urban waste water and sewage sludge, *I C Consultants Ltd., London*, 2001.
138 A. Khan, S. Khan, M. A. Khan, Z. Qamar and M. Waqas, *Environ. Sci. Pollut. Res.*, 2015, **22**, 13772–13799.
139 C. S. Seth, *Bot. Rev.*, 2012, **78**, 32–62.
140 European Commission, Working document on sludge, 2000.
141 US EPA, Process Design Manual Surface Disposal of Sewage Sludge and Domestic Septage, 1995.
142 N. B. Cook, Vet. Clin. North Am. - Food Anim. Pract., 2017, **33**, 195–225.
143 R. A. Laven and M. J. Proven, *Vet. Rec.*, 2000, **147**, 503–506.
144 M. A. Palmer and N. E. O. Connell, *Animals*, 2015, **5**, 512–535.
145 A. Relun, A. Lehebel, N. Bareille and R. Guatteo, *J. Dairy Sci.*, 2012, **95**, 3722–3735.
146 T. Fjeldaas, M. Knappe-Poindecker, K. E. Bøe and R. B. Larssen, *J. Dairy Sci.*, 2014, **97**, 2835–2846.
147 T. W. Downing, K. Stiglbauer, M. J. Gamroth and J. Hart, *Prof. Anim. Sci.*, 2010, **26**, 332–334.
148 N. B. Cook, J. Rieman, A. Gomez and K. Burgi, *Vet. J.*, 2012, **193**, 669–673.
149 Z. Yu, L. Gunn, P. Wall and S. Fanning, *Food Microbiol.*, 2017, **64**, 23–32.
150 A. Azimi, A. Azari, M. Rezakazemi and M. Ansarpour, *ChemBioEng Rev.*, 2017, **4**, 37–59.
151 C. F. Carolin, P. S. Kumar, A. Saravanan, G. J. Joshiba and M. Naushad, *J. Environ. Chem. Eng.*, 2017, **5**, 2782–2799.
152 S. A. Al-Saydeh, M. H. El-Naas and S. J. Zaidi, *J. Ind. Eng. Chem.*, 2017, **56**, 35–44.
153 S. Babel, *J. Hazard. Mater.*, 2003, **97**, 219–243.
154 T. A. Kurniawan, G. Y. S. Chan, W. H. Lo and S. Babel, *Chem. Eng. J.*, 2006, **118**, 83–98.
155 R. Yang, H. Li, M. Huang, H. Yang and A. Li, *Water Res.*, 2016, **95**, 59–89.
156 T. Mohammadi, A. Moheb, M. Sadrzadeh and A. Razmi, *Sep. Purif. Technol.*, 2005, **41**, 73–82.
157 U. Farooq, J. A. Kozinski, M. A. Khan and M. Athar, *Bioresour. Technol.*, 2010, **101**, 5043–5053.
158 Renu, M. Agarwal and K. Singh, *J. Water Reuse Desalin.*, 2017, **7**, 387–419.
159 V. N. Thekkudan, V. K. Vaidyanathan, S. K. Ponnusamy, C. Charles, S. Sundar, D. Vishnu, S. Anbalagan, V. K. Vaithyanathan and S. Subramanian, *IET Nanobiotechnology*, 2017, **11**, 213–224.
160 X. Ren, J. Li, X. Tan and X. Wang, *Dalton Trans.*, 2013, **42**, 5266–5274.
161 P. Hadi, M. H. To, C. W. Hui, C. S. K. Lin and G. McKay, *Water Res.*, 2015, **73**, 37–55.
162 K. Kadirvelu, K. Thamaraiselvi and C. Namasivayam, *Bioresour. Technol.*, 2001, **76**, 63–65.
163 C. Y. Yin, M. K. Aroua and W. M. A. W. Daud, *Sep. Purif. Technol.*, 2007, **52**, 403–415.
164 S. Wong, N. Ngadi, I. M. Inuwa and O. Hassan, *J. Clean. Prod.*, 2018, **175**, 361–375.
165 C. Tang, Y. Shu, R. Zhang, X. Li, J. Song, B. Li, Y. Zhang and D. Ou, *RSC Adv.*, 2017, **7**, 16092–16103.
166 X. Wang, S. Yang, W. Shi, J. Li, T. Hayat and X. Wang, *Environ. Sci. Technol.*, 2015, **49**, 11721–11728.
167 J. Li, C. Chen, S. Zhang and X. Wang, *Environ. Sci. Nano*, 2014, **1**, 488–495.
168 G. Sheng, S. Yang, J. Sheng, J. Hu, X. Tan and X. Wang, *Environ. Sci. Technol.*, 2011, **45**, 7718–7726.
169 C. Chen, X. Yang, J. Wei, X. Tan and X. Wang, *J. Colloid Interface Sci.*, 2013, **393**, 249–256.

170 S. Yu, X. Wang, S. Yang, G. Sheng, A. Alsaedi, T. Hayat and X. Wang, *Sci. China Chem.*, 2017, **60**, 170–187.
171 S. Wang and Y. Peng, *Chem. Eng. J.*, 2010, **156**, 11–24.
172 X. Lu, F. Wang, X. Li, K. Shih and E. Y. Zeng, *Ind. Eng. Chem. Res.*, 2016, **55**, 8767–8773.
173 M. Delkash, B. Ebrazi Bakhshayesh and H. Kazemian, *Microporous Mesoporous Mater.*, 2015, **214**, 224–241.
174 B. Lee, Y. Kim, H. Lee and J. Yi, *Microporous Mesoporous Mater.*, 2001, **50**, 77–90.
175 J. Li, S. Zhang, C. Chen, G. Zhao, X. Yang, J. Li and X. Wang, *ACS Appl. Mater. Interfaces*, 2012, **4**, 4991–5000.
176 S. Li, Y. Chen, X. Pei, S. Zhang, X. Feng, J. Zhou and B. Wang, *Chinese J. Chem.*, 2016, **34**, 175–185.
177 J. Wen, Y. Fang and G. Zeng, *Chemosphere*, 2018, **201**, 627–643.
178 H. Shayegan, G. A. M. Ali and V. Safarifard, *ChemistrySelect*, 2020, **5**, 124–146.
179 G. N. Lewis, Valence and the structure of atoms and molecules., 1923.
180 E. Rahimi and N. Mohaghegh, *Mine Water Environ.*, 2015, **35**, 18–28.
181 Y. Zhang, X. Zhao, H. Huang, Z. Li, D. Liu and C. Zhong, *RSC Adv.*, 2015, **5**, 72107–72112.
182 X. Luo, L. Ding and J. Luo, *J. Chem. Eng. Data*, 2015, **60**, 1732–1743.
183 Y. Zhang, Z. Xie, Z. Wang, X. Feng, Y. Wang and A. Wu, *Dalton Trans.*, 2016, **45**, 12653–12660.
184 A. Corma, H. García and F. X. Llabrés I Xamena, *Chem. Rev*, 2010, **110**, 4606–4655.
185 D. Yang and B. C. Gates, *ACS Catal.*, 2019, **8**, 1779–1798.
186 P. Z. Li, X. J. Wang, J. Liu, J. S. Lim, R. Zou and Y. Zhao, *J. Am. Chem. Soc.*, 2016, **138**, 2142–2145.
187 S. Dissegna, K. Epp, W. R. Heinz, G. Kieslich and R. A. Fischer, *Adv. Mater.*, 2018, **30**, 1–23.
188 K. Schlichte, T. Kratzke and S. Kaskel, *Microporous Mesoporous Mater.*, 2004, **73**, 81–88.
189 J. Jiang and O. M. Yaghi, *Chem. Rev.*, 2015, **115**, 6966–6997.
190 L. Zhu, X.-Q. Liu, H.-L. Jiang and L.-B. Sun, *Chem. Rev*, 2017, **117**, 8129–8176.
191 J. D. Evans, C. J. Sumby and C. J. Doonan, *Chem. Soc. Rev.*, 2014, **43**, 5933–5951.
192 Y. B. Huang, J. Liang, X. S. Wang and R. Cao, *Chem. Soc. Rev.*, 2017, **46**, 126–157.
193 C. C. Cao, C. X. Chen, Z. W. Wei, Q. F. Qiu, N. X. Zhu, Y. Y. Xiong, J. J. Jiang, D. Wang and C. Y. Su, *J. Am. Chem. Soc.*, 2019, **141**, 2589–2593.
194 H. R. Moon, D.-W. Lim and M. P. Suh, *Chem. Soc. Rev.*, 2013, **42**, 1807.
195 A. Aijaz and Q. Xu, *J. Phys. Chem. Lett*, 2014, **5**, 19.
196 A. Dhakshinamoorthy and H. Garcia, *Chem. Soc. Rev*, 2012, **41**, 5262–5284.
197 Z. W. Zhao, X. Zhou, Y. N. Liu, C. C. Shen, C. Z. Yuan, Y. F. Jiang, S. J. Zhao, L. B. Ma, T. Y. Cheang and A. W. Xu, *Catal. Sci. Technol.*, 2018, **8**, 3160–3165.
198 A. Dhakshinamoorthy, A. M. Asiri and H. Garcia, *Chem. Soc. Rev.*, 2015, **44**, 1922–1947.
199 B. Yuan, Y. Pan, Y. Li, B. Yin and H. Jiang, *Angew. Chem. Int. Ed.*, 2010, **49**, 4054–4058.
200 M. Annapurna, T. Parsharamulu, P. Vishnuvardhan Reddy, M. Suresh, P. R. Likhar and M. Lakshmi Kantam, *Appl. Organomet. Chem.*, 2015, **29**, 234–239.
201 A. Fujishima and K. Honda, *Nature*, 1972, **238**, 37-38.
202 T. Zhang, Y. Jin, Y. Shi, M. Li, J. Li and C. Duan, *Coord. Chem. Rev.*, 2019, **380**, 201–229.
203 T. Zhang and W. Lin, *Chem. Soc. Rev.*, 2014, **43**, 5982–5993.
204 S. Goswami, J. N. Nelson, T. Islamoglu, Y. L. Wu, O. K. Farha and M. R. Wasielewski, *Chem. Mater.*, 2018, **30**, 2488–2492.
205 M. Alvaro, E. Carbonell, B. Ferrer, F. X. Llabrés I Xamena and H. Garcia, *Chem. - A Eur. J.*, 2007, **13**, 5106–5112.
206 S. Hausdorf, J. Wagler, R. Mossig and F. O. R. L. Mertens, *J. Phys. Chem. A.*, 2008, **112**, 7567–7576.
207 C. G. Silva, I. Luz, F. X. Llabrés I Xamena, A. Corma and H. García, *Chem. A Eur. J.*, 2010, **16**, 11133–11138.
208 S. H. Xu and J. Ye, *Phys. Chem. Chem. Phys*, 2016, **18**, 7563.
209 J. Zhu, P. Z. Li, W. Guo, Y. Zhao and R. Zou, *Coord. Chem. Rev.*, 2018, **359**, 80–101.
210 M. A. Nasalevich, C. H. Hendon, J. G. Santaclara, K. Svane, B. Van Der Linden, S. L. Veber, M. V. Fedin, A. J. Houtepen, M. A. Van Der Veen, F. Kapteijn, A. Walsh and J. Gascon, *Sci. Rep.*, 2016, **6**, 1–9.
211 Y. Fu, D. Sun, Y. Chen, R. Huang, Z. Ding, X. Fu and Z. Li, *Angew. Chemie Int. Ed.*, 2012, **51**, 3364–3367.
212 Y. Lee, S. Kim, J. K. Kang and S. M. Cohen, *Chem. Commun.*, 2015, **51**, 5735–5738.
213 M. A. Nasalevich, R. Becker, E. V. Ramos-Fernandez, S. Castellanos, S. L. Veber, M. V. Fedin, F. Kapteijn, J. N. H. Reek, J. I. Van Der Vlugt and J. Gascon, *Energy Environ. Sci.*, 2015, **8**, 364–375.
214 K. Meyer, S. Bashir, J. Llorca, H. Idriss, M. Ranocchiari and J. A. van Bokhoven, *Chem. A Eur. J.*, 2016, **22**, 13894–13899.

215 J. Gao, J. Miao, P. Z. Li, W. Y. Teng, L. Yang, Y. Zhao, B. Liu and Q. Zhang, *Chem. Commun.*, 2014, **50**, 3786–3788.
216 M. Dan-Hardi, C. Serre, T. Frot, L. Rozes, G. Maurin, C. Sanchez and G. Férey, *J. Am. Chem. Soc.*, 2009, **131**, 10857–10859.
217 K. G. M. Laurier, F. Vermoortele, R. Ameloot, D. E. De Vos, J. Hofkens and M. B. J. Roeffaers, *J. Am. Chem. Soc.*, 2013, **135**, 14488–14491.
218 J. D. Xiao and H. L. Jiang, *Acc. Chem. Res.*, 2018, **52**, 356–366.
219 H. Q. Xu, J. Hu, D. Wang, Z. Li, Q. Zhang, Y. Luo, S. H. Yu and H. L. Jiang, *J. Am. Chem. Soc.*, 2015, **137**, 13440–13443.
220 M. Al Kobaisi, S. V Bhosale, K. Latham, A. M. Raynor and S. V Bhosale, *Chem. Rev.*, 2016, **116**, 11685–11796.

2 Chapter Two: Analytical techniques

2.1 X-Ray Diffraction

2.1.1 Powder X-Ray Diffraction

Powder X-Ray Diffraction (PXRD) is a non-destructive technique which is used to analyse the structure of materials. It is primarily used for the analysis of crystalline or partially crystalline materials but can be used to study amorphous material.[1,2]

During a diffraction experiment, an X-ray beam is directed towards a sample. X-rays are chosen as their wavelength is on the order of the atomic spacing of crystalline materials. When the X-rays hit a material they are scattered in many directions by the electrons of the atoms present in the solid. Most of the scattered X-rays are out of phase, resulting in destructive interference. However, under certain conditions, defined by Bragg's law, constructive interference occurs, giving rise to a diffraction pattern.[1–3]

2.1.1.1 Bragg's law

In a crystal lattice, sets of crystallographic planes can be identified, which intersect different sets of lattice points. Different sets of planes are defined using the Miller indices, *(hkl)*, where the values of *h, k,* and *l* are the reciprocals of the fractions at which the planes in question intercept the *a*, *b*, and *c* axes. Planes relating to the same *hkl* values are parallel to each other and evenly spaced. Figure 2.1 demonstrates that two X-ray beams with wavelength λ (1 and 2) may be diffracted by atoms in two parallel crystallographic planes by an angle θ. Constructive interference occurs when the diffracted waves (1' and 2') have the same phase. In other words, when:

$$n\lambda = AB + BC = 2AB$$

(Equation 1)

The angle of diffraction can be related to AB and the d spacing of the crystal:

$$\sin\theta = \frac{AB}{d}$$

(Equation 2)

This can be rearranged to give the Bragg equation:

$$n\lambda = 2d \sin\theta$$

(Equation 3)

The Bragg equation therefore defines the angles, 2θ, at which reflections will appear in the diffraction pattern and allows the *d* spacing of sets of (*hkl*) planes to be calculated.[3] The *d* spacing of these planes can then be related to the lattice parameters by using an equation appropriate to the crystal system in question. For example, the lattice parameters for an orthorhombic system can be calculated by the following equation:

$$\frac{1}{d^2} = \frac{h^2}{a^2} + \frac{l^2}{b^2} + \frac{k^2}{c^2}$$

(Equation 4)

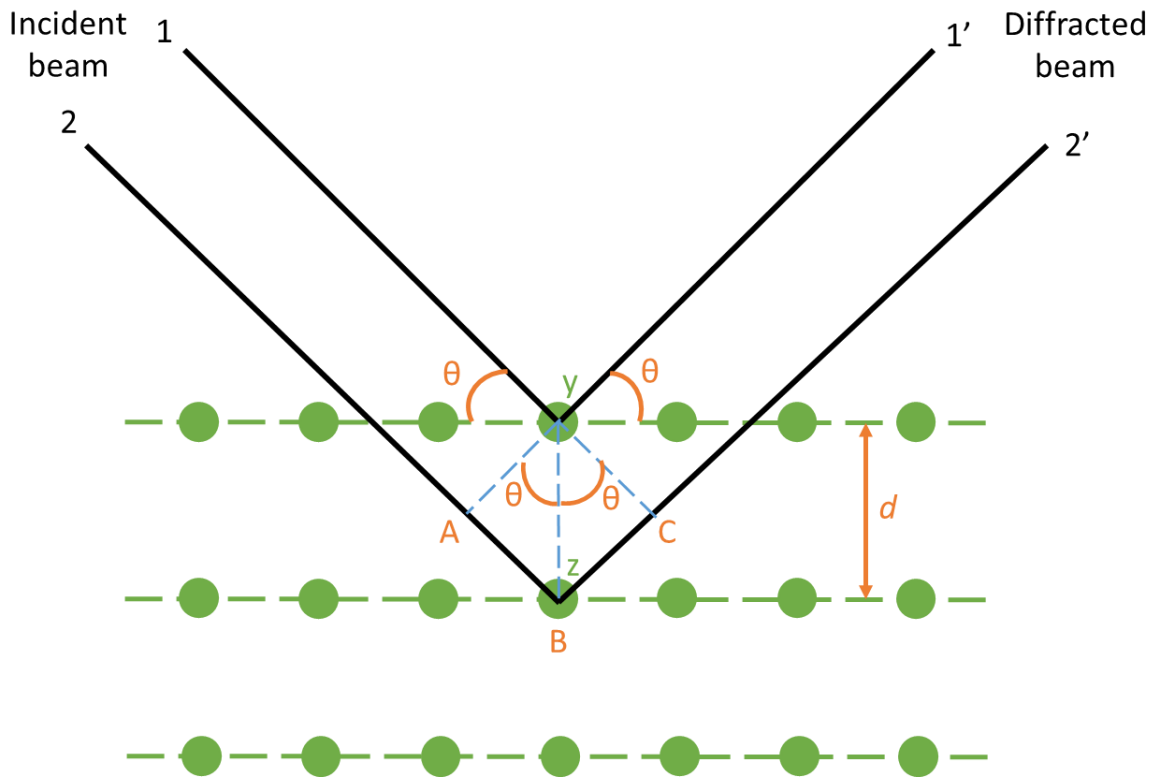

Figure 2.1 – Diffraction of X-rays by crystallographic planes.[1–3]

In this work, PXRD was used to confirm that a given synthesis yielded the target phase by comparing the PXRD pattern of the synthesised material to a simulated pattern for a known single crystal structure. This method was used to identify that some samples contained a mixture of multiple phases. Pawley fitting of patterns to known phases was carried out using TOPAS-Academic.[4]

Unknown phases that were synthesised in this work were also analysed by PXRD. In some cases, their space groups and lattice parameters were determined by indexing in the software TOPAS-Academic.[4] Pawley fitting of these indexing results was then carried out to confirm which results were best and refine the calculated lattice parameters. Attempts were also made to determine the structure of these unknown materials using simulated annealing in the CSD software DASH,[5] and Rietveld refinement of the resulting crystal structures was carried out in Topas.[5]

2.1.2 Instrument details

The majority of PXRD measurements were made using a Malvern PANalytical Xpert Pro X-ray diffractometer using a sealed tube Cu source, operating at 40 kV and 40 mA, with a PIXcel DK1W179H1 detector. A Johansson focussing beam monochromator selected pure Cu Kα1 radiation which was then passed through a 0.04 rad Soller slit to reduce axial beam divergence. Programmable divergence slits and anti-scatter slits were used in automatic mode to match the prepared sample length. A fixed mask matching the prepared sample width and a fixed 1° anti-scatter slit were used in the incident beam path. Measurements were taken from 2° to 70° 2θ on a zero-background silicon holder in Bragg–Brentano geometry, with the sample holder spinning at a speed of two revolutions per second. Data was collected with a step size of 0.013° in continuous mode using different scan speeds depending on the sample size and scattering power of the sample. Each sample was scanned three times and the data was merged after inspection to ensure that no sample degradation had occurred. High temperature PXRD measurements were performed using an Anton Parr (HTK 1200N) high temperature oven chamber. The sample was mounted on an alumina plate and heated in air in 20 °C increments to 400 °C and then 50 °C increments up to 600 °C.

PXRD patterns of all work relating to MIL-121 (Section 3.3.3) and DM-NDI MOFs (Section 4.6.2) were taking on a Bruker Da Vinci diffractometer using Cu(Kα1) radiation, operating at 40 kV and 40 mA, with a LYNXEYE XE-T detector. Samples were loaded onto a PMMA sample holder, and a pattern was recorded between 5-50° 2θ over in Bragg-Brentano geometry.

2.1.3 Single Crystal X-Ray Diffraction instrument details

SCXRD measurements were collected on the i19 beamline at Diamond Light Source (λ = 0.6889 Å) at 100 K and processed using Xia2 software. Absorption corrections were applied using empirical methods and the structures were solved by direct methods using SHELXT and refined by full-matrix least-squares by SHELXL in Olex2.[6,7]

2.2 Thermogravimetric Analysis

Thermogravimetric analysis (TGA) monitors the change in weight of a material as it is heated. The sample is usually heated at a rate of 1-10 °C per minute under a constant gas flow. Inert environments such as nitrogen or argon are often used to ensure that the mass losses are only due the sample being heated.[8] Having said this, compressed air is often used to ensure that materials are fully combusted.

In the case of MOF chemistry, TGA can be used to determine thermal stability, activation conditions, and porosity, as well as an indication of what might be occluded in the pores of a MOF.[9] The first mass loss that can be observed in the thermogram of a MOF is often due to the loss of solvent. For example, the loss of DMF can be seen in the example thermogram in Figure 2.2. The loss of solvents is usually observed up to around 150 °C, due to MOFs possessing pore space that is accessible by volatile solvents. These absorbed solvents are often present due to the synthesis conditions of the MOFs (for example, a MOF synthesis in DMF will often contain DMF in the pores), but the presence of water is often observed as MOFs can spontaneously absorb water from the air.

TGA can also be used to determine whether activation, a process in which reactants and solvents are removed from the pores of the MOF, has been successful. For example, the thermogram below (Figure 2.2) shows a mass loss occurring between around 250 and

350 °C, indicating that linker is still occluded in the pores of this material and the sample is not yet fully activated.

The thermal stability of a MOF is indicated by the temperature at which the last (and often largest) mass loss starts to occur. In the example below the MOF is stable up to around 380 °C. It is important to note that although a thermogram shows the temperature at which a material starts to degrade, it does not show if any structural changes have begun to occur before this temperature is reached. To understand the thermal stability of a crystalline material more fully, temperature dependent PXRD can be used to observe any structural changes occurring at elevated temperatures.

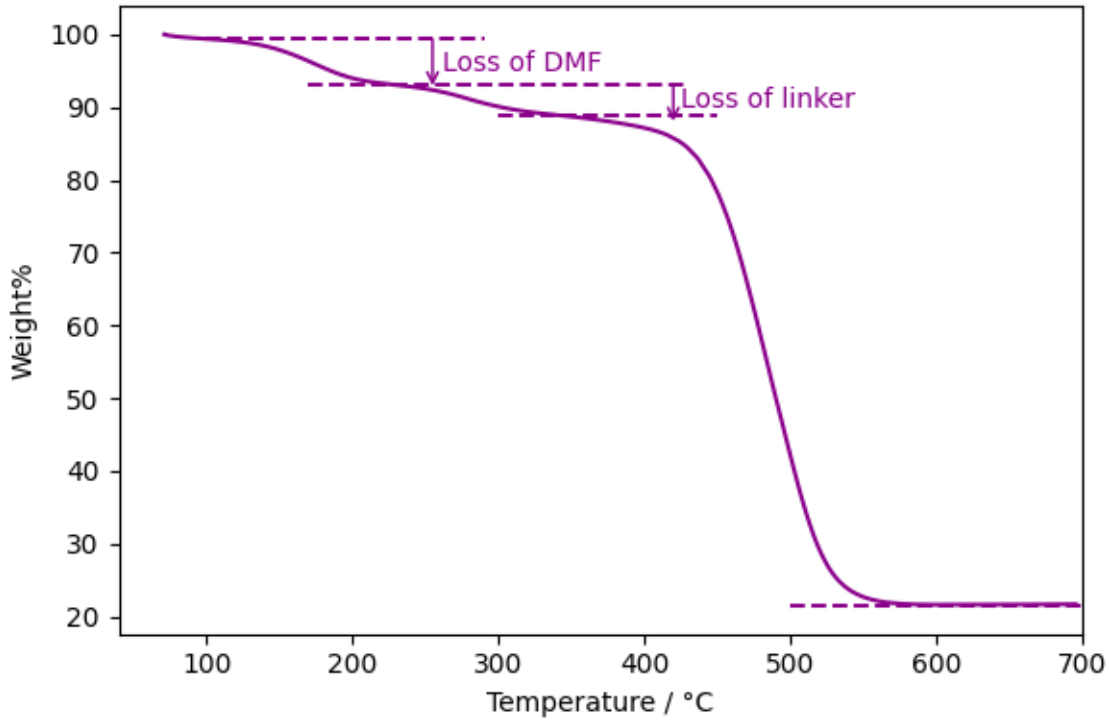

Figure 2.2 – Example thermogram for illustrative purposes. This is taken from Chapter 3 and is of sample NH90.

TGA is also an important technique for calculating accurate percentage yields of MOFs as the mass due to the presence of unreacted linker or solvents in a MOF must be considered and removed for the mass used in the calculation of yield.

2.2.1 TGA instrumentation

For samples of MIL-53(Al) and MIL-53(Al)-NH_2, TGA was performed using a TA Q550 thermogravimetric analyser. Samples were heated at a rate of 5 °C/min under a nitrogen atmosphere to a maximum of 700 °C.

For all other samples, thermogravimetric analysis was performed using a TA Q500 thermogravimetric analyser. Samples were analysed using a platinum pan and in the presence of air. The parameters for these experiments were: ramp 5 °C/min from 20-1000 °C with an isotherm for 10 minutes at 1000 °C, air flow: 60 mL/min. The isothermal step is carried out to ensure that all organic material had fully combusted and the mass remaining at the end of experiment was due only to the metal oxide.

2.3 Scanning Electron Microscopy

A Scanning Electron Microscope (SEM) makes use of an electron beam to observe very small surface structures which cannot be viewed using an optical microscope; imaging on the nanometre scale can take place when electrons are used in place of light due to their smaller wavelength.[10] An SEM directs an electron beam at a sample and detects electrons that have been reflected by the sample. This is in contrast to Transmission Electron Microscopy (TEM), where electrons that have travelled through a thin sample are detected.

Secondary electrons (SE) are produced from the surface regions due to inelastic interactions between the electron beam and the sample and provide detailed surface information. The incoming electrons from the beam transfer energy to atoms in the sample surface which can lead to the expulsion of SEs from the atom. If the lost electron is replaced with an electron from a higher-level orbital, an X-ray is emitted with a wavelength that is characteristic of the atom.[10,11]

Backscattered electrons (BSEs) are produced from deeper regions of the sample through elastic reactions. Electrons from the incident beam interact with the electron field of an atom's nucleus which results in a change of direction of the electron without a significant loss of energy. BSEs have higher energies than SEs but are produced less frequently. They are

sensitive to changes in atomic numbers, producing brighter images when heavier atoms are present.[10,11]

BSEs, SEs, and X-rays all require different detectors. Whilst backscattered (BSE) and secondary electrons (SE) are used to produce an SEM image, X-rays are detected in order to perform elemental analysis of the sample in a process called Energy Dispersive X-Ray spectroscopy (EDX).[10] A spectrum is produced that indicates the elements present. Although quantitative elemental analysis is possible with EDX, variations in the sample, such as surface height and angle, can result in changes to the spectrum which may affect the percentages of each element measured. In addition, and more importantly, samples are often prepared on carbon tabs and coated with a conductive material to reduce charging effects. This means that both carbon and the coating material will be detected in the sample, reducing the accuracy of the percentage of other elements measured.[12]

In this thesis, SEM is used to determine the morphology of MOF particles synthesised. This included particle size analysis which was conducted by measuring the longest edge of the imaged particles using imageJ. In some cases, particle morphology was compared to previous literature examples of the materials synthesis and in others the shape and size of new materials was observed. EDX measurements were used to qualitatively confirm which elements were present in the synthesised materials.

2.3.1 Instrument details

SEM images were taken using a JEOL 7100F field emission gun scanning electron microscope. Samples were prepared on 10 mm aluminium stubs with an adhesive carbon tab and coated with an 8 nm layer of Iridium using a QUORUM QISOT ES coater. Imaging was conducted at a working distance of 10 mm and an electron gun accelerating potential of 15 kV. Qualitative chemical microanalysis measurements were carried out using an Oxford Instruments XMax 80 solid state EDX detector, controlled by Aztec.

2.4 Gas adsorption

Gas sorption[13] is an analytical technique used to study porous materials and can be used to calculate the surface area, pore size, and pore shape of a material.[13] During a gas sorption

experiment a material is exposed to a gas, often nitrogen, which accumulates on the surface of the material (the adsorbent) forming a layer of molecules or atoms (the adsorbates). This process of adsorption occurs due to the presence of weak van der Waals forces between the adsorbates and adsorbent, in a process called physisorption.[13]

In a nitrogen adsorption isotherm experiment, the volume of nitrogen adsorbed by a solid is measured as the pressure is increased and temperature is kept constant at -196 °C (the boiling point of nitrogen). The isotherm is given by plotting the volume of nitrogen adsorbed against the relative pressure ratio, P/P_0, where P_0 is the saturation vapour pressure of the nitrogen at -196 °C. The shape of the isotherm can provide information about the type of porosity present in the sample being studied. According to IUPAC classification,[13] six types of isotherms are possible. Four of these common isotherms are shown below (Figure 2.3); Type I and Type IV most commonly apply to porous MOFs.

Type I isotherms are usually exhibited by microporous materials, where a large uptake of gas is seen at low pressures as the micropores fill. A plateau is seen once the micropores have been filled. Sometimes a further small increase in gas uptake can be seen which is due to multilayer adsorption of the external surfaces of the material.

Type II isotherms occur in cases where the material is non-porous or microporous. Any gas uptake that takes place is due to adsorption on the outer surface of the material. Type III isotherms are rare and mainly occur when adsorbate-adsorbate interactions are stronger than adsorbent-adsorbate interactions.

Type IV isotherms are common for mesoporous materials, where the first part of the isotherms is due to monolayer gas coverage. At higher pressures, multilayer adsorption takes place and capillary condensation of the gas within the mesopores takes place, which in turn creates a hysteresis loop on desorption of the gas.

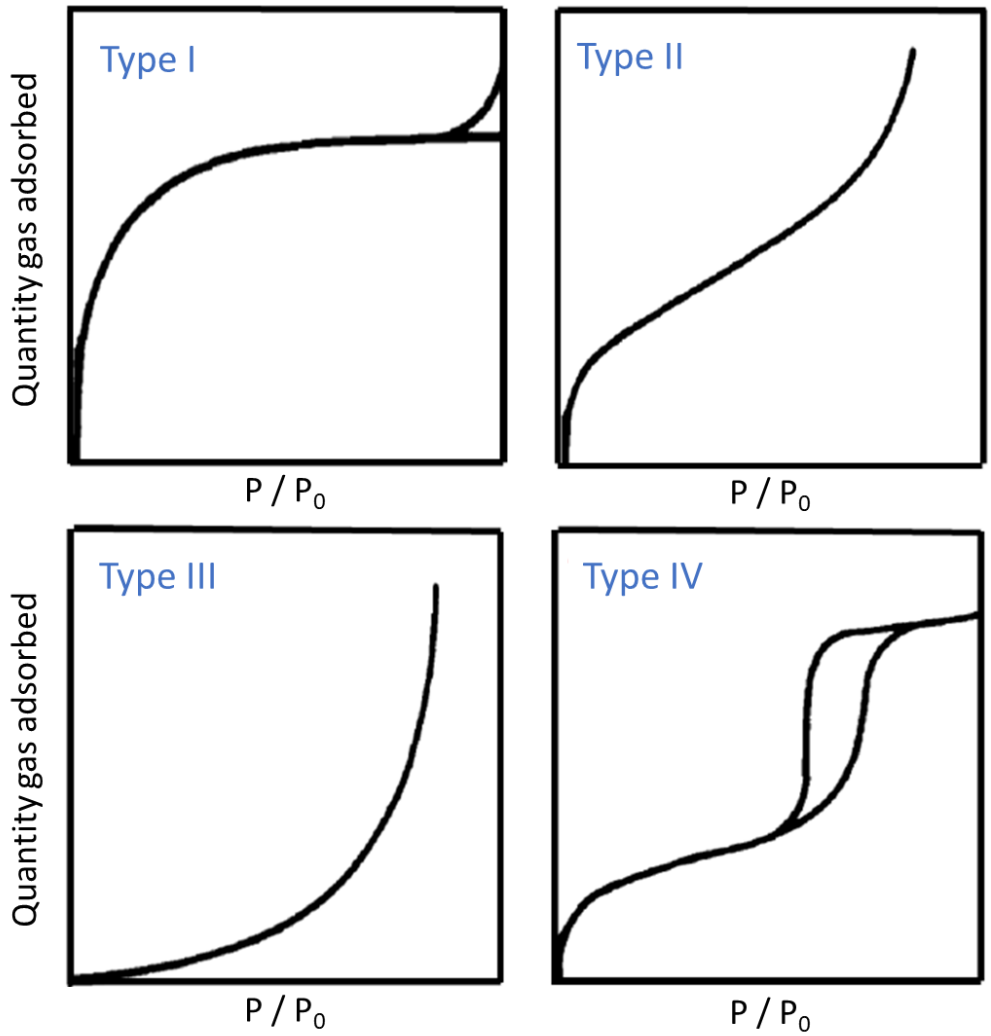

Figure 2.3 – Types of physisorption isotherms, defined by IUPAC. Figure adapted with permission from K. S. W. Sing, *Pure and Applied Chemistry*, **54**, 11, 1982, 2201-2218.[13]

The Brunauer-Emmett-Teller (BET) method is the most widely used procedure for the determination of the surface area of common porous materials, including MOFs. The BET equation is as follows:

$$\frac{P}{V(P_0 - P)} = \frac{1}{V_m C} + \frac{(C-1)}{V_m C} \cdot \frac{P}{P_0}$$

(Equation 5)

Where V is the amount of gas adsorbed at pressure P, V_m is the amount of gas in a monolayer and C is a constant. The BET plot is a plot of $P/V(P_0\text{-}P)$ against P/P_0 that shows a linear relationship. This linear relationship only occurs in the P/P_0 range of 0.05 to 0.30., where

processes such as capillary condensation and saturation are not taking place. C and V_m can be calculated from the BET plot and the surface area is calculated using:

$$\text{BET surface area} = V_m \cdot L \cdot a_m$$

(Equation 5)

Where L is Avogadro's constant and a_m is the molecular cross-sectional area of the adsorbate.[14]

Although BET is one of the most popular methods for calculating the surface area of porous material such as MOF, it is based on several assumptions, including:

- The surface energy of the material is completely uniform giving a constant heat of adsorption
- Adsorbed molecules on the surface do not interact
- One monolayer is adsorbed completely on the surface before another layer starts to be adsorbed
- The adsorbed molecules can act as a new surface and the adsorption process repeats itself
- The heat of adsorption for all monolayers but the first layer is equal to the heat of condensation
- When the system is at equilibrium the rates of evaporation and condensation are equal.[14]

These assumptions are unlikely to apply to most materials and therefore it is suggested that the BET method is oversimplified and that the calculated surface area should be used as a valuable guide but perhaps not an absolute empirical value.[15]

2.4.1 Instrument details

N_2 isotherms were measured at pressures up to 1 bar at -196 °C on a Micromeritics 3flex sorptometer. Prior to analysis, samples were degassed at high vacuum on the Micromeritics Smart VacPrep at 150 °C for 16 h.

2.5 Other instrument details

^{1}H NMR spectroscopy was carried out in d_6-DMSO using a AV(III)400 400 MHz spectrometer. IR spectra were recorded on solids using a Bruker Alpha FTIR Spectrometer using a Bruker Platinum ATR attachment over the range of 4000–400 cm^{-1}. ESI-MS spectra were taken in MeCN using a Bruker micrOTOF II mass spectrometer. Solid-state UV-vis diffuse reflectance measurements were carried out on a UV-Vis NIR Agilent Cary Spectrometer between 200-800 nm at a scan rate of 600 nm s^{-1}. ICP-measurements were undertaken on a Perkin Elmer Optima 2000 DV Inductively Coupled Plasma Optical Emission Spectrometer.

2.6 References

1 W. Clegg, X-ray crystallography, Oxford University Press, Oxford, 2nd ed., 2015.

2 A. Clearfield, J. H. Reibenspies and N. Bhuvanesh, Principles and applications of powder diffraction, Blackwell Publishing, Oxford, 2008.

3 P. W. H. Bragg and W. L. Bragg, *Proc. R. Soc. A*, 1913, **17**, 428–438.

4 A. A. Coelho, TOPAS-Academic, version 4.1 (Computer Software), Coelho Software.

5 W. I. F. David, K. Shankland, J. Van De Streek, E. Pidcock, W. D. S. Motherwell and J. C. Cole, *J. Appl. Crystallogr.*, 2006, **39**, 910–915.

6 O. V. Dolomanov, L. J. Bourhis, R. J. Gildea, J. A. K. Howard and H. Puschmann, J. Appl. Crystallogr., 2009, **42,** 339–341.

7 G. M. Sheldrick, *Acta Crystallogr.*, 2008, **64**, 112–122.

8 Perkin Elmer, Thermogravimetric Analysis (TGA) A Beginner's Guide, 2010.

9 I. A. Lázaro, *Eur. J. Inorg. Chem.*, 2020, 4284–4294.

10 K. D. Vernon-Parry, *III-Vs Rev.*, 2000, **13**, 40–44.

11 M. Suga, S. Asahina, Y. Sakuda, H. Kazumori, H. Nishiyama, T. Nokuo, V. Alfredsson, T. Kjellman, S. M. Stevens, H. S. Cho, M. Cho, L. Han, S. Che, M. W. Anderson, F. Schüth, H. Deng, O. M. Yaghi, Z. Liu, H. Y. Jeong, A. Stein, K. Sakamoto, R. Ryoo and O. Terasaki, *Prog. Solid State Chem.,* 2014, **42**, 1–21.

12 D. E. Newbury and N. W. M. Ritchie, *Scanning*, 2013, **35**, 141–168.

13 K. S. W. Sing, *Pure Appl. Chem.*, 1982, **54**, 2201–2218.

14 G. Leofanti, M. Padovan, G. Tozzola and B. Venturelli, *Catal. Today*, 1998, **41**, 207–219.

15 J. Rouquerol, D. Avnir, C. W. Fairbridge, D. H. Everett, J. H. Haynes, N. Pernicone, J. D. F. Ramsay, K. S. W. Sing and K. K. Unger, *Pure Appl. Chem.*, 1994, **66**, 1739–1758.

3 Chapter Three: Microwave synthesis of MIL-53, MIL-53(Al)-NH_2 and MIL-121 for their application in Cu(II) sorption from aqueous solution

3.1 Background

As described in Chapter 2, MOFs containing Lewis basic groups are often shown to have good heavy metal uptake properties. Specifically, previous work has shown that copper benzenedicarboxylate (BDC) MOF (structure shown in Figure 3.1) has promising adsorption capacities for both Cu(II) (~210 mg g^{-1}) and Zn^{2+} (~140 mg g^{-1}).[1] In addition, functionalisation of UiO-66(Zr) (structure shown in Figure 3.1) with Lewis basic groups such as an amine or carboxylate achieved higher Cu(II) uptake; ~6 mg g^{-1} for UiO-66(Zr)-NH_2 and ~20 mg g^{-1} for UiO-66(Zr)-2COOH, compared to ~4 mg g^{-1} for the unfunctionalised UiO-66(Zr).[2]

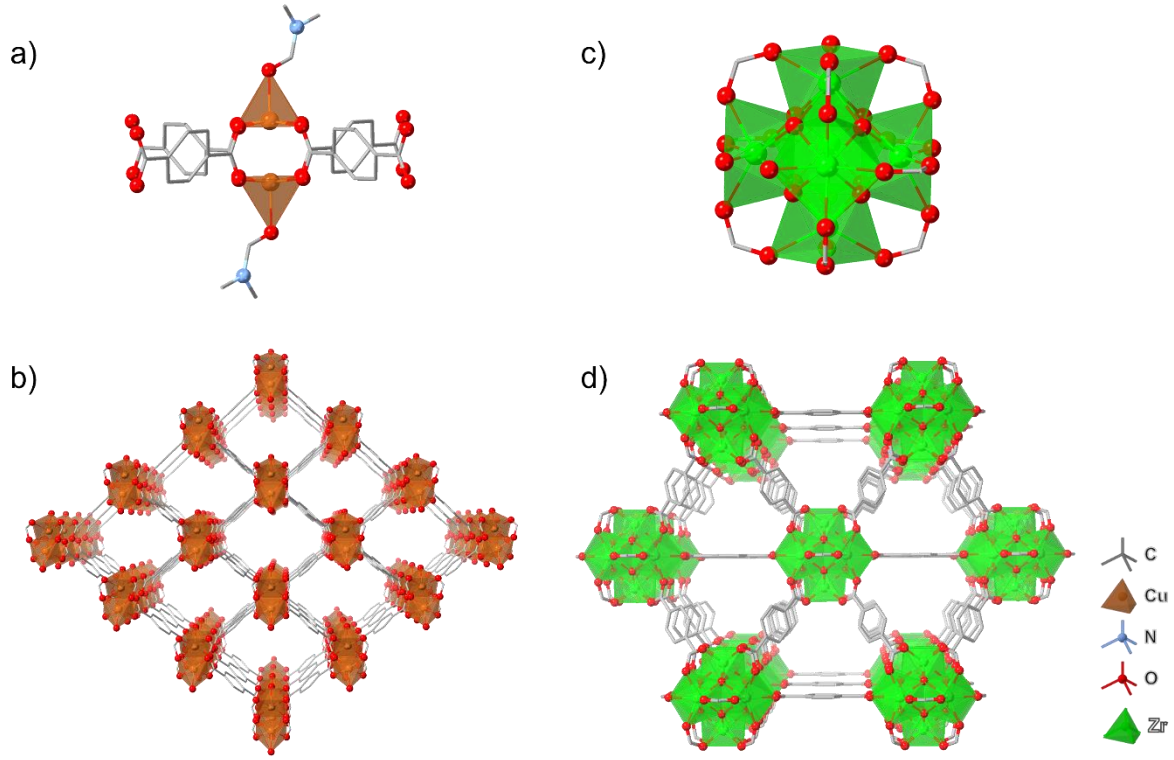

Figure 3.1 – Crystal structures of a) SBU of a copper BDC MOF. Each Cu(II) is coordinated to two BDCs in a bidentate bridging fashion and one DMF molecules to give a square-pyramidal geometry b) copper BDC MOF (CSD code = PUYREH), sheets containing Cu(II) coordinated to BDC are held together through weak stacking interactions, the structure is similar to MOF-2, c) Zr6O4(OH)4 SBU of d) UiO-66 (CSD code = RUBTAK) in which Zr clusters are connected by bridging BDC to form a 3D network.3,4 Hydrogens omitted for clarity.

This chapter discusses the synthesis of MIL-53(Al), MIL-53(Al)-NH_2 and MIL-121 and their Cu(II) uptake properties. This set of MOFs has been chosen due to their structural stability.

Water stability of MIL-53(Al) at different pHs has previously been investigated by Huang *et al.*, showing that the MOF is resistant to hydrolysis at pH 1, 7 and 14 up to 50 °C.[5] In addition, MIL-53(Al)-NH_2 and MIL-121 contain uncoordinated pendant Lewis basic groups (an NH_2 and COOH, respectively, see Figure 3.2) which should, in theory, enhance the heavy metal adsorption capabilities of the MOF due to an additional binding site being present.

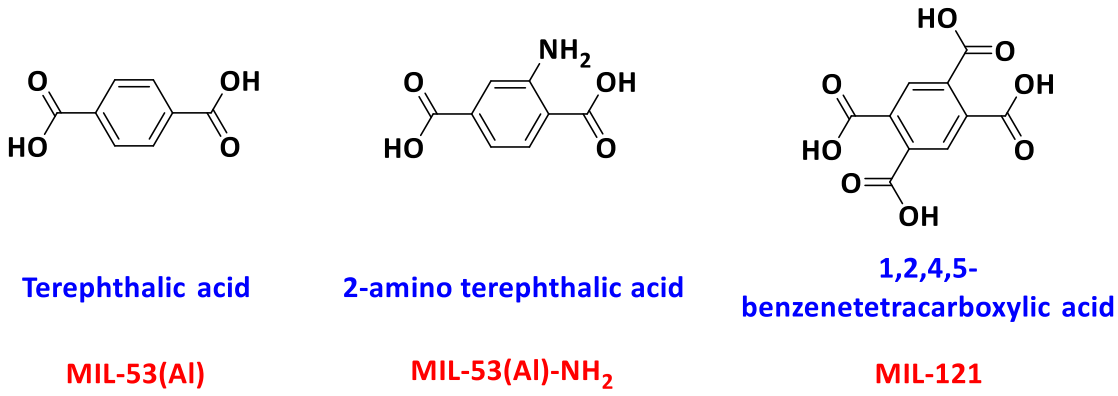

Figure 3.2 – Structures of the three organic linkers used in the synthesis of MIL-53(Al), MIL-53(Al)-NH_2 and MIL-121.

3.1.1 Introduction to the MIL-53(Al) series

MIL-53(Al) (MIL stands for Matériaux de l'Institut Lavoisier) is a well-studied material that was first synthesised by Loiseau *et al*. in 2003.[6] Its 3D framework is made up of infinite *trans* chains of corner sharing $AlO_4(OH)_2$ octahedra, connected by 1,4-benzenedicarboxylate (BDC) ligands (see Figure 3.3). The structure contains 1D rhombic-shaped channels, the size of which depends on the size and chemical properties of the guest molecules that are present inside them, giving rise to a phenomenon commonly known as a breathing effect (Figure 3.4).[7]

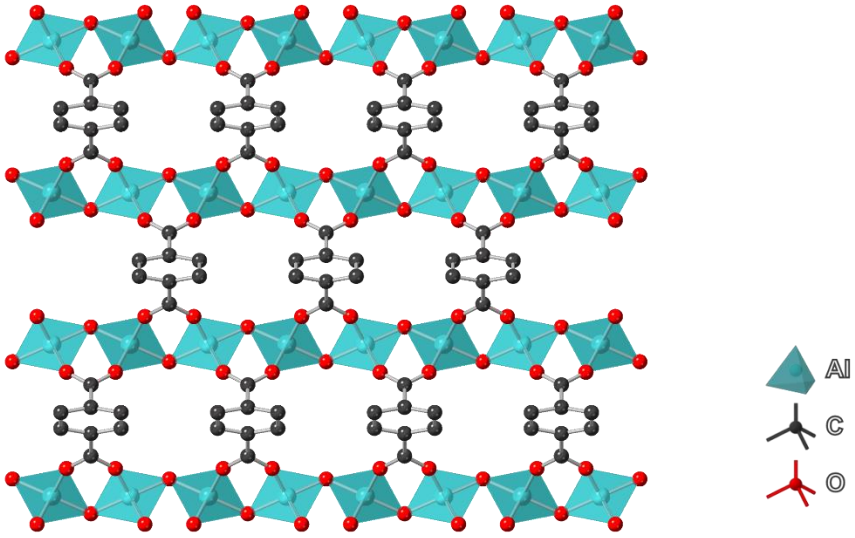

Figure 3.3 – View of the MIL-53(Al)op structure down the b axis, showing the trans-connected chains of $AlO_4(OH)_2$ octahedra. Hydrogen atoms are omitted for clarity. CSD code = SABVUN.[7] Hydrogens omitted for clarity.

The BDC ligand used to synthesise MIL-53(Al) can be exchanged for -Cl, -Br, $-CH_3$, $-NO_2$, $-(OH)_2$, $-NH_2$ and $-(COOH)_2$ substituted versions of BDC, to give functionalised versions of MIL-53(Al).[8–10] The addition of functional groups can impact the properties of the MOF, including changing its breathing behaviour, due to interactions of the functional groups with each other and any trapped species in the pore channels.[8,11] As the amino- and carboxylate-functionalised versions of MIL-53(Al) were the focus of this work, the next sections will describe their synthesis, and the synthesis of MIL-53(Al), in more detail.

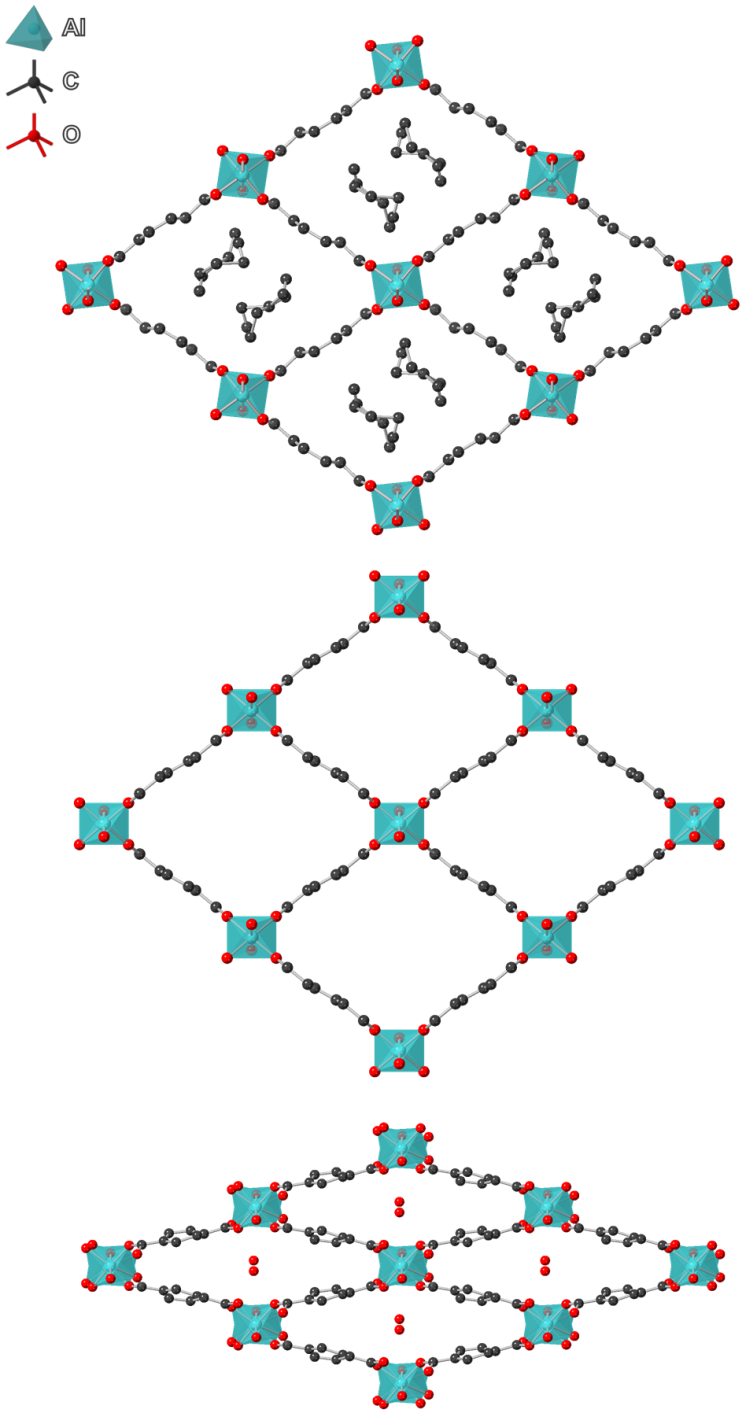

MIL-53(Al)as

CSD entry = SABVOH

Channels = 7.3 x 7.7 Å

As-synthesised - after synthesis, the channels are occupied with free disordered terephthalic acid molecule

MIL-53(Al)op

CSD entry = SABVUN

Channels = 8.5 x 8.5 Å

Open – channels are completely empty

MIL-53(Al)hyd

CSD entry = SABWAU

Channels = 2.6 x 13.6 Å

Hydrated - channels are occupied by water molecules

Figure 3.4 – Crystal structures of the three common forms of MIL-53(Al).[7] The channel sizes depend on what species is present in the pores of the MOF. Hydrogens are omitted for clarity.

3.1.1.1 MIL-53(Al)

The synthesis of MIL-53(Al) is well studied and has previously been carried out using various techniques, including hydrothermal,[7] electrochemical,[12] microwave (MW),[13] and in

continuous flow.[14,15] In most cases, the reaction (Scheme 3.1) is carried out with a 2:1 ratio of aluminium salt to H_2BDC and using water as a solvent.[6,7] Aluminium nitrate,[7] aluminium sulfate,[16] or aluminium chloride[17] have all been used previously as the metal source. The choice of heating method has a significant impact on the reaction time; under hydrothermal conditions, the reaction takes 3 days, whereas MW heating can produce MIL-53(Al) in minutes.[16]

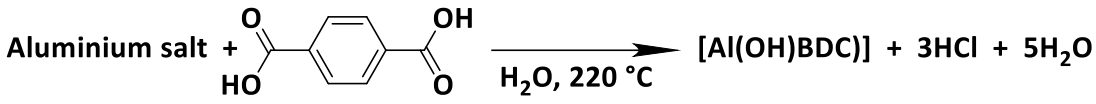

Scheme 3.1 - Hydrothermal synthesis of MIL-53(Al)as, as reported in the literature.[7]

During the synthesis, the channels in MIL-53(Al) become blocked with BDC (forming MIL-53(Al)as). To remove the excess H_2BDC to form MIL-53(Al)op, the MOF must be activated. A number of methods for the activation of MIL-53(Al) have been reported in the literature, including: calcination (heating in air at 330 °C for 3 days),[18] solvent extraction using DMF,[19] and treatment with supercritical ethanol.[15] When MIL-53(Al)op is exposed to air, H_2O is absorbed into the pores forming a narrow pored, hydrated from of MIL-53(Al) known as MIL-53(Al)hyd (Figure 3.4).

3.1.1.2 MIL-53(Al)-NH2

Several methods have been reported for the synthesis of MIL-53(Al)-NH_2 (see Table 3.1). The first reported synthesis of MIL-53(Al)-NH_2 was by Ahnfeldt *et al.* in 2009 (row 1, Table 3.1),[9] where they completed a synthesis optimisation using high throughput methodology. During this they looked at the effect of temperature (110-180°C), metal salt ($Al(NO_3)_3{\cdot}9H_2O$, $AlCl_3{\cdot}6H_2O$ and $Al(ClO_4)_3{\cdot}9H_2O$), and solvent (acetonitrile, DMF, methanol, and water) on the reaction product. From 350 experiments they found that the optimal conditions for MIL-53(Al)-NH_2 were as follows: (1) H_2O as the solvent, (2) a 1:1 molar ratio of Al^{3+}:H_2N-H_2BDC, (3) a reaction temperature of 150 °C. Lower reaction temperatures lead to less crystalline products and higher temperatures can cause the decomposition of the linker. Rationalisation for the choice of metal source and solvent were not given.

Table 3.1 – Details of syntheses of MIL-53(Al)-NH_2 found in the literature

Reference	Metal salt used	Molar ratio of metal salt to linker	Solvent used	Reaction type	Reaction temperature / °C	Reaction time / hours	Activation method	Yield
[9]	$AlCl_3 \cdot 6H_2O$	1:1	H_2O	Hydrothermal	150	5	Exchange with DMF at 150 °C then thermal treatment at 130 °C to remove DMF	50% w.r.t. linker
[21]	$AlCl_3 \cdot 6H_2O$	1:1	H_2O/DMF	Solvothermal	150	24	Boiled in DMF for 5 hours, centrifuged and washed with dimethyl ketone, dried in vacuum oven overnight	'Nearly 100% yield'
[20,24–26]	$Al(NO_3)_3 \cdot 9H_2O$	1:1.5	DMF	Solvothermal	130	72	Washed overnight with methanol under reflux and dried at 110 °C under in vacuo for 8 h	~ 40%
[27]	$AlCl_3 \cdot 6H_2O$	1:1	NaOH(aq) 0.9 M	Solvothermal	Room temperature	24	Exchange with DMF at 150 °C then thermal treatment at 130 °C to remove DMF	None reported
[23]	$Al(NO_3)_3 \cdot 9H_2O$	1:1.5	DMF	Microwave and ultrasonic	150 W Microwave 50 W Ultrasonic	0.42	Washed twice with DMF in an autoclave at 130 °C for 24 h, then acetone soxhlet extraction for 20 h	95%
[22]	$Al(NO_3)_3 \cdot 9H_2O$	2:1	H_2O	Microwave	200	0.87	Calcination at 150 °C for 12 h	73%

In the work by Ahnfeldt *et al.* structural determination was carried out by PXRD, so the structures they synthesised were not deposited into the CSD. Later, in 2012, single crystal structural determination of several forms of MIL-53(Al)-NH_2 was carried out (see row 3, Table 3.1, for synthesis details). This included a narrow pore form with empty pores and an open pore structure with CO_2 in the pores (**Error! Reference source not found.**), demonstrating t hat MIL-53(Al)-NH_2 exhibits a similar breathing effect to MIL-53(Al).[20]

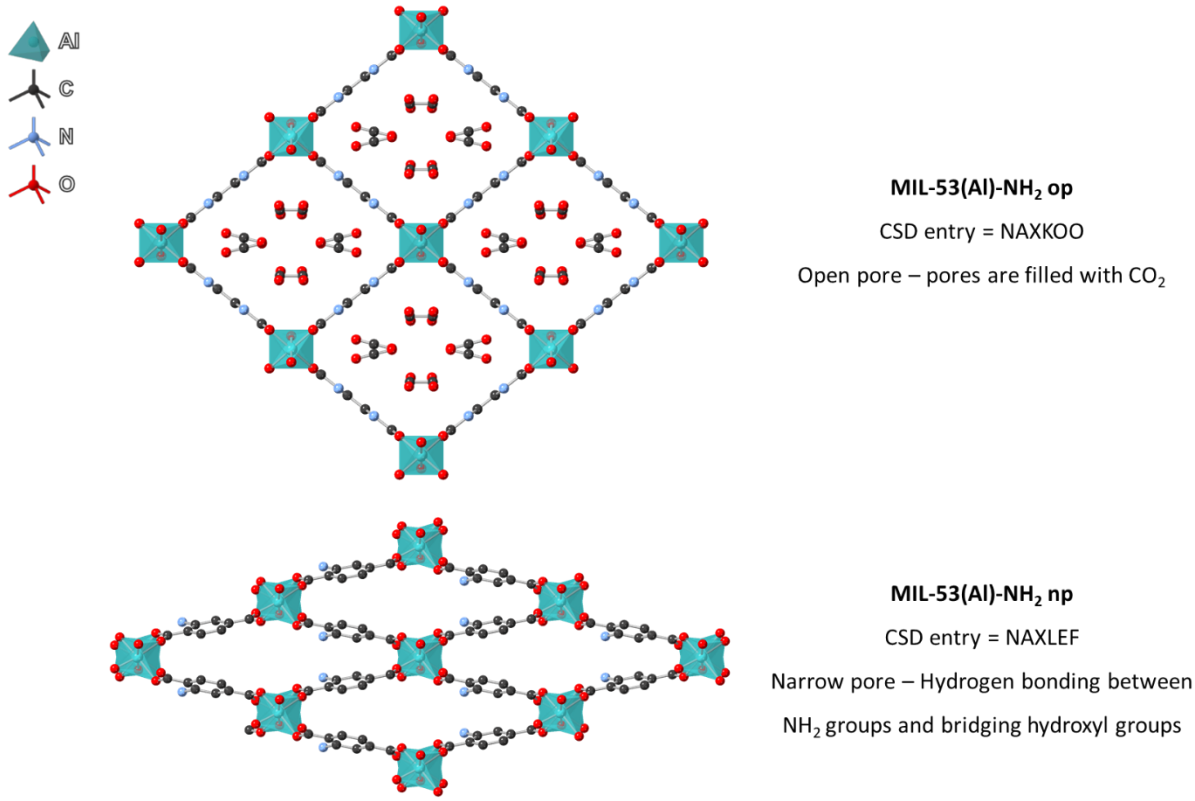

Figure 3.5 - Crystal structures of open and narrow pore forms of MIL-53(Al)-NH_2. Although the nitrogen atoms are shown on every position in the benzene ring in the open pore structure and in a fixed position in the narrow pore structure, the nitrogen atoms are randomly distributed on each position in both structures. Hydrogen atoms are omitted for clarity.

In 2013, Cheng *et al.* looked into the effect of changing the ratio of DMF to water in a mixed solvent system for the synthesis of MIL-53(Al)-NH_2.[21] They reported changes in crystal size, particle morphology, BET surface area and micropore volume as the amount of DMF was varied.

MIL-53(Al)-NH_2 has also been synthesised using microwave heating, using either DMF or water as a solvent (rows 5 and 6, Table 3.1).[22,23] The use of MWs significantly reduces the

reaction time as MIL-53(Al)-NH_2 is formed in under an hour compared to 5 hours for solvothermal synthesis.

Like MIL-53(Al), when MIL-53(Al)-NH_2 is synthesised, H_2N-H_2BDC is trapped inside the pores of the MOF, and the MOF must be activated to be used for adsorption applications. Volkinger *et al.* reported that MIL-53-NH_2(as) (Al(OH)[H_2N-BDC]·0.3-(H_2N-H_2BDC)) cannot be activated by thermal methods.[10] It was suggested that this is due to strong host-guest interactions that exist between the pores of the MOF and the excess H_2N-H_2BDC in the channels, due to the presence of the amine groups. Instead, activation of MIL-53-NH_2(as) to MIL-53-NH_2(DMF) was carried out by solvent exchange with DMF at 150 °C, followed by thermal treatment at 130 °C to remove the DMF and form MIL-53(Al)-NH_2(lt).[10] A number of different activation methods have since been used (see column 8, Table 3.1), most commonly solvent exchange with DMF.

3.1.1.3 MIL-121

MIL-121 is an analogue of MIL-53(Al) where 1,2,4,5-benzenetetracarboxylic acid (H_2BTEC) is used as the linker, resulting in a MOF that contains two extra uncoordinated carboxylic acid groups (Figure 3.6). The synthesis of MIL-121 is only reported in a handful of papers, in which the conditions were always kept the same. The original synthesis of MIL-121 (see Scheme 3.2) was found by a high throughput synthesis method, where the chemical system of $Al(NO_3)_3{\cdot}9H_2O$/1, 2, 4, 5-benzenetetracarboxylic acid/H_2O/NaOH was investigated.[10]

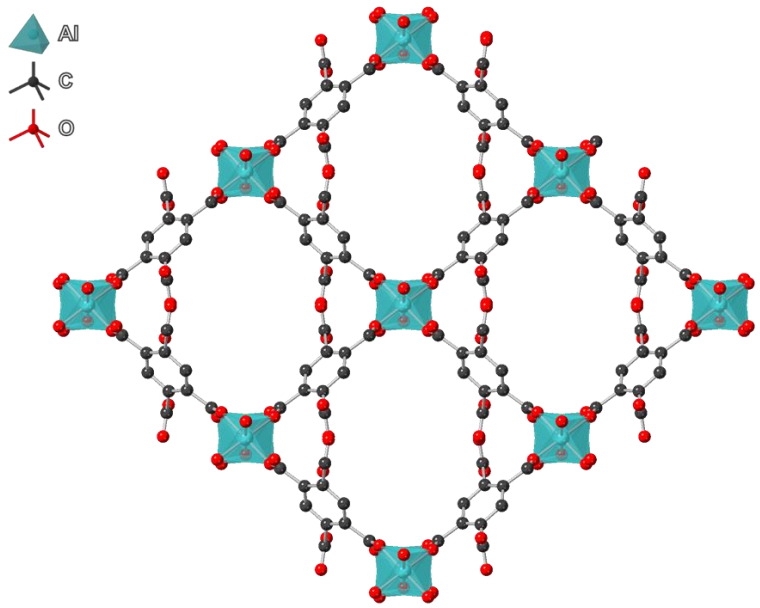

Figure 3.6 – Crystal structure of MIL-121. The pores are kept open due to the hydrogen bonds between the pendant carboxylate groups.[10] Hydrogen atoms are omitted for clarity.

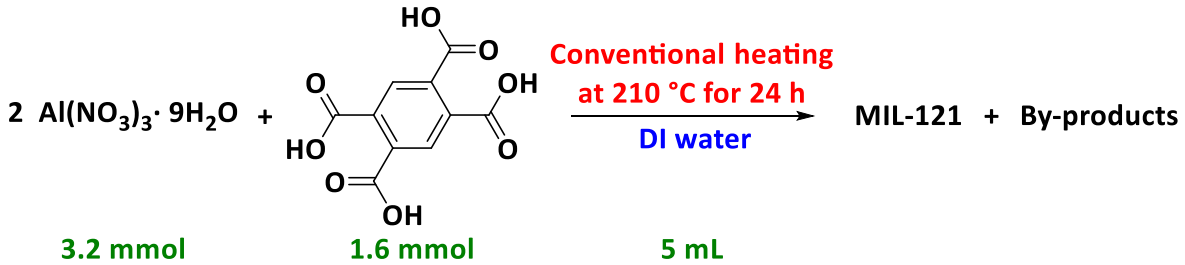

Scheme 3.2 - Reaction scheme for the first reported synthesis of MIL-121 by Volkringer *et al.*[10]

The pH of the initial reaction mixture must be controlled carefully (the starting pH is 1.41)[10] to obtain MIL-121 over two other possible phases, MIL-118 and MIL-120, which can be formed from the same metal salt and organic linker. In MIL-118 and MIL-120 the four carboxylate groups in BTEC are connected to four different aluminium octahedra, with MIL-118 possessing

trans connected Al octahedra and MIL-120 possessing zigzag edge sharing Al octahedra (connected in a *trans-cis-trans-cis* sequence (Figure 3.7)).[28,29] This tight control of reaction conditions is expected as the linker has four carboxylate groups, which are all capable of coordinating to the aluminium metal centre. Unlike MIL-53(Al) and MIL-53(Al)-NH_2, MIL-121 is reported to exist only in an open pore form, due to steric hindrance of the non-bonded carboxylate groups of the linker.

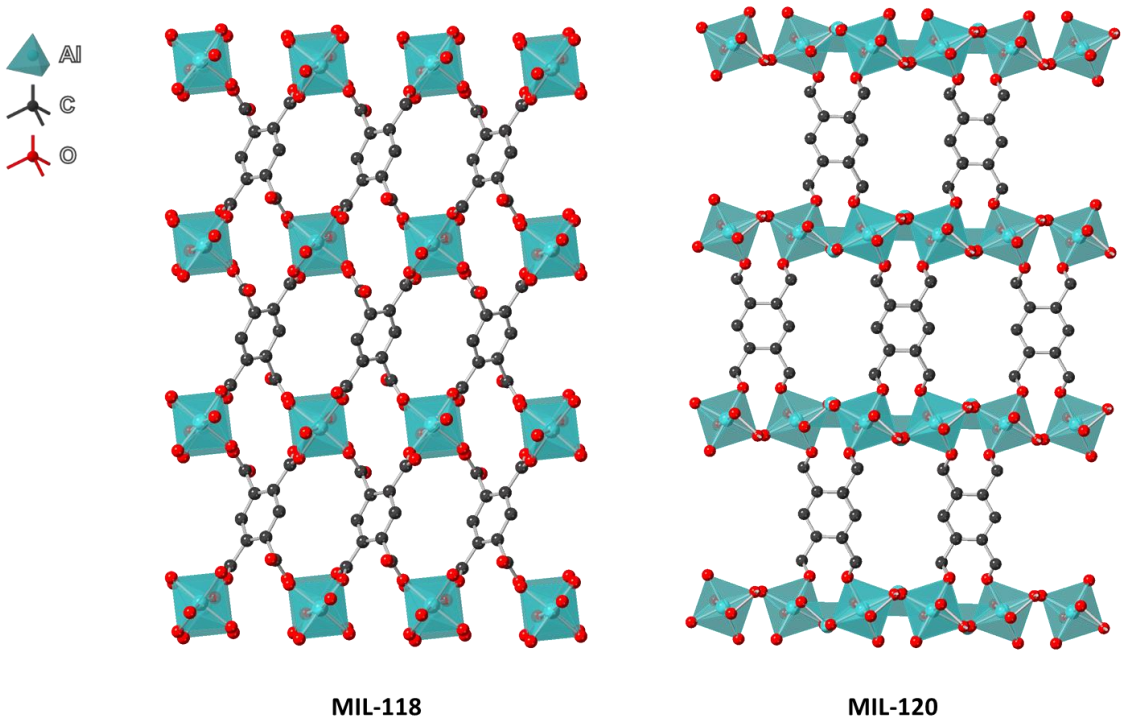

Figure 3.7 – Crystal structures of MIL-118 and MIL-120.[28,29] Hydrogen atoms are omitted for clarity.

Although the synthesis of MIL-121 is straightforward, several methods have been reported for its activation. Originally, Volkringer *et al.* carried out calcination at 380 °C for 5 hours to remove the trapped H_2BTEC from the pores of the MOF.[10] However, later it was shown that activation at such a high temperature leads to partial decarboxylation of the pendant carboxylate groups.[30] A number of calcination temperatures were investigated and used evidence from PXRD, TGA and IR analyses to show that:

- At 180 °C the trapped H_2BTEC dehydrates to form pyromellitic dianhydride (evidenced by two peaks at 1806 and 1831 cm^{-1} in the IR spectra, which indicate the C=O stretches of an anhydride)

- The linker and newly formed acid anhydride are partially removed by calcination at 250, 300 and 350 °C (IR and TGA)
- The pores become completely free after activation at 380 °C
- The pendant carboxylate groups are fully intact at 300 °C but decarboxylation of these groups starts above this temperature
- The MOF structure completely decomposes to Al_2O_3 after heating at 530 °C.

More recently, the impact of thermal treatment on the extent of decarboxylation and resulting porosity was investigated.[31] It was found that treating MIL-121 at 440 °C for 16h creates a mesoporous material which is well suited to CO_2 adsorption (uptake is 215.7 $cm^3\ g^{-1}$ at 195 K and 1 bar, compared to 25.4 $cm^3\ g^{-1}$ for MIL-121 treated at 250 °C). It is also confirmed that treatment above 380 °C leads to the formation of anhydrides in the pores of the MOF (Figure 3.8).

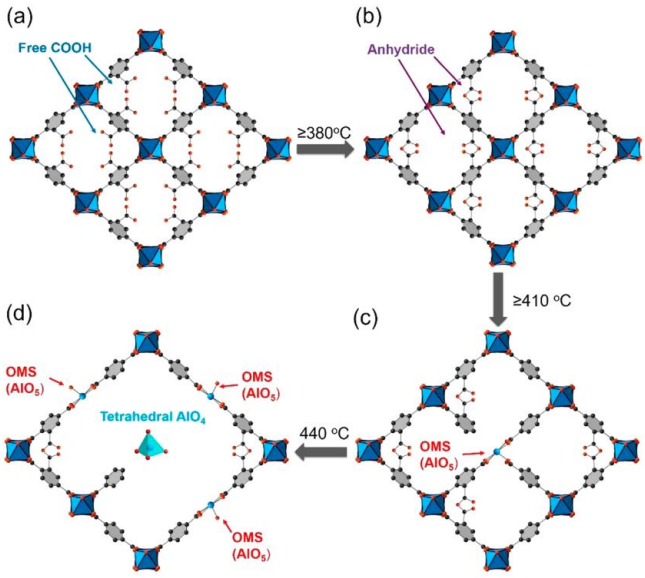

Figure 3.8 – "The free carboxylic acid linker groups in (a) are condensed to an anhydride group after thermal treatment (b), and treatment at further elevated temperatures leads to the creation of AlO_5 OMSs in (c), followed by collapse of the local structure to generate the tetrahedral AlO_4 alumina sites and additional AlO_5 OMSs in (d)".[31] Reprinted with permission from *J. Am. Chem. Soc.*, 2019, **141**, 14257−14271. Copyright (2019) American Chemical Society.

The work described above used methanol solvent exchange to activate the MOF, prior to the thermal treatment experiments. The as-synthesised MOF is soaked in MeOH and heated to

150 °C in an autoclave for 2 days.[31,32] Alternatively, Soxhlet extraction with MeOH has also been reported as an activation method.[33]

3.1.2 Examining the stability of MOFs

As described in Chapter 1, MOFs must possess mechanical, thermal and chemical stability if they are to be applied to real-world challenges such as catalysis, gas sorption and metal removal. For the application addressed in this Chapter, Cu(II) sorption from aqueous solution, hydrolytic stability is of the upmost importance, specifically over a range of pHs, to account for differences in the waste streams that the MOFs might be exposed to.

There are various reviews available that explore the water stability of a range of MOFs, and the reader is directed to these for a more comprehensive understanding of the status of research into water stable MOFs.[34–40] In general, MOFs that exhibit greater stability often possess one of the following characteristics:

- High valent metals
- Highly coordinated metal centres or metal ions
- Hydrophobic ligands.

The stability of MOFs is indicated by the retention of crystallinity after exposure to a specified environment. This is measured by carrying out PXRD before and after exposure, and observing any changes in the patterns, specifically the positions, widths, and intensities of the observed reflections. For a more complete view of whether the MOFs characteristics are maintained after exposure to different environments, gas sorption experiments should be carried out to determine whether the surface area has been affected by the environment that the MOF has been exposed to. Loss of surface area can indicate pore collapse and amorphization of the MOF.[34,35]

Although the analysis methods for establishing whether a MOF is stable is clear, the methods for conducting stability experiments are varied and inconsistent across the literature.[34] Different masses, volumes, soaking times and temperatures are used, making it difficult to compare studies and evaluate which MOFs are truly the most stable. Having said this, a recent paper conducted a thorough evaluation of the “robustness” of 17 MOFs by exposing them to

a wide range of environments. Various carboxylate, salicylate and azolate based MOFs were suspended in aqueous and organic Bronsted acids and bases, as well as nucleophiles, electrophiles, oxidants and reductants.[37] Stability was determined by PXRD, specifically measuring changes in the full width half maximum (FWHM) of reflections. The systematic method used in this study is a step-change compared to other studies that usually focus on a few MOFs or a few environments. It could, however, have been improved by exposing MOFs to the different environments for more than 24 hours, as this might not be long enough to observe any changes that could occur over time. This is especially important when considering that MOFs could be exposed to different conditions for extremely long times if they are to be used in certain applications.

The analogues of MIL-53(Al) were chosen as they contain a high valence metal and no free metal sites, properties that are known to give rise to strong bonds between the metal centres and the carboxylate containing linkers. It was hoped that this will make the MOFs less susceptible to attack by hydroxide ions and therefore linker displacement and framework degradation. The stability of MIL-53(Al) has been investigated a few times in the literature. Firstly, it was shown to be stable in 25 mol% steam at 350 °C or 50 mol% steam at 225 °C.[41] Secondly, MIL-53(Al) was shown to be stable in neutral and acidic aqueous conditions, with a structural transformation seen after exposure to a basic aqueous solutions.[42] These reports are promising, but the stability of the synthesis analogues of MIL-53(Al) will be investigated further, using a method similar to that used by Milner *et al.*.[37]

3.1.3 Examining metal uptake of MOFs

As stated in Chapter 1, the subject of heavy metal sorption using MOFs has been subject to a number of recent reviews.[43–47] The metal removal properties of a MOF from aqueous environment are usually examined through batch experiments where the MOF is added to a solution of specified metal concentration for a defined period of time. Often, parameters such as metal concentration, MOF loading, pH of the starting solution and time of exposure are varied to give a more complete picture of what properties favour metal uptake by the MOF. Despite this, some key issues remain in this area of research:

- An inconsistent approach to these experiments across the literature means that different metal removal studies (different MOF and different metal ions, for example) are often incomparable due to the use of different parameters. The most important factors that are varied are MOF loading and metal concentration which can have a significant impact on the results achieved.
- Metal uptake is commonly measured at metal concentrations that are higher than those that would be seen in real environmental conditions.[43]
- The stability or recyclability of the materials is not examined, so the potential lifetime of the material in the conditions used in unknown. [43,44,46]

Overall, there is no agreed method across the literature for examining the metal uptake capabilities of a MOF, and it is suspected that the parameters used are either those that gave the best results or relate to the amount of adsorbent available to the researchers.

3.2 Aims

The overall aim of the work presented in this Chapter is to produce materials that could be used to remove Cu(II) ions from aqueous environments. The MIL-53(Al) series of MOFs have been chosen due to their predicted structural stability and because they contain Lewis basic functionality. As it is imperative that the materials produced can withstand real-world conditions, a key part of this work is determining of the structure of these materials is affected on exposure to different conditions. Ideally, the MOFs will undergo very little structural change under a wide range of conditions and will exhibit a high percentage of Cu(II) removal over a range of Cu(II) concentrations. The detailed aims are as follows.

3.2.1 Synthesis of MIL-53(Al), MIL-53(Al)-NH_2 and MIL-121

At least 1 g of MIL-53(Al), MIL-53(Al)-NH_2 and MIL-121 will be synthesised in order for these MOFs to be tested for their ability to remove Cu(II) from aqueous environments. Microwave (MW) synthesis will be used to produce these materials because it is significantly faster than other methods. Appropriate activation methods will also be examined, to ensure that the pores of the MOFs are free for metal uptake, and the MOFs will be characterised by PXRD, TGA, SEM, FTIR and gas sorption.

3.2.2 Examining the stability and Cu(II) uptake of MIL-53(Al), MIL-53(Al)-NH_2 and MIL-121

The MOFs will be exposed to different aqueous environments across a wide pH range, due to possible variations in the pHs of wastewater streams that contain Cu(II). Any changes to structure will be observed by PXRD.

Cu(II) uptake from aqueous solutions will be examined. Solutions with four different Cu(II) concentrations will be used to determine if this impacted uptake, and also because real-world wastewater streams contain varying amounts of Cu(II). The change in Cu(II) concentration will be examined over a week.

3.3 Synthesis and activation of analogues of MIL-53(Al)

3.3.1 Synthesis, activation, characterisation of MIL-53(Al)

3.3.1.1 Microwave synthesis of MIL-53(Al)as

The synthesis of MIL-53(Al) was carried out using microwave heating in a CEM batch reactor. The reaction (see Scheme 3.3) was carried out in deionised water, using a 2:1 ratio of $AlCl_3 \cdot 6H_2O$ to H_2BDC. Due to the large amount of material (~1 g) required for the stability and metal removal experiments, the reaction was repeated several times yielding approximately 1 g in an individual reaction (see experimental for further details, Section 3.6.2). The reaction gave a white, microcrystalline powder, which was collected using centrifugation.

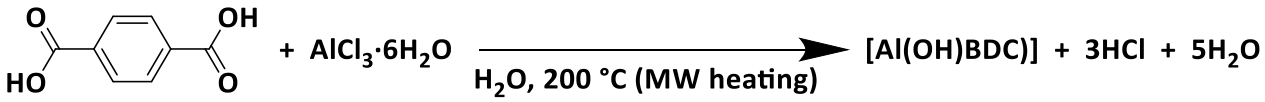

Scheme 3.3 - Synthesis of MIL-53(Al), where BDC = p-C_6H_4-$(CO_2^-)_2$.

To determine whether MIL-53(Al) was successfully synthesised, the white powder was analysed using PXRD (Figure 3.9). As described in Section 3.1.1, MIL-53(Al) exists in three forms, MIL-53(Al)as, MIL-53(Al)hyd, and MIL-53(Al)op. The PXRD of the synthesised material, was plotted against the simulated powder patterns of these three forms and H_2BDC, to determine which phases are in the product. The reflections in the synthesised material correspond well to those in MIL-53(Al)as form, as expected. The sample also contains some

of the MIL-53(Al)op and MIL-53(Al)hyd phases, as well as some unreacted H_2BDC (reflections at 17.2, 27.8 and 29.5° 2θ).

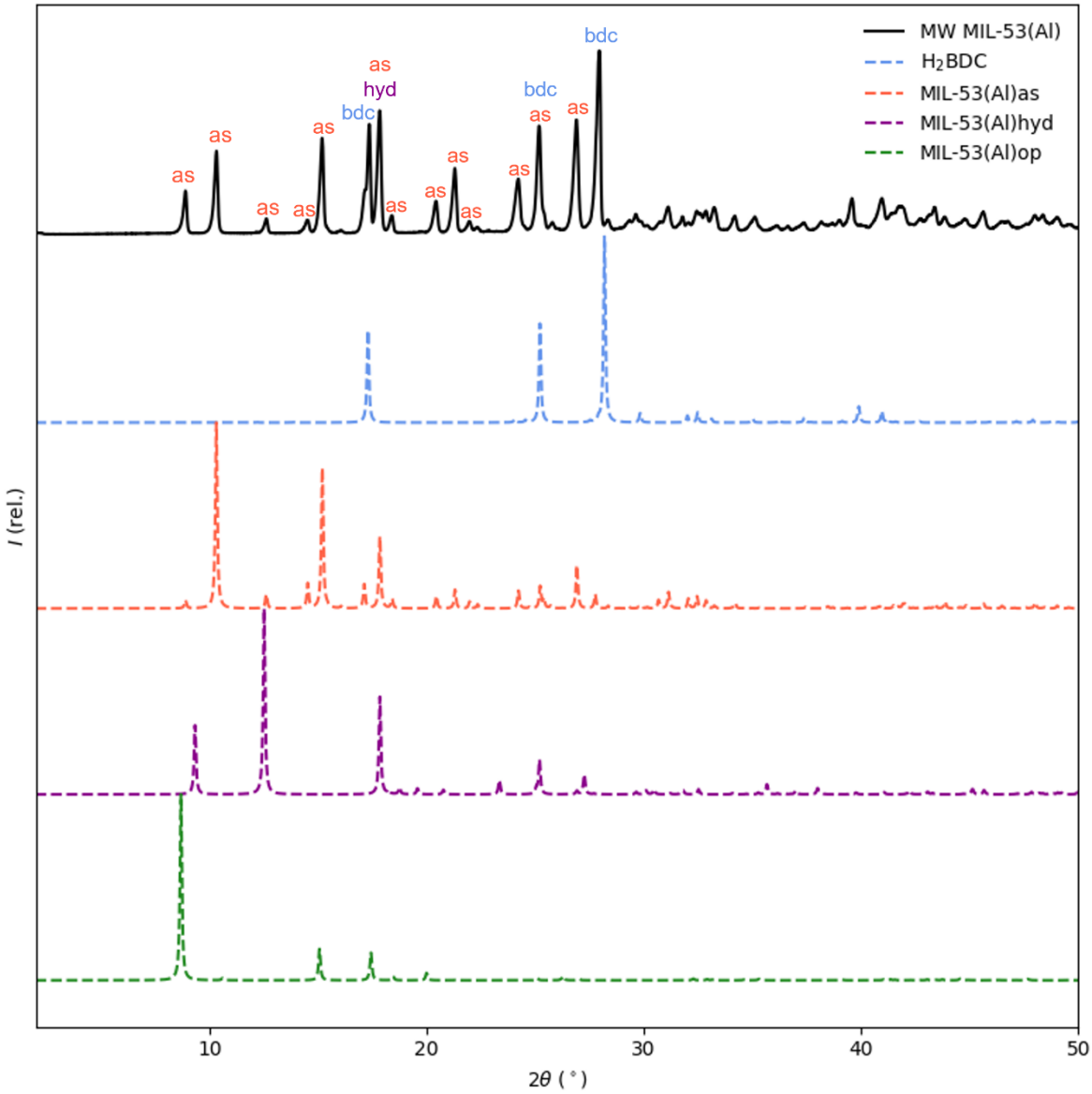

Figure 3.9 - PXRD patterns of MW synthesised MIL-53(Al)as, alongside simulated patterns of H_2BDC, and the three forms of MIL-53(Al). Reflections up to 30° 2θ are labelled with which phase they correspond to. as = MIL-53(Al)as, op = MIL-53(Al)op, hyd = MIL-53(Al)hyd, bdc= H_2BDC.

Thermogravimetric analysis confirmed that the MW synthesised MOF was in the as-synthesised form because the mass loss at 160 – 420 °C indicates the presence of H_2BDC in the pores Figure 3.10). The decomposition occurring between 450 and 650 °C is due to the decomposition of MIL-53(Al), which is consistent with the literature.[18]

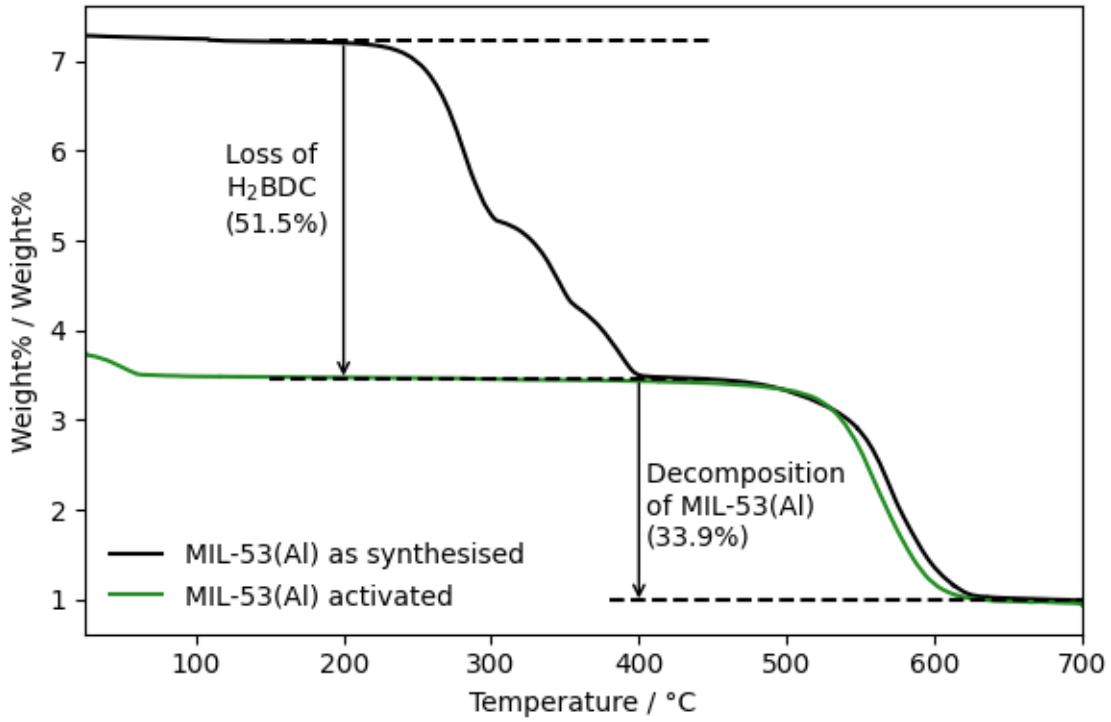

Figure 3.10 – TGA of MW synthesised MIL-53(Al)as and activated MIL-53(Al)hyd.

3.3.1.2 Activation of MIL-53(Al)

H_2BDC was found in the sample both as separate microcrystalline particles and trapped inside the pores of the MOF. The presence of microcrystalline H_2BDC was identified by observing peaks related to both H_2BDC and MIL-53(Al)as in the PXRD pattern (Figure 3.9). Activation was carried out using calcination, wherein samples were placed into ceramic boats in a furnace at 330 °C for 3 days.

TGA and PXRD were used to determine if the activation process was successful. There is no mass loss between 160 – 420 ° in the TGA of the activated sample (Figure 3.10), indicating that the sample no longer contains uncoordinated H_2BDC. The PXRD pattern (Figure 3.11) showed that most reflections correspond to MIL-53(Al)hyd, due the MOF absorbing H_2O from

the air, and that one reflection at 8.6° 2θ corresponds to the open pore form. This is another confirmation that activation was successful in removing excess, unreacted H_2BDC.

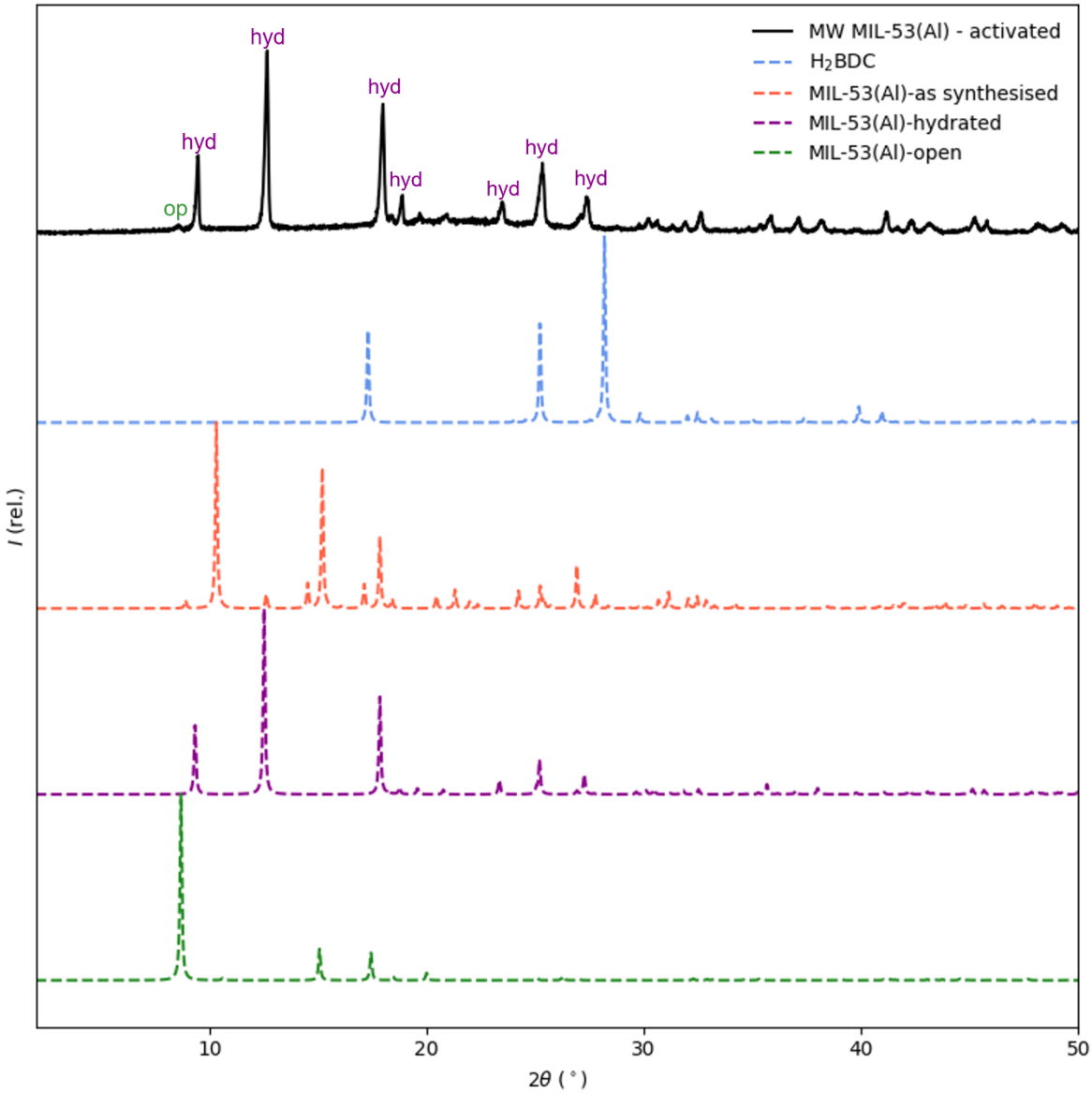

Figure 3.11 - PXRD patterns of activated MW synthesised MIL-53(Al), alongside simulated patterns of H_2BDC, and the three forms of MIL-53(Al).

A Pawley fit of the activated sample to the narrow pore phase (with H_2O in the pores) was carried out using Topas, to find the Goodness of Fit (GOF) to this phase and calculate the unit cell parameters of the activated sample (Table 3.2 and Figure 3.12). The data from the activated sample matches well with literature reported values; unit cell lengths are within 0.02 Å, angles are within 0.01° and a good GOF value of 1.45 was achieved.

Table 3.2 – Lattice parameters and GOF calculated from Pawley fit of an activated sample of MIL-53(Al), compared to np form of MIL-53(Al) reported in the literature (CSD code = SABWAU).[7]

	Space group	a	b	c	α	β	γ	GOF
Activated sample	*Cc*	19.5268	7.6144	6.5845	90.00	104.1810	90.00	1.45
Literature[7]	*Cc*	19.513	7.612	6.576	90.00	104.24	90.00	n/a

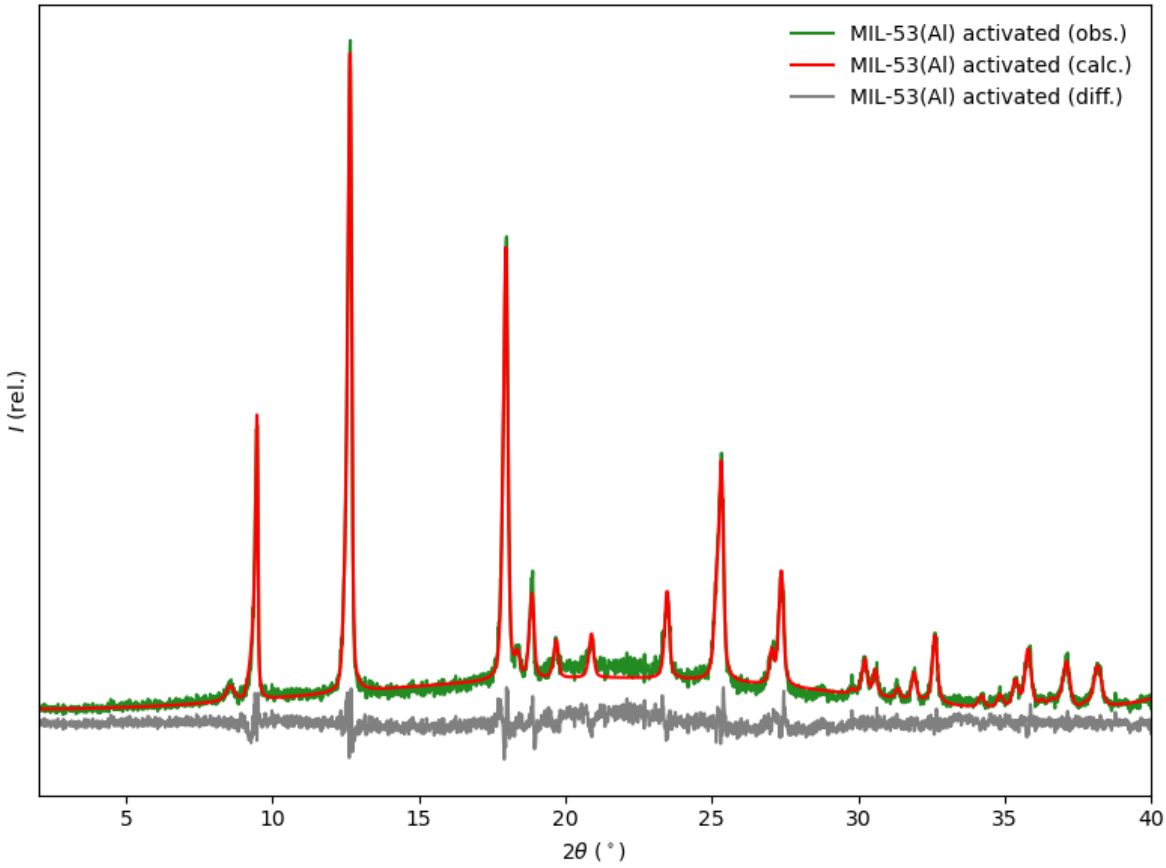

Figure 3.12 – Pawley fitting of the activated sample to the hydrated phase of MIL-53(Al) reported in the literature. The peak at 8.40° 2θ was fitted manually and corresponds to MIL-53(Al)op.[7]

SEM imaging of two successfully activated samples were undertaken to carry out particle size analysis (Figure 3.13). All particles measured were defined as irregular, due to the absence of uniformity between the particles. The size of particle was found by measuring the longest clear and definite crystal edge or face in imageJ software. Particle size analysis (Table 3.3, Figure 3.14) was carried out by measuring the size of ten particles in five different images (50 particles in total for each sample). The analysis showed that the two calcined products possess a similar range and distribution of particle sizes (Table 3.3, Figure 3.14).

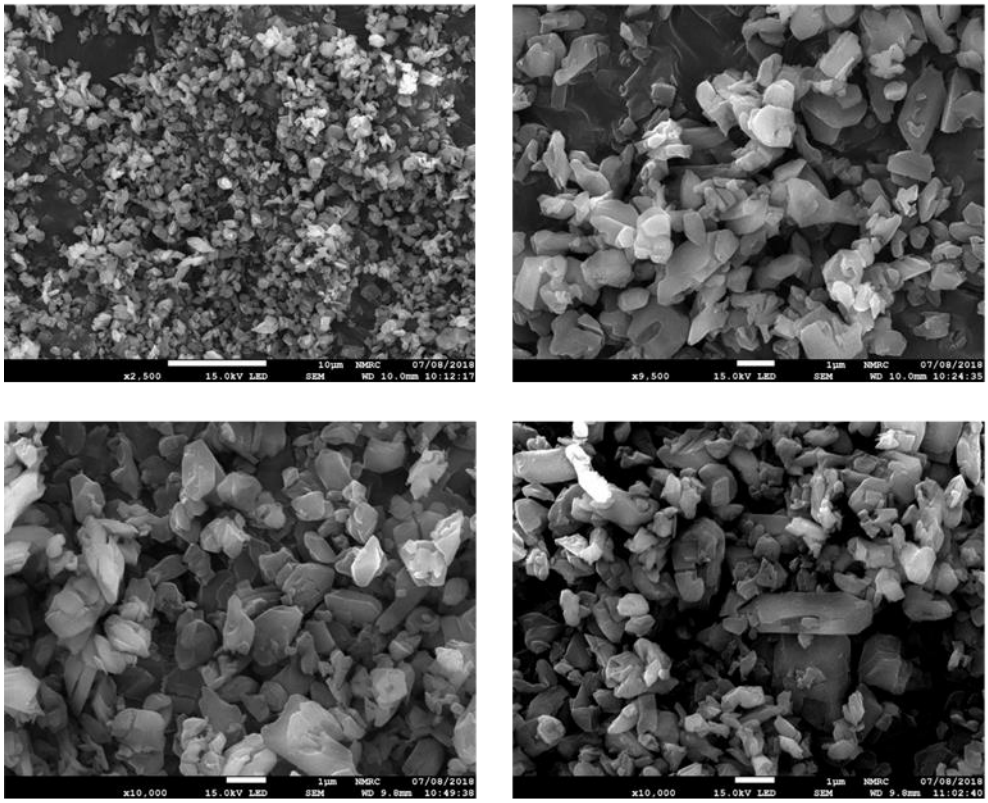

Figure 3.13 - SEM images of activated samples of MIL-53(Al): Sample 1 (top) and Sample2 (bottom). Sample 1 and 2 were synthesised and activated in the same way. Scale bars: top left = 10 µm, top right = 1 µm, bottom left = 1 µm, bottom right = 1 µm.

Table 3.3 - Average and range of particle sizes found in two samples of calcined MIL-53(Al). Sample 1 and 2 were synthesised and activated in the same way.

Sample ID	Average size / nm	Median / nm	Modal range / nm	Standard deviation / nm
Sample 1	1250 ± 90	1170	800-1000	630
Sample 2	1080 ± 90	940	600-800	640

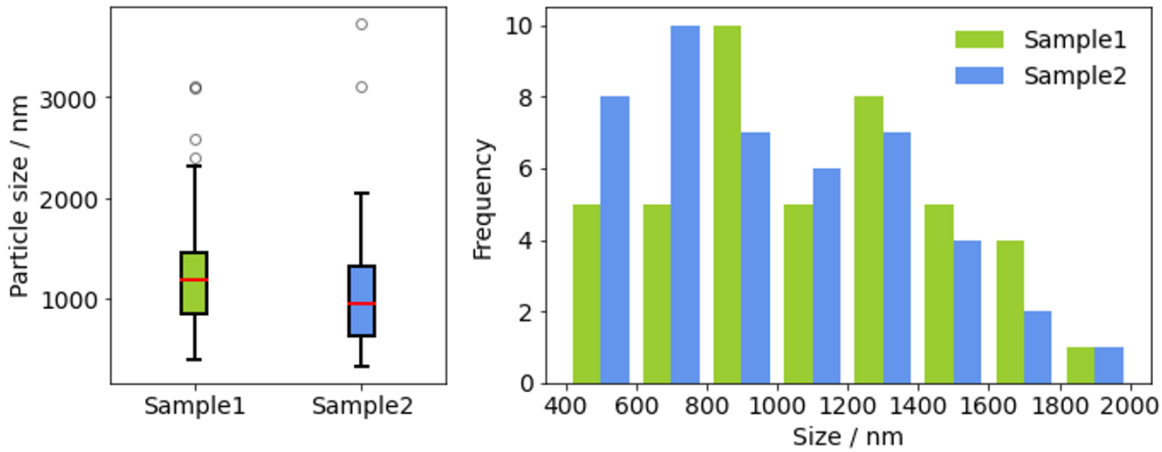

Figure 3.14- Boxplot and histogram showing the range of particle sizes in two samples of activated MIL-53(Al). Particles with sizes above 2000 nm are not shown in the histogram. Sample 1 and 2 were synthesised and activated in the same way.

Gas sorption analysis was carried out on a successfully calcined sample of MIL-53(Al) in order obtain a BET surface area measurement (Figure 3.15). Figure 3.15 shows that the material exhibits a Type I isotherm, which is characteristic of a microporous material.[48] The adsorption/desorption that occurs above 0.8 P/P_o is due to adsorption on the external surface of the closely packed particles. A BET surface area of 1242.4 ± 0.4 $m^2 g^{-1}$ was calculated from the data (Figure 3.16), which is in line with previously reported values.[7,16,42,49]

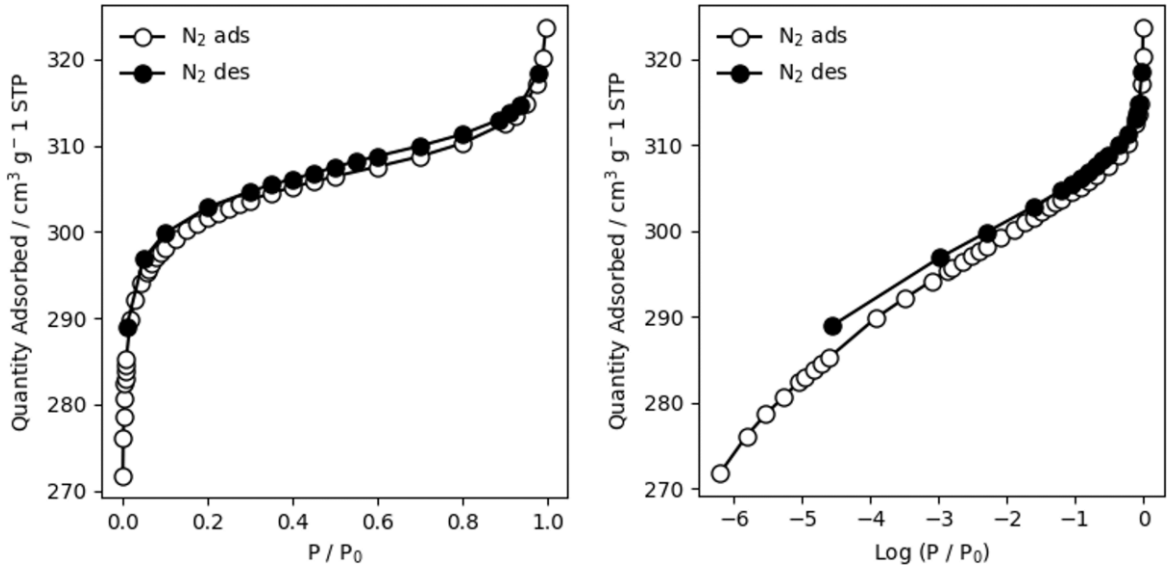

Figure 3.15 - Nitrogen adsorption-desorption isotherm of a calcined sample of MIL-53(Al). Log plot shown on right.

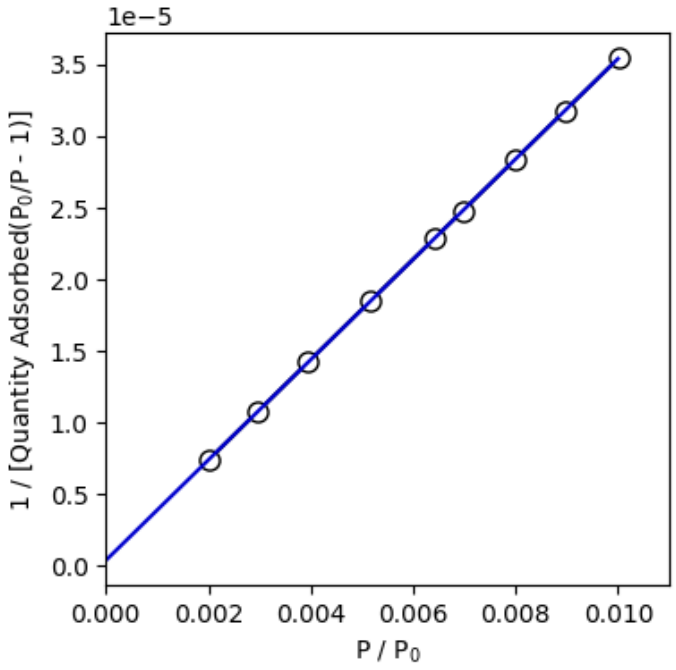

Figure 3.16 – Plot used to calculate BET surface area. The surface area is equal to the cross-sectional area of adsorbate / (slope + intercept).[50]

3.3.2 Synthesis, activation, characterisation of MIL-53(Al)-NH_2

3.3.2.1 Investigating the effect of changing the metal to linker ratio

Due to the lack of previous investigations into the effect of metal to linker ratio on the MIL-53(Al)-NH_2 synthesis, the effects of adjusting the Al(III):H_2BDC-NH_2 ratio on the synthesis of MIL-53(Al)-NH_2 were investigated. The general parameters used in these reactions are shown in Scheme 3.4 and the ratios used, and yields obtained are shown in Table 3.4.

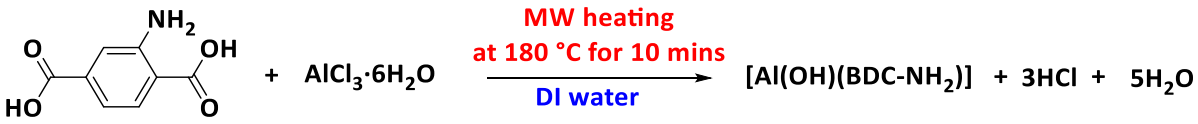

Scheme 3.4 – Scheme for the reaction carried out to investigate the effect of changing the metal to linker ratio used in the synthesis of MIL-53(Al)-NH_2.

It would have been preferable to explore a larger range of metal to linker ratios, but this was limited by the solubility of the linker in water and the size of a reaction vial.

Table 3.4 – Results of varying metal to linker ratio in the synthesis of MIL-53(Al)-NH_2. The red text shows the % yield w.r.t to the limiting reagent.

Sample	Moles of $AlCl_3 \cdot 6H_2O$ / moles	Moles of H_2BDC-NH_2	Ratio of metal salt:linker	Mass of product / g	% yield w.r.t. to $AlCl_3 \cdot 6H_2O$	% yield w.r.t. to H_2BDC-NH_2
NH-1:2	2.01	4.01	1:2	0.246	40.2	20.1
NH-1:1	2.00	2.01	1:1	0.101	16.5	16.4
NH-2:1	2.01	1.02	2:1	0.067	11.7	23.1

The reaction where a 1:2 molar ratio of metal salt to linker was used gave the highest yield (40.2%) with respect to the limiting reagent. This could be considered unexpected, as it would be anticipated that using an excess of linker may result in more linker becoming trapped in the pores of the MOF (the required stoichiometry of the reaction is 1:1). However, it is expected that the linker may act to template the formation of the MOF, so increased concentrations of the linker enhance the templating affect and favour MOF formation, with the templating linker becoming trapped in the pores of the MOF as it forms. The higher yield when using excess linker could also be because the linker may decompose at the temperature used in the reaction (180 °C), as reported previously.[9] If the linker is decomposing then increasing its concentration helps to counteract this effect, *i.e.* more linker will be present in the reaction mixture and therefore able to react to form the MOF.

PXRD (Figure 3.17) patterns for the three samples are similar, with peak positions and relative intensities matching, suggesting that the structure of each product is similar. Comparison of these products with the open pore form of MIL-53(Al)-NH_2 (green pattern)[25] showed good agreement of the principal reflections (8.7 and 10.4°, 2θ), suggesting that the synthesised MIL-53(Al)-NH_2 is also in the open pore form. This is due to the unreacted linker remaining in the pores of the MOF after synthesis. Discrepancies from the open pore form are seen at 15.2 and 26.8° 2θ, which correspond to peaks seen in the linker. Additionally, the first two peaks in the sample are slightly shifted (8.7 and 10.4° 2θ) compared to the literature pattern of the open form (8.6 and 10.9° 2θ), this is likely because the literature pattern is for MIL-53(Al)-NH_2 with CO_2 in the pores, whereas the synthesised sample contains H_2BDC-NH_2 in the pores (see TGA, Figure 3.19, below), so the lattice parameters of the two phases will be slightly different.

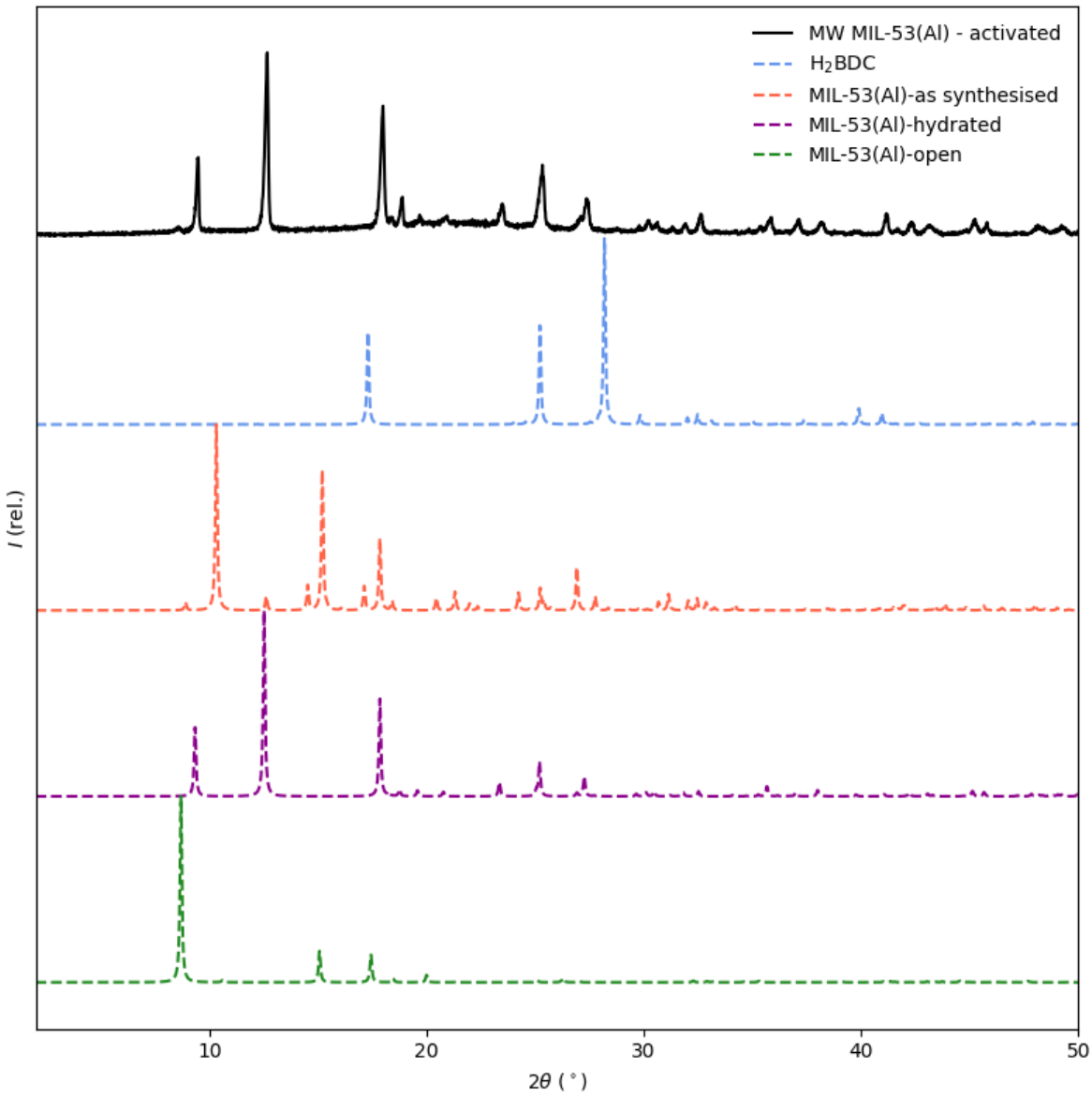

Figure 3.17 - PXRD patterns for syntheses of MIL-53(Al)-NH_2 where metal to linker ratio was varied as shown by the legend, alongside the simulated pattern for the open pore form of MIL-53(Al)-NH_2 and H_2BDC-NH_2.

The PXRD patterns can also be compared to those given in the supplementary information of the first reported synthesis of MIL-53(Al)-NH_2,[9] (see Figure 3.18, single crystal data was not collected so a simulated pattern is not available), where the PXRD pattern of the as-synthesised (with linker trapped in the pores) is reported. The positions of the first two peaks (8.7 and 10.4° 2θ) correspond more closely with this data (~8.5 and ~10.4° 2θ), which is expected as both data sets are MIL-53(Al)-NH_2 with linker in the pores.

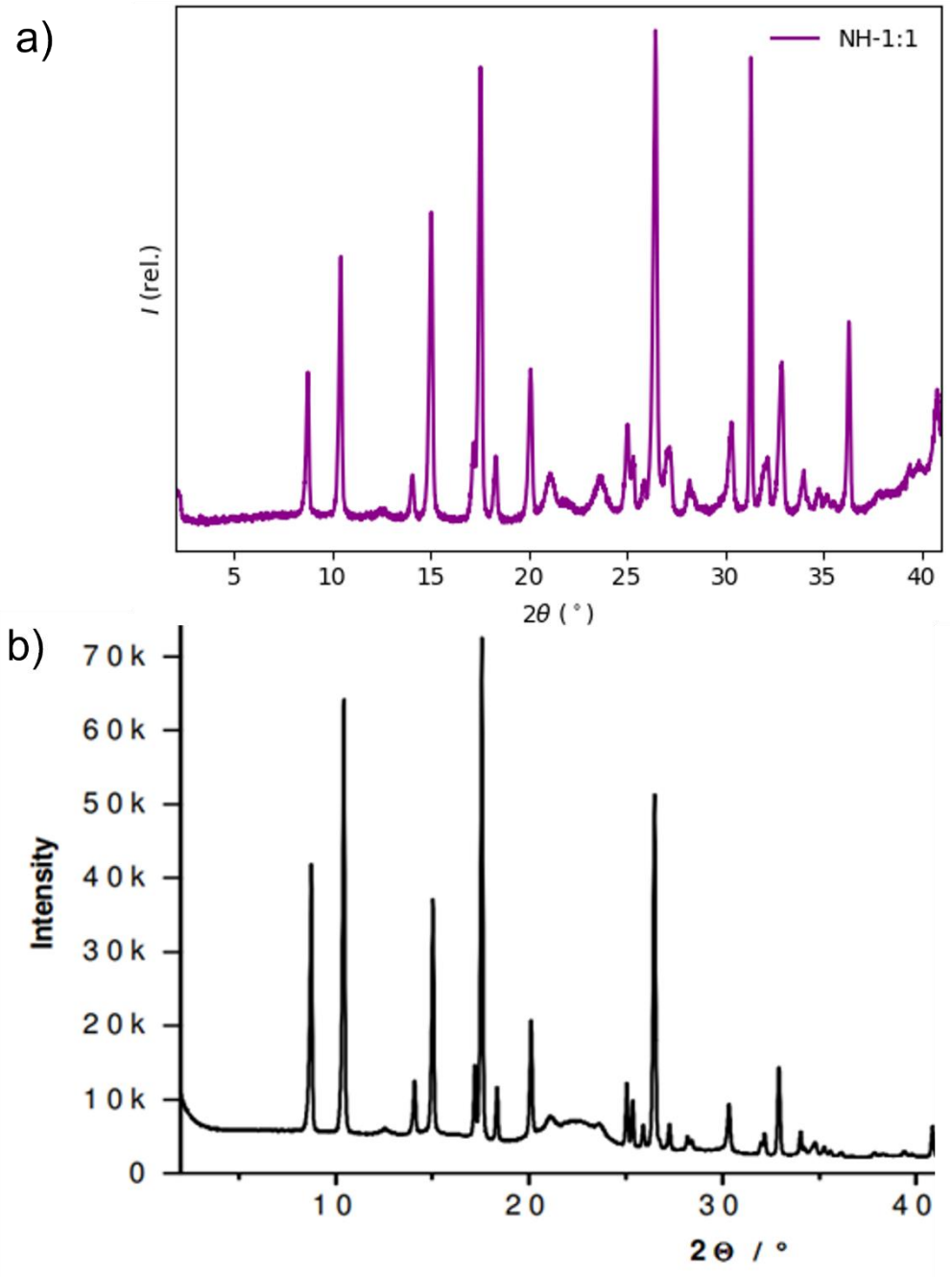

Figure 3.18 – a) PXRD of MW synthesised MIL-53(Al)-NH_2(as) using 1:1 ligand to metal salt ratio, b) PXRD of MIL-53(Al)-NH_2(as), reprinted with permission from Inorg. Chem. 2009, 48, 3057-3064. Copyright 2009 American Chemical Society.

The TGA data of the three samples (Figure 3.19) shows a decomposition event occurring from 250-350 °C due to the loss of linker (27-31% of mass) from the pores of the MOF. Above 420 °C the decomposition of the MOF occurs, which is consistent with literature.[9,21,25] At ~600 °C the MOF decomposition is complete and the 15-16% mass remaining is aluminium oxide.

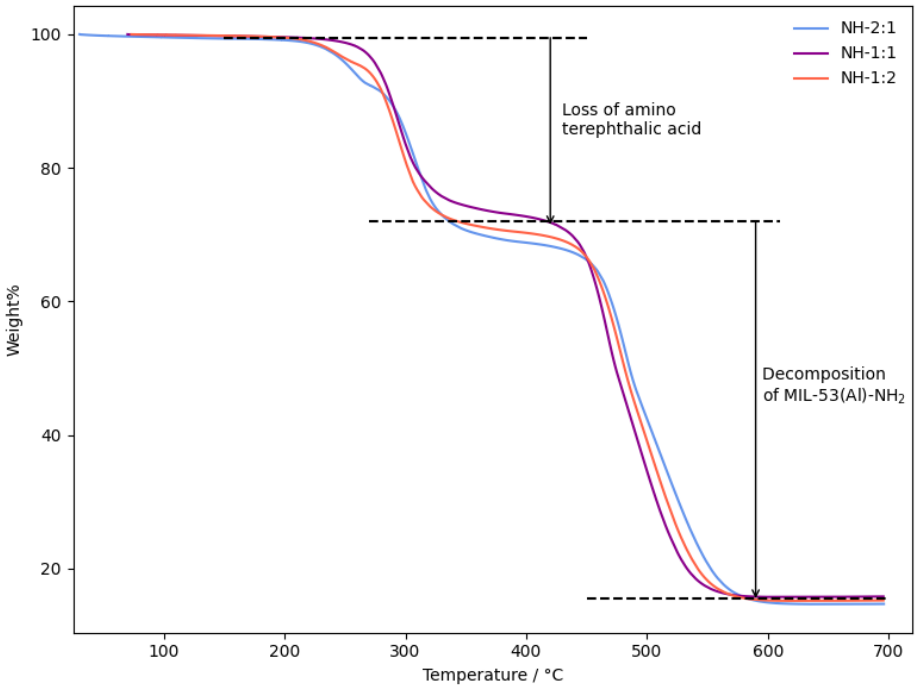

Figure 3.19 – TGA analyses of products of the varying metal to linker ratio experiments.

The TGA and PXRD results presented here show that the products obtained whilst varying the molar ratios of reactants used are consistent with one another and the literature. The key difference between reaction conditions is in the yield produced (highest for the 2:1 reaction, 40.2%) which is expected to be due to the linker decomposing above 150 °C. To investigate the effect of varying the ratio of reactants more thoroughly, the reactions would need to be repeated at 150 °C, and other metal salt to ligand ratios should be included (at least 1:3, 1:4, 3:1 and 4:1).

3.3.2.2 Investigating the effect of a DMF/water solvent mixture

It has previously been reported that the yield, particle morphology and BET surface area of MIL-53(Al)-NH_2 can be controlled by adjusting the solvent ratios used in a DMF-H_2O mixed solvent system in solvothermal synthesis.[21] With this in mind, the use of DMF/H_2O solvent systems for the microwave synthesis of MIL-53(Al)-NH_2 was investigated.

In total, thirteen syntheses were carried out, where the DMF loading was varied in 10% increments from 0 to 100%. The MIL-53-NH_2 samples will be referred to as NHXX, where XX is the % DMF used in the synthesis. The reactions were carried out with a 1:1 ratio of metal salt to linker, as this is most commonly reported in the literature and was used for previous

investigations into these solvent systems.[21] A reaction temperature of 150 °C was chosen as DMF decomposes above this temperature (see Scheme 3.5).

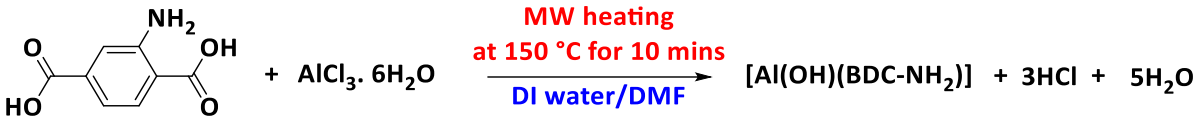

Scheme 3.5 – Scheme for the reactions carried out to investigate the effect of varying the DMF/H_2O solvent mixture used.

The products were all characterised by TGA and PXRD. The TGA of MIL-53(Al)-NH_2 synthesis in water only (NH0) possesses a two-step mass loss (Figure 3.20). The first (26.3%) is the sublimation of the unreacted H_2BDC-NH_2 linker which occurs between 200 and 380 °C, the second (58.4%) is the decomposition of the MOF itself, starting at around 380 °C. This decomposition temperature is around 100 °C less than the non-functionalised MIL-53(Al) and is consistent with previous results.[7,9]

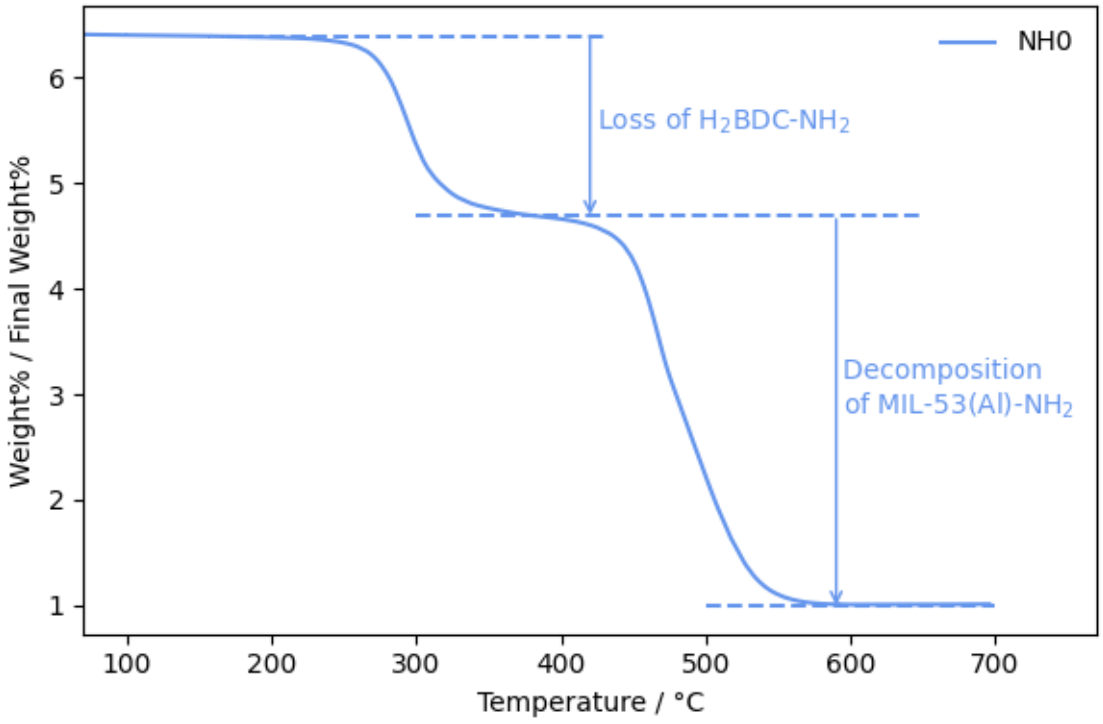

Figure 3.20 – TGA of MIL-53(Al)-NH_2 synthesised in 100% water (NH0).

NH100 (100% DMF synthesis, Figure 3.21, purple curve), possessed three weight loss events. The first (5.9%), occurring between 100 and 220 °C is due to the loss of DMF. The second

(4.4%), between 220 and 380 °C is due to the loss of unreacted $H_2BDC\text{-}NH_2$ and the third is due to the decomposition of the MOF (67.3%). Only two weight losses were observed for the 90% DMF synthesis (Figure 3.21, orange curve). The first (20.0%), occurring between 100 and 220 °C is due to the loss of DMF and the second (55.8%), starting at around 380 °C, is due to the decomposition of the MOF. It is important to note that there is no mass loss between 220 and 380 °C, suggesting that there is no unreacted linker present in the sample.

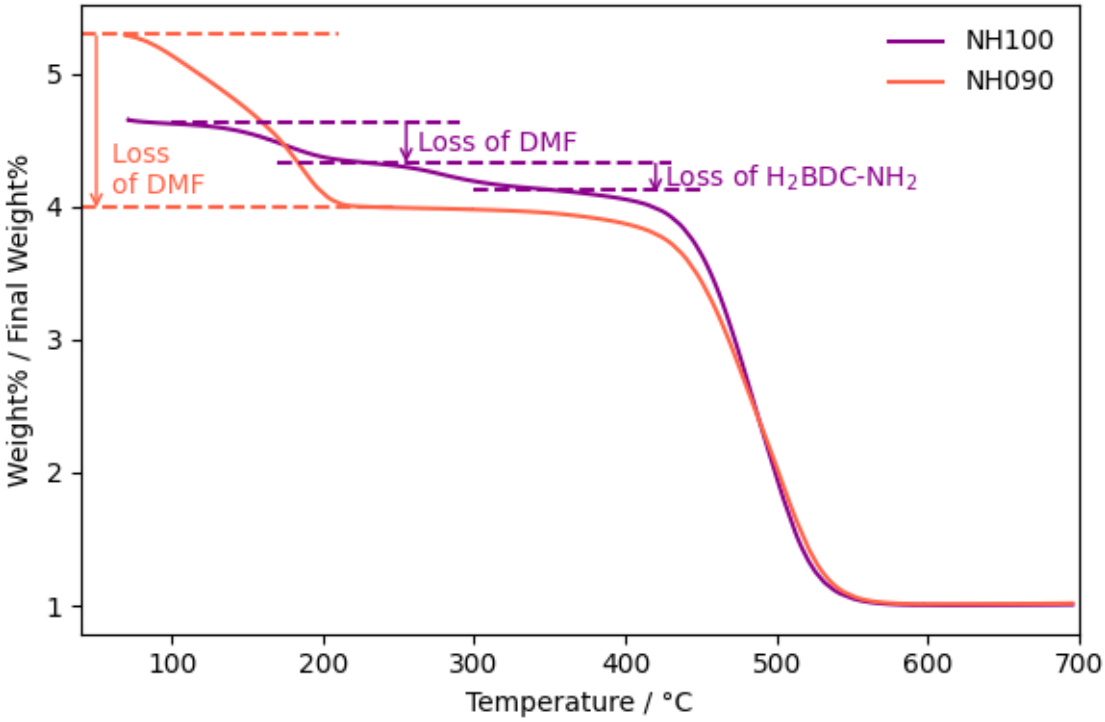

Figure 3.21 - TGA analyses of 100% (NH100) and 90% (NH090) DMF syntheses of MIL-53(Al)-NH_2. Decomposition of MOF is not labelled for clarity.

The yield obtained in these reactions and the % of linker and DMF that is present in each product was calculated from the TGA data (Figure 3.22). The yield is calculated by taking the weight% at approximately 370 °C (after the linker and DMF have sublimed, and before the MOF starts to decompose), and using the molecular weight of the repeating unit of the MOF without any linker of solvent in the pores to calculate the moles of MOF produced. As the PXRD analysis (shown below) shows that these sample contain multiple phases of MOF, this yield calculation is therefore an approximation. It is noted that calculating the individual yields for the two phases would be challenging. Although Rietveld requirement could be attempted to calculate the proportions of the two phases, this would have to be done on patterns that

had been collected with extreme care, ensuring the sample heights and instrument set-up was completely consistent across each sample. As this was not possible with the samples obtained in this work, the calculation of yields for each phase was not possible.

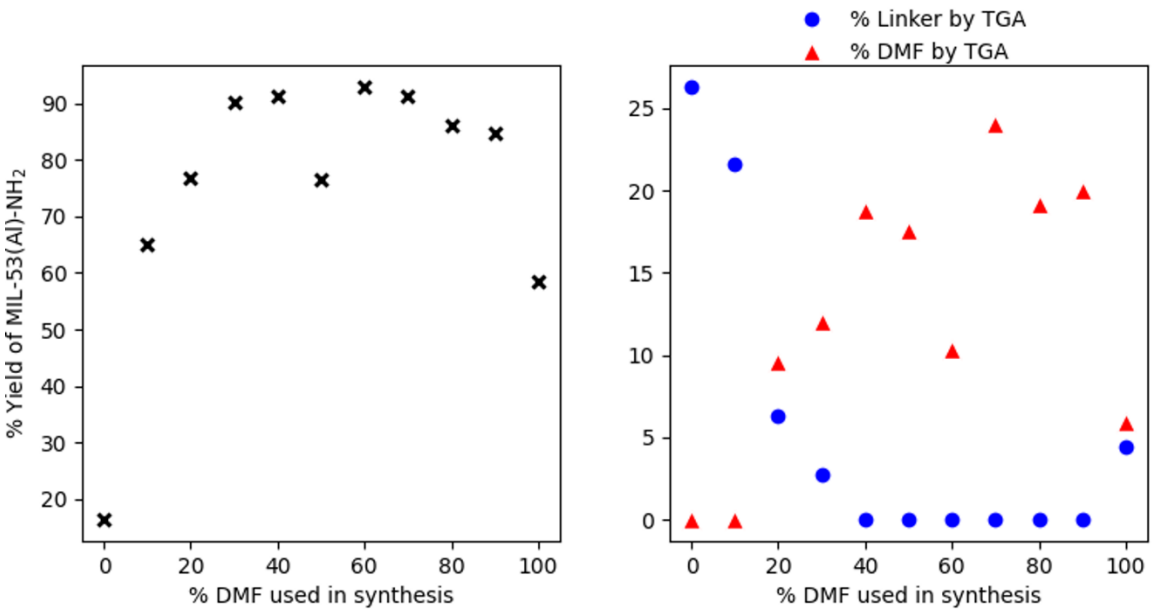

Figure 3.22 - Percentage yields (left) and percentage amounts of linker and DMF present (right) in the products where the percentage of DMF in DMF/H_2O solvent mix was changed. Please note that NH0 was carried out at 180 °C, rather than 150 °C.

The yield of MIL-53(Al)-NH_2 increases as the percentage of DMF increases, reaching a maximum at 60-70% DMF, where the yield is 91-93%. The yield then decreases slightly (by 5%) when 80-90% DMF is used and dropped further to around 58% when only DMF is used as a solvent.

TGA suggests that using between 40% and 90% DMF results in no unreacted linker being present in the product and that decreasing the percentage of DMF to below 30% results in larger amounts of unreacted linker being present in the product and therefore a decrease in the yield of MIL-53(Al)-NH_2 obtained.

The percentage of DMF found in the samples varies greatly (4 – 24%) over the syntheses, with no noticeable correlation, apart from a reduction that mirrors the increased percentage of linker in the samples synthesised using 30% DMF or less. As each MOF was washed with water twice after synthesis, and before TGA was carried out, it was suspected that the inconsistency

in DMF quantities present was due to different degrees being removed following water washing, and that it is not indicative of synthetic variations.

In the previous work that investigated DMF/H_2O solvent mixes, all samples were activated by refluxing in DMF before TGA was carried out, so it is not possible to determine whether samples had unreacted linker in pores prior to activation. The TGA of the activated samples resembles the 40-90% DMF synthesis (NH40-90) reported here, with a mass loss between 80 and 280 °C relating to loss of DMF, and MOF decomposition at 410 °C (a slightly higher temperature than the samples studied herein which start decomposing at 380 °C).[21]

Further to the TGA results, PXRD analysis shows that the percentage of DMF used changes the phase of MIL-53(Al)-NH_2 that is produced, and that some products contain multiple phases. These different phases are indicated by shifts in the principal peaks of the PXRD patterns. Table 3.5 shows the position of the first two peaks of the three common phases of MIL-53(Al)-NH_2.[9,25]

Table 3.5 – 2θ values of the first two peaks in the PXRD patterns of different phases of MIL-53(Al)-NH_2.[9,25]

Phase indicated	Symbol	Position of 1st peak / ° 2θ	Position of 2nd peak / ° 2θ
Open pore (linker)	OP_L	8.8	10.4
Open pore (DMF)	OP_{DMF}	9.1	10.0
Narrow pore (H_2O)	NP	9.3	12.1

The peak values were used to identify which phases of MIL-53(Al)-NH_2 are present in the samples. As an example, Figure 3.23 contains the PXRD patterns of the 100% water (NH0), 100% DMF (NH100), 90% DMF (NH90) and 60% DMF syntheses (NH60).

- The 100% water sample only contains the open pore form of MIL-53(Al)-NH_2 with unreacted linker in the pores, which is consistent with the TGA results.
- The 100% DMF sample contains both the open pore form containing unreacted linker and a narrow pore form with H_2O in the pores, which is again consistent with the TGA results.
- The 60% DMF sample contains the narrow pore form with H_2O in the pores but also an open pore form with DMF in the pores. It is hard to distinguish the presence of H_2O from DMF in the TGA.

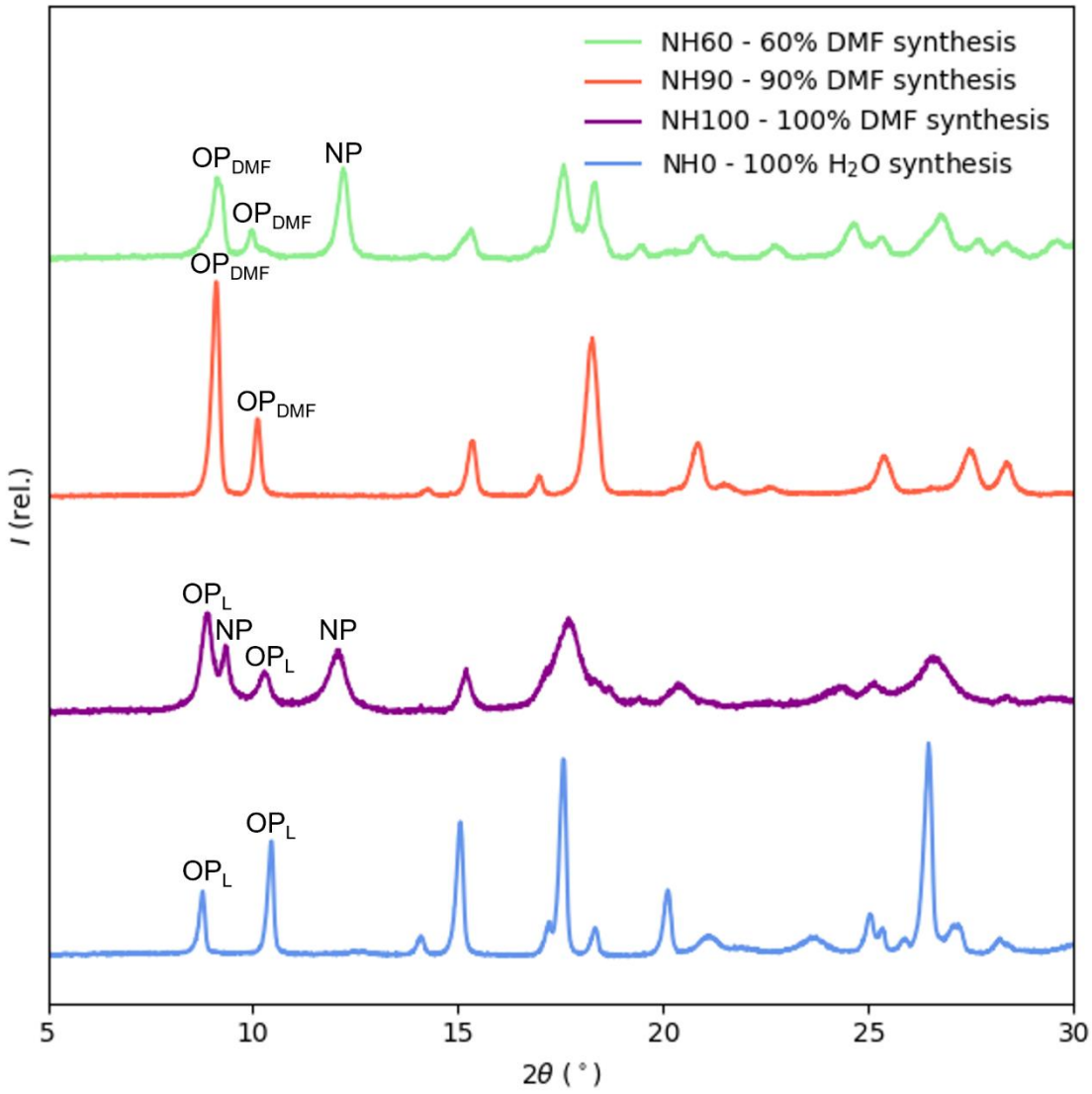

Figure 3.23 – PXRD patterns (5-30° 2θ) of 100% water, 100% DMF, 90% DMF and 60% DMF MIL-53(Al)-NH_2 syntheses, with peaks labelled to show which phases are present.

All other samples were analysed by PXRD and the phases present in the samples are identified in Table 3.6. This analysis confirms that samples synthesised using between 40 and 90% DMF do not contain any unreacted linker. Within this range (NH40-90) of samples there was no correlation between the amount of DMF used and whether the sample contained the OP_{DMF} phase or NP phase, or a mixture of both. This is expected to be due to the washing procedure after each MW synthesis was carried out. Each product was washed twice with deionised water, which could have changed the amount of DMF within the pores of the MOF, giving rise to the presence of the NP phase.

Table 3.6 – MIL-53(Al)-NH_2 phases observed in the PXRD analysis of synthesised MIL-53(Al)-NH_2 with varying amount of DMF.

Sample ID	OP_L	OP_{DMF}	NP
NH100	✓	✓	✓
NH90		✓	
NH80		✓	
NH70		✓	
NH60		✓	✓
NH50		✓	✓
NH40		✓	✓
NH30	✓	✓	✓
NH20	✓	✓	
NH10	✓		
NH0	✓		

Alongside these experiments, repeats of syntheses using 50, 80 and 90% DMF were performed to observe consistency of results (see Table 3.7). All three repeats contain no pore bound linker by TGA, which was promising. The repeats of NH80 and NH90 syntheses show consistent yields, but the repeat of NH50 gave a significantly lower yield (51.3% for NH50B, compared with 76.5% for NH50A). The mass of product obtained in this reaction was significantly reduced (0.26 g, compared to 0.4-0.5 g obtained in reactions using various amount of DMF) but no abnormalities were seen during the MW synthesis. Further repeats would need to be carried out to see if this result was an anomaly.

Additionally, the percentage of DMF present in the samples varies strongly between the repeats, as does the phases present. As suggested previously, this is likely due to the samples being washed with DI H_2O before PXRD is carried out. It is possible that there was variation in washing time and mixing (as the washing process was carried out by shaking by hand and timing 1 minute using a clock on the wall). If these experiments were repeated, a more consistent washing method would need to be used, for instance, placing the centrifuge tube onto a vortex mixer and timing the washing procedure carefully using a stopwatch.

Table 3.7 – Result of the repeats of the 50, 80 and 90% DMF MIL-53(Al)-NH_2 syntheses

Sample ID	% Yield	% Linker by TGA	% DMF by TGA	Phase(s) present
NH90A	84.7	0.0	20.0	OP_{DMF}
NH90B	82.0	0.0	4.1	OP_{DMF}/NP
NH80A	86.0	0.0	19.2	OP_{DMF}
NH80B	93.3	0.0	15.6	OP_{DMF}/NP
NH50A	76.5	0.0	17.6	OP_{DMF}/NP
NH50B	51.3	0.0	11.9	OP_{DMF}/NP

From this investigation into using mixed DMF/H_2O solvent systems, a synthesis that produces MIL-53(Al)-NH_2 in good yield (93%, using 70% DMF) in 10 minutes with no unreacted linker in the pores before any form of activation was carried out was found. This presents an opportunity to reduce both the chemical and energetic requirements needed to synthesise MIL-53(Al)-NH_2, which has not been seen before in the literature.

3.3.2.3 Activation of MIL-53(Al)-NH_2

Most of the reported activation processes for MIL-53(Al)-NH_2 (see Table 3.1) involve refluxing the as-synthesised material in either methanol or DMF, followed by oven drying (sometimes a vacuum oven was used) at > 110 °C. As MIL-53(Al)-NH_2 was synthesised that only contained DMF in the pores (as shown by TGA), it was decided to use solvent exchange with MeOH to remove the DMF. MeOH has a lower boiling point than DMF (65 °C vs 153 °C) and can therefore be removed more readily by oven drying than DMF. The 70% DMF synthesis of MIL-53(Al)-NH_2 was repeated as this gave a high yield (91.3%) and then the sample was washed three times with MeOH and oven dried to remove the MeOH.

The TGA (Figure 3.24) of the activated sample possesses no mass loss between 80-252 °C suggesting that the DMF has been successfully removed. The initial ~7% mass loss in the activated sample indicates the presence of a low boiling point solvent. This could be either H_2O or MeOH in the pores of the MOF; MeOH may not have been fully removed by oven drying and H_2O is readily adsorbed from the atmosphere when the MOF is exposed to air.

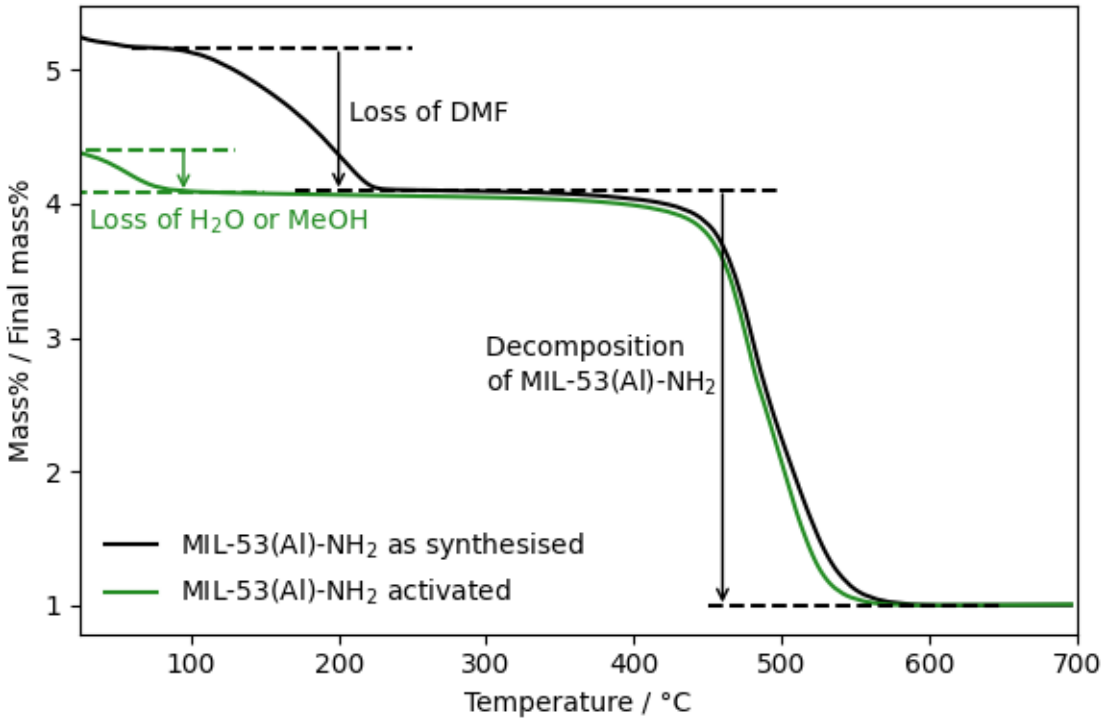

Figure 3.24 – TGA of a 70% DMF synthesis of MIL-53(Al)-NH_2, before and after activation *via* solvent exchange with MeOH and oven drying.

The success of activation by MeOH exchange was confirmed by PXRD analysis (Figure 3.25) which shows that before activation, both the open pore (DMF) and narrow pore (H_2O) forms of MIL-53(Al)-NH_2 are present, indicated by reflections at 9.1, 10.0 and 12.1° 2θ. After activation, only the narrow pore form with H_2O (or possibly MeOH) in the pores is present, indicated by principal peaks 9.3 and 12.1° 2θ. [26,51]

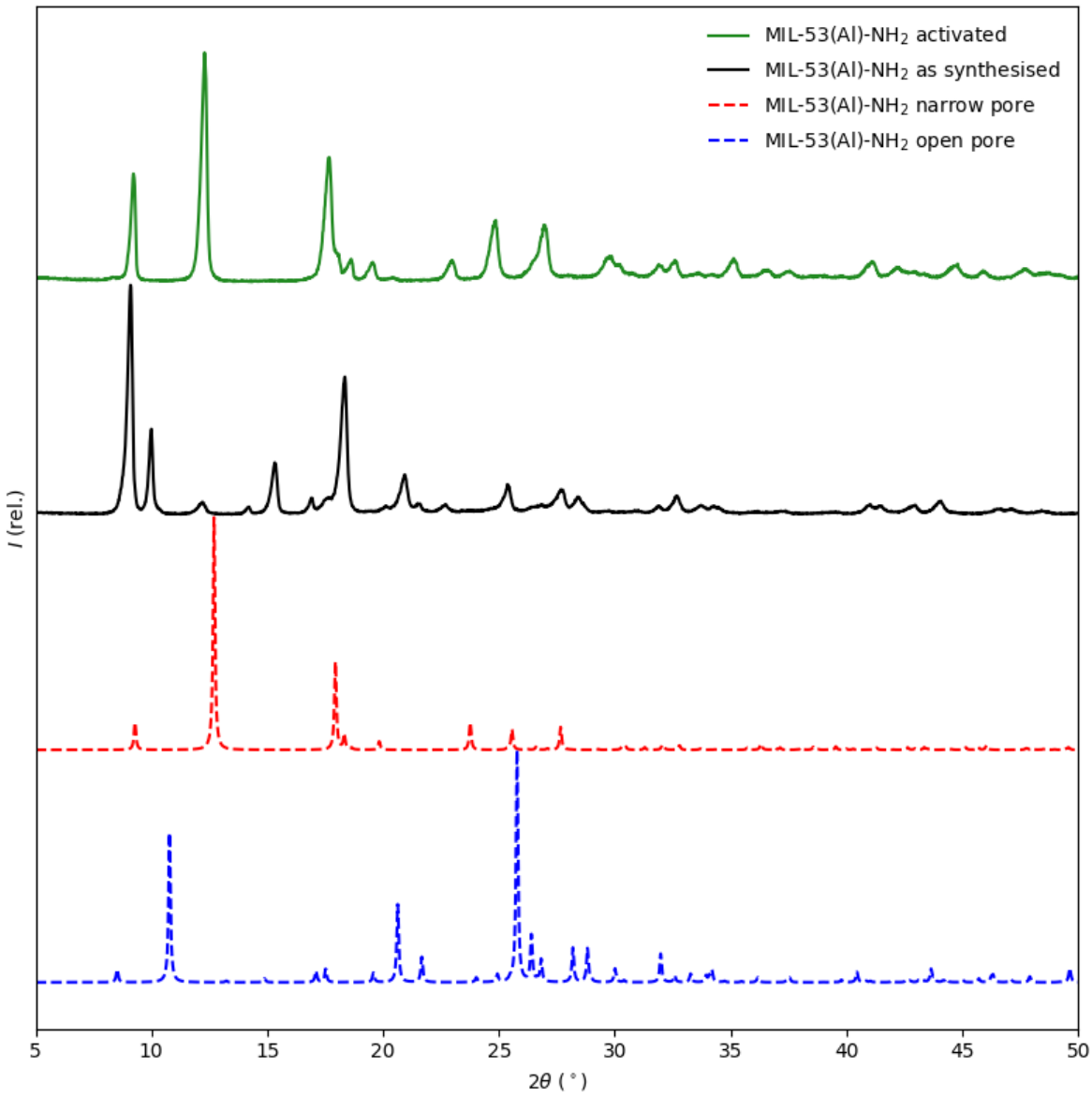

Figure 3.25 - PXRD analysis of a 70% DMF synthesis of MIL-53(Al)-NH_2, before and after activation, alongside simulated patterns for large and narrow pore forms of MIL-53(Al)-NH_2.

FT-IR analysis (Figure 3.26) of the activated sample is consistent with literature reports and confirmed the presence of NH_2 groups in the MOF, which were indicated by the bands at 3497 and 3388 cm^{-1}.[9]

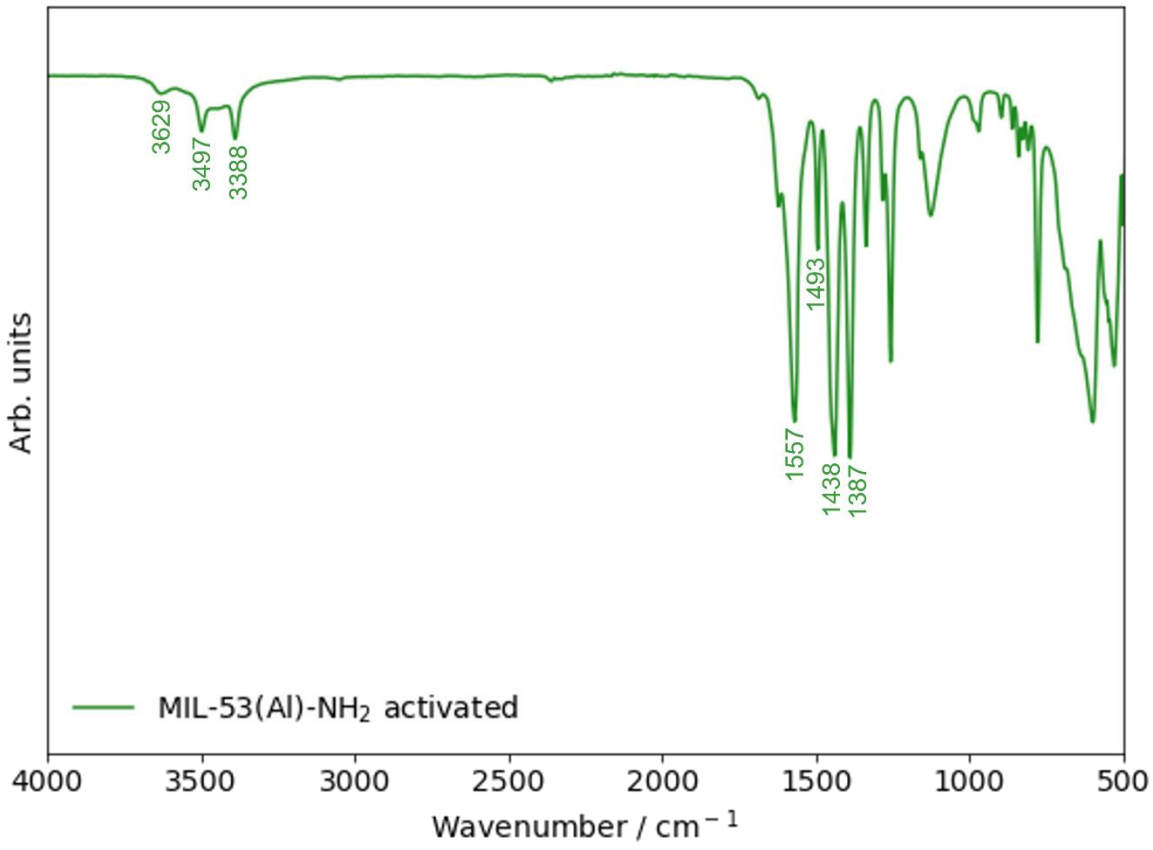

Figure 3.26 – FT-IR analysis of an activated 70% DMF synthesis of MIL-53(Al)-NH_2, Bridging O-H (3629), NH_2 (3497, 3388), asymmetric C=O stretch (1557, 1493), symmetric C=O stretch (1438, 1387).

A Pawley fit of the activated sample to the narrow pore phase (with H_2O in the pores) was carried out using Topas software to find the Goodness of Fit (GOF) to this phase and calculate the unit cell parameters of the activated sample (Table 3.8 and Figure 3.27).

Table 3.8 – Lattice parameters and GOF calculated from Pawley fit of our activated sample of MIL-53(Al)-NH_2 , compared to np form of MIL-53(Al)-NH_2 reported in the literature (CSD code = NAXLEF).[20]

	Space group	**a**	**b**	**c**	**α**	**β**	**γ**	**GOF**
Activated sample	*Cc*	19.7746	7.7428	6.6025	90.000	105.5749	90.000	1.69
Literature[20]	*Cc*	19.7567	7.4815	6.5899	90.000	105.7318	90.000	n/a

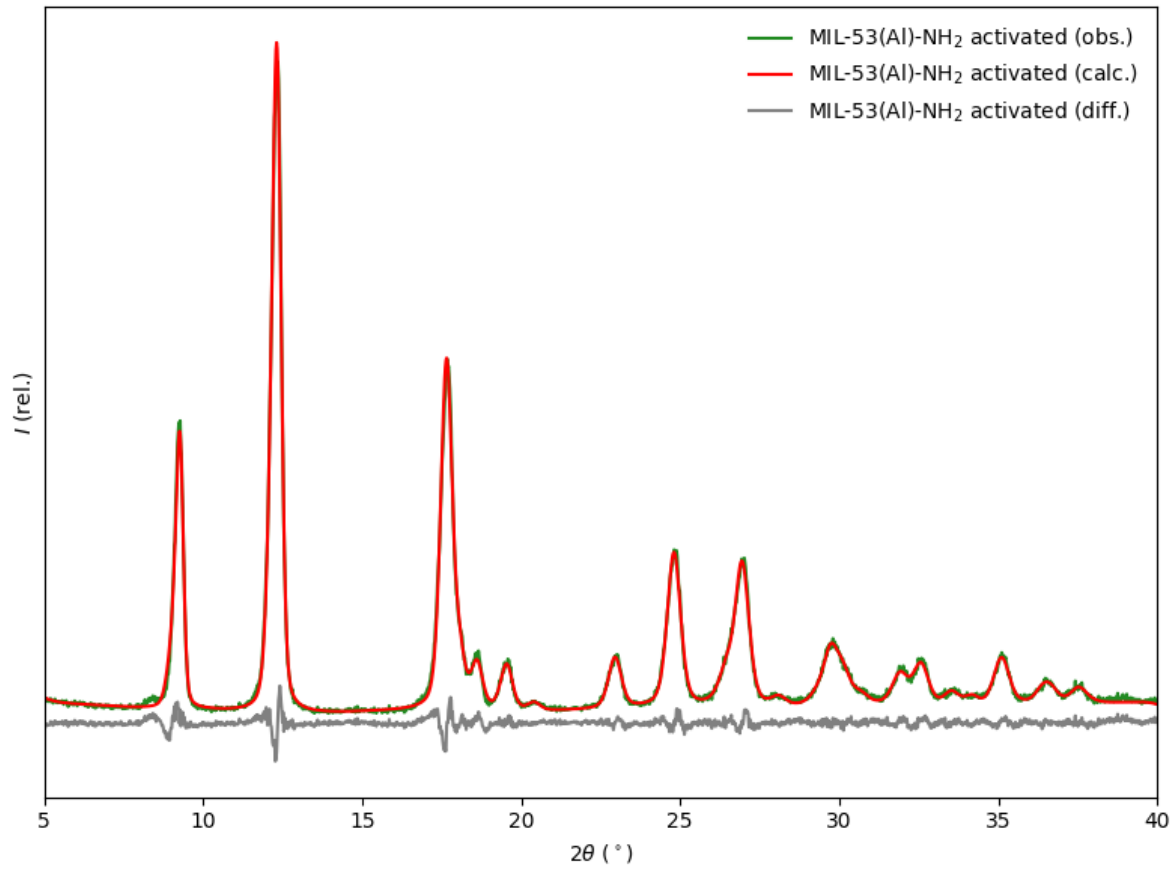

Figure 3.27 – Pawley fitting of the activated sample to the NP phase of MIL-53(Al)-NH_2 reported in the literature.[20]

The data from the activated sample matched well with literature reported values; unit cell lengths are within 0.3 Å, angles are within 0.2° and a good GOF value of 1.69 was achieved. A slight discrepancy between the calculated and observed diffraction patterns was seen at 2θ = 8.35°, which may be due to the presence of a small amount of open pore form of MIL-53(Al)-NH_2, with DMF in the pores.

SEM imaging of two successfully activated samples were undertaken to carry out particle size analysis (Figure 3.28). All particles measured were defined as irregular, due to the absence of uniformity between the particles. Particle size analysis (Table 3.9, Figure 3.29) was carried out by measuring the longest side of fifty particles from seven images per sample. The two samples possess a similar range and distribution of particle sizes, but their modal ranges are different. More than double the number of particles with sizes 100-200 nm were observed in Sample 2, compared to Sample 1 and Sample 1 contains a much higher number of particles with sizes 400-500 nm than Sample 2. This could be due to differences in the samples

themselves, but it also could be due to inaccuracies in measuring. As the particles were so irregular in shape, measuring the longest side of the particles was challenging. To improve the accuracy of the data, a larger range of particles from these samples, and further samples would need to be measured.

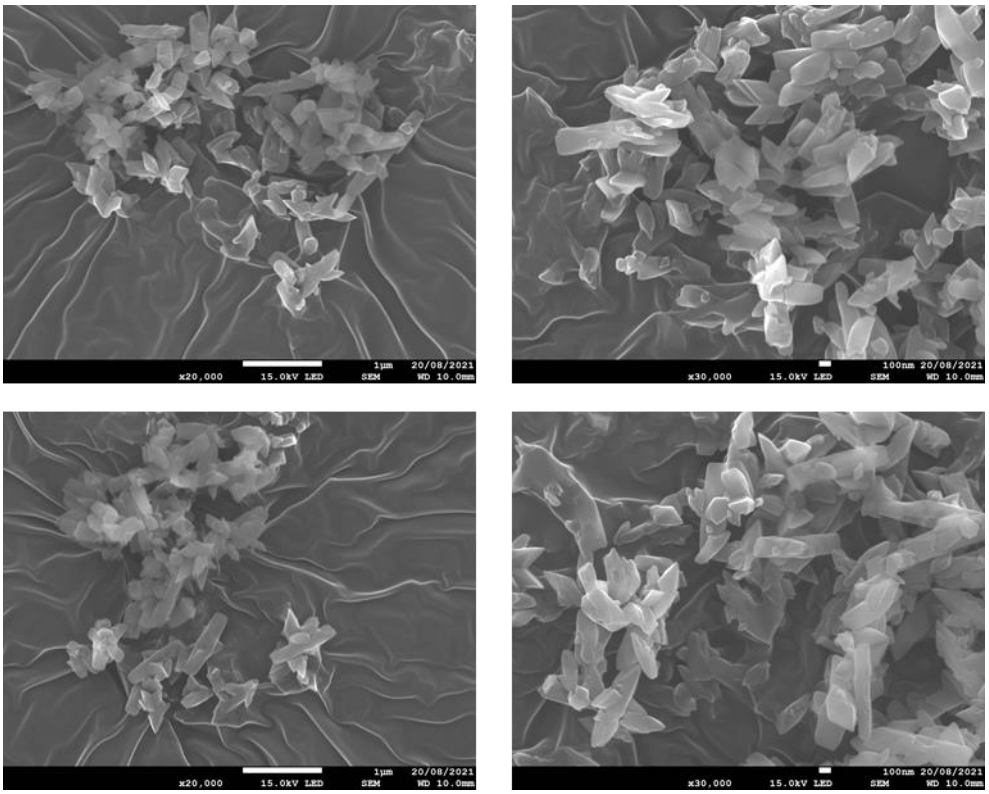

Figure 3.28 - SEM images of activated samples of MIL-53(Al)-NH_2: Sample 1 (top) and Sample2 (bottom). Scale bars: top left = 1 µm, top right = 100 nm, bottom left = 1 µm, bottom right = 100 nm.

Table 3.9 - Average and range of particle sizes found in two samples of activated MIL-53(Al)-NH_2. Sample 1 and 2 were synthesised and activated in the same way.

Sample ID	Average size / nm	Median / nm	Modal range / nm	Standard deviation / nm
Sample 1	430 ± 30	410	400-500	230
Sample 2	400 ± 40	360	100-200	260

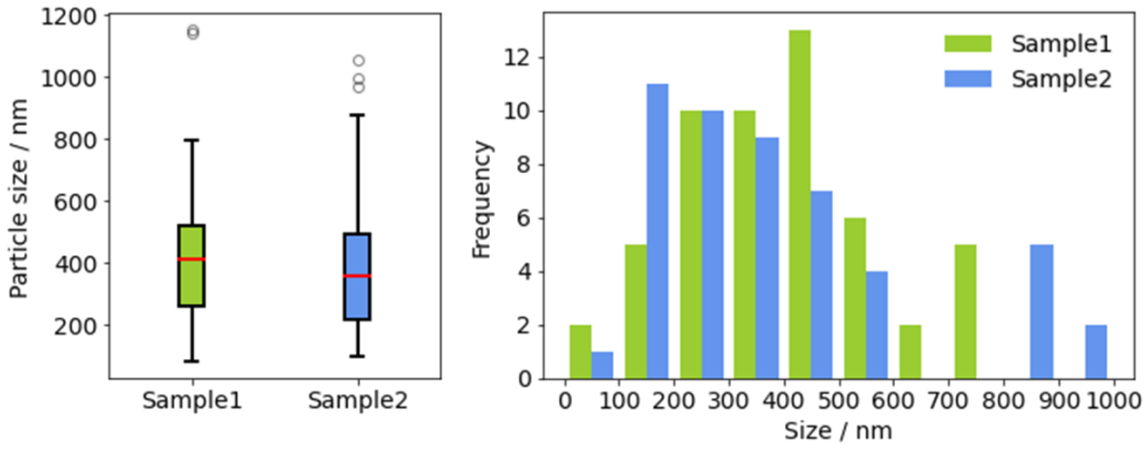

Figure 3.29 - Boxplot and histogram showing the range of particle sizes in two samples of activated MIL-53(Al)-NH_2. Particles with sizes above 1000 nm are not shown in the histogram (two in Sample 1 and one in Sample 2). Sample 1 and 2 were synthesised and activated in the same way.

Gas sorption analysis was carried out on a successfully activated sample of MIL-53(Al)-NH_2 to obtain a BET surface area measurement (Figure 3.30). Figure 3.30 shows that the material exhibits a two-step isotherm. This indicates that at relative pressure < 0.12, MIL-53(Al)-NH_2 is in its narrow pore form, and the uptake of N_2 is low. As the relative pressure increases above 0.12 the pores of the MOF are forced open and a larger amount of N_2 can enter the pores. This gate opening phenomena has been reported for MIL-53(Al)-NH_2 previously, when CO_2 has been used as the analyte.[52–54] The desorption exhibits a very significant hysteresis behaviour, where the N_2 is not fully desorbed when the pressure was decreased. This is likely due to the MOF being in its open pore form and it being energetically unfavourable for the N_2 to exit the pores. This hysteresis effect has been reported previously.[9] The adsorption/desorption that occurs above 0.8 P/P_o is due to adsorption on the external surface of the closely packed particles.

The gate opening effect that this material exhibited made it difficult to calculate the BET surface area of this material. If a BET plot is taken when $0.0 < P / P_0 < 0.11$, in the region where MIL-53(Al)-NH_2 is in its narrow pore form, then the BET surface area is calculated to be 105.0 ± 0.8 $m^2 g^{-1}$, which is much lower than expected, and much higher values have been reported for MIL-53(Al)-NH_2 previously.[21] As the sorption that occurs after the pores have opened (when $0.43 < P / P_0 < 0.94$) is a much truer reflection of the materials surface area, it would be better to use this region for the BET plot. However, if this region of relative pressure is

used in the BET plot, a negative value for the y axis is returned indicating a negative surface area. To gain an insight into the value of surface area, a BET plot was fitted using the quantity adsorbed in this region but altering the relative pressures to fit into the standard BET region so a surface area could be calculated. Doing this analysis gave a surface area of 1441 ± 11 m^2 g^{-1}, which is comparable to values reported in the literature.[21] This value is very much an approximation of the BET surface area and should not be taken as an exact surface area. The quantity of gas adsorbed can also be used to evaluate the sample's internal area. At $P/P_o = 0.9$ this sample had adsorbed 317.97 cm^3 g^{-1} of N_2, which is just greater than the MIL-53(Al) sample, which adsorbed 312.58 cm^3 g^{-1} of N_2 at $P/P_o = 0.9$.

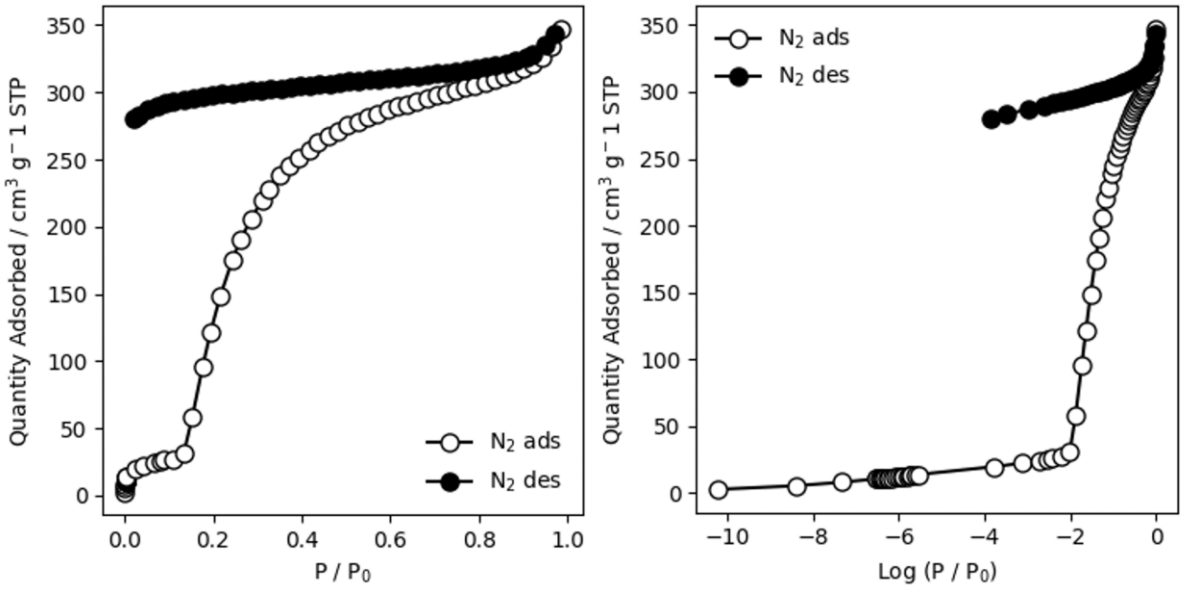

Figure 3.30 - Nitrogen adsorption-desorption isotherm of an activated sample of MIL-53(Al)-NH_2. Log plot shown on right.

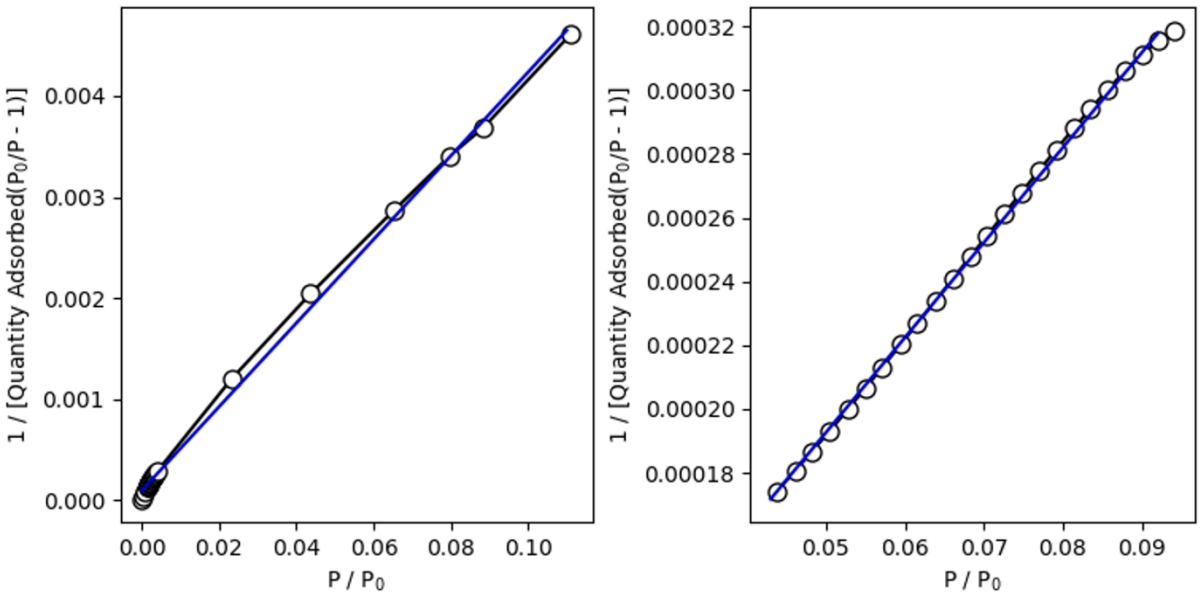

Figure 3.31 - Plots used to calculate BET surface areas. Left = plot of standard BET region where initial sorption has occurred when MIL-53(Al)-NH_2 is in its narrow pore form. Right = plot of data adjusted to fit the BET region where P/P_0 has been divided by 10 to gain an estimate for the surface area. The surface area is equal to the cross-sectional area of adsorbate / (slope + intercept).[50]

3.3.3 Synthesis, activation and characterisation of MIL-121

As described in Section 3.1, the third version of MIL-53(Al) to be synthesised was MIL-121 (where the linker used is 1, 2, 4, 5-benzenetetracarboxylic acid, H_2BTEC), due to the presence of pendant Lewis basic carboxylate groups in the MOF, which should be available for post-synthetic Cu(II) coordination.

3.3.3.1 Synthesis of MIL-121

The synthesis of MIL-121 (Scheme 3.6) was attempted using the same ratios of metal salt to linker to H_2O (2:1:174) as reported in the literature, but MW heating at 200 °C for 10 mins was used instead of conventional heating at 210 °C for 24 hours. A temperature of 210 °C (the temperature used in literature) could not be obtained in the CEM MW reactor due to problems with over pressurisation.

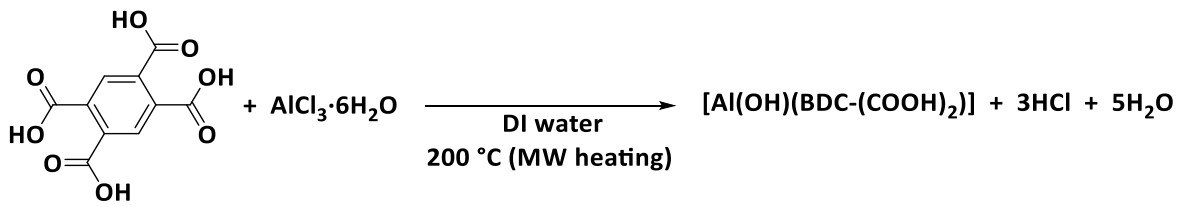

Scheme 3.6 – MW synthesis of MIL-121, where BDC = C_6H_4 $(CO_2^-)_2$.

The reaction gave a white microcrystalline powder product which was collected by centrifugation and analysed by PXRD. The PXRD pattern (Figure 3.32) matched well with the simulated pattern of MIL-121 found in the literature,[10] with peaks in similar positions.

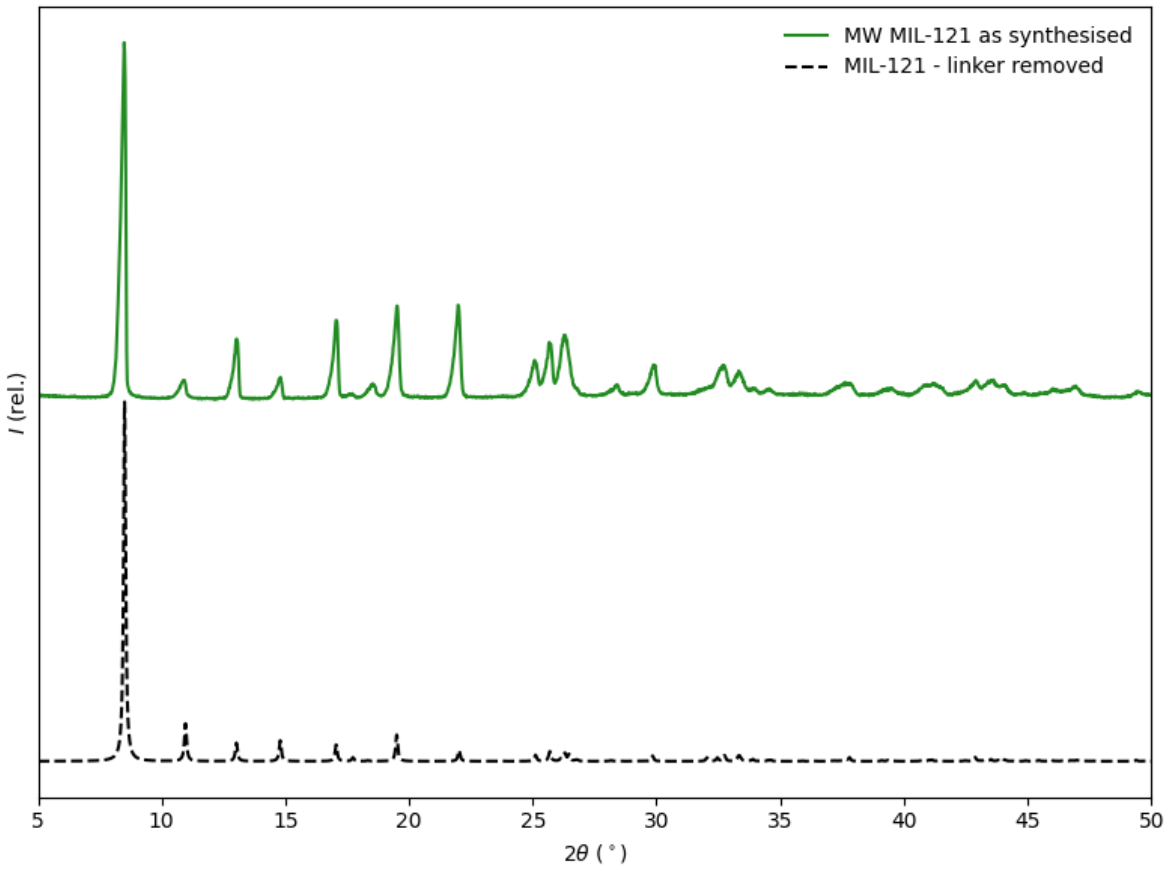

Figure 3.32 – PXRD of MW synthesised MIL-121 against the simulated pattern of MIL-121.[10]

The TGA (Figure 3.33) was also consistent with the literature with decomposition events occurring at: 20-160 °C corresponding to the loss of water (4.7%), 160-220 °C due to the loss of unreacted H_2BTEC linker (2.1%), 260-440 °C from the loss of COOH groups (18.3%), and 440-590 °C from the decomposition of MOF (60.3%). The percentage mass loss attributed to the loss of the non-bonded COOH groups is greater than that reported in the literature (here = 18.3%, in literature = 10%), this will be discussed further when the activation process is discussed below. Overall, the TGA and PXRD results confirm that the synthesis of MIL-121 has been successful.

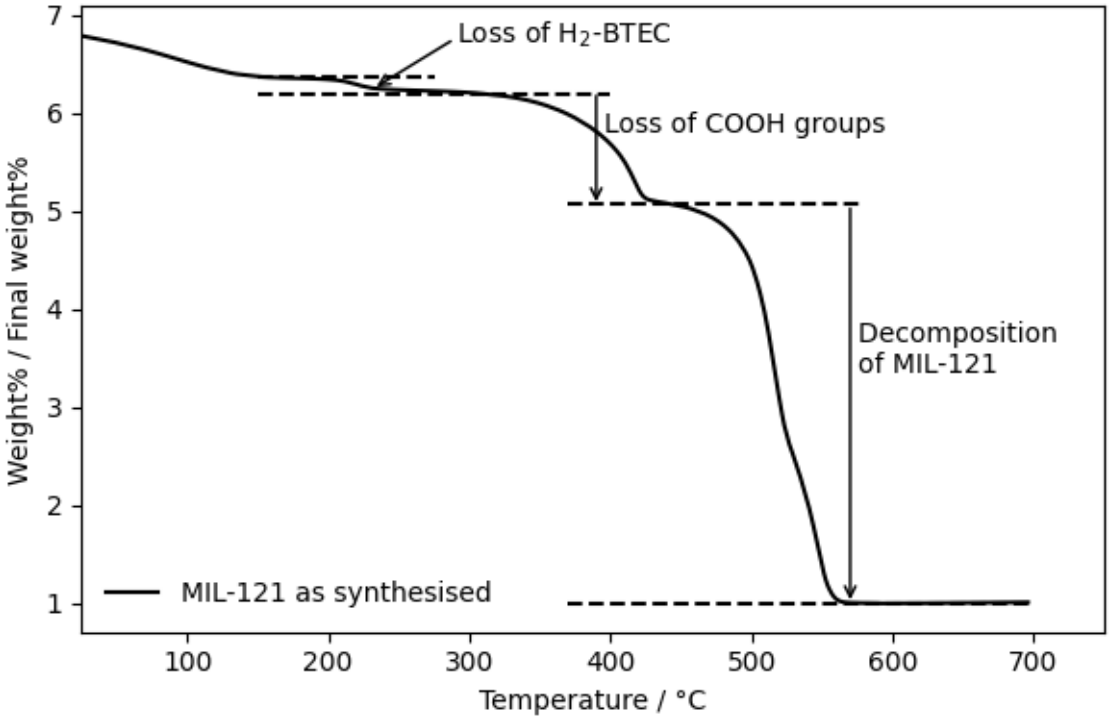

Figure 3.33 – TGA of MW synthesised MIL-121.

3.3.3.2 Activation of MIL-121

The first reported activation route of MIL-121 was calcination at 380 °C for 5 hours, which successfully removed the trapped H_2BTEC from the pores of the MOF, as shown by TGA. However, later it was shown that calcination at temperatures above 180 °C leads to the formation of pyromellitic dianhydride from H_2BTEC and calcination above 300 °C leads to partial decarboxylation of the pendant carboxylate groups.[30,31] As an alternative, solvent exchange with MeOH has been reported, either by heating in an autoclave at 150 °C or by Soxhlet extraction.[31–33]

Due to the issues created by calcination, it was decided to attempt activation by Soxhlet extraction using MeOH. Following a procedure reported in the literature,[33] a 24 hour extraction was performed, but TGA (Figure 3.34) revealed that uncoordinated H_2BTEC was still present in the sample, shown by the presence of a mass loss between 160-220 °C. A second attempt was made using DMF to wash the sample, due its higher boiling point and the high solubility of H_2BTEC in DMF. Again, TGA (Figure 3.34) showed that linker remained in the sample, showing that the activation was unsuccessful.

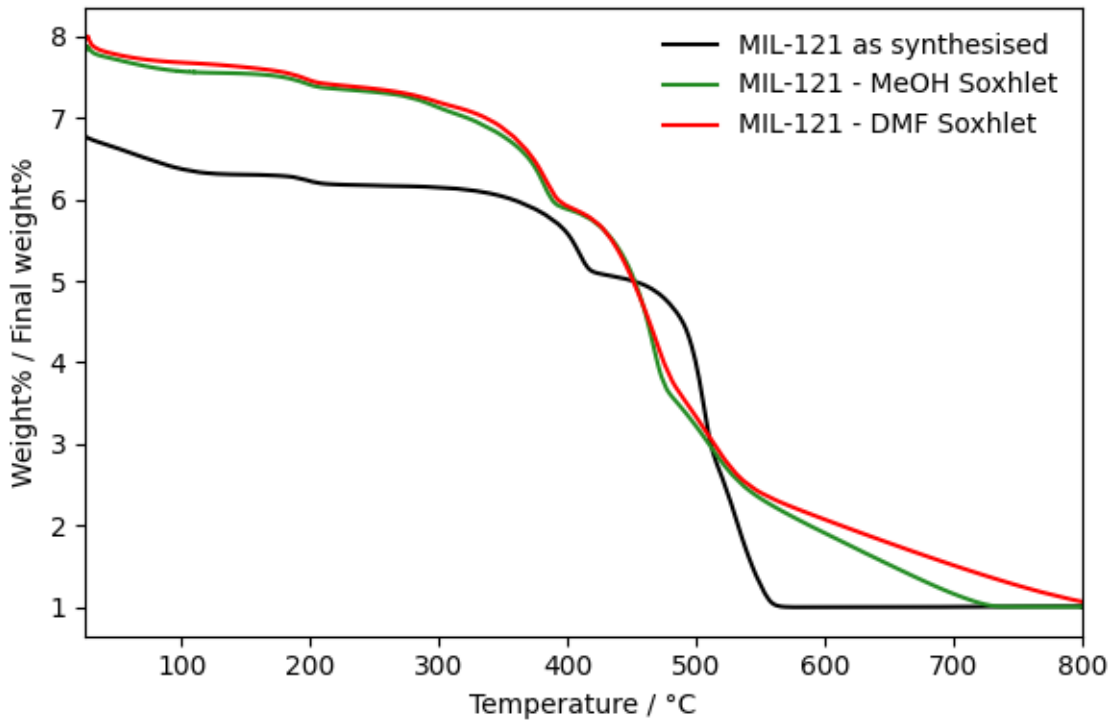

Figure 3.34 – TGA of as-synthesised MIL-121 and MIL-121 after activation attempts using MeOH and DMF Soxhlet extraction.

Following these results, activation in MeOH at 150 °C would be the logical next step, however a high-pressure vessel of adequate size was not available to carry this out on a large enough scale to obtain the amount of MIL-121 required for the stability and metal removal experiments. Instead, activation was attempted by calcination at 200 °C for 24 hours. This temperature was chosen to remove as much remaining linker as possible, with as little dianhydride formation and loss of COOH groups as possible. TGA (Figure 3.35) showed that there is no longer a decomposition occurring between 160-220 °C, suggesting that the activation has been successful. The mass loss associated with the loss of pendant COOH groups remains at 18.3%, equal to the as-synthesised sample, suggesting that no decarboxylation has occurred during the activation process.

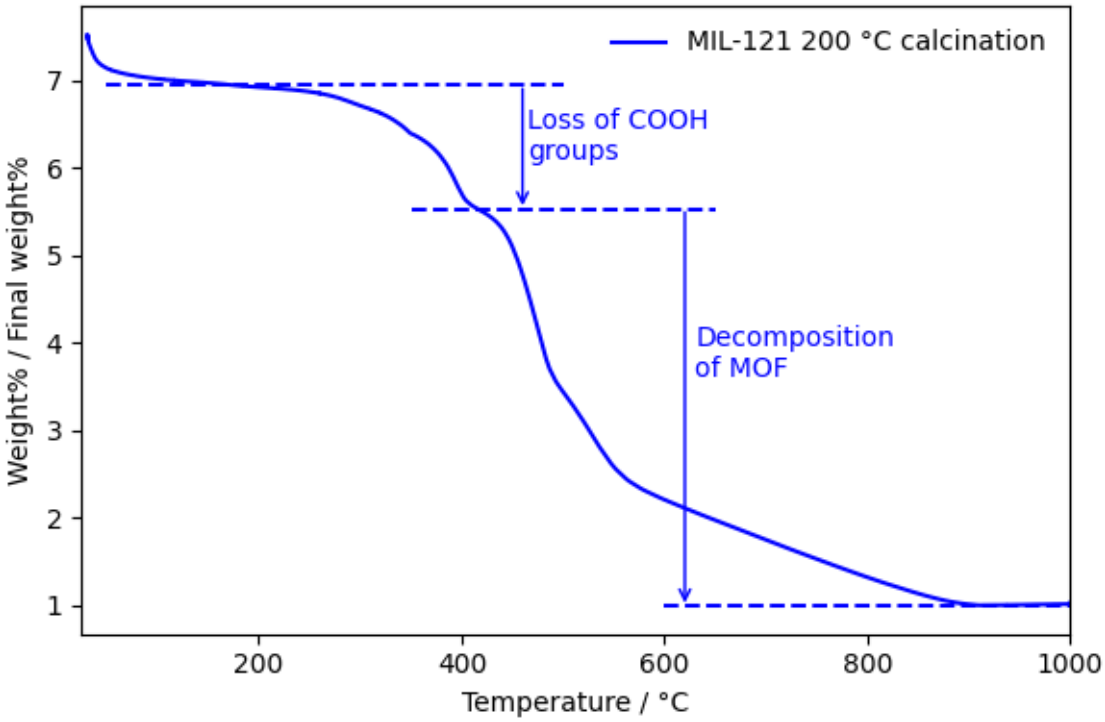

Figure 3.35 - TGA of as-synthesised MIL-121 and MIL-121 calcined at 200 °C for 24 hours.

FTIR analysis of the activated sample (Figure 3.36) shows two absorbance bands at 1864 and 1801 cm^{-1}, which indicate the presence of a C=O stretch of an acid anhydride, suggesting that the dehydration of H_2BTEC had occurred and this anhydride remained in the activated sample.[30] However, as this anhydride was undetectable by TGA and the pendant COOH groups remain intact after calcination at 200 °C it was decided to use this method to activate MIL-121 for further experiments.

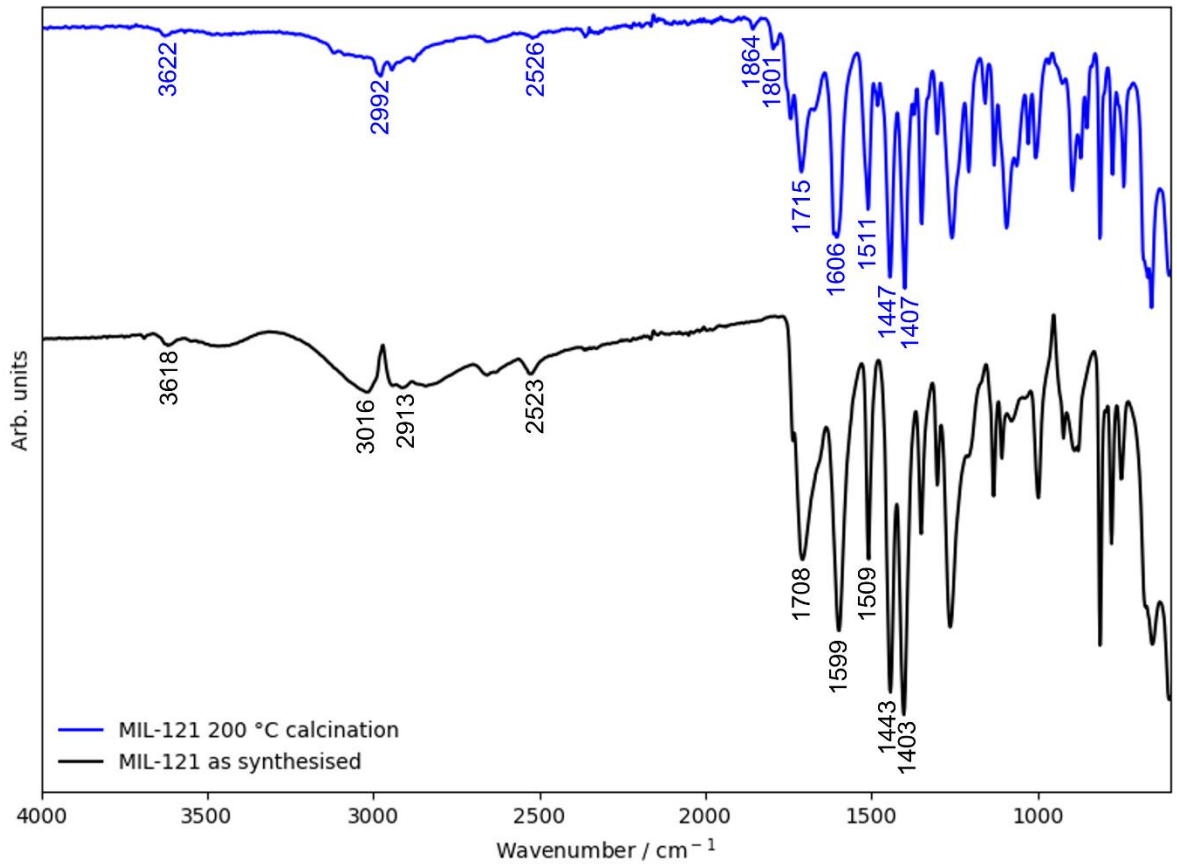

Figure 3.36 – FTIR of MIL-121 before and after calcination at 200 °C. MIL-121 as synthesised: Bridging O-H (3618), OH from pendant COOH (2500-3200, b), C=O from pendant COOH (1708) asymmetric C=O stretch (1599, 1509), symmetric C=O stretch (1443, 1403). MIL-121 200 °C calcination: Bridging O-H (3622), OH from pendant COOH (2500-3200, b), C=O in acid anhydride (1864, 1801), C=O from pendant COOH (1715) asymmetric C=O stretch (1606, 1511), symmetric C=O stretch (1447, 1407).

The PXRD pattern (Figure 3.37) of the calcined MIL-121 matches the simulated pattern of MIL-121, with one reflection missing at 10.84° 2θ. This reflection corresponds to the (110) hkl plane which cuts through the aluminium octahedra, its reduced intensity could be accounted for by preferred orientation effects in the diffraction experiment.

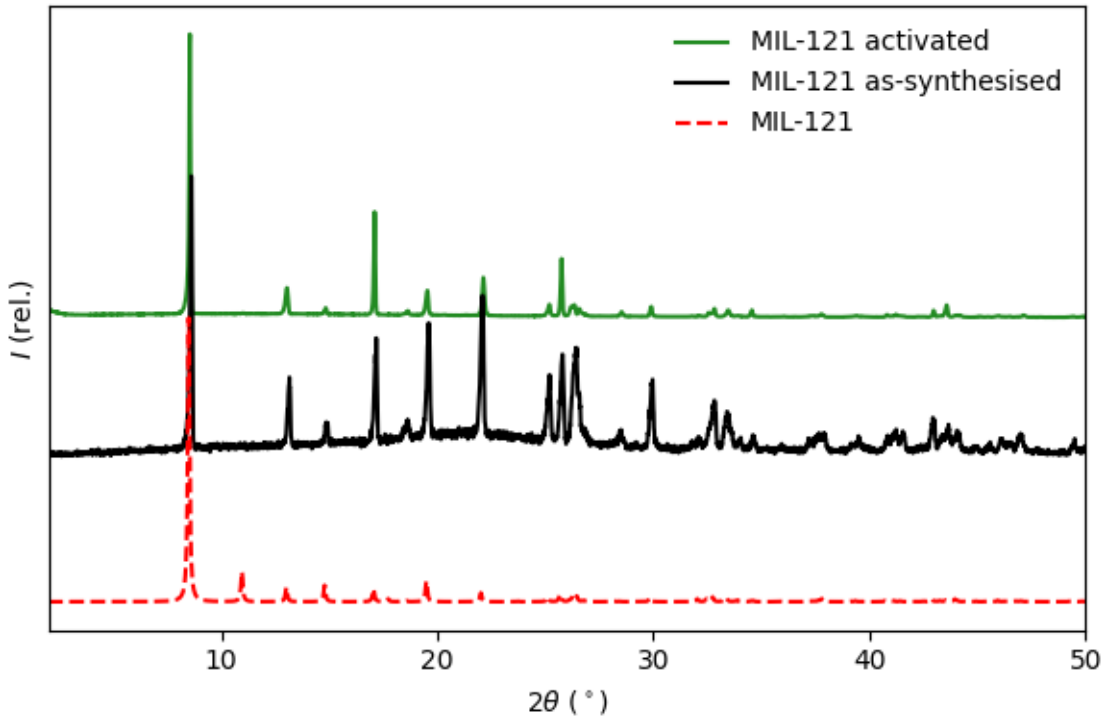

Figure 3.37 - PXRD of as-synthesised and activated MIL-121 against the simulated pattern of MIL-121.[10]

A Pawley fit of the activated sample to the phase reported in the literature was carried out using Topas software, to find the Goodness of Fit (GOF) to this phase and calculate the unit cell parameters of the activated sample (Table 3.10 and Figure 3.38).

Table 3.10 – Lattice parameters and GOF calculated from Pawley fit of our activated sample of MIL-121, compared to MIL-121 reported in the literature (CSD code = RAWZIA).[20]

	Space group	**a**	**b**	**c**	**α**	**β**	**γ**	**GOF**
Activated sample	*C*2/c	17.5448	13.5781	6.6642	90.000	113.1957	90.000	3.03
Literature[10]	*C*2/c	17.5036	13.6185	6.6601	90.000	113.214	90.000	n/a

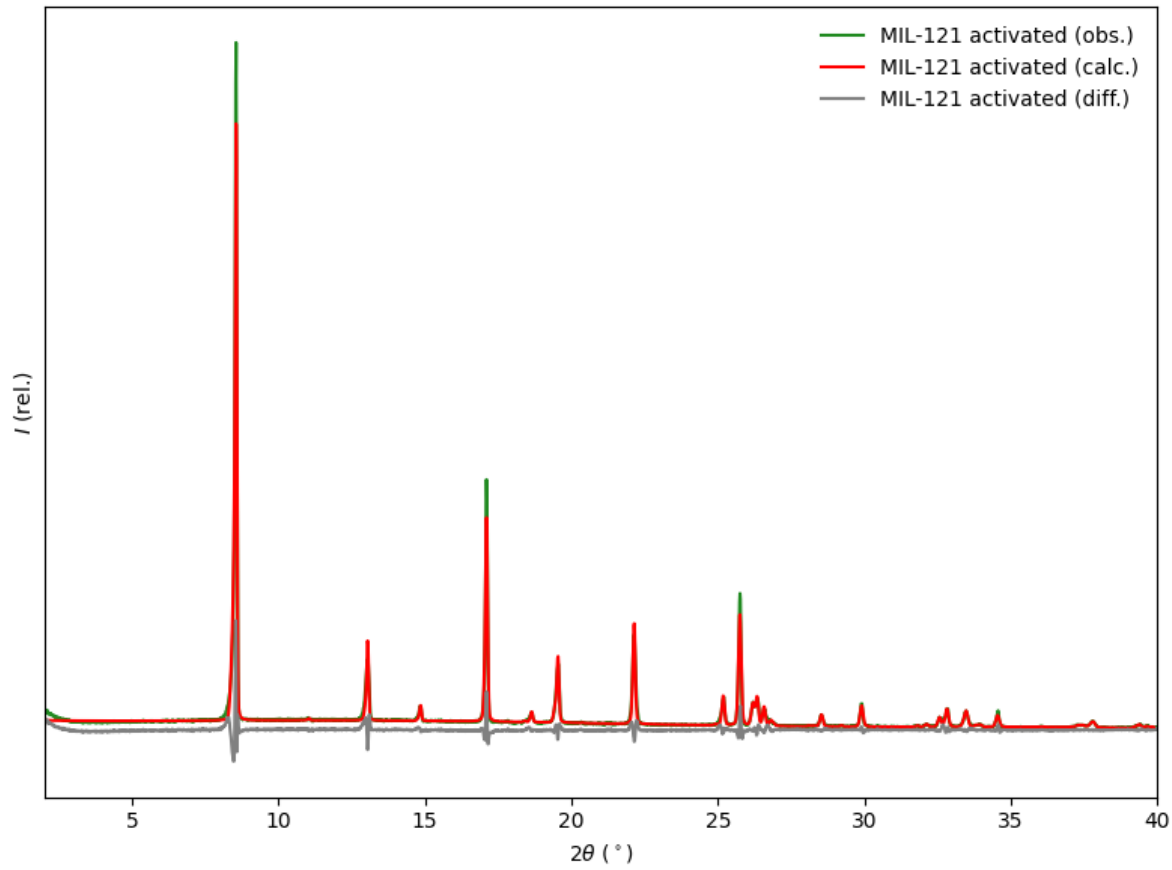

Figure 3.38 – Pawley fitting of the activated sample of MIL-121 to the phase reported in the literature.[10]

SEM imaging of two successfully activated samples were undertaken to carry out particle size analysis (Figure 3.39). The particles were cuboid-shaped with distinct and sharp 90° angles. Particle size analysis (Table 3.11, Figure 3.40) was carried out by measuring the longest side of fifty particles from seven images per sample. The two samples possessed a similar range and distribution of particle sizes.

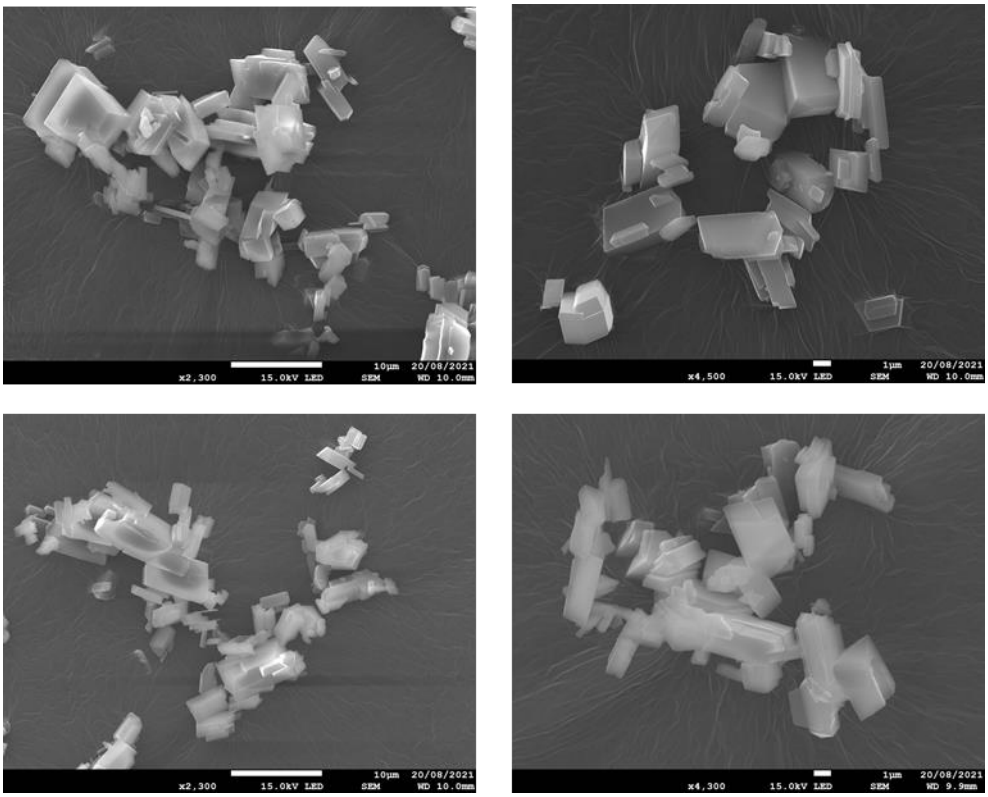

Figure 3.39 - SEM images of activated samples of MIL-121: Sample 1 (top) and Sample2 (bottom). Scale bars: top left = 10 µm, top right = 1 µm, bottom left = 10 µm, bottom right = 1 µm.

Table 3.11 - Average and range of particle sizes found in two samples of activated MIL-121. Sample 1 and 2 were synthesised and activated in the same way.

Sample ID	Average size / µm	Median / µm	Modal range / µm	Standard deviation / µm
Sample 1	3.7 ± 0.3	3.3	2-3	1.9
Sample 2	3.8 ± 0.3	3.5	3-4	1.8

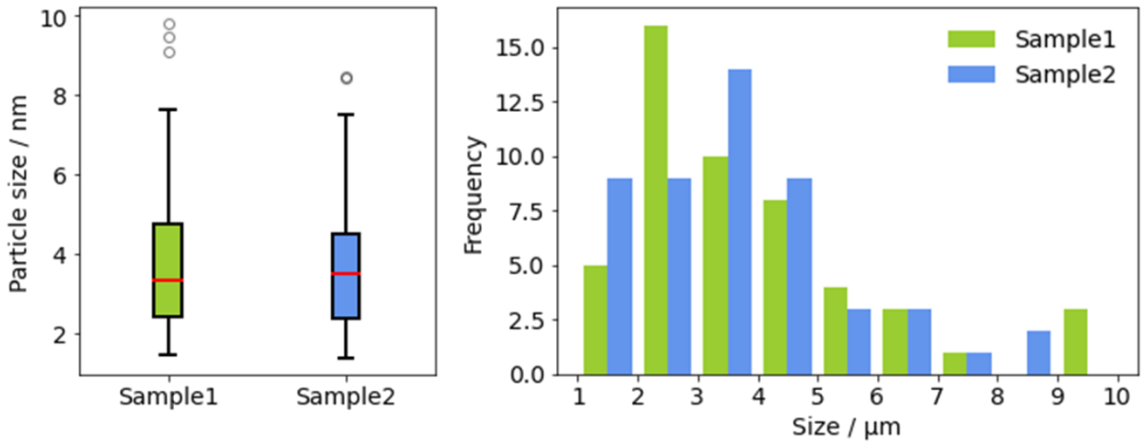

Figure 3.40 - Boxplot and histogram showing the range of particle sizes in two samples of activated MIL-121 Sample 1 and 2 were synthesised and activated in the same way.

Gas sorption analysis was carried out on an activated sample of MIL-121 in order obtain a BET surface area measurement (Figure 3.43). Figure 3.15 shows that the material has very limited porosity, and the BET calculation gives a surface area of 15.7 ± 0.1 m^2 g^{-1}. The literature suggests that this low surface area is likely due to the uncoordinated carboxylate groups blocking the pores of the MOF and therefore preventing adsorption of N_2.[31] The low uptake could also be due the presence of the acid anhydride group that was formed during calcination (as shown by FTIR, Figure 3.36) blocking the pores.

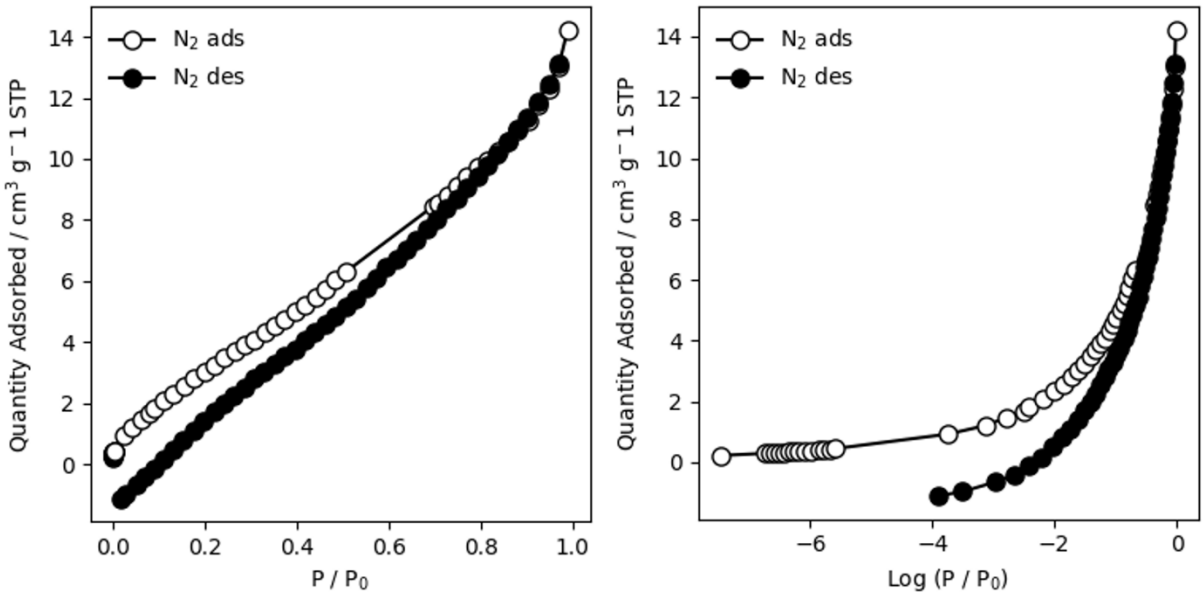

Figure 3.41 - Nitrogen adsorption-desorption isotherm of a calcined sample of MIL-121. Log plot shown on right.

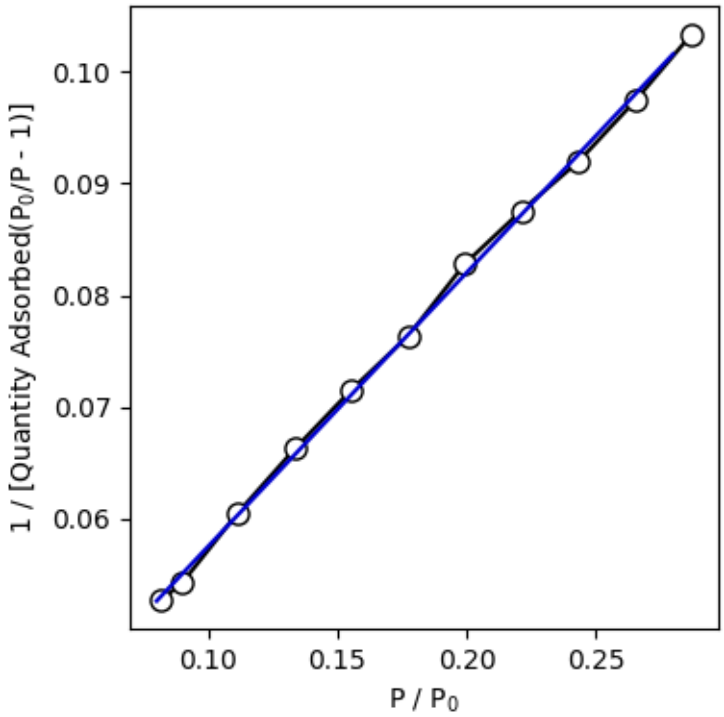

Figure 3.42 – Plot used to calculate BET surface area of MIL-121. The surface area is equal to the cross-sectional area of adsorbate / (slope + intercept).[50]

3.4 Stability and Cu(II) sorption properties of analogues of MIL-53(Al)

Before stability and metal removal tests could be carried out, a large amount (around 1 g) of each MOF needed to be synthesised and characterised. Due to limitations with the size of vials that fit into the CEM MW reactor, repeat reactions and activations for each MOF were carried out and the products combined. For reference, the characterisation (PXRD, TGA, FTIR and SEM) of each combined sample is shown in the Appendix (Section 3.7).

3.4.1 Stability of analogues MIL-53(Al)

The stability of the MOFs was examined by exposing samples of the MOF to aqueous buffer solutions of various pH's: DI water, neat HCl, sat NaOH, and buffer solutions of pH 1, 4, 7, 10, and 13. Buffer solutions were used to account for changes in H^+ or ^-OH concentrations that occur if these species react with the MOF. A limitation of using these buffers is that the stability of MOF then also depends on the ions used to prepare the buffer.[37] For this reason, two types of pH 7 buffer were used, due to previous reports that the phosphate ion present in a standard pH 7 buffer can impact the stability of some MOFs.[37] These will be labelled "pH

7 phosphate" and "pH 7 Tris" throughout. Details of how all buffer solutions were prepared can be found in Section 0.

The samples were kept in the solutions for either one day or one week and were then analysed by PXRD to determine if the MOF had undergone any phase changes or loss in crystallinity. If the samples are stable, the PXRD patterns before and after the samples are added to the solutions should be the same, or similar, indicating that the MOF structure is maintained.

3.4.1.1 Stability of MIL-53(Al)

The PXRD patterns (Figure 3.43) indicate that MIL-53(Al) lacks stability in most of the aqueous solutions used. When exposed to very low pH (conc. HCl) and very high pH (sat. NaOH) there are no reflections matching the MIL-53(Al) phase, suggesting the MOF has decomposed. In pH 1, 4, and 7 (phosphate only) the MIL-53(Al) structure is present, but several other reflections are seen, suggesting the presence of a new phase and that MIL-53(Al) is not stable in these environments (Figure 1.46). The sample that has been exposed to the Tris pH 7 solution underwent significant changes, including a new reflection at 10.84° 2θ. To determine if these new phases correspond to one of the other known MIL-53(Al) phases, the H_2O and Tris pH 7 soaked sample are plotted alongside the PXRD patterns of these phases (Figure 3.44). The new reflections that appear in the soaked samples do not correspond to any of the known forms of MIL-53(Al).

The sample exposed to pH 10 and pH 13 solutions for one day appears to have undergone a complete phase change, but after seven days the MIL-53(Al) is still present, with some other phases present too. It is expected that the result at seven days is anomalous, as it would be unlikely that the MOF structure would have decomposed after one day and re-formed after seven days. This experiment would need to be repeated to gain a true understanding of the phases present after exposing MIL-53(Al) to pH 10 or 13. Regardless, the loss of the MIL-53(Al) structure at one day suggest that MIL-53(Al) is not stable at pH 10 or above. This is likely due to ^{-}OH coordinating to the aluminium displacing the H_2BDC linker and thereby degrading the MOF.

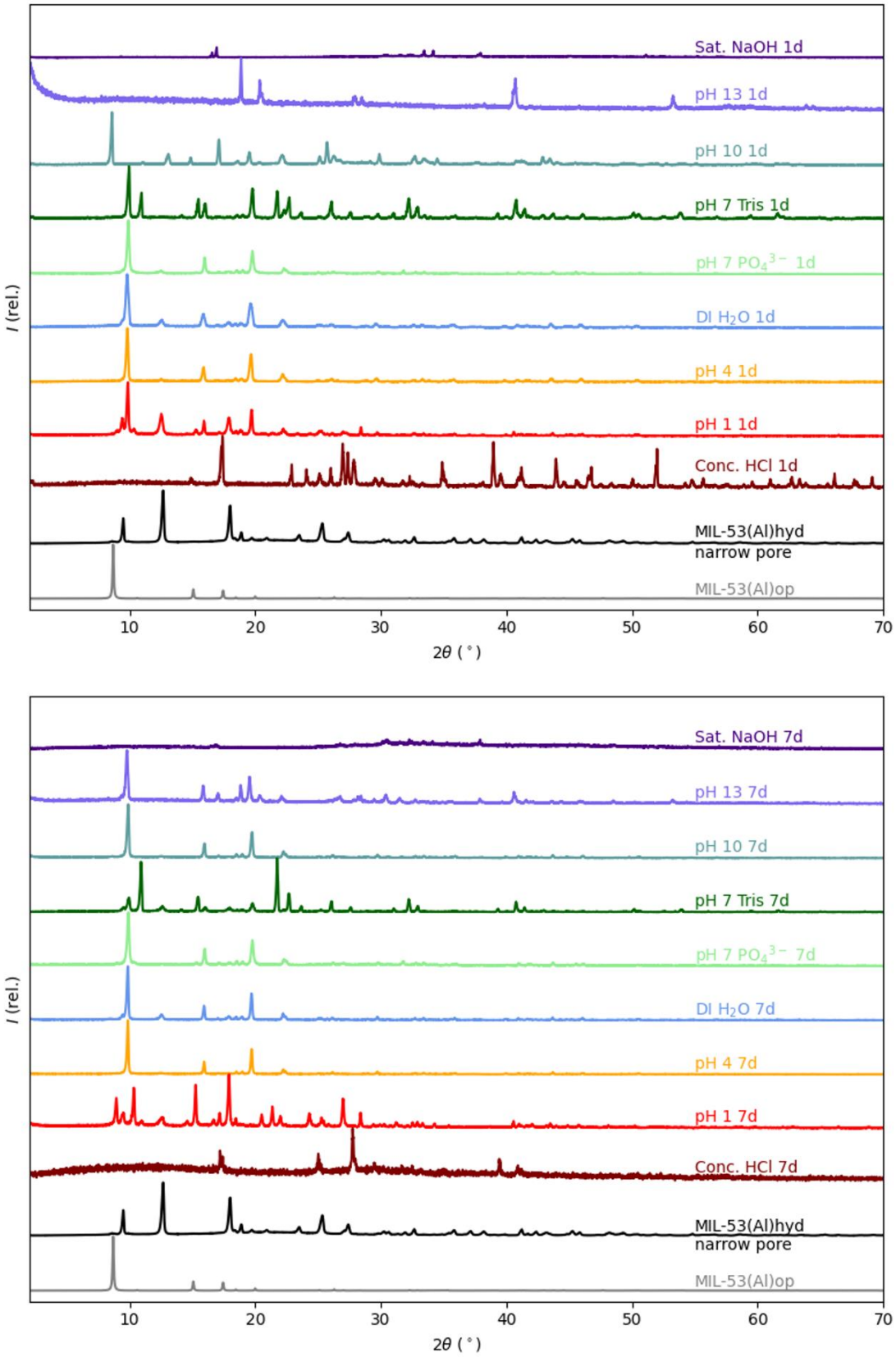

Figure 3.43 – PXRD of MIL-53(Al) samples exposed to aqueous solutions of varying pH for one day (upper) and seven days (lower). The synthesised MIL-53(Al) (black curve) was in the narrow pore, hydrated form to start with.

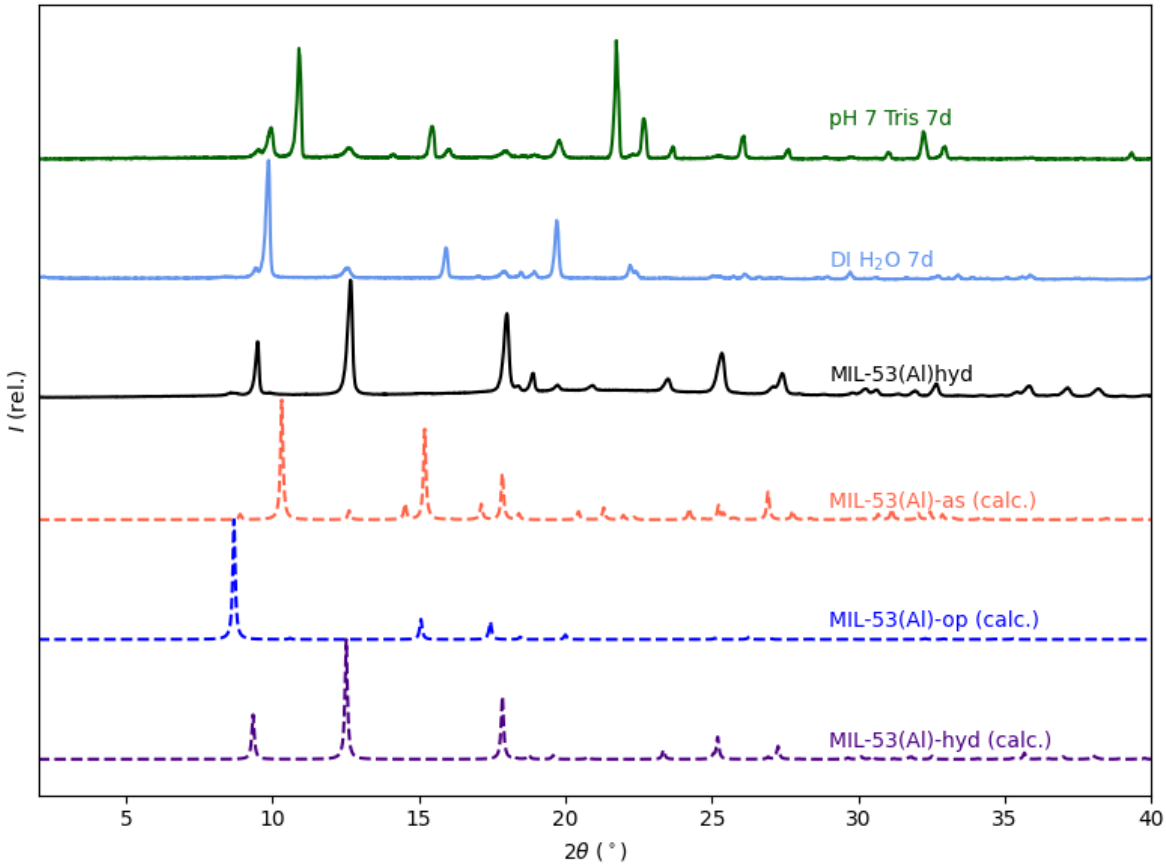

Figure 3.44 – PXRD of MIL-53(Al)hyd soaked in DI H_2O and Tris pH 7 for seven days against the simulated pattens of hydrated, open and as-synthesised MIL-53(Al).

3.4.1.2 Stability of MIL-53(Al)-NH2

The PXRD data from the MIL-53(Al)-NH_2 stability experiments (Figure 3.45) show that MIL-53(Al)-NH_2 is less stable than MIL-53(Al) in most aqueous solutions used. In concentrated HCl, pH 13 and sat. NaOH MIL-53(Al)-NH_2 has completely decomposed. After one day at pH 1, the MOF has undergone significant changes, with multiple phases, including some of the original narrow pore MIL-53(Al)-NH_2 appearing. After seven days, it appears that the sample has undergone further changes. Comparing the one and seven day samples soaked in pH 1 to the open and narrow pore forms of MIL-53(Al)-NH_2 (Figure 3.46) suggests that the MOF might be undergoing a change from the narrow to open pore form, due the changes in the positions of the first two reflections. Having said this, both samples contain several peaks that don't match either of the known forms of MIL-53(Al)-NH_2, showing that the MOF is not stable at pH 1.

MIL-53(Al)-NH_2 is indicated to be stable at pH 4 and 10, with the positions and intensities of the peaks in the PXRD matching the starting sample of MIL-53(Al)-NH_2. In both pH 7 buffers,

MIL-53(Al)-NH_2 undergoes significant changes (light and dark green patterns, Figure 3.45). After one day in the phosphate buffer the peaks associated with MIL-53(Al)-NH_2-np undergo significant broadening and after seven days new reflections appear, suggesting the presence of other phases. In the Tris buffer, many new reflections are present at both time points and the reflections associated with the MIL-53(Al)-NH_2-np are no longer present after seven days, showing that the MOF is not stable in the presence of this solution.

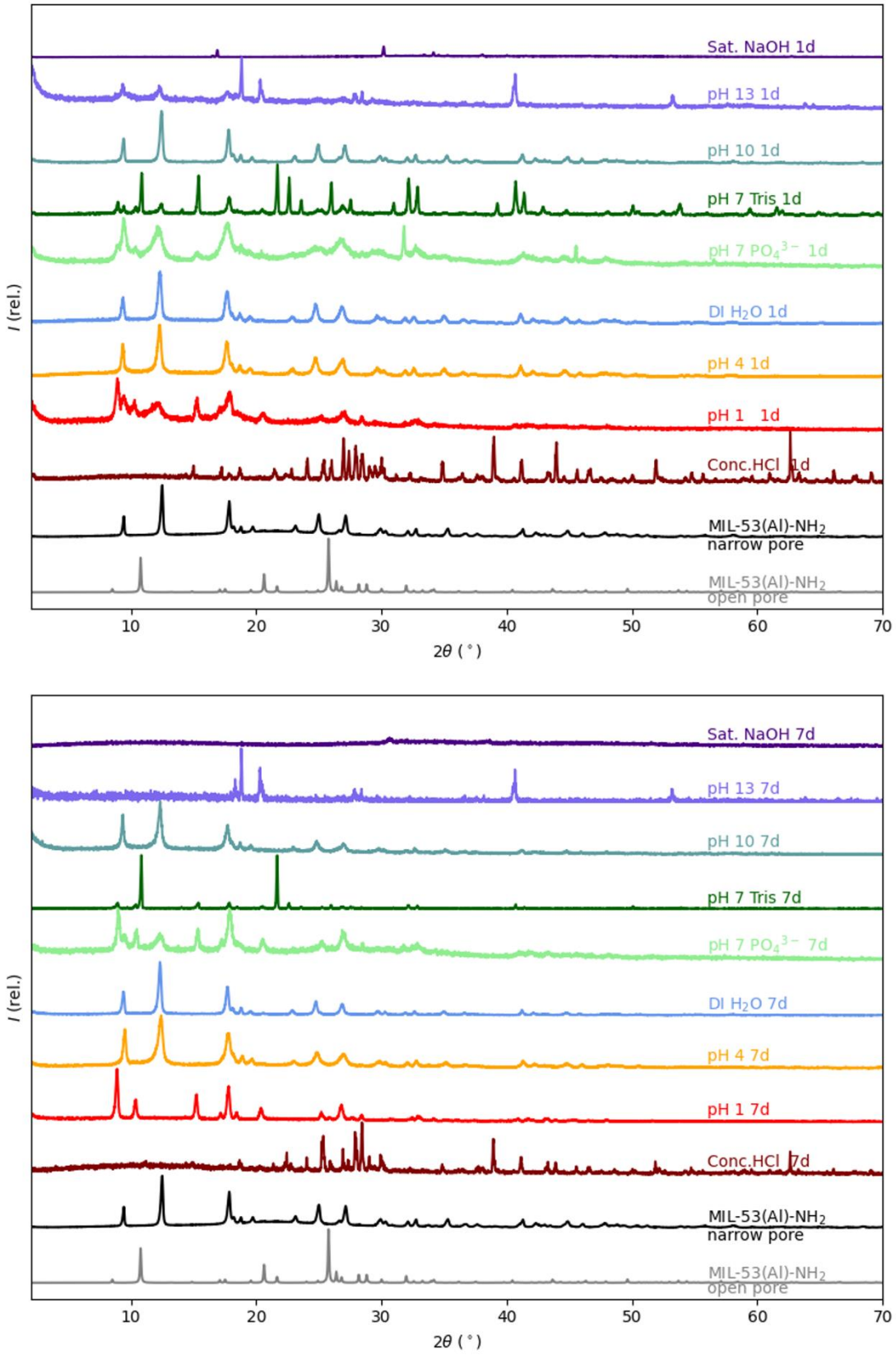

Figure 3.45 - PXRD of MIL-53(Al)-NH_2 samples exposed to aqueous solutions of varying pH for one day (upper) and seven days (lower). The synthesised MIL-53(Al)-NH_2 (black curve) is in its narrow pore, hydrated form to start with.

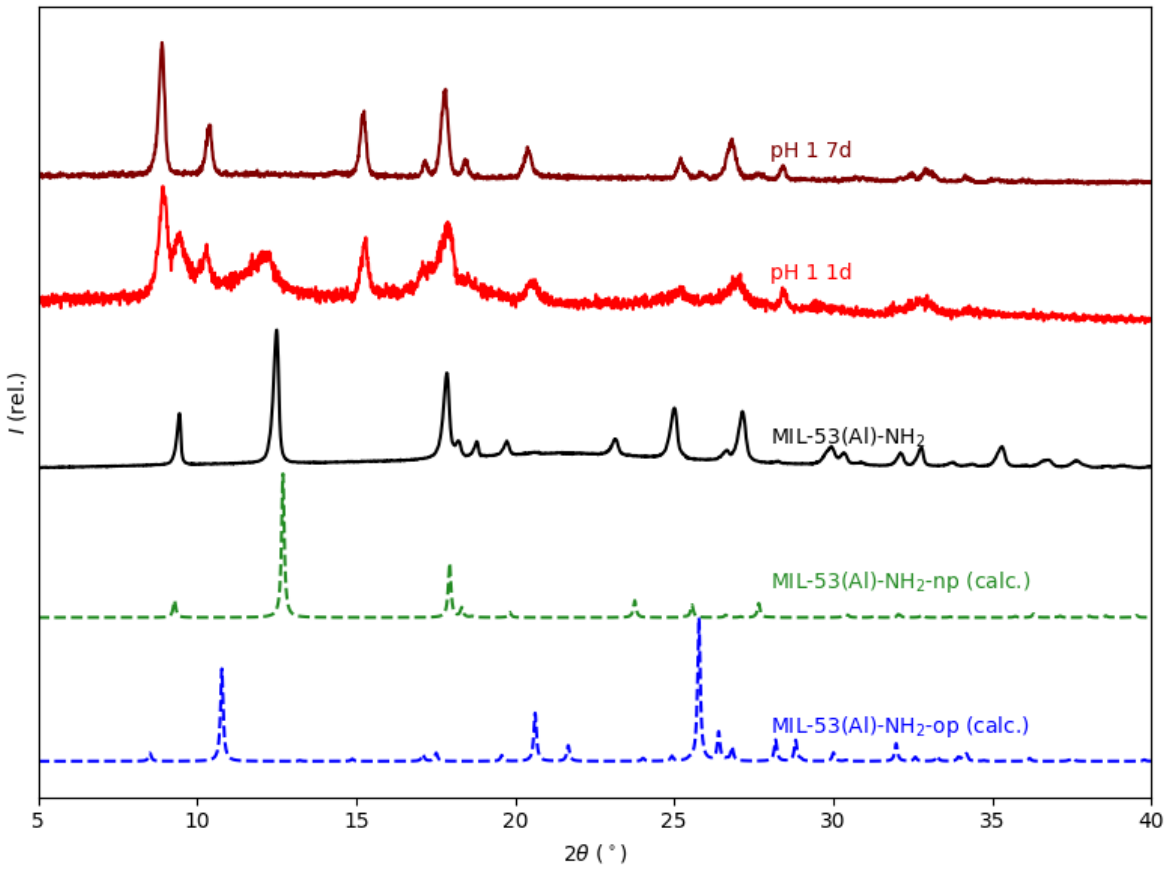

Figure 3.46 - PXRD of MIL-53(Al)-NH_2 soaked pH 1 for one and seven days against the simulated patterns of the open and narrow pore forms of MIL-53(Al)-NH_2.

3.4.1.3 Stability of MIL-121

MIL-121 is stable under most of the conditions examined, suggesting that it is less susceptible to attack from H^+ and ^-OH and is less impacted by the ions present in the buffer solutions used than both MIL-53(Al) and MIL-53(Al)-NH_2. The MIL-121 framework unstable in very high pH solutions; no reflections corresponding to the MOF are present after exposure to pH 13 and sat. NaOH solutions (no pattern is shown for pH 13 after seven days as there was no solid left). After soaking in pH 10 solutions, some of the MOF peaks remain but new peaks are present, showing that the MOF is not completely stable in solutions of pH 10 or more. Lastly, in the pH 7 Tris solutions the framework does appear to be intact, but new reflections have appeared that suggest the formation of new phases. As the sample is stable in the phosphate-based pH 7 buffer and in DI H_2O, the new phases must be caused by the Tris buffer.

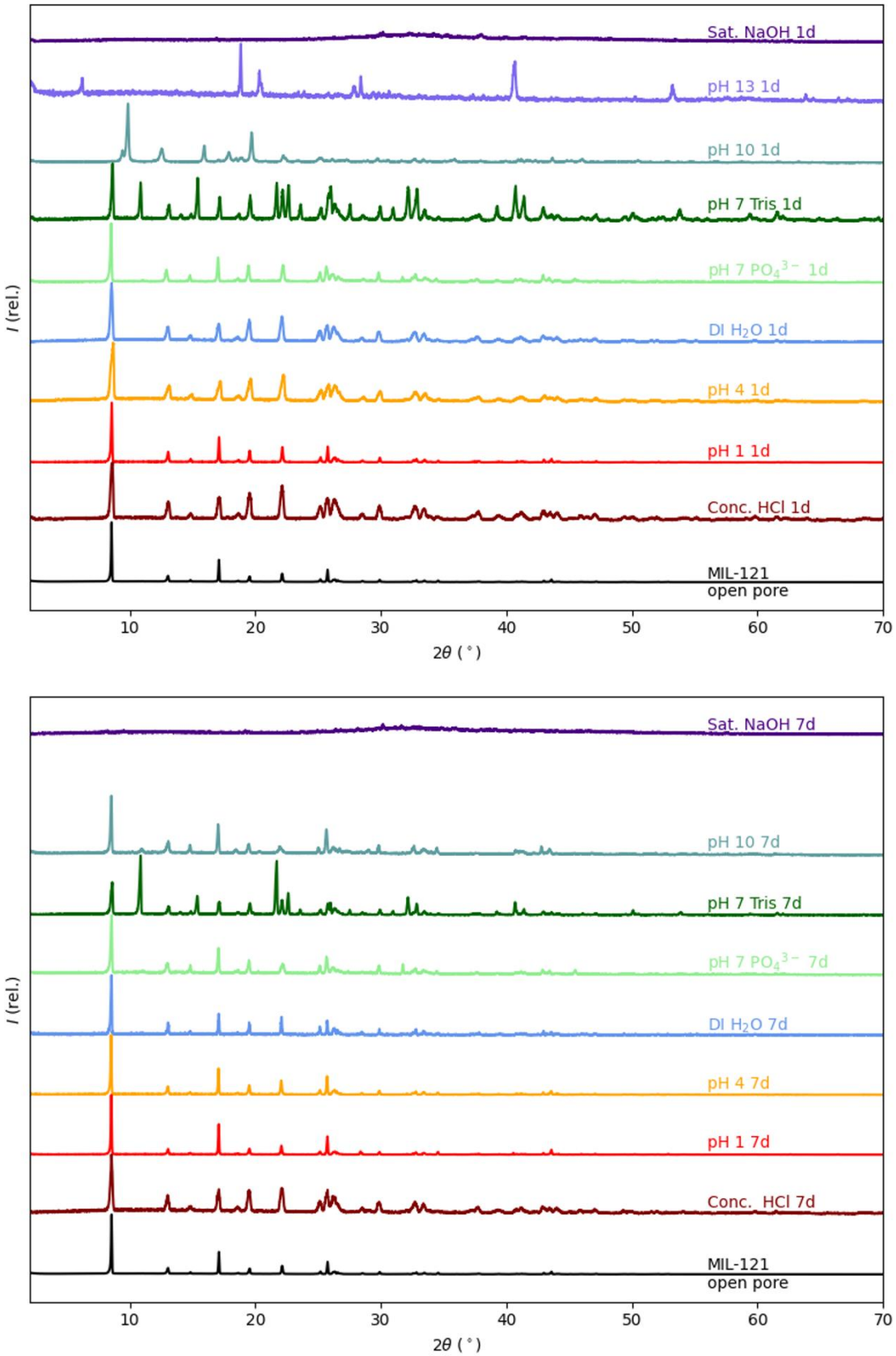

Figure 3.47 - PXRD of MIL-121 samples exposed to aqueous solutions of varying pH for one day (upper) and seven days (lower).

Although PXRD has given a good indication of changes to the structure of the MOF due to exposure to different solutions, ideally, the material would have been further characterised by TGA, gas sorption, FTIR and SEM if material quantity and time had allowed. This would show, especially in materials where PXRD has shown that the MOF structure remains, if any other characteristics had changed.

3.4.2 Cu(II) sorption using derivatives of MIL-53(Al)

The Cu(II) sorption capacity of MIL-53(Al), MIL-53(Al)-NH_2 and MIL-121 were examined by exposing samples of each MOF to Cu(II) solutions at four different Cu(II) concentrations: 50, 250, 500 and 1000 mg L^{-1}. To observe whether Cu(II) uptake changes over time, five time points (0.5, 1, 4, 24 and 168 hours) were examined for each MOF and each concentration.

Each MOF led to a slight reduction in the Cu(II) concentration after one week (168 hours) had passed (see Figure 3.48). For every MOF, greater sorption occurred when the Cu(II) concentration was 250 or 500 mg L^{-1}. When a starting concentration of 50 mg L^{-1} was used, the metal removal capacity exhibited by each MOF was very low. For starting concentrations of 250 and 500 mg L^{-1} MIL-53(Al)-NH_2 removed the highest amount of Cu(II): 11 ± 2 mg g^{-1} and 57 ± 7 mg g^{-1}, respectively. When the starting concentration was 1000 mg L^{-1}, MIL-53(Al) and MIL-121 resulted in similar Cu(II) uptakes, both of which were greater than MIL-53(Al)-NH_2 (see Table 3.13 for calculated adsorption capacities). Overall, the percentage of Cu(II) removed with each MOF had very little dependence on the starting concentration of Cu(II) (see Table 3.12), this could suggest that rather becoming adsorbed into the pores of the MOF, which would favour higher percentage removal at higher concentration due the effect of the increased concentration gradient, the Cu(II) only binds to the outside of MOF particles.

In general, the Cu(II) uptake exhibited by each MOF is low, removing only 0.5-22% of the Cu(II) depending on the MOF and concentration used. This means that they are not suitable for use in industry as Cu(II) sorbents. It is noted that low uptake for MIL-121 was expected, as the activated sample of this MOF possesses a very low surface area (15.7 ± 0.1 m^2 g^{-1}) so the pores are unlikely to be readily available for Cu(II) sorption. It is also suspected that when MIL-53(Al) and MIL-53(Al)-NH_2 are exposed to water (which they are in these metal removal experiments), the channels in the MOFs adopt the narrow pore form, preventing large

amounts of Cu(II) ions from entering the pores. In addition to this, the stability experiments showed that the presence of different counter ions such as sulfate and phosphate degraded the MOF structure. It is likely that these ions would be present in common metal waste streams, such as the waste cow footbath solution and metal mining waste, meaning that the MOFs will not withstand real-world metal waste stream, removing its ability to act as an effective sorbent.

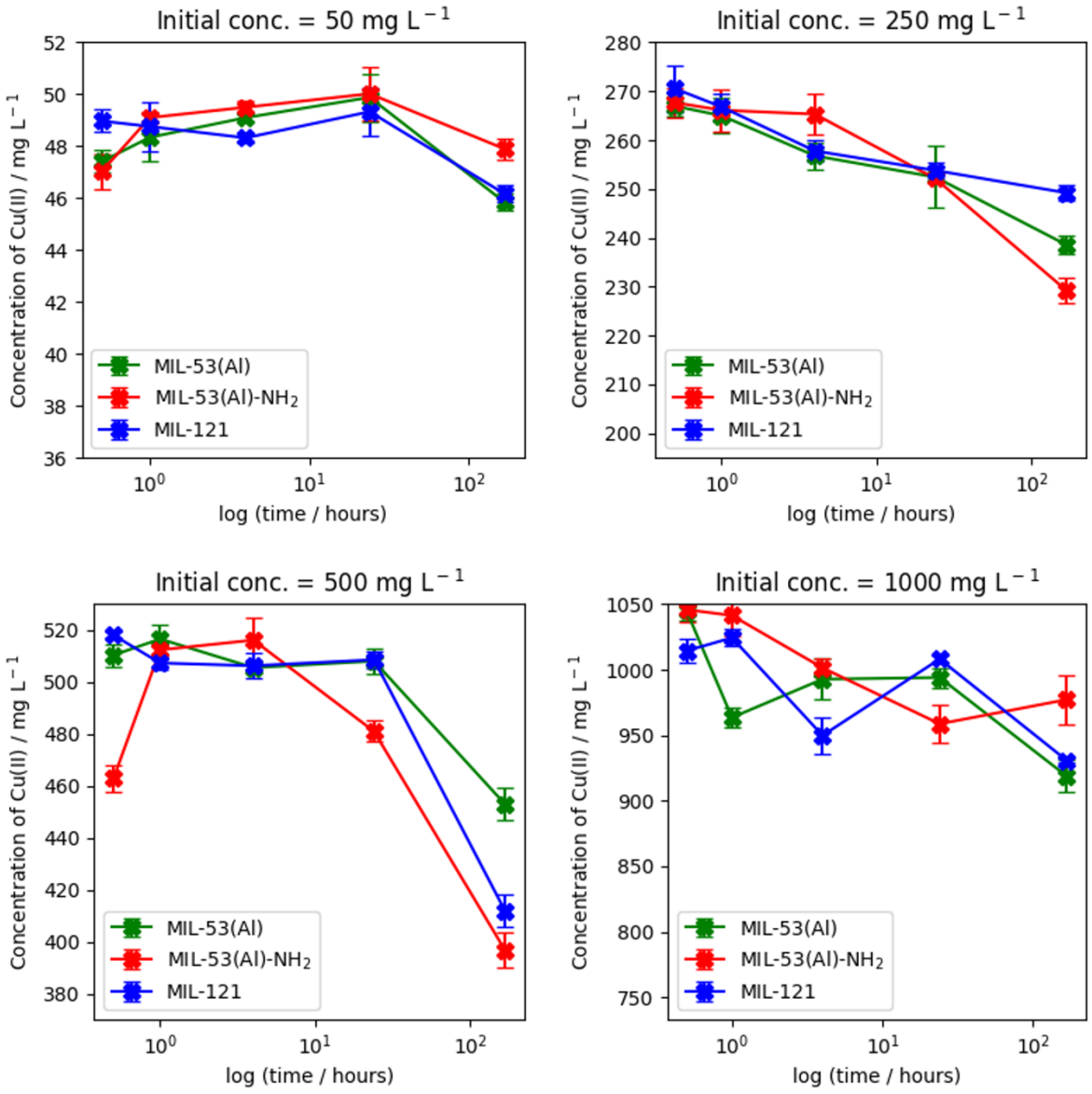

Figure 3.48 – Changes in Cu(II) concentration over time when 50, 250, 500, 1000 mg L^{-1} Cu(II) solutions are exposed to MIL-53(Al) (green), MIL-53(Al)-NH_2 (red) and MIL-121 (blue). Time is plotted in the log scale to improve readability. Although the region of concentration shown in each plot is different, the proportion shown compared to the total concentration is kept constant, so it is easier to see the significance of change in Cu(II) concentration.

Table 3.12 - Percentage of Cu (II) removed for each MOF and each concentration used

MOF	% of Cu(II) removed after one week			
	50 mg L^{-1}	**250 mg L^{-1}**	**500 mg L^{-1}**	**1000 mg L^{-1}**
MIL-53(Al)	7.99	4.71	10.65	11.87
MIL-53(Al)-NH_2	3.89	8.43	21.74	6.26
MIL-121	7.35	0.46	18.75	10.72

Table 3.13 - Cu (II) adsorption capacities for each MOF and each concentration used

MOF	Cu (II) adsorption capacities at the specified concentration / mg g^{-1}			
	50 mg L^{-1}	**250 mg L^{-1}**	**500 mg L^{-1}**	**1000 mg L^{-1}**
MIL-53(Al)	2.0 ± 0.3	6 ± 2	27 ± 7	62 ± 11
MIL-53(Al)-NH_2	1.0 ± 0.5	11 ± 2	55 ± 7	33 ± 14
MIL-121	1.8 ± 0.5	1 ± 2	48 ± 7	56 ± 5

3.5 Conclusions

MIL-53(Al), MIL-53(Al)-NH_2 and MIL-121 were synthesised using microwave heating, shortening the reaction time from up to 3 days to 10 minutes for all three MOFs. The synthesis of MIL-53(Al)-NH_2 improved on literature methods, as using a mixed solvent system of DMF and H_2O produced a material with no linker trapped in the pores. To the best of my knowledge, the microwave synthesis of MIL-121 has not been carried out previously. Unfortunately, the activation of MIL-121 was complex and the calcination carried out at 200 °C resulted in some dianhydride contaminating the sample, either in the pores or in the MOF structure itself. This resulted in a material with a very low surface area.

The structure of the calcined MIL-121 could provide a focus for future studies, for example digesting the MOF and recording NMR spectra to calculate the percentage of pyromellitic dianhydride present in the sample. Further examination of other activation techniques would be beneficial, such as solvothermal heating in MeOH that may have removed the H_2BTEC trapped in the pores, without causing the formation of the dianhydride or decarboxylating the pendant carboxylate groups.

The stability of these materials in aqueous environments was examined, with MIL-53(Al) and MIL-53(Al)-NH_2 being very susceptible to phase change (shown by PXRD), bringing into questions their ability to act as sorbents for metals from wastewater. This was further proved by their lack of Cu(II) uptake in the Cu(II) removal experiments carried out. Although MIL-121

showed better stability across a range of aqueous environments (shown by PXRD), it also exhibited low uptake of Cu(II). This may have been due to its low surface area and its pores being blocked. Characterisation of the MOF samples by gas sorption, TGA, FTIR and SEM would have helped to further understanding any structural changes to the MOFs in these stability experiments, especially changes that were not shown by PXRD, and therefore could provide valuable future experiments.

Further work in the area could investigate the use of alternative MOFs for Cu(II) uptake. Specifically, MOFs that do not exhibit a breathing effect that could be preventing the metal ions from entering the pores of the MOF. For example, a recent study shows that MOF-808 functionalised with EDTA can effectively remove 22 different metal ions from aqueous solution.[55] This MOF removed 90% of the metal ions over four repeat cycles, suggesting that it could be stable. The authors examined the stability of MOF-808-EDTA in solutions containing the various metals tested. This work could be improved by exposing MOF-808-EDTA to industrial wastewater samples or investigating the stability of the MOF in solutions containing other counter ions.

3.6 Experimental

3.6.1 Materials and Chemicals

All chemicals were obtained from commercial sources and used as received unless otherwise stated.

3.6.2 Synthesis and activation of MIL-53(Al)

3.6.2.1 Microwave synthesis of MIL-53(Al)as

$AlCl_3 \cdot 6H_2O$ (3.04 g, 12.6 mmol) was combined with H_2BDC (1.04 g, 6.3 mmol) and 10.0 mL of deionised water in a 35 mL CEM glass vial equipped with a stirrer bar. The vial was sealed and placed inside a CEM Discover microwave cavity. A stepped heating program was used: 110 °C for three minutes, 140 °C for three minutes, 180 °C for three minutes and 200 °C for 30 minutes, followed by cooling. The white microcrystalline powder product (1.15 g) was separated using centrifugation, washed three times with deionised water, and dried in an oven at 50 °C.

3.6.2.2 Activation of MIL-53(Al)as to form MIL-53(Al)hyd

As-synthesised MIL-53(Al) (around 0.3 g) was weighed out and placed into an alumina ceramic boat. The boat was then placed into a Carbolite muffle furnace and heated to 330 °C for three days in air. After allowing the furnace to cool to room temperature, the sample was retrieved and weighed. Between calcinations, the boats were washed with soap and water, and isopropyl alcohol (IPA).

3.6.3 Synthesis and activation of MIL-53(Al)-NH_2

In a standard reaction, $AlCl_3 \cdot 6H_2O$ (0.49 g, 2.0 mmol) was combined with $H_2BDC\text{-}NH_2$ (0.36 g, 2.0 mmol)[i] and DI water or a DI water/DMF mix (3.50 mL total volume)[ii] in a 10 mL CEM glass vial, equipped with a stirrer bar. The vial was sealed and placed inside a CEM Discover microwave cavity. A stepped heating program was used: 80 °C for one minute, 110 °C for one minute, 140 °C for one minute, 150 (experiments involving DMF) or 180 °C (experiments involving DI water only) for 10 minutes. The yellow powder product (0.4 - 0.5 g) was separated using centrifugation (4200 rpm), washed twice with deionised water, and dried in an oven at 50 °C overnight.

For activation, a sample of MIL-53(Al)-NH_2 (synthesised using 70% DMF) was placed into a centrifuge vial. 50 mL of MeOH was added, the vial was shaken for one minute and centrifuged for 20 minutes, before decanting the MeOH. This addition and separation were carried out twice more before the centrifuge vial was placed into an oven at 50 °C for 16 hours. The partially dried sample was then transferred to a crucible and dried at 110 °C for seven hours.

[i] The moles of $H_2BDC\text{-}NH_2$ was varied (1.0-4.0 mmol) for the metal salt to linker ratio experiments.
[ii] The % volume of DI water was varied in 10% increments from 0 to 100 for the DMF/H_2O experiments.

3.6.4 Synthesis and activation of MIL-121

$AlCl_3 \cdot 6H_2O$ (0.54 g, 2.25 mmol) was combined with H_2BTEC (0.28 g, 1.12 mmol) and DI water (3.5 mL) in a 10 mL CEM glass vial, equipped with a stirrer bar. The vial was sealed and placed inside a CEM Discover microwave cavity. A stepped heating program was used: 110 °C for one minute, 140 °C for one minute, 170 °C for one minute, 200 °C for ten minutes. The white powder product (~0.19-0.21 g) was separated using centrifugation, washed twice with deionised water, and dried in an oven at 50 °C.

For activation attempts using Soxhlet extraction, as synthesised MIL-121 (0.2 g) was placed into thimble and extraction was carried out used either MeOH or DMF (300 mL approx.) After 24 hours, the white powder was collected by removing the thimble from the Soxhlet glassware and allowing it to dry in air, before carrying out PXRD and TGA.

For activation *via* calcination, samples of as synthesised MIL-121 were placed in porcelain crucibles which were then placed into an oven at 200 °C for 24 hours. After allowing the oven to cool, the samples were collected and weighed.

3.6.5 Repeat reactions of MIL-53(Al), MIL-53(Al)-NH_2 and MIL-121

3.6.5.1 Repeat syntheses and activations of MIL-53(Al)

Samples (see Table 3.14) were synthesised according to the method described in section 3.6.2.1.

Table 3.14 - Mass of reagents and products for repeat MW synthesis of MIL-53(Al).

Sample ID	Mass of $AlCl_3 \cdot 6H_2O$ / g	Moles of $AlCl_3 \cdot 6H_2O$ / mmol	Mass of H_2BDC / g	Moles of H_2BDC / mmol	Volume of DI H_2O / mL	Mass of product / g
1	3.04	12.6	1.04	6.28	10	1.15
2	3.04	12.6	1.04	6.24	10	1.14
3	3.04	12.6	1.04	6.26	10	1.13
4	3.04	12.6	1.04	6.25	10	1.14
5	3.04	12.6	1.05	6.31	10	1.23
6	3.04	12.6	1.04	6.26	10	1.14

Repeat activations (see Table 3.15) were carried out according to the method described in 3.6.2.2. Yields were calculated by TGA. The samples listed in Table 3.15 were then combined, ready to be used for stability and metal removal experiments.

Table 3.15 - Masses used and obtained for the calcinations of MIL-53(Al). * indicates samples used for particle size analysis.

Sample ID	New Sample ID	Mass before calcination/ g	Mass after calcination / g	Yield %
1	1A-i*	0.30	0.18	49.5
	1A-ii	0.31	0.22	-
2	2A	0.32	0.15	41.3
3	3A	0.80	0.45	45.1
4	4A*	0.32	0.11	20.2
5	5A	0.70	-	-
6	6A	0.60	0.26	34.1

3.6.5.2 Repeat syntheses and activations of MIL-53(Al)-NH_2

Samples (see Table 3.16) were synthesised according to the method described in section 3.6.3.

Table 3.16 - Mass of reagents and products for repeat MW synthesis of MIL-53(Al)-NH_2

Sample ID	Mass of $AlCl_3 \cdot 6H_2O$ / g	Moles of $AlCl_3 \cdot 6H_2O$ / mmol	Mass of H_2-BDC-NH_2 / g	Moles of H_2-BDC-NH_2 / mmol	Volume of DMF: DI H_2O / mL	Mass of product / g
NH70-1	0.48	2.00	0.36	2.00	2.45:1.05	0.45
NH70-2	0.48	2.00	0.36	2.01	2.45:1.05	0.51
NH70-3	0.48	2.00	0.37	2.01	2.45:1.05	0.48
NH70-4	0.48	2.00	0.36	2.01	2.45:1.05	0.51
NH70-5	0.48	2.00	0.36	2.01	2.45:1.05	0.70
NH70-6	0.48	2.00	0.36	2.00	2.45:1.05	0.61
NH70-7	0.48	2.00	0.36	2.00	2.45:1.05	0.63
NH70-8	0.48	2.00	0.36	2.00	2.45:1.05	0.60

Repeat activations (see Table 3.17) were carried out according to the method described in Section 3.6.3. Yields were calculated by TGA. The samples listed in Table 3.17 were then combined, ready to be used for stability and metal removal experiments.

Table 3.17 - Masses used and obtained for the calcinations of MIL-53(Al)-NH_2. * Indicates samples used for particle size analysis.

Sample ID	Mass before calcination/ g	Mass after calcination / g	Yield %

NH70-1A	0.34	0.30	80.2
NH70-2A*	0.42	0.34	86.5
NH70-3A	0.41	0.35	84.3
NH70-4A	0.42	0.34	83.0
NH70-5A	0.49	0.28	82.0
NH70-6A*	0.45	0.32	91.4
NH70-7A	0.55	0.29	68.5
NH70-8A	0.43	0.29	84.2

3.6.5.3 Repeat syntheses and activations of MIL-121

Table 3.18 - Mass of reagents and products for repeat MW synthesis of MIL-121

Sample ID	Mass of $AlCl_3.6H_2O$ / g	Moles of $AlCl_3.6H_2O$ / mmol	Mass of H_2-BTEC / g	Moles of H_2-BTEC / mmol	Volume of DMF: DI H_2O / mL	Mass of product / g
COOH-1	0.54	2.25	0.28	1.12	3.5:1.5	0.22
COOH-2	0.54	2.25	0.27	1.12	3.5:1.5	0.21
COOH-3	0.54	2.24	0.27	1.12	3.5:1.5	0.21
COOH-4	0.54	2.24	0.27	1.12	3.5:1.5	0.19
COOH-5	0.54	2.24	0.28	1.12	3.5:1.5	0.21
COOH-6	0.54	2.24	0.28	1.12	3.5:1.5	0.21
COOH-7	0.54	2.26	0.27	1.12	3.5:1.5	0.20
COOH-8	0.54	2.26	0.27	1.12	3.5:1.5	0.22

Prior to activation, samples listed in Table 3.18 were combined. The samples were then activated according to the method described in section 3.6.4. The bulk sample was split across four crucibles, with masses before and after shown in Table 3.19. The calcined sample were then re-combined before further analysis was carried out.

Table 3.19 – Mass of MIL-121 samples before and after calcination. * Indicates samples used for particle size analysis.

Crucible	Mass before / g	Mass after / g
1*	0.22	0.20
2*	0.19	0.19
3	0.19	0.18
4	0.13	0.12

3.6.6 Stability experiments

Aqueous solutions of appropriate pH's were prepared according to the details in Table 3.20.

Table 3.20 – Preparation methods of aqueous solutions with various pH's required for the stability experiments.

Condition	Solution used
DI water	MilliQ H_2O
Conc. HCl	Neat HCl (37%)
pH 1	5.4 mL of aqueous 0.2 M KCl and 14.6 mL of aqueous 0.2 M HCl combined
pH 4	Buffer (potassium hydrogen phthalate, formaldehyde, methanol, and water) purchased from Fisher Scientific
pH 7 (phosphate based)	Buffer (monopotassium phosphate, sodium hydroxide, water) purchased from Fisher Scientific
pH 7 (Tris based)	Tris(hydroxymethyl)aminomethane (6.057 g, 0.05 mol) was dissolved in MilliQ H_2O (40 mL) and the pH adjusted to 7 by dropwise addition of conc. HCl. The solution was then added to a 50 mL volumetric flask and diluted up to 50 mL
pH 10	Buffer (potassium hydroxide, potassium carbonate, potassium borate, water) purchased from Fisher Scientific
pH 13	5.5 mL of aqueous 0.2 M KCl and 14.5 mL of aqueous 0.2 M NaOH combined
Sat. NaOH	MilliQ water saturated with NaOH

For the stability experiments samples of MIL-53(Al), MIL-53(Al)-NH_2 and MIL-121 (20 mg) were placed into centrifuge vials and the aqueous solutions (2 mL) listed in Table 3.20 were added to each vial (27 vials in total). The samples were left for either one day or one week before being centrifuged and the aqueous solution decanted off. Acetone (12 mL) was added

to the vial and the sample mixed with a vortex mixer, before centrifuging and decanting the acetone and leaving the sample to dry in air.

3.6.7 Cu(II) sorption experiments

Cu(II) solutions were prepared by adding $Cu(NO_3)_2 \cdot 3H_2O$ (masses and moles shown in Table 3.21) to MilliQ H_2O water.

Table 3.21 – Masses and moles of $Cu(NO_3)_2 \cdot 3H_2O$ used in the preparation of Cu(II) solutions.

Cu(II) concentration / mg L^{-1}	**Volume of solution / mL**	**$Cu(NO_3)_3 \cdot 3H_2O$ / mg**	**$Cu(NO_3)_3 \cdot 3H_2O$ / mmol**
50	250	46.7	0.19
250	250	235.0	0.97
500	250	468.2	1.94
1000	250	936.7	3.88

For the metal removal experiments, each time point and concentration were carried out individually to give a total of 60 samples (three MOFs x four concentrations x five time points). Samples of MIL-53(Al), MIL-53(Al)-NH_2 and MIL-121 (10 mg) were placed in 12 mL centrifuge vials, equipped with small stirrer bars. Cu(II) solution (5 mL) of the appropriate concentration (50, 250, 500 or 1000 mg L^{-1}) was pipetted into each vial and the vials placed on a stirrer plate. The samples were left for the required time (0.5, 1, 4, 24 or 168 hours) and then centrifuged and the Cu(II) solution decanted off the MOF. The Cu(II) solution was then diluted to a Cu(II) concentration appropriate for ICP analysis and stabilised with 5% concentrated HCl.

3.7 Appendix

3.7.1 Bulk characterisation of MOF samples

3.7.1.1 Characterisation of a bulk sample of activated MIL-53(Al)

PXRD of the combined activated MIL-53(Al) sample (Figure 3.49) indicates that the sample mainly consists of the hydrated phase, as expected. The TGA profile (Figure 3.50) supports this, showing only two decomposition stages. The first, occurring between 25 and 50 °C (8.0%) is due to the loss of water from the pores of the MOF, the second which occurs 450 and 650 °C (67.8%) is due to the decomposition of the MOF framework. The FTIR spectrum (Figure 3.51) shows the expected functional groups and SEM imaging (Figure 3.52) shows irregular particles that are roughly 0.5-2 µm in size.

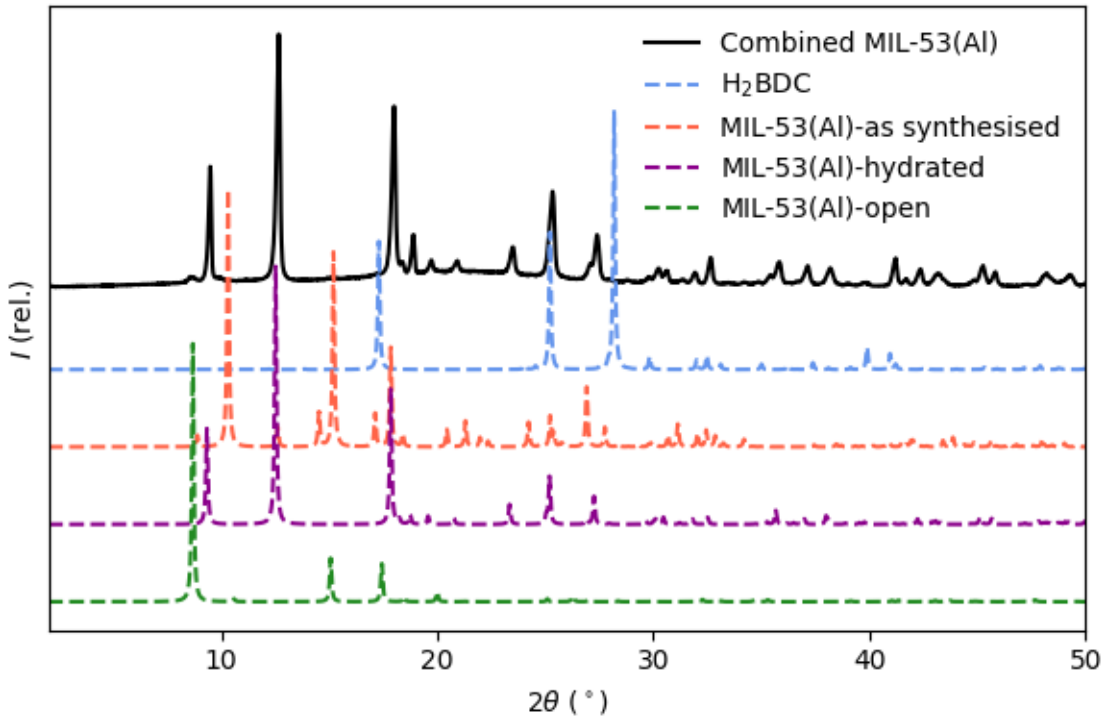

Figure 3.49 -PXRD of the combined sample of activated MIL-53(Al).

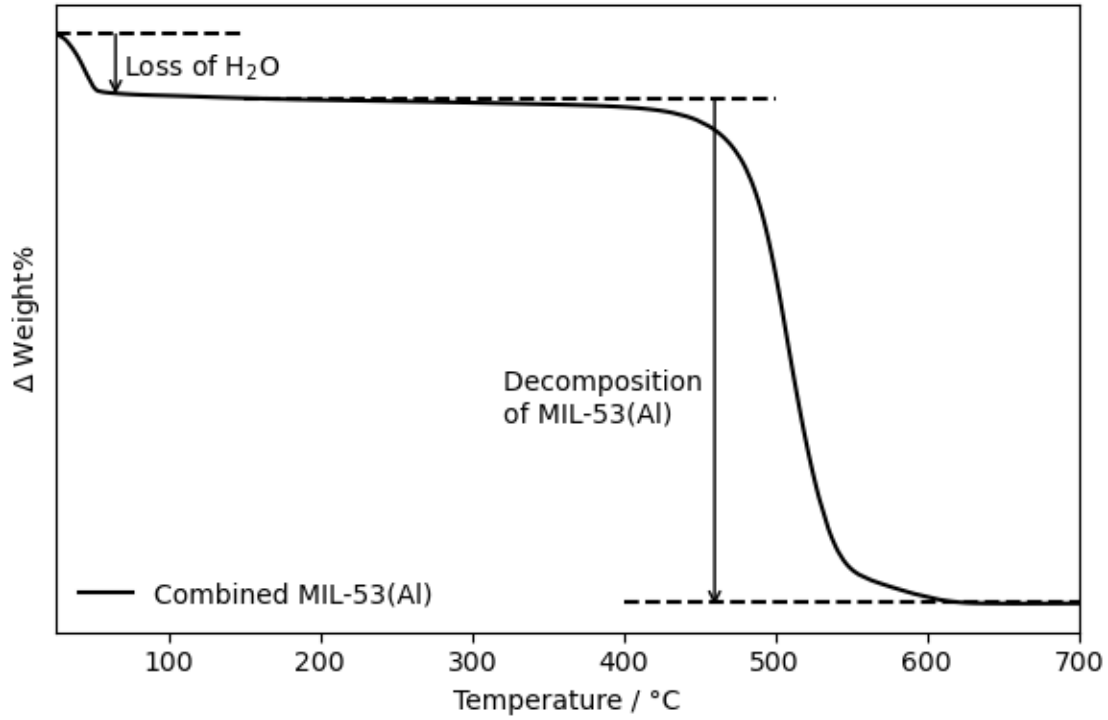

Figure 3.50 – TGA profile of the combined sample of MIL-53(Al).

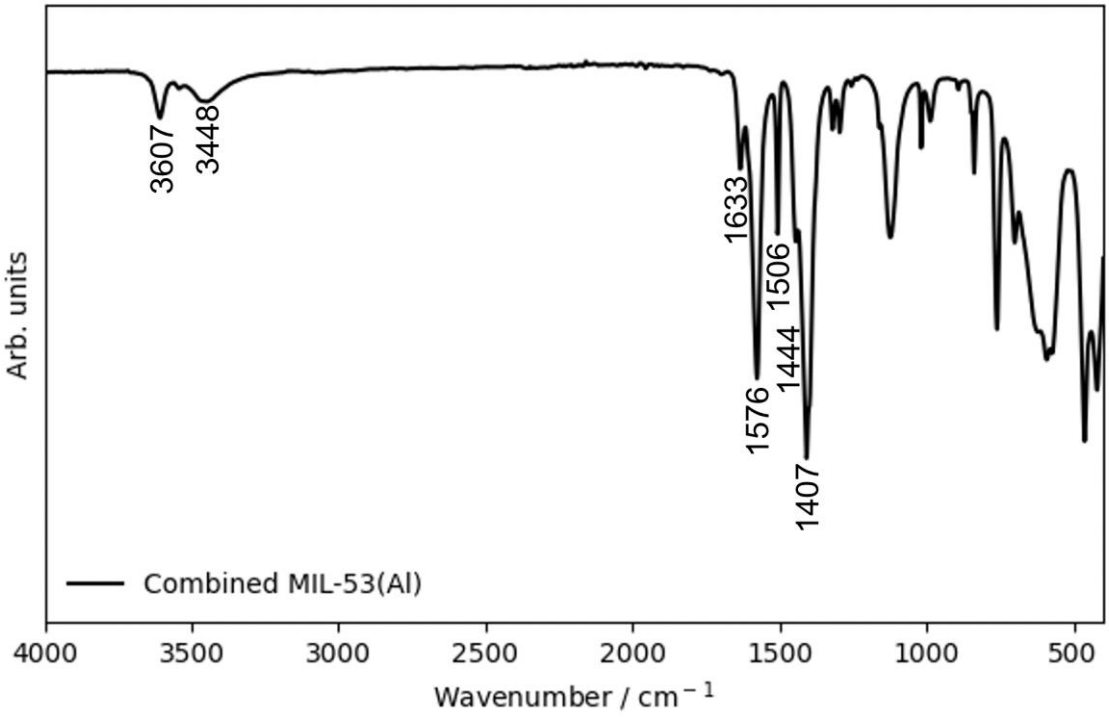

Figure 3.51 – FTIR spectrum of the combined sample of MIL-53(Al), displaying bridging O-H (3607), stretching OH in H_2O (3500-3400), bending O-H in free H_2O (1633), asymmetric C=O stretch (1576, 1506), symmetric C=O stretch (1444, 1407).

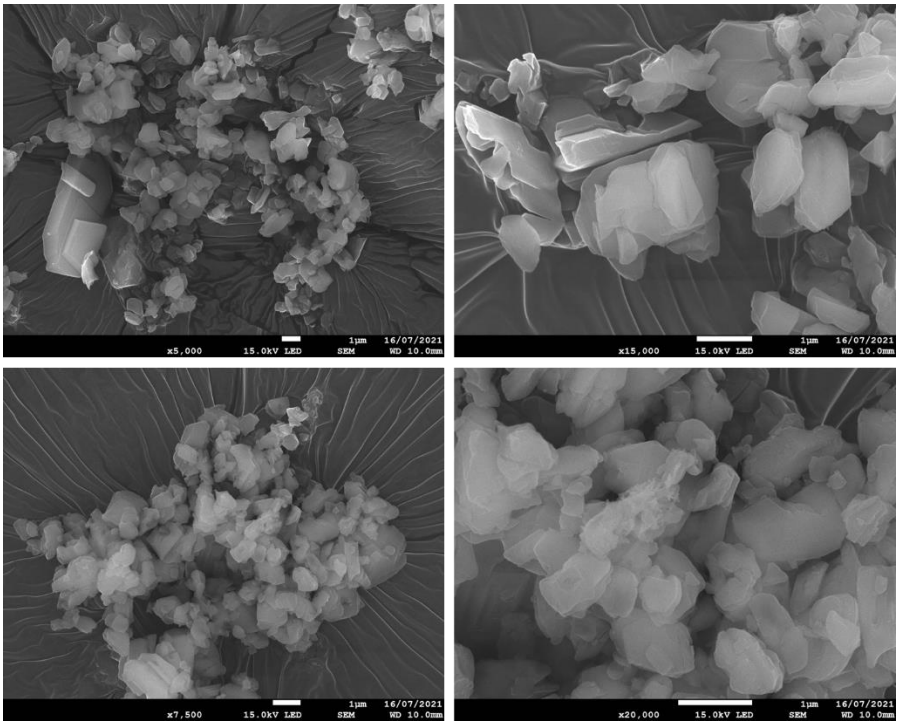

Figure 3.52 – SEM images of combined MIL-53(Al). Scale bars: top left = 1 µm, top right = 1 µm, bottom left = 1 µm, bottom right = 1 µm.

3.7.1.2 Characterisation of a bulk sample of activated MIL-53(Al)-NH_2

PXRD of the combined activated MIL-53(Al)-NH_2 sample (Figure 3.53) indicates that the sample mainly consists of the narrow pore form, as expected. The TGA profile (Figure 3.54) supports this, showing only two decomposition stages. The first, occurring between 25 and 60 °C (8.0%) is due to the loss of water from the pores of the MOF, the second which starts at 450 °C, but is not completed even at 1000 °C, is due to the decomposition of the MOF framework. The FTIR spectrum (Figure 3.55) shows the expected functional groups and SEM imaging (Figure 3.56) shows irregular oblong particles that are roughly 300-500 nm long.

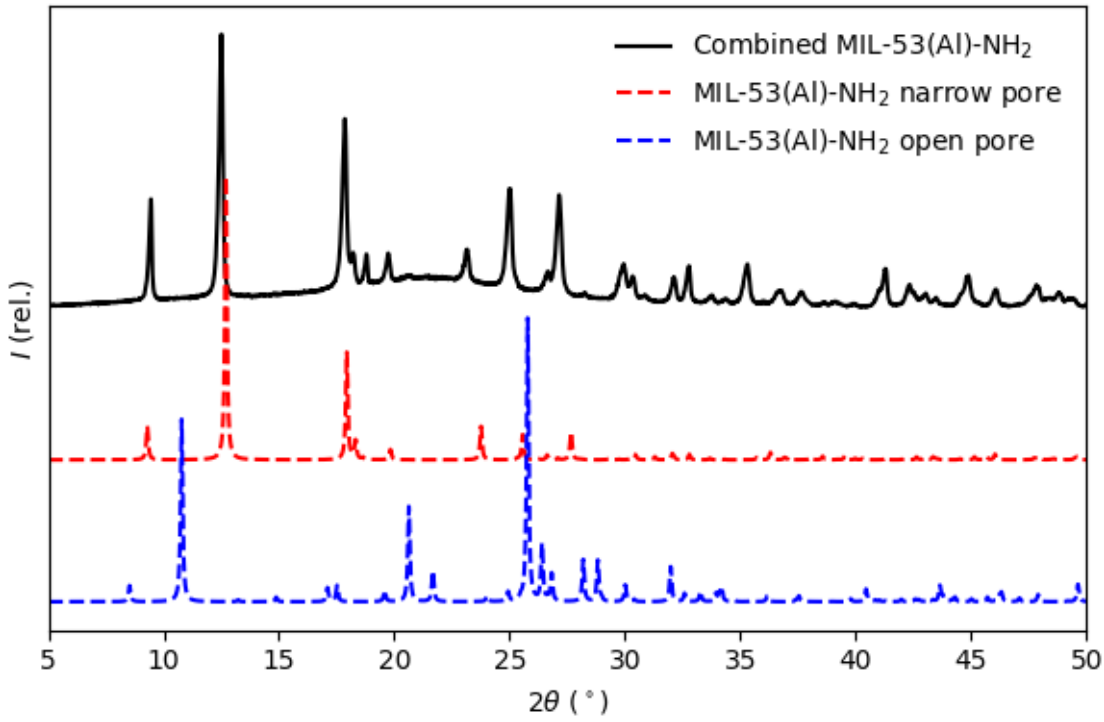

Figure 3.53 - PXRD of the combined sample of activated MIL-53(Al)-NH_2.

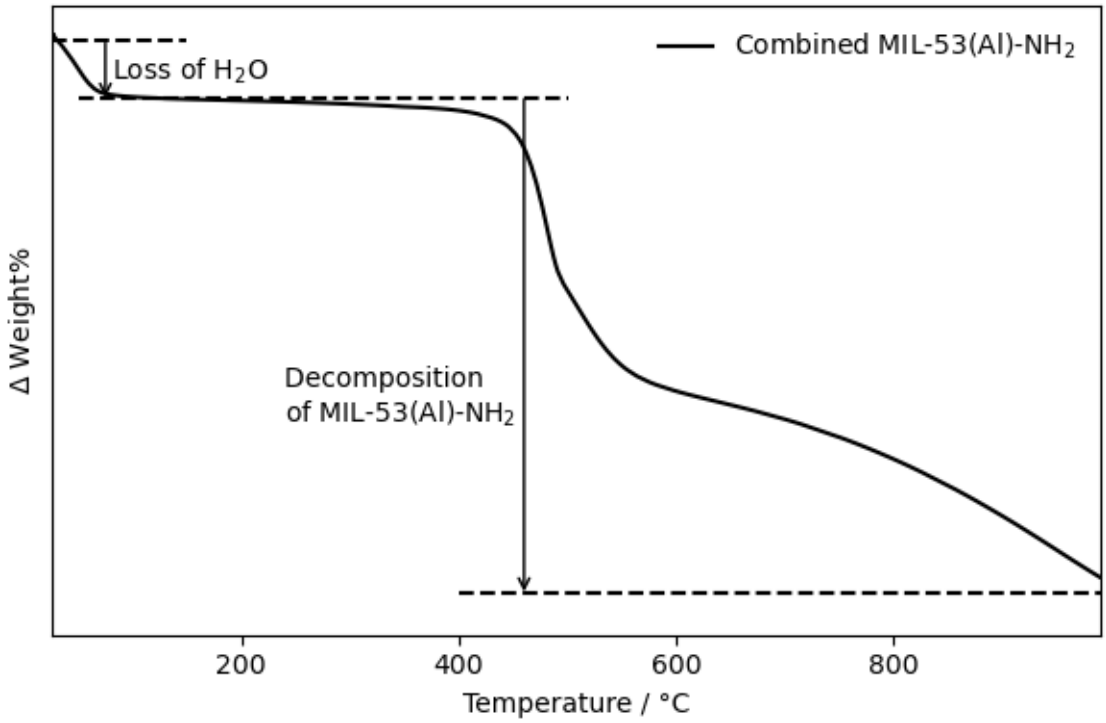

Figure 3.54 – TGA profile of the combined sample of MIL-53(Al)-NH_2.

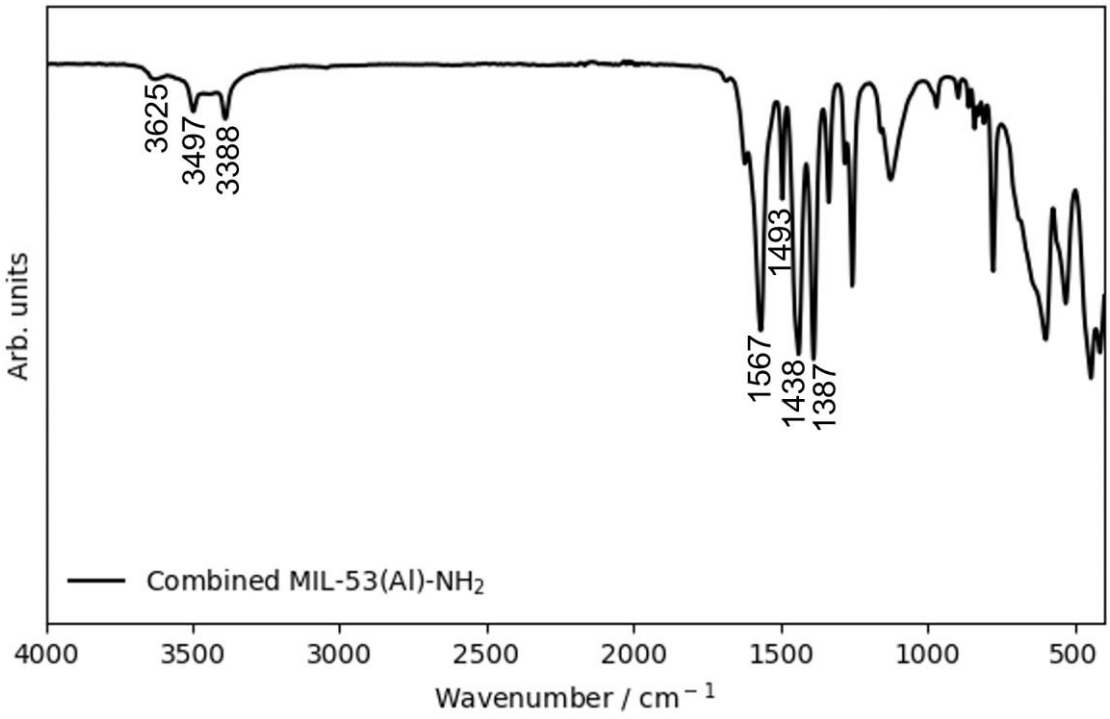

Figure 3.55 – FTIR spectrum of the combined sample of MIL-53(Al)-NH_2. Bridging O-H (3625), NH_2 (3497, 3388), asymmetric C=O stretch (1567, 1493), symmetric C=O stretch (1438, 1387).

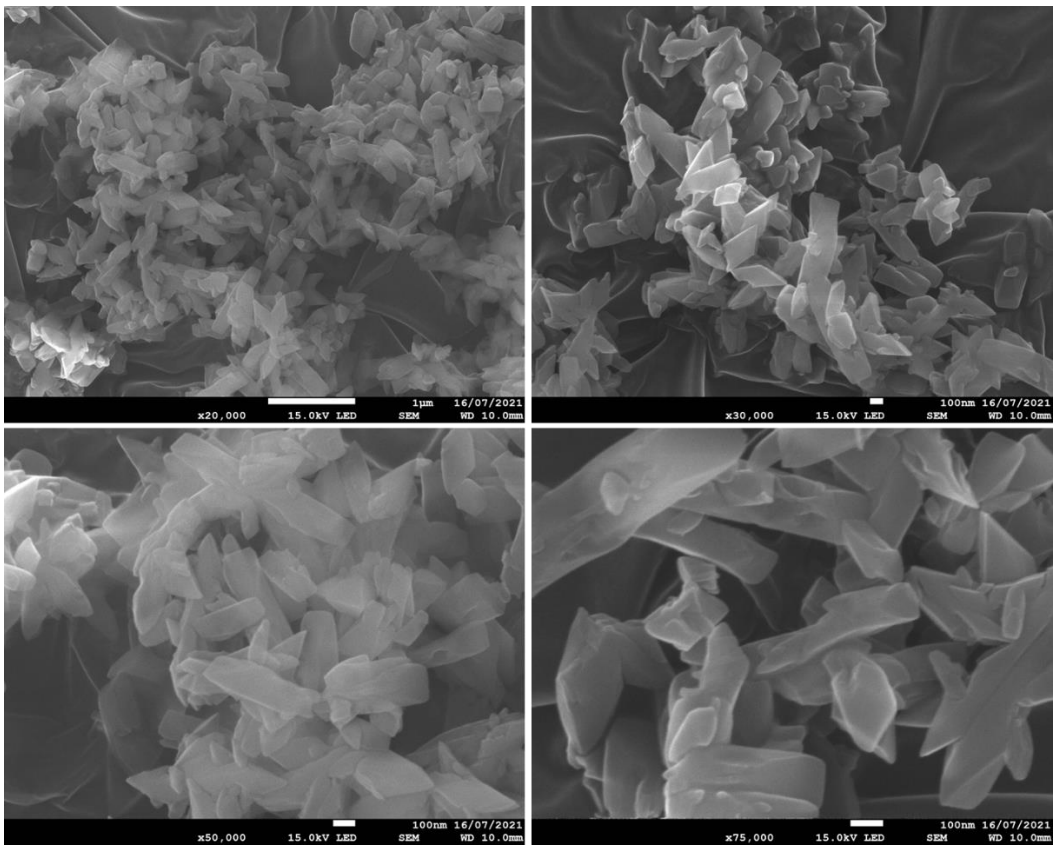

Figure 3.56 – SEM images of combined MIL-53(Al)-NH_2. Scale bars: top left = 1 µm, top right = 100 nm, bottom left = 100 nm, bottom right = 100 nm.

3.7.1.3 Characterisation of a bulk sample of activated MIL-121

PXRD of the combined activated MIL-121 sample (Figure 3.57) shows that the expected MIL-121 phase is present. The TGA profile (Figure 3.58) shows several decomposition events. The first, occurring between 25 and 40 °C (8.0%) is due to the loss of water from the pores of the MOF. Between 370 and 410 °C (13.3%) the loss of pendant COOH groups occurs and above 420 °C the MOF framework decomposes (75.8%). The FTIR spectrum (Figure 3.59) indicates that some anhydride may be present in the sample due the presence of an absorbance band at 1784 cm^{-1}, but as there is no mass loss associated with this in the TGA profile, it was assumed that the amount present, and therefore potentially blocking the pores of the MOF, is negligible, and should not affect the stability and metal removal experiments. SEM imaging (Figure 3.60) shows irregular oblong-shaped particles with sharp 90° edges particles that are roughly 2-5 µm long.

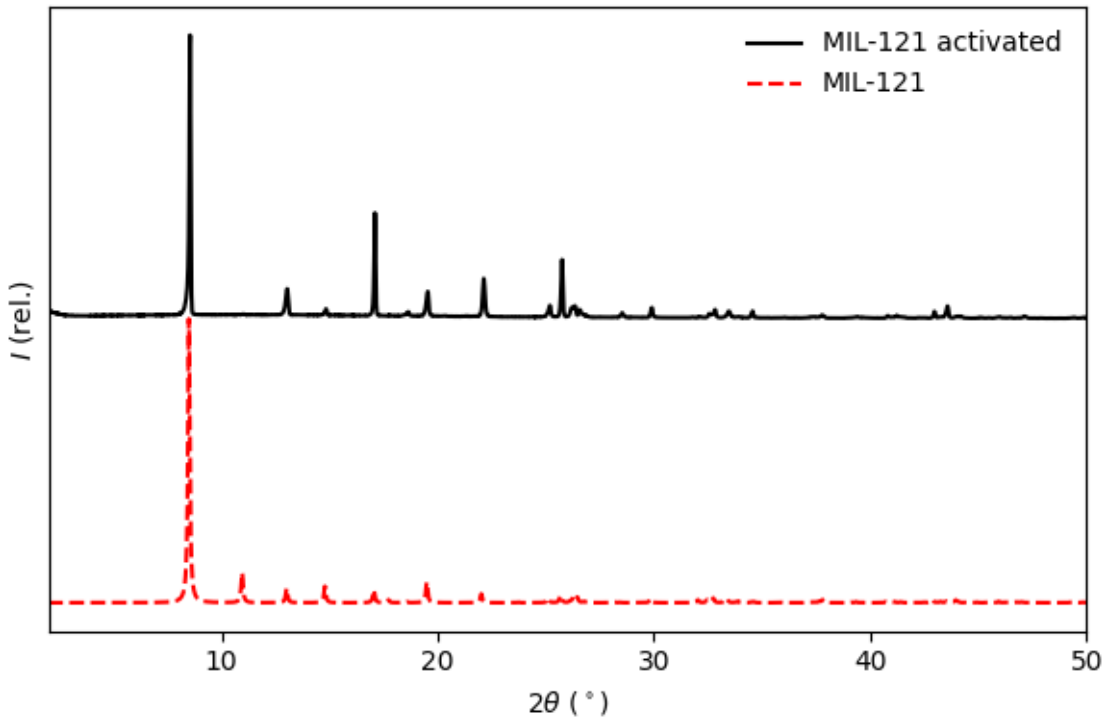

Figure 3.57 -PXRD of the combined sample of activated MIL-121.

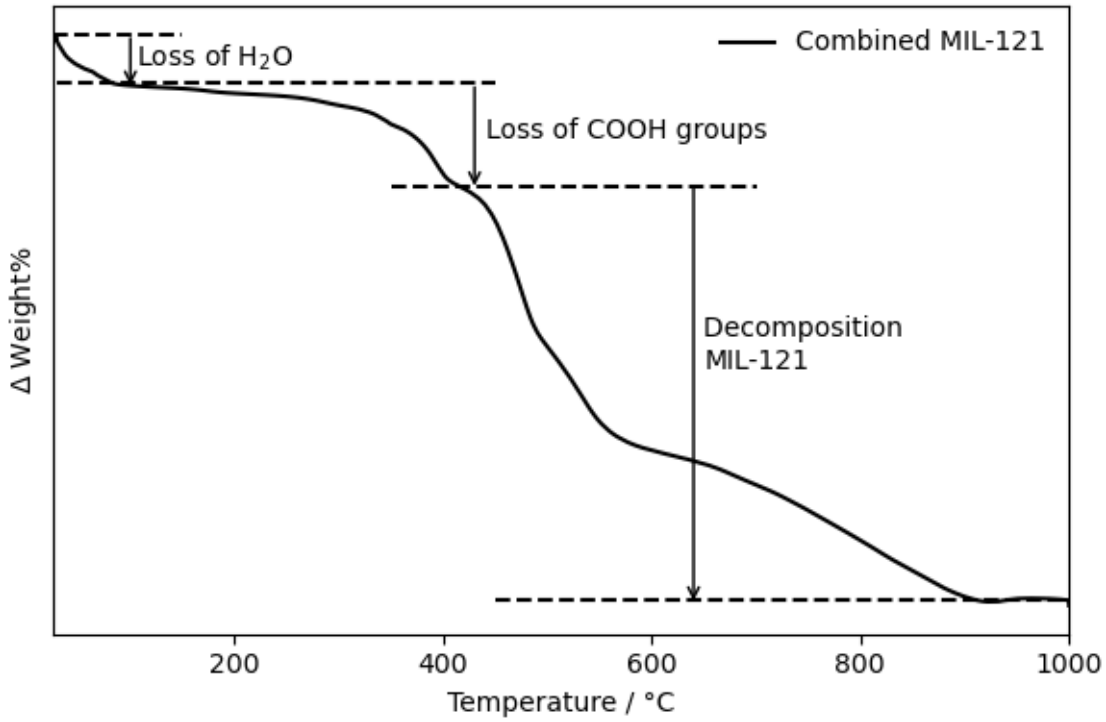

Figure 3.58 – TGA profile of the combined sample of MIL-121.

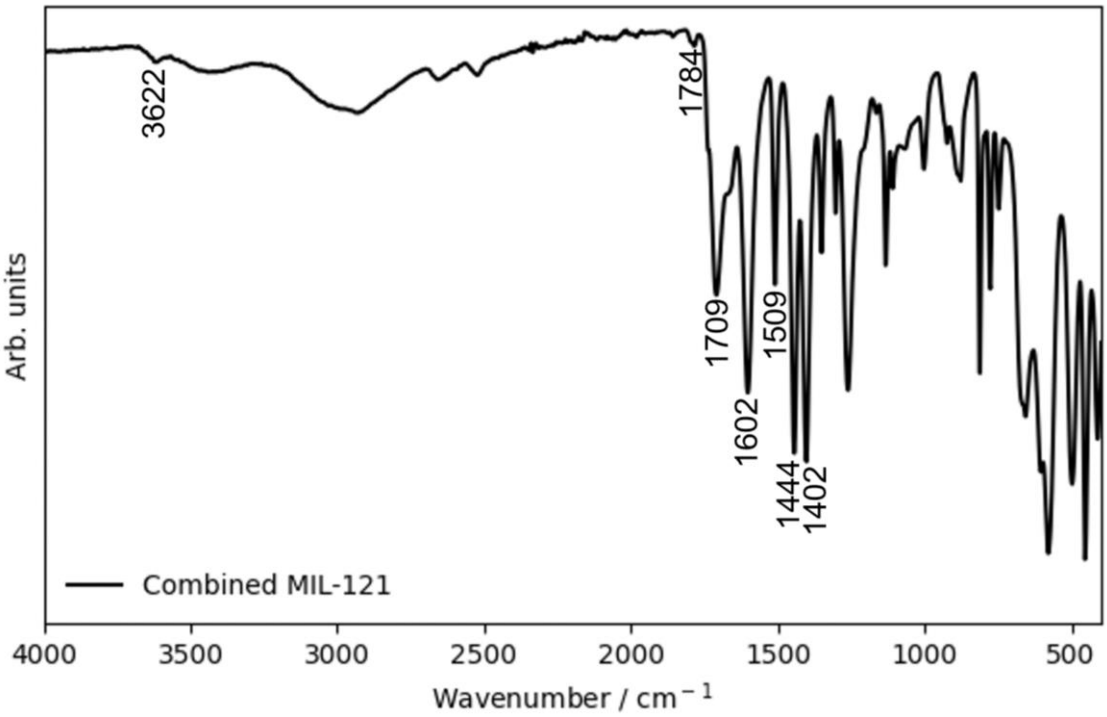

Figure 3.59 – FTIR spectrum of the combined sample of MIL-121. Bridging O-H (3622), OH from pendant COOH (2500-3200, b), C=O in acid anhydride (1784), C=O from pendant COOH (1709) asymmetric C=O stretch (1602, 1509), symmetric C=O stretch (1444, 1402).

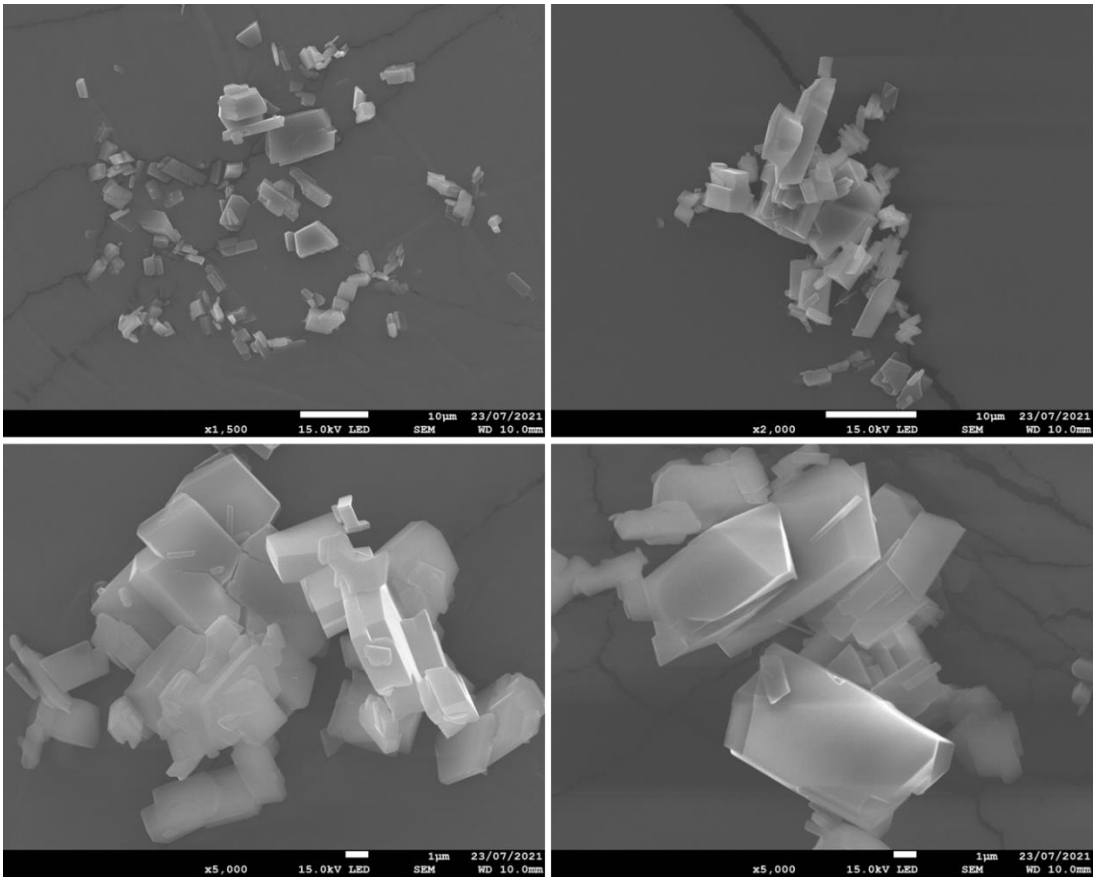

Figure 3.60 – SEM images of combined MIL-121. Scale bars: top left = 10 µm, top right = 10 µm, bottom left = 1 µm, bottom right = 1 µm.

3.8 References

1 E. Rahimi and N. Mohaghegh, *Mine Water Environ.*, 2015, **35**, 18–28.
2 Y. Zhang, X. Zhao, H. Huang, Z. Li, D. Liu and C. Zhong, *RSC Adv.*, 2015, **5**, 72107–72112.
3 C. G. Carson, K. Hardcastle, J. Schwartz, X. Liu, C. Hoffmann, R. A. Gerhardt and R. Tannenbaum, *Eur. J. I*norg. *Chem.*, 2009, 2338–2343.
4 J. H. Cavka, C. Lamberti, N. Guillou, S. Bordiga, S. Jakobsen, U. Olsbye, N. Guillou, S. Bordiga and K. P. Lillerud, *J. Am. Chem. Soc.*, 2008, **130**, 13850–13851.
5 M. R. Azhar, H. R. Abid, V. Periasamy, H. Sun, M. O. Tade and S. Wang, *J. Colloid Interface Sci.*, 2017, **500**, 88–95.
6 G. Férey, M. Latroche, C. Serre, F. Millange, T. Loiseau and A. Percheron-Guégan, *Chem. Commun.*, 2003, **3**, 2976–2977.
7 T. Loiseau, C. Serre, C. Huguenard, G. Fink, F. Taulelle, M. Henry, T. Bataille and G. Férey, *Chem. Eur. J.*, 2004, **10**, 1373–1382.
8 S. Biswas, T. Ahnfeldt and N. Stock, *Inorg. Chem.*, 2011, **50**, 9518–9526.
9 T. Ahnfeldt, D. Gunzelmann, T. Loiseau, D. Hirsemann, J. Senker, G. Férey and N. Stock, *Inorg. Chem.*, 2009, **48**, 3057–3064.
10 C. Volkringer, T. Loiseau, N. Guillou, G. Férey, M. Haouas, F. Taulelle, E. Elkaim and N. Stock, *Inorg. Chem.*, 2010, **49**, 9852–9862.
11 A. Schneemann, V. Bon, I. Schwedler, I. Senkovska, S. Kaskel and R. A. Fischer, *Chem. Soc. Rev.*, 2014, **43**, 6062–6096.
12 A. Martinez Joaristi, J. Juan-Alcañiz, P. Serra-Crespo, F. Kapteijn and J. Gascon, *Cryst. Growth Des.*, 2012, **12**, 3489–3498.
13 E. Haque, N. A. Khan, H. J. Park and S. H. Jhung, *Chem. A Eur. J.*, 2010, **16**, 1046–1052.
14 M. Taddei, D. A. Steitz, J. A. Van Bokhoven and M. Ranocchiari, *Chem. A Eur. J.*, 2016, **22**, 3245–3249.
15 P. A. Bayliss, I. A. Ibarra, E. Pérez, S. Yang, C. C. Tang, M. Poliakoff and M. Schröder, *Green Chem.*, 2014, **16**, 3796–3802.
16 A. Laybourn, J. Katrib, R. S. Ferrari-John, C. G. Morris, S. Yang, O. Udoudo, T. L. Easun, C. Dodds, N. R. Champness, S. W. Kingman and M. Schröder, *J. Mater. Chem. A*, 2017, **5**, 7333–7338.
17 V. I. Isaeva, A. L. Tarasov, V. V. Chernyshev and L. M. Kustov, *Mendeleev Commun.*, 2015, **25**, 466–467.
18 C. Serre, F. Millange, C. Thouvenot, M. Noguès, G. Marsolier, D. Louër and G. Férey, *J. Am. Chem. Soc.*, 2002, **124**, 13519–13526.
19 P. Rallapalli, D. Patil, K. P. Prasanth, R. S. Somani, R. V. Jasra and H. C. Bajaj, *J. Porous Mater.*, 2010, **17**, 523–528.
20 S. Couck, E. Gobechiya, C. E. A. Kirschhock, P. Serra-Crespo, J. Juan-Alcaçiz, M. Joaristi, E. Stavitski, J. Gascon, F. Kapteijn, G. V Baron and J. F. M. Denayer, *ChemSusChem*, 2012, **5**, 740–750.
21 X. Cheng, A. Zhang, K. Hou, M. Liu, Y. Wang, C. Song, G. Zhang and X. Guo, *Dalton Trans.*, 2013, **42**, 13698–13705.
22 M. Vinu, W. C. Lin, D. S. Raja, J. L. Han and C. H. Lin, *Polymers*, 2017, **9**, 498–509.
23 J. Ge, L. Liu, L. Qiu, X. Jiang and Y. Shen, *J. Porous Mater.*, 2016, **23**, 857–865.
24 J. Gascon, U. Aktay, M. D. Hernandez-Alonso, G. P. M. van Klink and F. Kapteijn, *J. Catal.*, 2009, **261**, 75–87.
25 S. Couck, J. F. M. Denayer, G. V. Baron, T. Rémy, J. Gascon and F. Kapteijn, *J. Am. Chem. Soc.*, 2009, **131**, 6326–6327.
26 J. Gascon, E. Stavitski, J. Denayer, B. M. Weckhuysen, E. J. M. Hensen, E. A. Pidko, S. Couck, T. Remy and F. Kapteijn, *Langmuir*, 2011, **27**, 3970–3976.
27 M. Sánchez-Sánchez, N. Getachew, K. Díaz, M. Díaz-García, Y. Chebude and I. Díaz, *Green Chem.*, 2015, **17**, 1500.
28 F. Taulelle, C. Volkringer, G. Férey, N. Audebrand, M. Haouas, T. Loiseau, M. Burghammer, I. Margiolaki, C. Riekel, D. Popov and N. Guillou, *Cryst. Growth Des.*, 2009, **9**, 2927–2936.
29 C. Volkringer, T. Loiseau, M. Haouas, F. Taulelle, D. Popov, M. Burghammer, C. Riekel, C. Zlotea, F. Cuevas, M. Latroche, D. Phanon, C. Knöfelv, P. L. Llewellyn and G. Férey, *Chem. Mater.*, 2009, **21**, 5783–5791.
30 R. Ou, H. Zhang, J. Wei, S. Kim, L. Wan, N. S. Nguyen, Y. Hu, X. Zhang, G. P. Simon and H. Wang, *Adv. Mater.*, 2018, **30**, 1802767.

31 S. Chen, S. Mukherjee, B. E. G. Lucier, Y. Guo, Y. T. A. Wong, V. V. Terskikh, M. J. Zaworotko and Y. Huang, *J. Am. Chem. Soc.*, 2019, **141**, 14257–14271.
32 S. Chen, B. E. G. Lucier, W. Luo, X. Xie, K. Feng, H. Chan, V. V. Terskikh, X. Sun, T. K. Sham, M. S. Workentin and Y. Huang, *ACS Appl. Mater. Interfaces*, 2018, **10**, 30296–30305.
33 J. N. Hao and B. Yan, *J. Mater. Chem. A*, 2014, **2**, 18018–18025.
34 A. J. Howarth, Y. Liu, P. Li, Z. Li, T. C. Wang, J. T. Hupp and O. K. Farha, *Nat. Rev. Mater.*, 2016, **1**, 1–15.
35 N. C. Burtch, H. Jasuja and K. S. Walton, *Chem. Rev.*, 2014, **114**, 10575–10612.
36 B. S. Gelfand and G. K. H. Shimizu, *Dalton Trans.*, 2016, **45**, 3668–3678.
37 Z. Wang, A. Bilegsaikhan, R. T. Jerozal, T. A. Pitt and P. J. Milner, *ACS Appl. Mater. Interfaces*, 2021, **13**, 17517–17531.
38 N. U. Qadir, S. A. M. Said and H. M. Bahaidarah, *Microporous Mesoporous Mater.*, 2015, **201**, 61–90.
39 C. Wang, X. Liu, N. Keser Demir, J. P. Chen and K. Li, *Chem. Soc. Rev.*, 2016, **45**, 5107–5134.
40 M. Bosch, M. Zhang and H.-C. Zhou, *Adv. Chem.*, 2014, 182327.
41 J. J. Low, A. I. Benin, P. Jakubczak, J. F. Abrahamian, S. A. Faheem and R. R. Willis, *J. Am. Chem. Soc.*, 2009, **131**, 15834–15842.
42 X. Qian, B. Yadian, R. Wu, Y. Long, K. Zhou, B. Zhu and Y. Huang, *Int. J. Hydrogen Energy*, 2013, **38**, 16710–16715.
43 G. R. Xu, Z. H. An, K. Xu, Q. Liu, R. Das and H. L. Zhao, *Coord. Chem. Rev.*, 2021, **427**, 213554.
44 Y. Wu, H. Pang, Y. Liu, X. Wang, S. Yu, D. Fu, J. Chen and X. Wang, *Environ. Pollut.*, 2019, **246**, 608–620.
45 J. Wen, Y. Fang and G. Zeng, *Chemosphere*, 2018, **201**, 627–643.
46 Q. Gao, J. Xu and X. H. Bu, *Coord. Chem. Rev.*, 2019, **378**, 17–31.
47 M. Feng, P. Zhang, H. C. Zhou and V. K. Sharma, *Chemosphere*, 2018, **209**, 783–800.
48 K. S. W. Sing, *Pure Appl. Chem.*, 1982, **54**, 2201–2218.
49 A. Taheri, E. G. Babakhani and J. Towfighi, *Adsorpt. Sci. Technol.*, 2018, **36**, 247–269.
50 S. Brunauer, P. H. Emmett and E. Teller, *J. Am.Chem.Soc.*, 1938, **60**, 309–319.
51 S. Bauer, C. Serre, T. Devic, P. Horcajada, J. Marrot, G. Férey and N. Stock, *Inorg. Chem.*, 2008, **47**, 7568–7576.
52 E. Stavitski, E. A. Pidko, S. Couck, T. Remy, E. J. M. Hensen, B. M. Weckhuysen, J. Denayer, J. Gascon and F. Kapteijn, *Langmuir*, 2011, **27**, 3970–3976.
53 S. Couck, E. Gobechiya, C. E. A. Kirschhock, P. Serra-Crespo, J. Juan-Alcañiz, A. Martinez Joaristi, E. Stavitski, J. Gascon, F. Kapteijn, G. V. Baron and J. F. M. Denayer, *ChemSusChem*, 2012, **5**, 740–750.
54 S. Couck, J. F. M. Denayer, G. V. Baron, T. Rémy, J. Gascon and F. Kapteijn, *J. Am. Chem. Soc.*, 2009, **131**, 6326–6327.
55 Y. Peng, H. Huang, Y. Zhang, C. Kang, S. Chen, L. Song, D. Liu and C. Zhong, *Nat. Commun.*, 2018, **9**, 187.

4 Chapter Four: Synthesis of Naphthalene Diimide Metal or Hydrogen Organic Frameworks

4.1 Background

4.1.1 Naphthalene diimides

1,4,5,8-naphthalenediimides (NDIs) are a class of aromatic compounds that possess an electron deficient and redox-active core (see Scheme 4.1). They have a rigid, linear structure, which can be defined as a "end-core-end" type ligand, which makes them ideal candidates to be used as linkers in MOFs.[1,2] NDIs can be functionalised *via* core substitution (substitution on the naphthalene core) and through the diimide nitrogen (shown in red in Scheme 4.1), allowing their properties to be tuned. Core substitution specifically leads to variation in the absorption and fluorescence properties of the NDI, giving highly colourful and conductive compounds.[3] Functionalisation at the imide position has little effect on the optical and electrochemical properties but a wide variety of different groups can be added with a view to enhancing solubility or allowing for further chemistry to take place, such as coordination.[2,4]

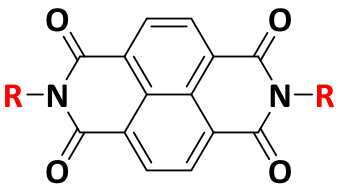

Scheme 4.1 – Structure of a NDI, with the red "R" group indicating that functionalisation through the imide nitrogen can occur.

NDIs undergo single reversible one-electron reduction, *via* chemical or electrochemical means, at modest potentials (NDI: E^1_{red} = -1.10 vs. Fc/Fc^+ in CH_2Cl_2) to form stable radical anions in high yield.[5] These radical anions can be detected by intense and characteristic visible and to near-infrared adsorption bands, occurring at longer wavelength that the parent NDI; the non-functionalised NDI radical anion ($NDI^{\bullet-}$) absorbs in the visible and NIR region, with maxima at 470, 610, 700 and 780 nm.[6] Strong and highly structured signals are also present in their EPR spectra.[1] Their interesting redox chemistry and facile functionalisation has led to NDIs being widely utilised in applications such as artificial photosynthesis,[7,8] n-type semiconductors,[9,10] as well as many supramolecular self-assembled structures.[11,12]

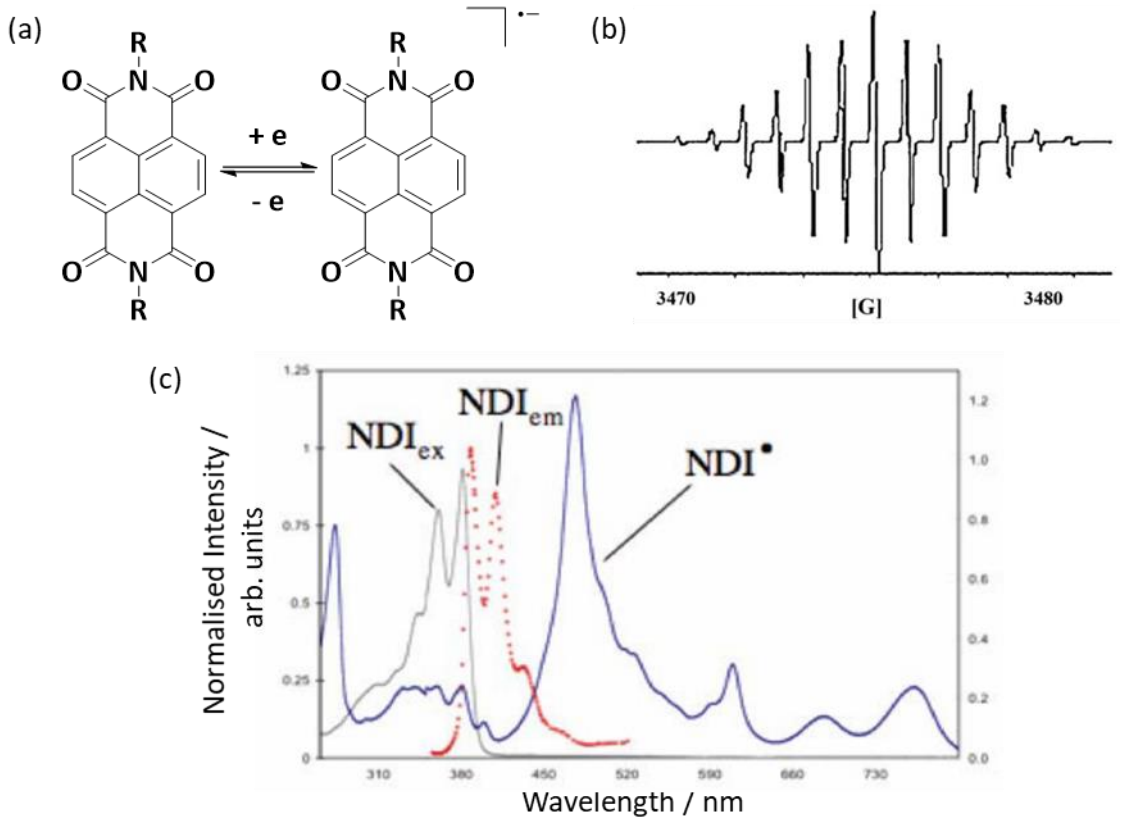

Figure 4.1 - (a) Bulk electron reduction of NDIs lead to high yields of the corresponding radical anion. (b) The electron paramagnetic resonance spectrum of the radical anion of *N,N'*-dipentyl-NDI in DMF solution shows excellent structure consistent with coupling between the unpaired electron and the naphthalene diimide nitrogen's and hydrogen's and the NCH hydrogens of the appropriate side chains. (c) Characteristic absorption (grey) and emission spectra (red, normalised, λ_{ex} = 348 nm) for *N,N'*-dipentyl-NDI in DCM are obtained as well as the absorption spectrum for the radical anion of *N,N'*-dipentyl-NDI (blue) generated by electrochemical reduction. Near-infrared (NIR) absorption bands aid in the unambiguous identification of NDI radical anions. Adapted with permission from *Chem. Soc. Rev.*, 2008, **37,** 331–342, Copyright (2008) RSC.[1]

Due to the planar, aromatic nature of their core, NDIs have the tendency to form aggregates through π-π stacking. Although this often leads to the NDIs having limited solubility, it can provide interesting properties as π electrons can delocalise along the stacks.[1] Having said this, incorporating an NDI into a supramolecular structure allows the characteristics of the NDI to be both controlled and utilised. Here, the focus will be placed on examples where NDIs are combined with metals to form NDI-containing MOFs.

4.1.2 Naphthalene diimide metal organic frameworks

In 2005, Hupp *et al.* synthesised one of the first examples of an NDI-containing MOF. A mixed linker paddle-wheel Zn MOF was formed with *N,N'*-di(4-pyridyl)-1,4,5,8-naphthalenetetracarboxydiimide and 2,6-naphthalene dicarboxylic acid or 1,4-biphenyldicarboxylic acid (Figure 4.2).[13] The MOF was reducible by lithium naphthalenide (in

THF) and exhibited a colour change from yellow to dark green/brown on this reduction. Although no further studies were conducted, they highlighted the prospect that the reduction of these materials could yield interesting conductive properties.

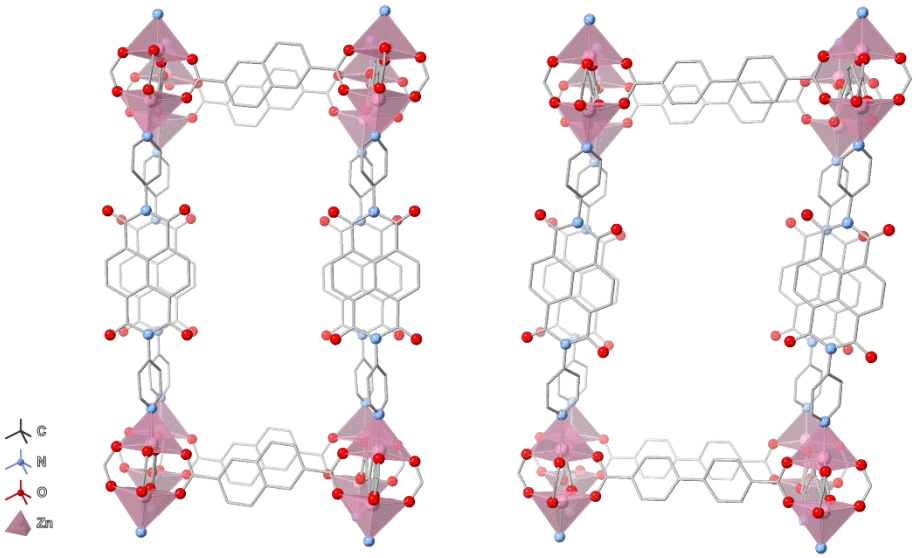

Figure 4.2 - Single units that form the pillared frameworks of the Zn MOFs in work by Hupp et al.[13] Left (CSD code = MATVAF) linkers are *N,N'*-di(4-pyridyl)-NDI and 2,6-naphthalene dicarboxylic acid. Right (CSD code = MATVEJ): linkers are *N,N'*-di(4-pyridyl)-NDI and 1,4-biphenyldicarboxylic acid.

Since, a wide range of NDIs have been combined with a variety of metal ions to form NDI MOFs that possess interesting characteristics. NDI MOFs have found application in photochromism,[14–16] electrochromism,[17–20] catalysis,[21–24] gas storage and separation,[25–28] and energy storage and conversion.[29–31] Due to the focus on synthesising stable MOFs in this thesis, the following section will discuss MOFs that contain Group 4 metals or NDIs functionalised with carboxylate groups that could coordinate to Group 4 metals (Scheme 4.2).

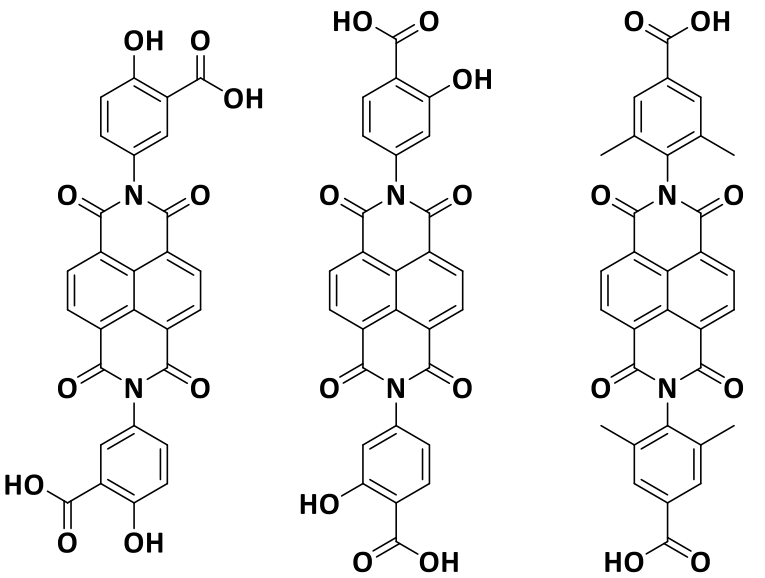

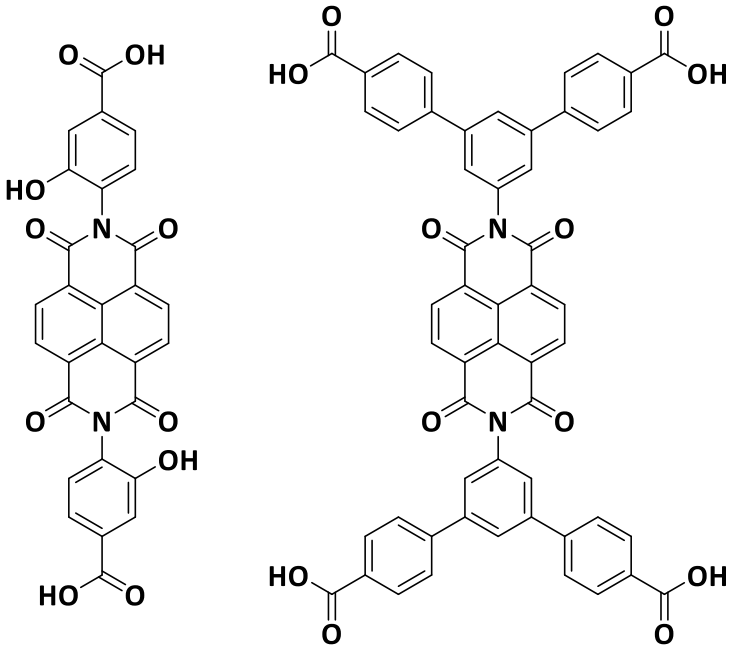

Scheme 4.2 - Carboxylate functionalised NDIs, synthesised to used MOFs, as described below.

4.1.2.1 MOFs formed from salicylic naphthalene diimide (SA-NDI)

Salicylic naphthalene diimide (SA-NDI) has been used as a linker in Ni(II) and Mg(II) MOFs that possess a MOF-74 type structure (Figure 4.3), with the formula $M_2(SA\text{-}NDI)_2$.[32] MOF-74 possesses a honeycomb-type structure with both carboxyl and hydroxyl groups coordinating to Group 2 metals. The metals form helical rods of edge-sharing MO_6 octahedra which are bonded to 3 carboxyl groups and two bridging hydroxyl groups, with one open metal site. The

Ni(II) and Mg(II) SA-NDI MOFs were synthesised *via* a solvothermal reaction of SA-NDI with Ni(II) or Mg(II) nitrate salts in a DMF/EtOH/H_2O mixture at 120 °C for 24 hours. Their structures were determined by PXRD analysis.

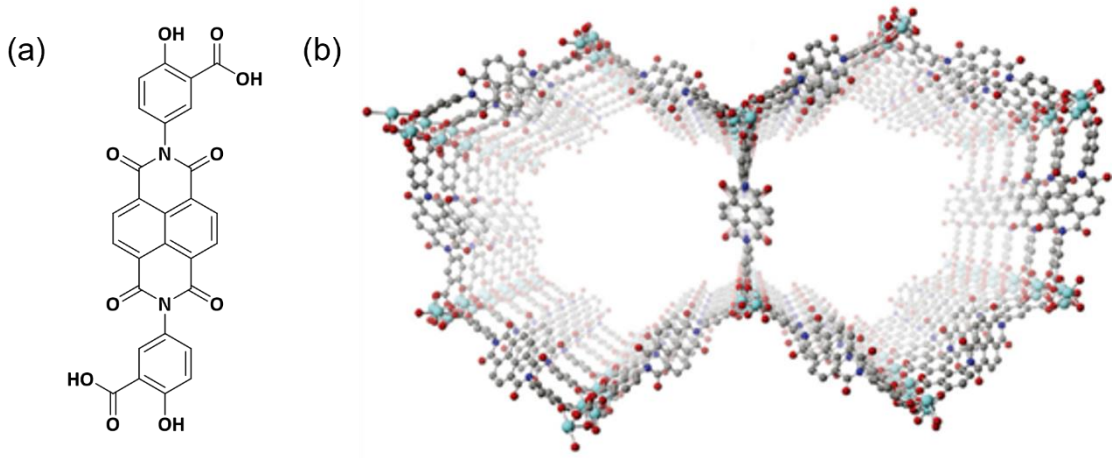

Figure 4.3 – a) Structure of SA-NDI, b) Structure of M_2(SA-NDI) where M = Ni, Mg (teal) and N, O, and C are shown in blue, red, and grey, respectively.[32] Reprinted with permission from *Chem 1*, 264–272. Copyright (2016) Elsevier Inc.

Thin films of the two MOFs were produced by deposition onto on fluorine-doped tin oxide. The thin films were shown to undergo two reversible one-electron reductions, accompanied by a colour change from the transparent to dark (Figure 4.4). This process was shown to be reversible for Ni-SA-NDI and occurred in as little as 7s.

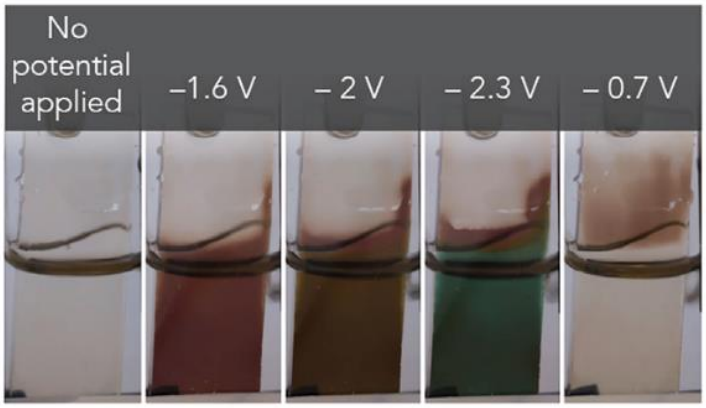

Figure 4.4 - Images of reversible colour switching of Ni-NDISA films at several reducing potentials (–1.6, –2, and -2.3 V versus Fc/Fc+). Reprinted with permission from *Chem 1*, 264–272. Copyright (2016) Elsevier Inc.

Thin films of Ni SA-NDI have also been applied to fluorine detection. The MOF exhibits a colour change from red/orange to black on exposure to tetra-n-butylammonium fluoride (TBAF) in

solutions of DMF, DMSO or a DMSO/H_2O mix. The colour change occurs in the presence of F^- ions but not Cl^-, Br^- or I^- ions.[33]

Furthermore, the porosity of Ni(II), Co(II), Mg(II) and Zn(II) SA-NDI MOFs has been improved by carrying out polymerisation of dopamine to polydopamine (PDA) inside the pores of the MOF. The presence of the polymer inside the MOF effectively holds the pores of the MOF open, significantly increasing the surface areas of the MOF composites, compared with non-functionalised MOFs.[23]

A similar NDI (DS-NDI), in which the carboxyl and hydroxyl group positions are exchanged (see Scheme 4.2) has also been used in the synthesis of MOF-74 -type structures. Firstly, tetrathiafulvalene (TTF) was π-intercalated between the stacks of NDI ligands in a Zn NDI MOF, to lower the band gap of the material. The electrical conductivity of the material was expected to improve due to improved electron delocalisation through the π-donor/acceptor stacks that are formed from the intercalation process.[34] More recently, the same Zn DS-NDI MOF showed improved CO_2 binding when reduced due to enhanced host-guest interactions.[25]

4.1.2.2 Zr NDI MOFs

With a view to creating an NDI MOF that exhibits high thermal and chemical stability Wasielewski *et al.* synthesised a UiO-type MOF, utilising the Zr_6-based cluster with *N,N*-bis(2,6-dimethyl-4-benzoic acid)-NDI (DM-NDI) as the linker; the methyl groups are said to enhance the solubility of the linker to aid MOF formation (Figure 4.5).[35] The MOF was made *via* solvothermal synthesis, DM-NDI was combined with $ZrCl_4$ in DMF with TFA added as a modulator. The mixture was then heated at 100 °C for 48 hours and the structure of the powder product was determined by PXRD.

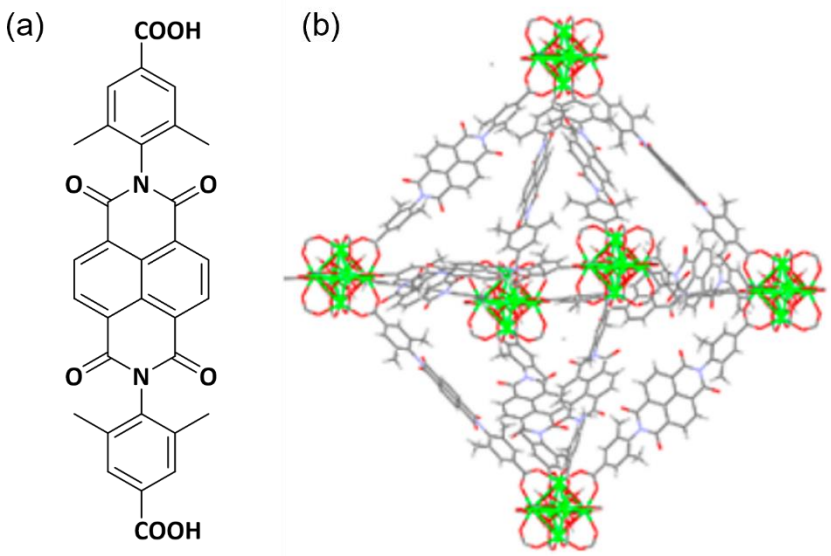

Figure 4.5– a) Structure of DM-NDI, b) Structure of UiO-NDI where Zr = green, O = red, N = blue, C = grey.[35] Adapted with permission from Chem. Mater. 2018, 30, 2488−2492. Copyright 2018 American Chemical Society.

The reduced MOF (UiO-NDI$^{\bullet-}$) was shown to exhibited strong photoreducing power, reducing CH_2Cl_2 to the $^{\bullet}CH_2Cl$ radical on irradiation with 480 nm in the presence of *N*-tert-butyl-α-phenylnitrone (PBN). PBN acts as a "spin-trapping" agent; it reacts with a species that has a short-lived excited state to form a radical with a longer lifetime. Without the trapping agent, the excited state of the MOF was deactivated, likely *via* intermolecular interactions.

A theoretical study has been carried out on this UiO-NDI MOF, to determine how functionalisation at different positions on the NDI and substitution of the metal centre changes the structural and electronic properties of the NDI MOFs.[36] Functionalisation *via* the addition of by NH_2, Br, Cl, CH_3 and OH on different parts of the NDI was considered. It was predicted that through functionalisation of the NDI, the band levels and band gaps of the MOF can be tailored and that many of the structures containing Zr-, Ti-, Th- and Ce-clusters would have suitable optical band gaps to induce H_2O or CO_2 splitting.[36] Further to this, it was suggested that in Ti- or Ce-containing UiO-NDI MOFs, the metal node-based bands are lowered in energy, which suggests potential for ligand to metal charge transfer to occur.[36]

Another Zr UiO-type NDI MOF has been synthesised using dcphOH-NDI as the linker. The extra hydroxyl group on the NDI was carefully chosen with hopes that would improve the proton transport capabilities of the MOF (Figure 4.6). The MOF powder was synthesised in DMF at 120°C, with acetic acid as the modulator, and the UiO-type structure was confirmed by PXRD. The MOF was successfully grown on an FTO thin film and exhibited reversible electrochromic

behaviour where 97% of the NDI sites were active due to efficient charge propagation through the NDIs.[37]

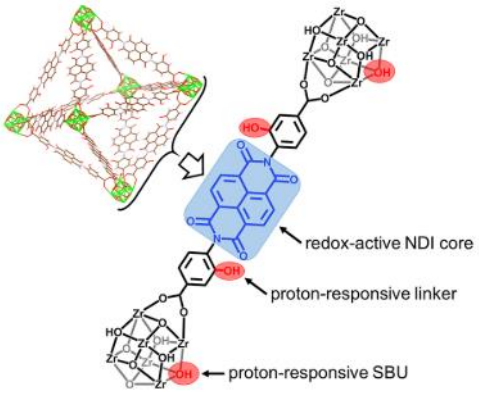

Figure 4.6 - MOF design strategy for developing a redox-active framework featuring UiO topology with proton-responsive functionalities. Reproduced with permission from J. Am. Chem. Soc. 2018, 140, 2985−2994, Copyright 2018 American Chemical Society.[37]

A final example of a Zr NDI MOF is one where *N,N'*-bis(terphenyl-4,4''-dicarboxylic acid)naphthalenediimide (H_4BTD-NDI) has been used as a linker, coordinated to a $[Zr_6O_8(H_2O)_8]^{8+}$ cluster.[29] Single crystals of the MOF were obtained *via* solvothermal reaction of $ZrCl_4$ with the linker in DMF and 2-fluorobenzoic[iii] and formic acid. The authors noticed that this MOF was flexible in the crystallographic *a* and *b* directions, limiting its performance as a supercapacitor, so they added 2,2'-bipyridine-5,5'-dicarboxylic acid as a pillar ligand to increase the MOFs rigidity in the *b* direction. This addition increased both the surface area of the MOF and increased the capacitance performance of the MOF.

[iii] Note that the SI of this paper states that F-BzA was used in the synthesis of the MOF but does not define this elsewhere in the paper or SI. It is assumed that this is 2-fluorobenzoic acid as this is used elsewhere as a modulator.

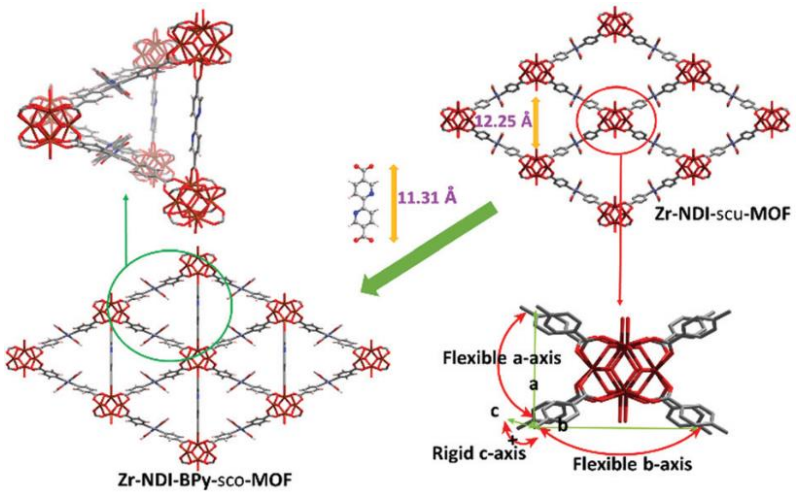

Figure 4.7 - Schematic representation of the synthesis of Zr-NDI-BPy-**sco**- MOF via insertion of the 2,2'-bipyridine-5,5'-dicarboxylic acid pillar along the a-axes of Zr-NDI-**scu**-MOF.[29] Republished with permission from *Chem. Commun.*, 2020, **56**, 1883, Copyright 2020 Royal Society of Chemistry.

4.1.2.3 Ti NDI MOFs

In Chapter 1, the interesting properties of Ti MOFs were introduced, including their chemical and thermal stability, and their excellent photocatalytic activity. The theoretical potential of NDI containing Ti MOFs was highlighted in the study described above, where Cramer *et al.* found that incorporating Ti clusters into a UiO-type NDI MOF could create a material capable of catalysing H_2O or CO_2 splitting.[36]

To the best of my knowledge, there are no reports of Ti NDI MOFs in the literature, which is likely due to the general challenges of synthesising Ti MOFs because of the strong, barely labile Ti-O bond that forms and prevents the formation of the MOF structure. Many NDIs are also poorly soluble in many organic solvents, which again increases the difficulty of NDI MOF synthesis, let alone synthesis of crystalline Ti NDI materials. Having said this, there are a few examples of Ti MOF synthesis, addressed below, that could help to inform approaches to the synthesis of a Ti NDI MOF.

Previously, the synthesis of porphyrin-containing Ti MOFs (PCN-222 and DGIST-1) was described (see Section 1.2.2, Chapter 1), where a Ti containing cluster, $Ti_6O_6(O^iPr)_6(abz)_6$ (abz = 4-aminobenzoate) was used as the starting material, allowing reversible bond association/dissociation to occur and therefore facilitating the formation of single crystals.[38,39] The same cluster has also been used to form Ti MOFs *via* a covalent reaction with

benzene-1,4-dialdehyde (BDA).[40] MOF-901 (Figure 4.8) was synthesised using a one-pot approach in which the $Ti_6O_6(O^iPr)_6(abz)_6$ was formed *in situ* from 4-aminobenzoic acid and $Ti(O^iPr)_4$, and then linked together with BDA in an imine condensation to form a MOF with **hxl** topology.

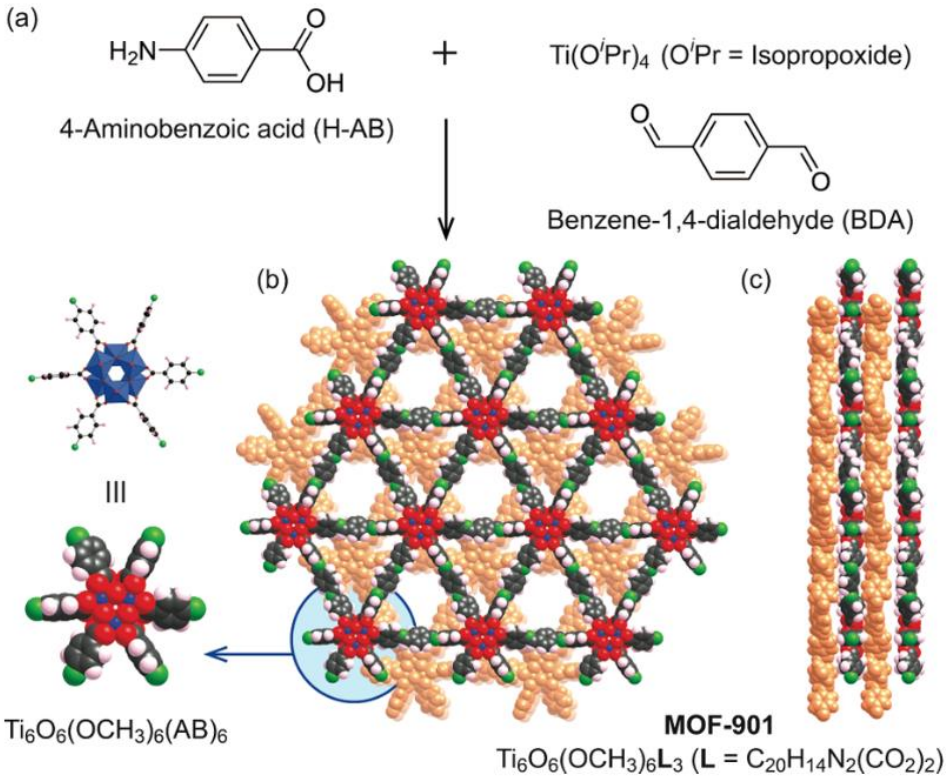

Figure 4.8 – a) *in situ* formation of hexameric Ti(IV) oxo cluster, with cluster shown in the inset to the left of b) the crystal structure of MOF-901 along the *c*-axis and c) *a*-axis. Reprinted with permission from *J. Am. Chem. Soc.,* 2016, **138**, 13, 4330–4333. Copyright 2016 American Chemical Society.[40]

This one-pot approach has been used elsewhere to form Zr NDI MOFs. $ZrOCl_2{\cdot}8H_2O$ can be combined with 1,4,5,8-tetracarboxylic dianhydride and 4-aminobenzoic acid in DMF and acetic acid, forming the Zr_6 cluster and imide bond in one step to create a two-fold interpenetrated network with **ftw** topology, containing an NDI (Figure 4.9).[41]

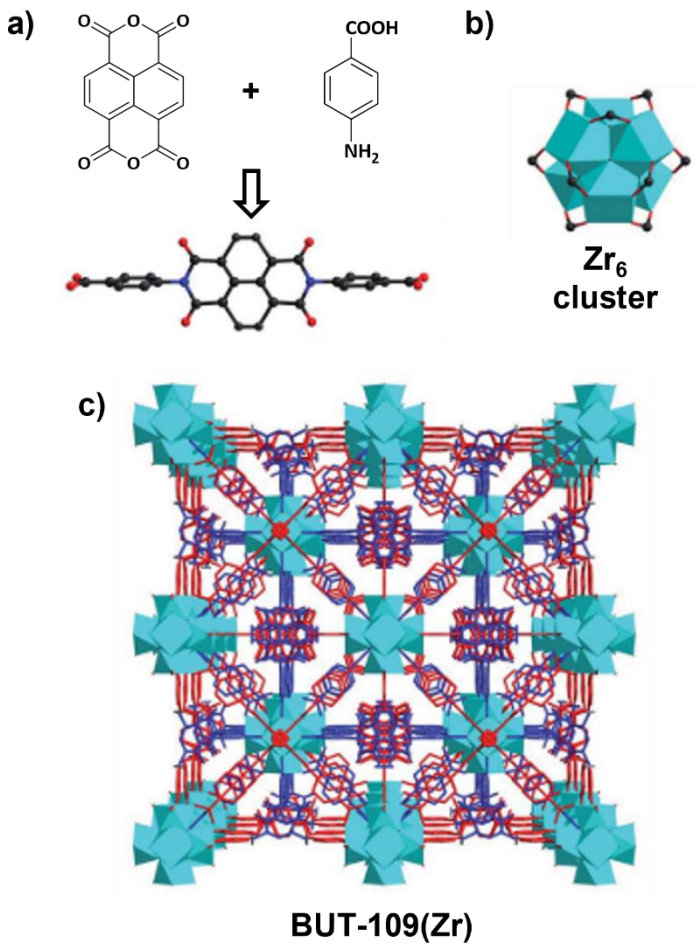

Figure 4.9 – a) *In situ* formation of NDI from 1,4,5,8-tetracarboxylic dianhydride and 4-aminobenzoic acid, b) Zr_6 cluster in c) BUT-109(Zr). Adapted with permission from *Chem. Sci*.,2019, **10**, 3949–3955. Copyright 2019 the Royal Society of Chemistry.[41]

4.2 Aims

The background material presented here demonstrates that NDI containing MOFs exhibit a range of interesting properties that allows them to be applied in fields such as gas adsorption, photocatalysis, electrochromism and energy storage and conversion.[42] Despite this, there are limited reports of stable NDI MOFs, with only a handful of Group 4 NDI MOFs being reported. In addition, these MOFs often lack crystallinity and structure solution is often carried out *via* PXRD, rather than analysis of single crystals.

As the thermal and chemical stability of MOFs is vital for their use in industrial applications such as sensing or in supercapacitors, this work seeks to expand the range of Group 4 NDI MOFs. The synthesis of these materials is challenging and techniques to combat these

challenges are described, such as modulation or the use of pre-formed clusters and covalent chemistry.

Salicylic naphthalene diimide (SA-NDI) and dimethyl naphthalene diimide (DM-NDI) were chosen as linkers. As well as the potential applications for MOF using these linkers that have been discussed in Section 4.1.2, SA-NDI and DM-NDI contain oxygen containing end groups which are necessary for coordination to Group 4 metals. In addition, their syntheses have previously reported and are relatively straightforward.

4.3 Synthesis of Zr salicylic acid NDI MOFs

To be the best of my knowledge, there are currently no reports of Group 4 MOFs that contain salicylic naphthalene diimide (SA-NDI). As such, the aim was to synthesise a Zr MOFs using SA-NDI as a linker.

4.3.1 Naming conventions

In the following work, reaction conditions are scrupulously changed to carry out the synthesis of new crystalline materials. To make the identification of samples and the parameters used easier, a naming convention is applied. For example, a sample named SA-1:5-BA(40)-DMF/MeCN(120) denotes an experiments where a 1:5 ratio of metal to linker was used, with 40 equivalents of benzoic acid as a modulator, using a DMF/MeCN mix as the solvent at 120 °C. All reaction mixtures in this work were heated for three days, unless otherwise stated.

4.3.2 Synthesis of *N,N'*-Bis(3-carboxy-4-hydroxyphenyl)-1,4,5,8-naphthalenetetracarboxydiimide (SA-NDI)

The synthesis of *N,N'*-Bis(3-carboxy-4-hydroxyphenyl)-1,4,5,8-naphthalenetetracarboxy diimide (SA-NDI) was adapted from previous work (Scheme 4.3).[32] The reaction was carried out for 15 minutes, rather than overnight as reported in the literature, as even in this short time a large amount of brick red precipitate had formed.

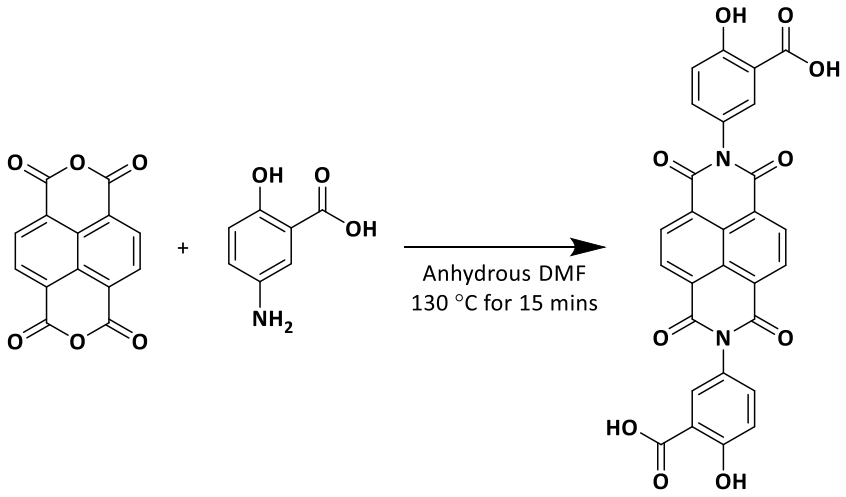

Scheme 4.3 - Synthesis of *N,N'*-Bis(3-carboxy-4-hydroxyphenyl)- 1,4,5,8-naphthalenetetracarboxydiimide (SA-NDI).

4.3.3 Initial attempts at synthesising a Zr-SA-NDI MOF

Although there are no reports of Zr MOFs containing SA-NDI, there are a several (approx. 10) reports of Zr, Hf and Ti MOFs that contain 2,5-dihydroxyterephthalic acid (H_4dobdc). Exploring the synthesis conditions used to make these MOFs is of interest as the linker has a similar arrangement of OH and COOH groups that are available for coordination to metal centres.[43–45] In one of these examples, the structure of Zr and Hf MOFs with the formula $(H_3O)_x[M(dobdc)(bz)_x]$ (M = Zr or Hf), bz = benzoate) were reported,[45] and the authors noted that "the discovery of the Zr-dobdc phase has been achieved only after painstaking control of the synthetic parameters of solvothermal reactions" and that crystals were only formed after hundreds of synthesis attempts. The structure possesses Zr_3 SBUs, each of which is bonded to six dobdc and three bz ligands. Three of the dobdc linkers connect with neighbouring Zr_3 SBUs to form a puckered layer with a six-membered ring in the *ab* plane, the other three dobdc connect in the c direction to create a 3D network (Figure 4.10).[45]

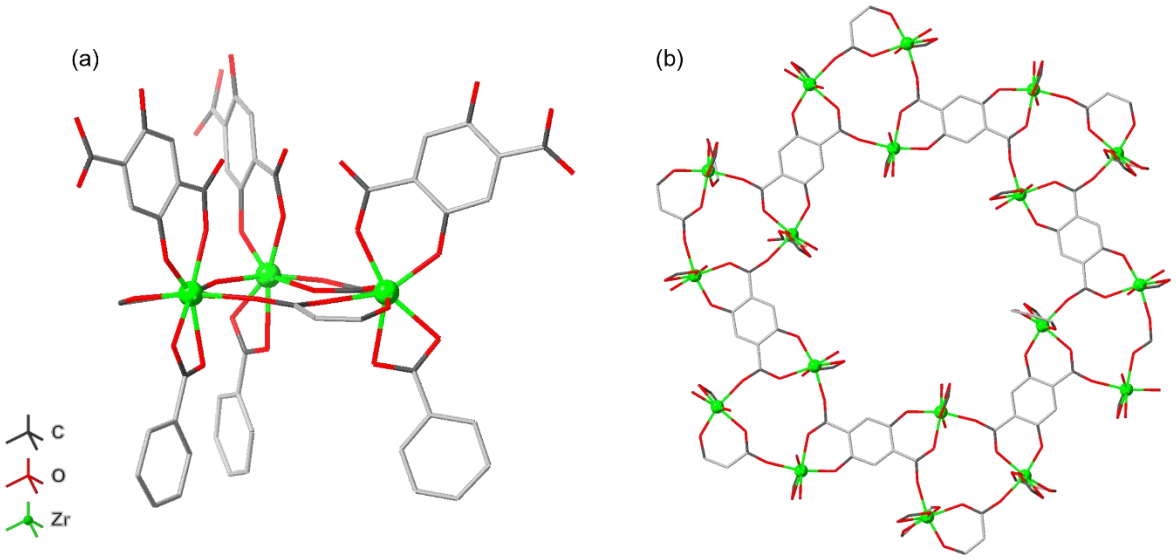

Figure 4.10 - Crystal structure of Zr-dobdc, (a) Trinuclear SBU showing (b) View of the 6-ring of Zr_3 SBU in the *ab* plane. CSD code = NAVPAE.[45]

$(H_3O)_x[Zr(dobdc)(bz)_x]$ was synthesised using a 1:4 ratio of metal to linker, a solvent mixture of DMF and MeCN, with benzoic acid (10 equivalents) as modulator. As such, the synthesis of a Zr-SA-NDI MOF was attempted using similar conditions.

One of the first attempts, SA-1:5-BA(40)-DMF/MeCN(120), using a 1:5 ratio of metal to linker in a DMF/MeCN solvent mixture and using benzoic acid (BA) as a modulator produced an orange-brown powder which shows some crystallinity by PXRD (blue curve,

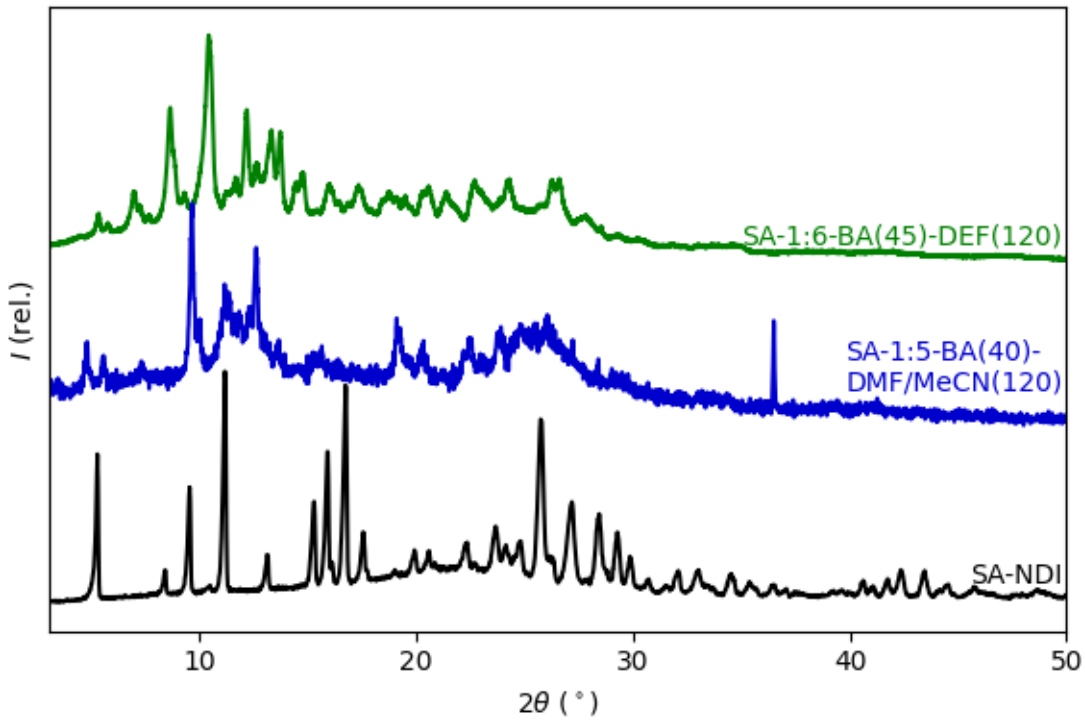

Figure 4.11). There are reflections present at low angle, which are not related to the SA-NDI linker, suggesting a new phase has been formed. Having said this, the peaks are quite broad, and the background is quite large, suggesting that the sample contains some amorphous material too.

Due to limited solubility of SA-NDI in DMF, a further reaction, SA-1:6-BA(45)-DEF(120), was conducted in DEF, which SA-NDI dissolves in much more readily, to see if this would yield a more crystalline material. The reaction produced an orange powder and the PXRD (green curve, Figure 4.11) shows a crystalline phase has been produced, which is different to that of SA-1:5-BA(40)-DMF/MeCN(120).

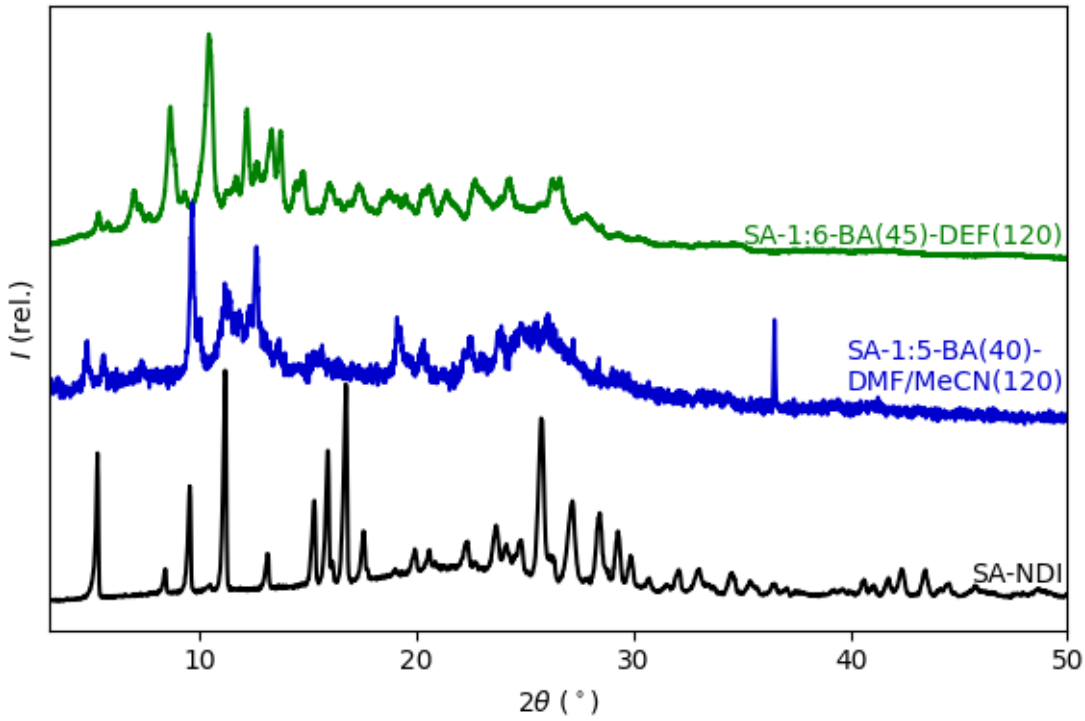

Figure 4.11 – PXRD of SA-NDI against the materials obtained in two attempted Zr-SA-NDI MOF syntheses. Conditions: SA-1:5-BA(40)-DMF/MeCN(120) = 1:5 metal to linker ratio, 40 equivalents of benzoic acid, DMF/MeCN solvent mix, 120°C, 72 hours, SA-1:6-BA(45)-DEF(120) = 1:6 metal to linker ratio, 45 equivalents of benzoic acid, DEF, 120°C, 72 hours.

Due to the success of these reactions, several sets of reactions were carried out using slightly different conditions, changing the metal to linker ratio, modulator, solvent, and reaction temperature, to see if a single crystal of a Zr-SA-NDI MOF could be formed to allow us to determine the crystal structure of the material(s) obtained in these reactions.

4.3.4 Varying the metal to linker to modulator ratio in Zr-SA-NDI MOF reactions with BA as a modulator

Firstly, a series of experiments were carried out, where the ratio was varied from 1:6 to 1:2, using DEF or DMF/MeCN as the solvent, to see if the metal to linker ratio made a difference to the crystallinity of the materials obtained. A reaction temperature of 100 °C was used, compared to 120 °C used in the two previous successful reactions, for comparison.

All of the reactions carried out in DMF/MeCN did not undergo any changes after heating for 72 hours at 100 °C; the brick red precipitate that was collected at the end of the reaction looked very similar in appearance to SA-NDI and the PXRD confirmed that the free, unreacted, linker was isolated from the reaction (reflection positions and intensities are very similar, Figure 4.12). This was attributed to the SA-NDI not dissolving in the DMF/MeCN solution at this lower temperature of 100 °C, and therefore was not able to react. Although SA-1:5-BA(40)-DMF/MeCN(100) (described in Section 4.3.3) gave a different phase to SA-1:6-BA(45)-DEF(120) and SA-1:6[or 4]-BA(20)-DMF/MeCN(120), the success of the reactions in DEF (described below), meant that reactions using a MeCN/DMF mix were discontinued.

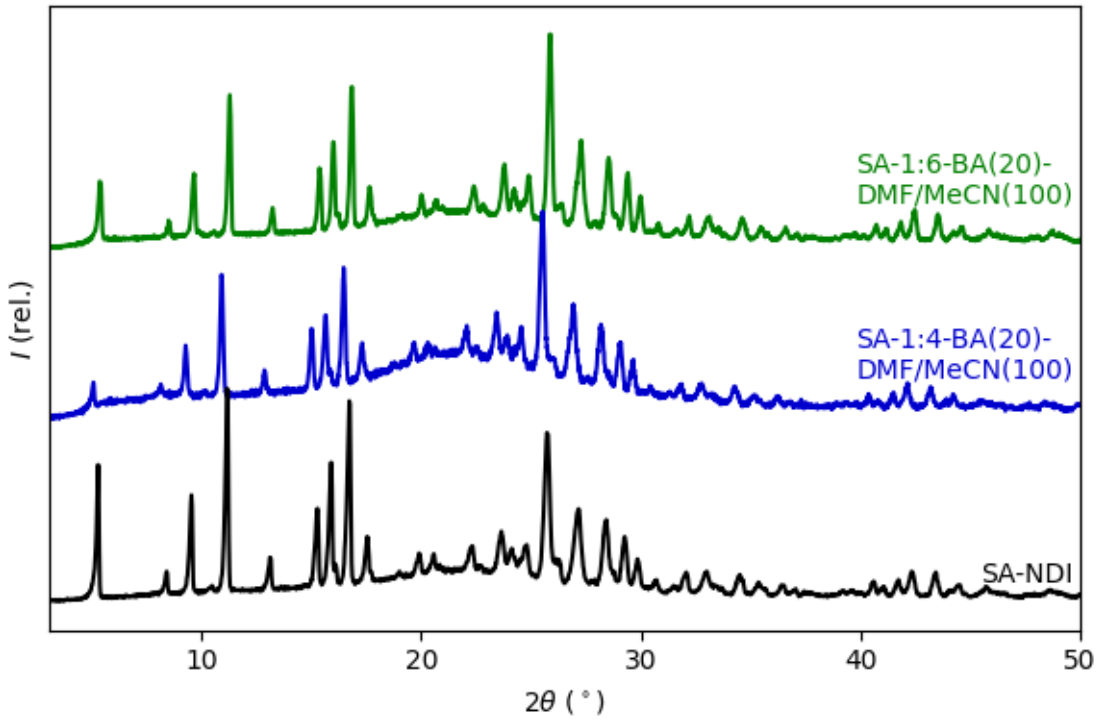

Figure 4.12 - PXRD of SA-NDI against the materials obtained in attempted Zr-SA-NDI MOF syntheses. Conditions: Blue = SA-1:4-BA(20)-DMF/MeCN(100) = 1:4 metal to linker ratio, 20 equivalents of benzoic acid, DMF/MeCN solvent mix, 100°C, 72 hours, Green = SA-1:4-BA(20)-DMF/MeCN(100) = 1:6 metal to linker ratio, 20 equivalents of benzoic acid, DMF/MeCN solvent mix, 100°C, 72 hours.

Overall, reactions using DEF and 40 equivalents of BA showed that increasing the equivalents of linker used increases the crystallinity in the orange-brown powder obtained (Figure 4.13), with the PXRD of SA-1:6-BA(40)-DEF(100) and SA-1:5-BA(40)-DEF(100), showing sharp and intense peaks, with minimal background. No precipitate was obtained for SA-1:2-BA(40)-DEF(100) and the PXRD of SA-1:3-BA(40)-DEF(100) (red curve) indicates that the material contains a different phase that lacks crystallinity as there are no sharp, distinct reflections.

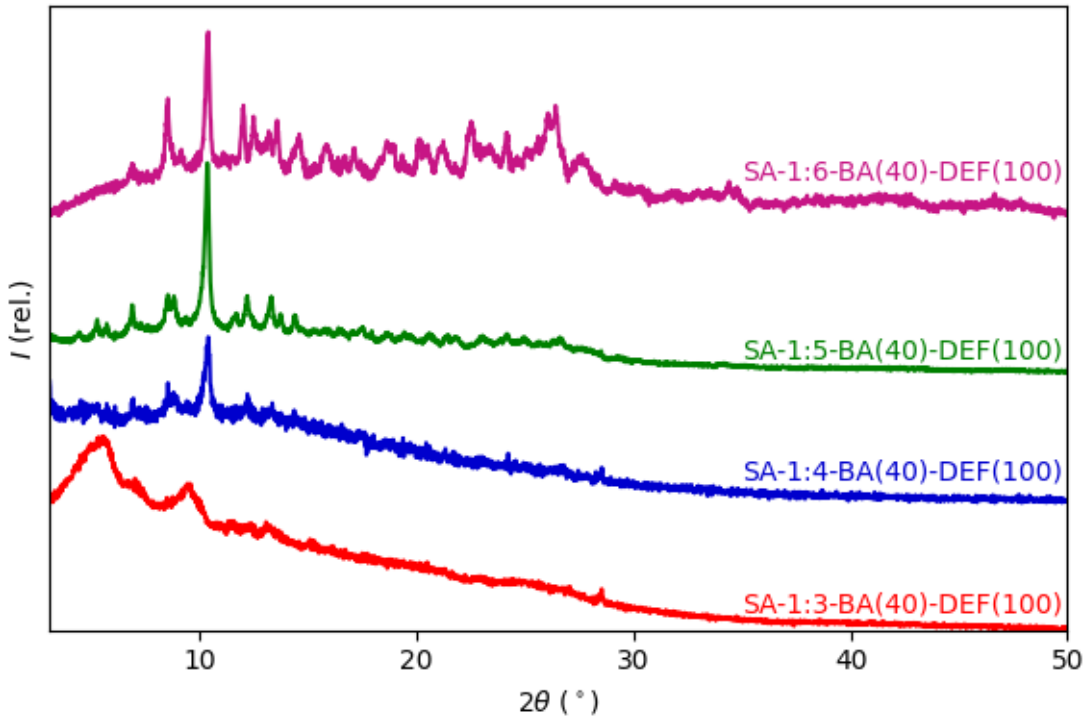

Figure 4.13 - PXRD of the materials obtained in attempted Zr-SA-NDI MOF syntheses. Conditions: Red = SA-1:3-BA(40)-DEF(100) = 1:3 metal to linker ratio, 40 equivalents of benzoic acid, DEF, 100°C, 72 hours, Blue = SA-1:4-BA(40)-DEF(100) = 1:4 metal to linker ratio, 40 equivalents of benzoic acid, DEF, 100°C, 72 hours, Green = SA-1:5-BA(40)-DEF(100) = 1:5 metal to linker ratio, 40 equivalents of benzoic acid, DEF, 100°C, 72 hours, Pink = SA-1:6-BA(40)-DEF(100) = 1:6 metal to linker ratio, 40 equivalents of benzoic acid, DEF, 100°C, 72 hours.

The same reaction set was carried out using 20 equivalents of BA instead of 40 (Figure 4.14). Overall, the orange-brown powders collected in these reactions were more crystalline than those obtained in the reactions carried out with 40 equivalents of BA, indicated by sharper and more intense reflections in their PXRD. Just like SA-1:2-BA(40)-DEF(100), SA-1:2-BA(20)-DEF(100), did not produce any solid product. SA-1:3-BA(20)-DEF(100) was a lot less crystalline than the others, although it does appear that the phase produced was the same as the other 20 equivalent reactions. SA-1:4-BA(20)-DEF(100), SA-1:5-BA(20)-DEF(100), and SA-1:6-BA(20)-DEF(100) possess similar crystallinity, with the SA-1:5-BA(20)-DEF(100) being slightly more crystalline (but this could be due to variation in sample preparation for PXRD).

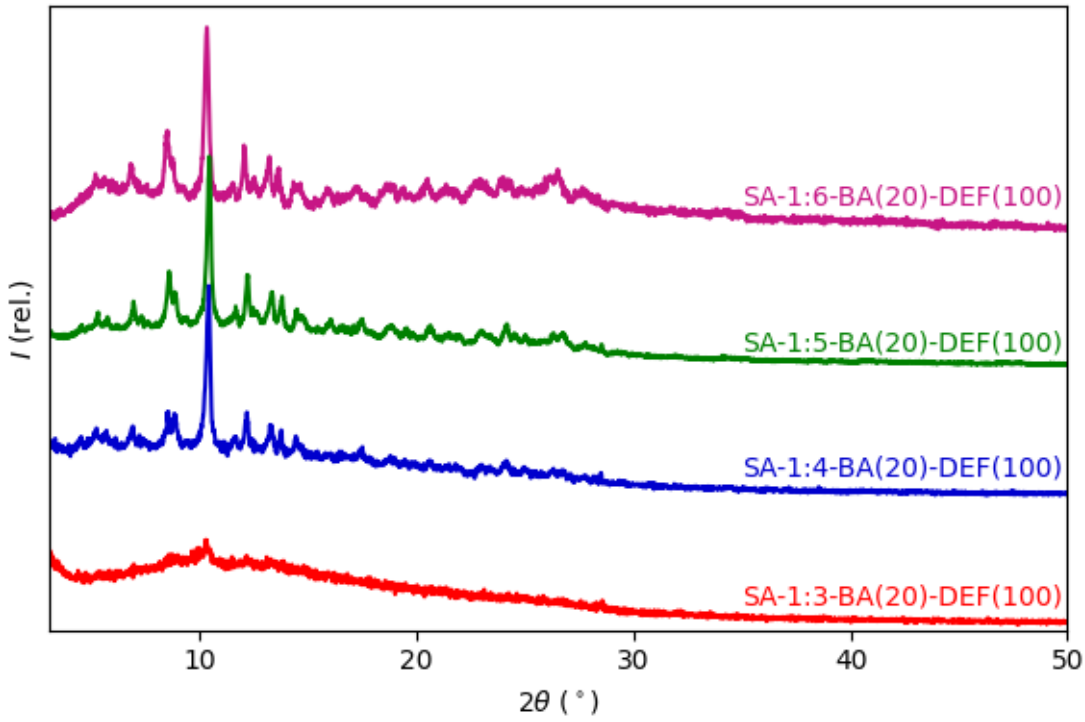

Figure 4.14 - PXRD of the materials obtained in attempted Zr-SA-NDI MOF syntheses. Conditions: Red = SA-1:3-BA(20)-DEF(100) = 1:3 metal to linker ratio, 20 equivalents of benzoic acid, DEF, 100°C, 72 hours, Blue = SA-1:4-BA(20)-DEF(100) = 1:4 metal to linker ratio, 20 equivalents of benzoic acid, DEF, 100°C, 72 hours, Green = SA-1:5-BA(20)-DEF(100) = 1:5 metal to linker ratio, 20 equivalents of benzoic acid, DEF, 100°C, 72 hours, Pink = SA-1:6-BA(20)-DEF(100) = 1:6 metal to linker ratio, 20 equivalents of benzoic acid, DEF, 100°C, 72 hours.

4.3.5 Varying the temperature of the Zr-SA-NDI MOF synthesis

To try to improve the crystallinity further, a set of experiments were carried out where the reaction temperature was varied (Figure 4.15). The conditions used for SA-1:6-BA(20)-DEF(100) were used as this had formed one of the most crystalline materials so far. SA-1:6-BA(20)-DEF(80) gave an amorphous yellow-orange powder and the SEM-EDX mapping of this sample suggested that this material contained no carbon, but did contain zirconium, oxygen and chlorine (Figure 4.16). This suggests that no reaction has occurred, and the material obtained is likely $ZrOCl_2$. The other reactions gave a dark red-brown precipitate, which show increased crystallinity as the temperature was increased up to 140°C. This crystallinity is indicated by well-defined reflections, and very little background which shows that there is little/no amorphous material present in the sample.

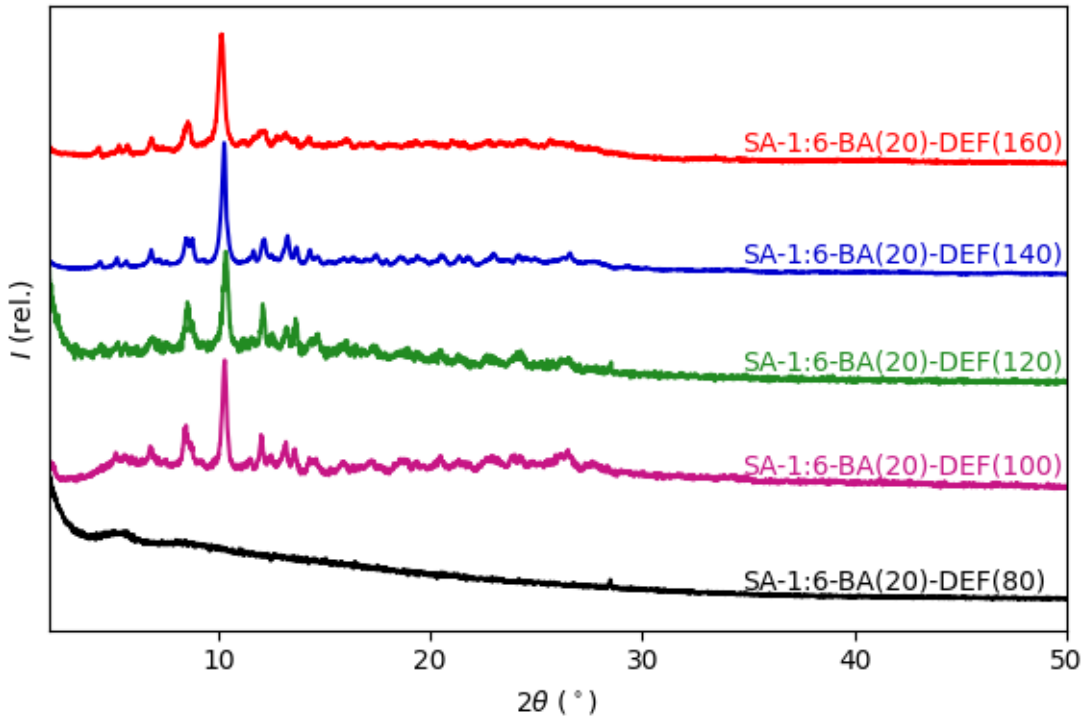

Figure 4.15 - PXRD of the materials obtained in attempted Zr-SA-NDI MOF syntheses. Conditions: Black = SA-1:6-BA(20)-DEF(80) = 1:6 metal to linker ratio, 20 equivalents of benzoic acid, DEF, 80°C, 72 hours, Pink= SA-1:6-BA(20)-DEF(100) = 1:6 metal to linker ratio, 20 equivalents of benzoic acid, DEF, 100°C, 72 hours, Green = SA-1:6-BA(20)-DEF(120) = 1:6 metal to linker ratio, 20 equivalents of benzoic acid, DEF, 120°C, 72 hours, Blue = SA-1:6-BA(20)-DEF(140) = 1:6 metal to linker ratio, 20 equivalents of benzoic acid, DEF, 140°C, 72 hours, Red = SA-1:6-BA(20)-DEF(160) = 1:6 metal to linker ratio, 20 equivalents of benzoic acid, DEF, 160°C, 72 hours.

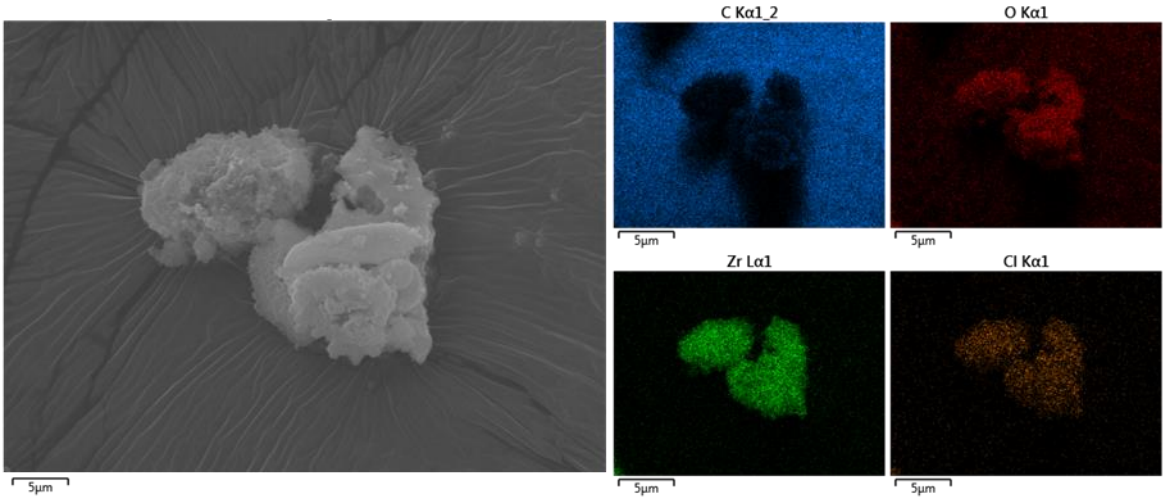

Figure 4.16 – SEM-EDX mapping of SA-1:6-BA(20)-DEF(80).

4.3.6 Varying the modulator of the Zr-SA-NDI MOF synthesis

To check that benzoic acid is the modulator that gives the most crystalline product in these MOF reactions, some reactions were carried out in the presence of alternative modulators: trifluoroacetic (TFA), salicylic (SA), formic (FA) and acetic (AA) acid. The conditions used to

produce SA-1:6-BA(20)-DEF(100) were once again chosen for this set of reactions (with the modulator being the only variable that was changed). It is clear from the PXRD patterns (Figure 4.17) that benzoic acid gives rise to the most crystalline product, with the sharpest reflections present in SA-1:6-BA(20)-DEF(100).

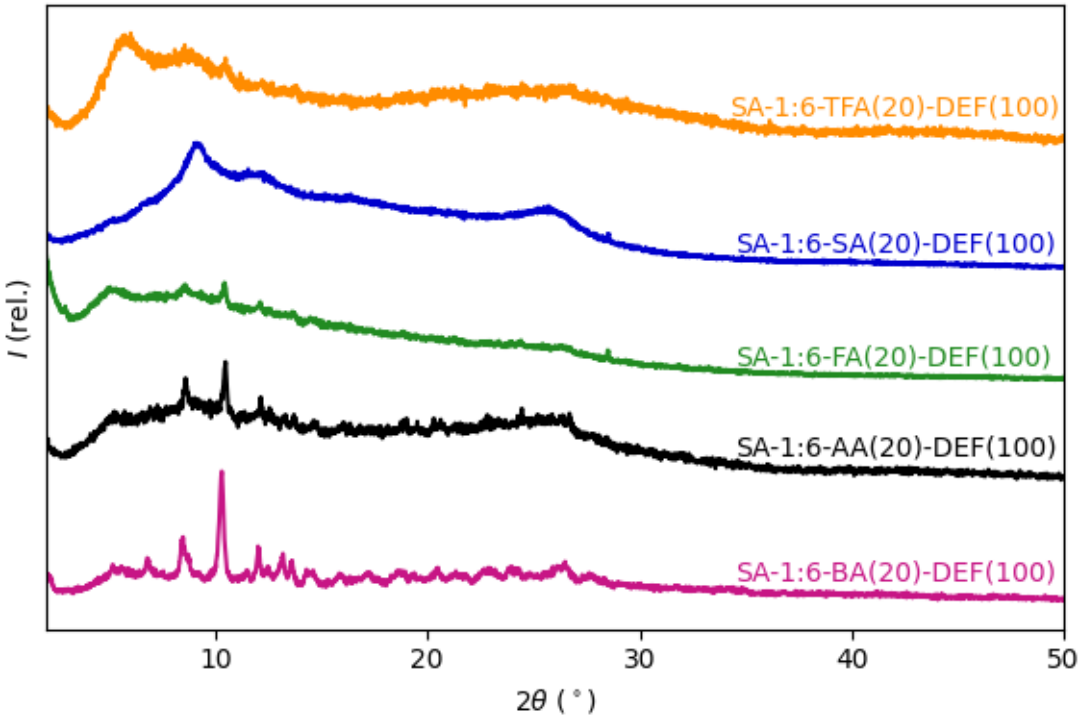

Figure 4.17 - PXRD of the materials obtained in attempted Zr-SA-NDI MOF syntheses. Conditions: Pink = SA-1:6-BA(20)-DEF(100) = 1:6 metal to linker ratio, 20 equivalents of benzoic acid, DEF, 100°C, 72 hours, Black = SA-1:6-AA(20)-DEF(100) = 1:6 metal to linker ratio, 20 equivalents of acetic acid, DEF, 100°C, 72 hours, Green = SA-1:6-FA(20)-DEF(100) = 1:6 metal to linker ratio, 20 equivalents of formic acid, DEF, 100°C, 72 hours, Blue = SA-1:6-SA(20)-DEF(100) = 1:6 metal to linker ratio, 20 equivalents of salicylic acid, DEF, 100°C, 72 hours, Orange = SA-1:6-TFA(20)-DEF(100) = 1:6 metal to linker ratio, 20 equivalents of trifluoroacetic acid, DEF, 100°C, 72 hours.

4.3.7 A single crystal Zr SA-NDI phase–Zr-SA-NDI-α

Whilst studying the reaction conditions used to make Zr SA-NDI MOFs, a reaction that used a 1:4 ratio of metal to linker, TFA (20 equivs) as the modulator with DEF as the solvent and was conducted at 100°C for 72 hours, gave small bright orange single crystals (Figure 4.18). This result was unfortunately anomalous, as repeating the reaction under the exact same conditions failed to give the same single crystal product. Nevertheless, these crystals were sent for analysis at Diamond Light Source (DLS) and a structure was obtained. Dr Stephen Argent and Dr Georgia Orton mounted the crystals and carried out the remote data collection.

They both, along with Dr Rosemary Young, assisted with the structure solution using Olex2, with Dr Argent carrying out the final refinements.

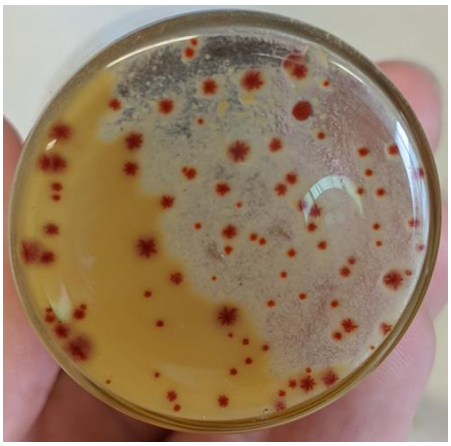

Figure 4.18 – An image of the product (Zr-SA-NDI-α) obtained in an attempted Zr SA-NDI reaction with the conditions: = 1:4 metal to linker ratio, 20 equivalents of trifluoroacetic acid, DEF, 100°C, 72 hours. Note that compared to the normal reaction regime, 4.5 mL of DEF was used instead of the 5 mL that was usually used, due to running out of solvent.

It is noted that the crystal structure solution for this material was challenging, so the interpretation of the refined solution should be confined to the gross features of the framework. Further details about the refinement can be found on the Appendix, Section 4.9.3.1.

The structure (Figure 4.19) consists of alternating ZrO_7 and ZrO_6 clusters. These clusters are joined by SA-NDI linkers that coordinate *via* the hydroxyl oxygen and one carboxylate oxygen (a, Figure 4.19). Every Zr has three SA-NDI moieties coordinated to it and every other Zr also has a DMF molecule coordinated to it. The ratio of linker to Zr in the structure is 3:2 so it is expected that the excess negative charge is balanced by the presence of diethyl ammonium fragments in the pores, although it was not possible to locate and refine these crystallographically. This coordination regime results in honeycomb-type structure where sheets of NDIs π-stack in the *b*-direction to form a 3D network (a and b, Figure 4.19). Each layer of the structure contains two parallel interdigitate sheets (Figure 4.20).

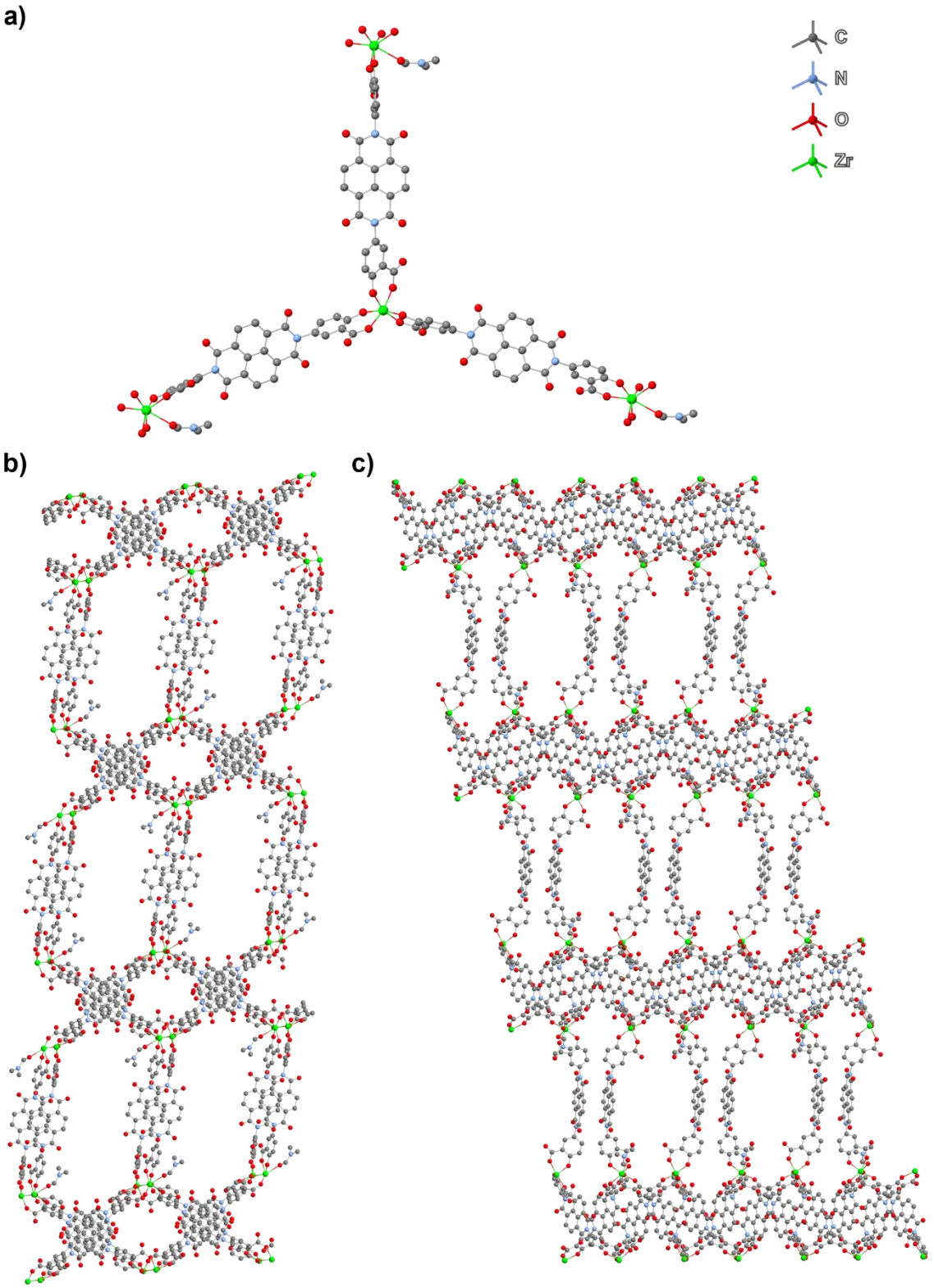

Figure 4.19 – Crystal structure of Zr-SA-NDI-α. a) Repeating unit of two six coordinate Zr atoms with three SA-NDI molecules, b) view along the *b*-axis and c) view along the *a*-axis.

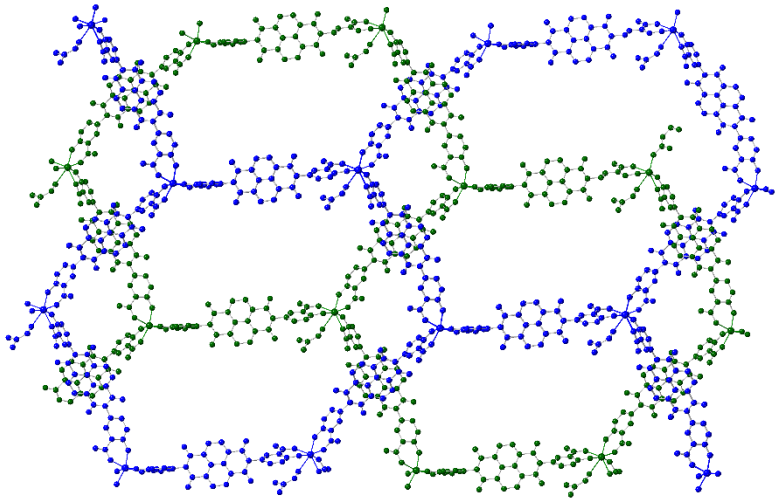

Figure 4.20 – Two parallel sheets that make up the Zr-SA-NDI-α phase.

The PXRD of Zr-SA-NDI-α (Figure 4.21) was taken after the reaction mixture containing the single crystals (pictured in Figure 4.18, above) had been left for several months due to the pandemic. The reaction mixture was centrifuged and washed with twice with DEF and then twice with acetone, to obtain a red precipitate (named Zr-SA-NDI-α-powder) which was ground, before PXRD was carried out. The PXRD pattern (red curve, Figure 4.21) shows that Zr-SA-NDI-α-powder is poorly crystalline. The pattern contains a significant background below 30° 2θ, suggesting Zr-SA-NDI-α-powder is partially amorphous, and the peaks that are present are not sharp or well-defined. When compared to the simulated PXRD pattern of the crystal structure obtained (Figure 4.21), there are some similarities, but even the principal reflection of Zr-SA-NDI-α-powder is shifted slightly compared to the simulated pattern of Zr-SA-NDI-α; the first reflection in the simulated pattern is at 2.72° 2θ and in the Zr-SA-NDI-α-powder's pattern it is at 2.87° 2θ with a second peak at 3.02° 2θ, which is not in the simulated pattern. It is possible that there were multiple phases in the sample, which were not picked up in the single crystal analysis as only one crystal was analysed. Alternatively, as the sample was stored for a long time before analysis, the sample may have undergone phase change during this time or when it was washed or dried.

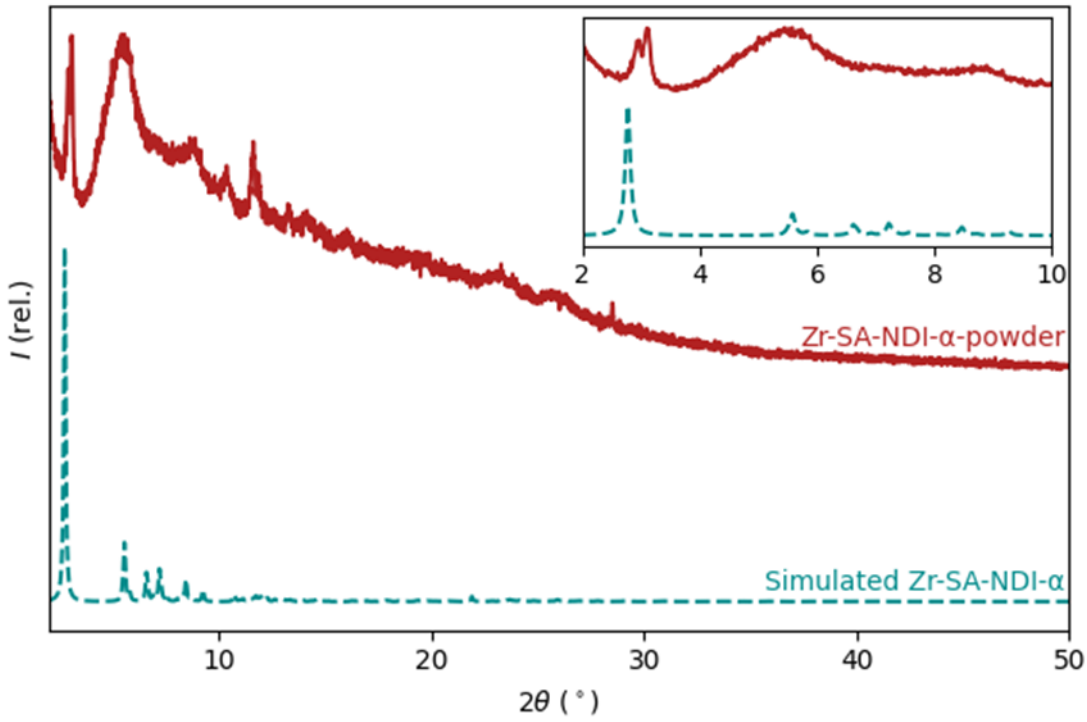

Figure 4.21 – PXRD of SA-NDI-α-powder compared to the simulated pattern from the crystal structure of Zr-SA-NDI-α.

Unfortunately, when this reaction was repeated, the same single crystals could not be obtained. A brick red precipitate was obtained which was analysed by PXRD which revealed that the samples were amorphous (green and blue traces, Figure 4.22). As well as exact repeats, the reaction was repeated in a round bottomed flask. The PXRD of this material (orange trace, Figure 4.22) possesses a Bragg peak, suggesting that the material might possess some long-range order with a large unit cell, but the absence of other reflections suggests that the material is poorly crystalline, and this synthesis route was therefore discontinued. Ramped heating was also attempted for the solvothermal reaction, to see if this would slow down the crystallisation process, but no product was obtained.

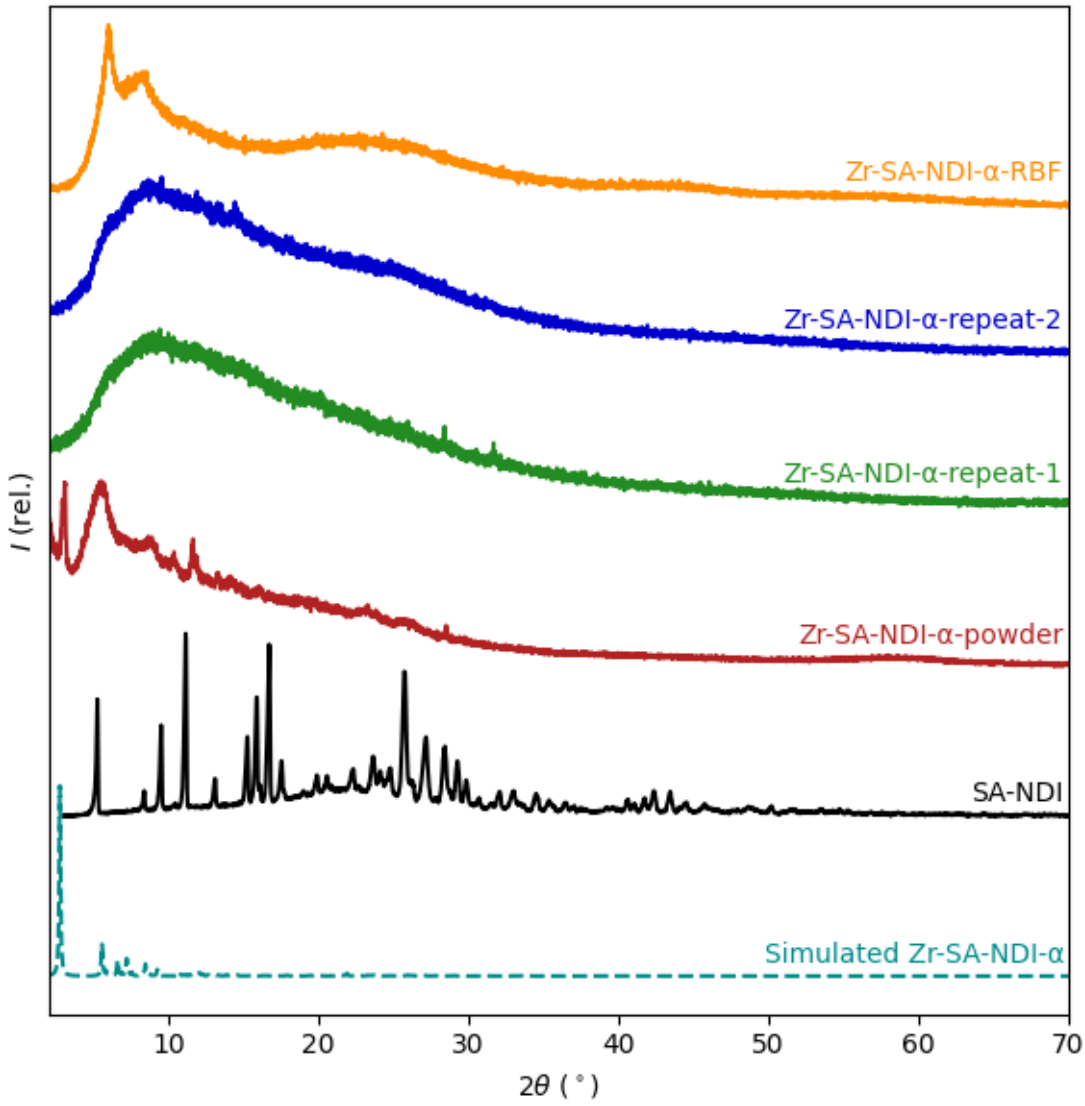

Figure 4.22 – PXRD pattern of: Zr-SA-NDI-α (teal), SA-NDI (black), Zr-SA-NDI-α-powder (red), the powders produced in two repeats of the reaction that formed Zr-SA-NDI-α (green and blue) and the powder produced when the reaction was repeated in a round bottomed flask (orange).

4.3.8 Further characterisation of Zr-SA-NDI-β

After conducting the large range of experiments described in sections 4.3.3 to 4.3.6 to produce a Zr SA-NDI MOF, the reaction yielding the most crystalline product was repeated, to produce enough material for further characterisation. The conditions chosen were: 1:6 metal to linker ratio, 20 equivalents of benzoic acid, DEF, 140°C and 72 hours (blue curve, Figure 4.15) and the material was named Zr-SA-NDI-β. This reaction was carried out four times and the products combined, before carrying out PXRD, TGA, CHN, SEM and UV-vis.

The PXRD pattern (Figure 4.23) below shows that the combined sample of Zr-SA-NDI-β is crystalline and plotting it against the PXRD of the linker and the simulated pattern of Zr-SA-NDI-α obtained shows that Zr-SA-NDI-β is a new phase.

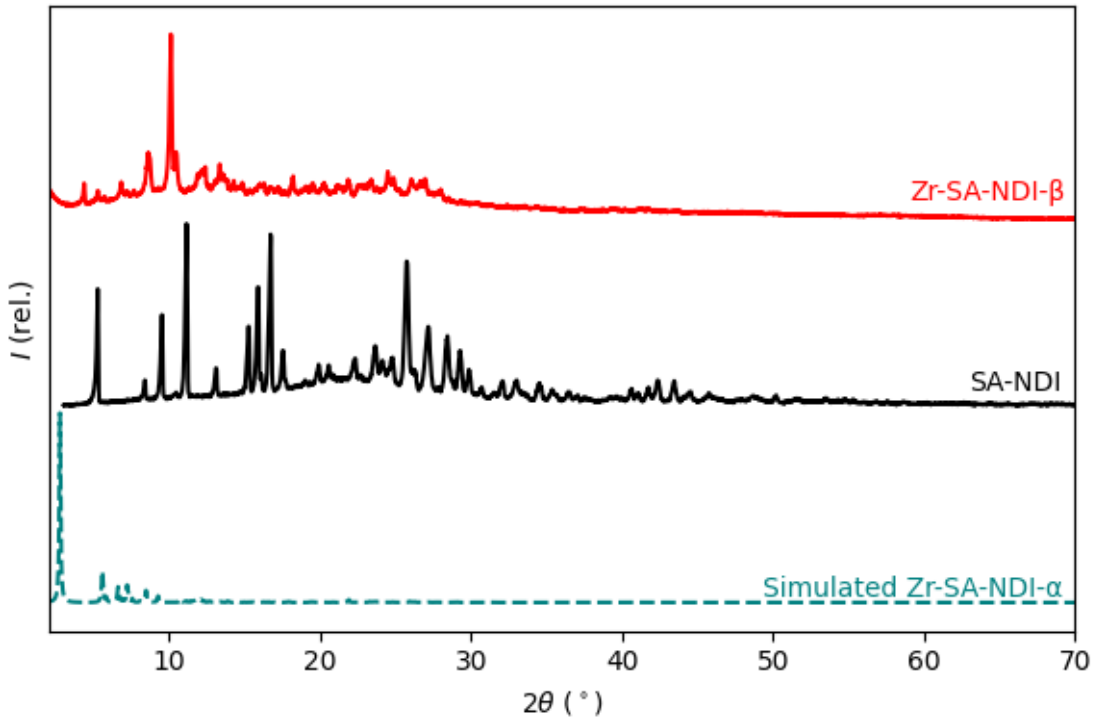

Figure 4.23 – PXRD of: Simulated pattern of Zr-SA-NDI-α (teal), SA-NDI (black), and Zr-SA-NDI-β synthesised by repeating four reactions with the following conditions: 1:6 metal to linker ratio, 20 equivalents of benzoic acid, DEF, 140°C, 72 hours (red).

TGA of Zr-SA-NDI-β (Figure 4.24) shows three distinct mass losses, the first occurring between 30 and 90 °C (8.6%) is likely due to the loss of H_2O which has been absorbed from the atmosphere when the sample has been left to dry in air. The second, between 90 and 280 °C is due to the loss of DEF (13.6%) which was present in the reaction mixture. After 280 °C SA-NDI (64.0%) starts to decompose and at 440 °C the 12.9% remaining is due to ZrO_2. The molecular weights of these fragments can be used to calculate the ratio of Zr to SA-NDI in the sample (Table 4.1), which was estimated to be 1:1. The CHN (Table 4.2) data supports this, with a combination of 3 Zr, 14 H_2O molecules, 4 DEFs and 3 SA-NDIs giving a CHN values on 49.1%, 4.5% and 5.5%, which matches quite closely with the experimental CHN values.

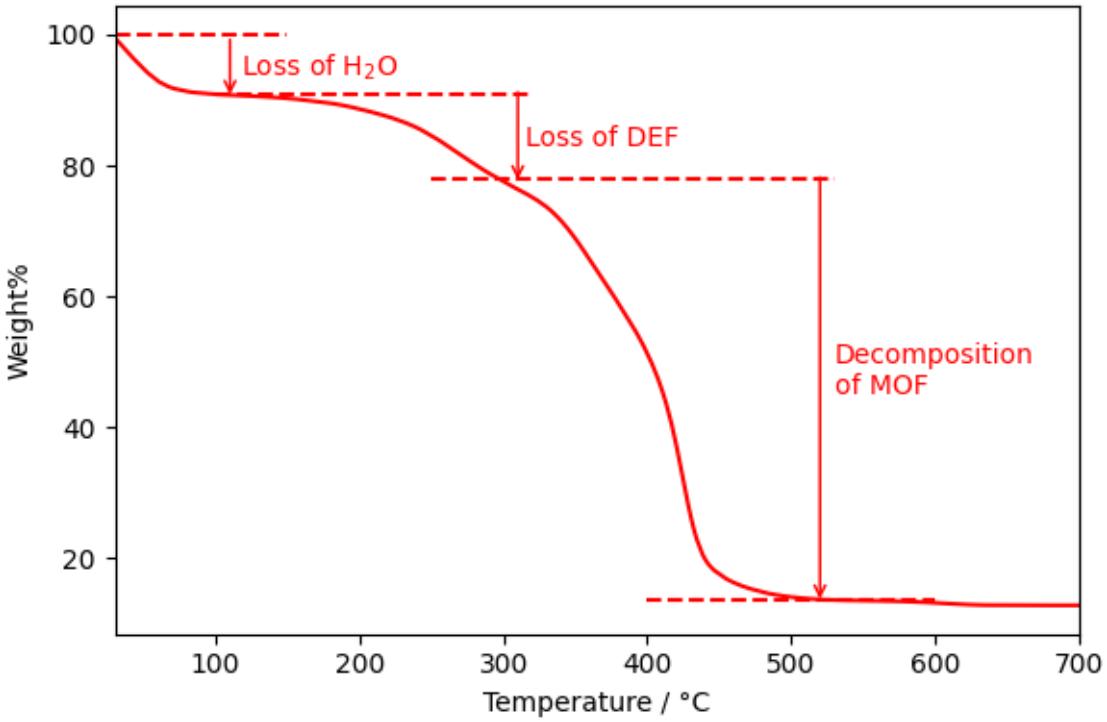

Figure 4.24 – TGA of Zr-SA-NDI-β with labelled decomposition steps.

Table 4.1 – Ratios of the components in the Zr-SA-NDI-β sample, determined through TGA.

%Loss	Assignment	Molecular weight	Ratios w.r.t. Zr
8.6	H_2O	41.05	4.6
13.6	DEF	101.15	1.3
64.0	SA-NDI	538.06	1.1
12.9	ZrO_2	123.22	
9.5	Zr	91.22	1.0

Table 4.2 – CHN results for the Zr-SA-NDI-140. The analysis was repeated once, and an average is taken.

Element	Result 1 / %	Result 2 / %	Average / %	Predicted assuming 3 Zr, 14 H_2O, 4 DEFs and 3 SA-NDIs
C	50.70	50.93	50.8	49.1
H	4.40	4.37	4.4	4.5
N	6.65	5.77	6.2	5.5

The FTIR (Figure 4.25) shows the expected functional groups of the SA-NDI and also includes some transmittance in the OH region which could suggest that the OH groups in the SA-NDI are still present, or this could be caused by H_2O in the sample.

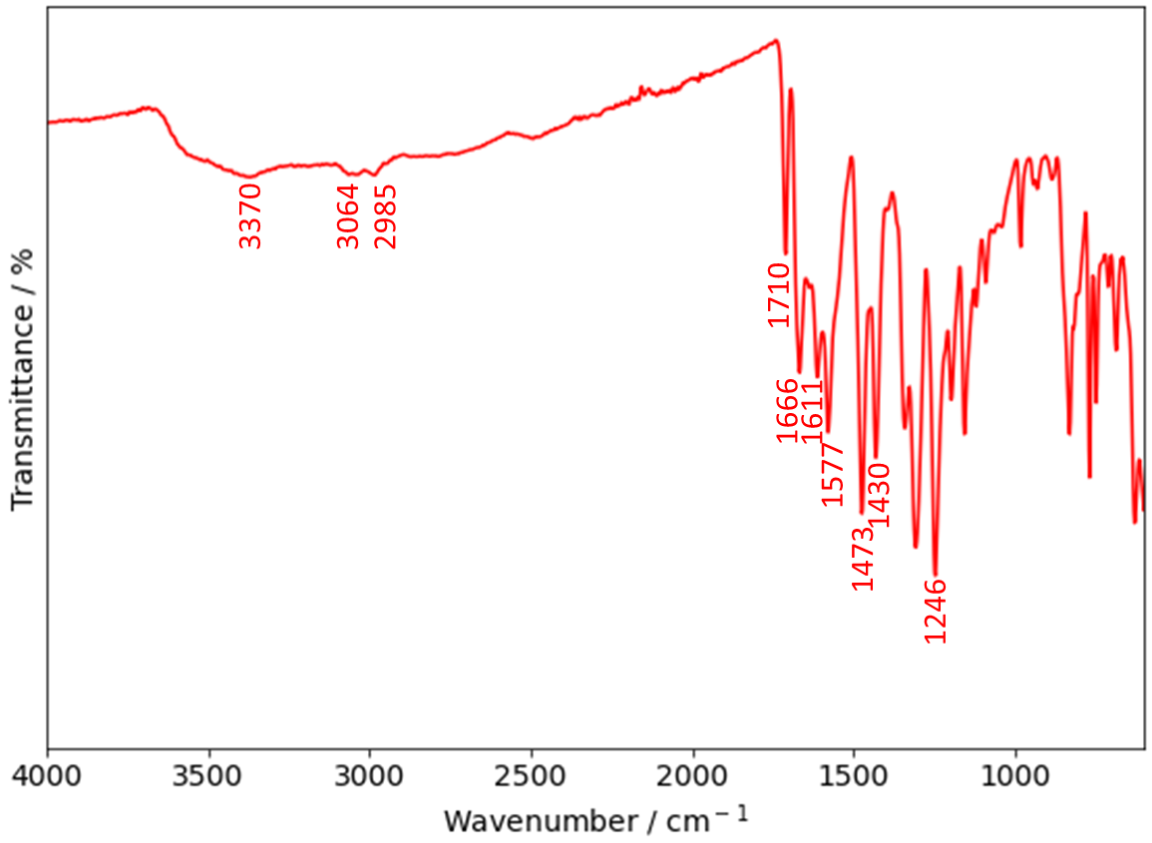

Figure 4.25 – FTIR spectrum of Zr-SA-NDI-β. OH in COOH and OH in SA-NDI (2500-3200). Diimide C=O in SA-NDI (1666, 1577), Pendant C=O in SA-NDI (1473, 1430), C-N in SA-NDI (1246).

The solid-state UV-vis of Zr-SA-NDI-β (Figure 4.26) shows an absorption band below 650 nm and is similar to the UV-vis of SA-NDI. This is consistent with the red colour of each sample. SEM-EDX was also carried out which confirmed that Zr was present in the material (see section 4.9.4.4 for images and spectra).

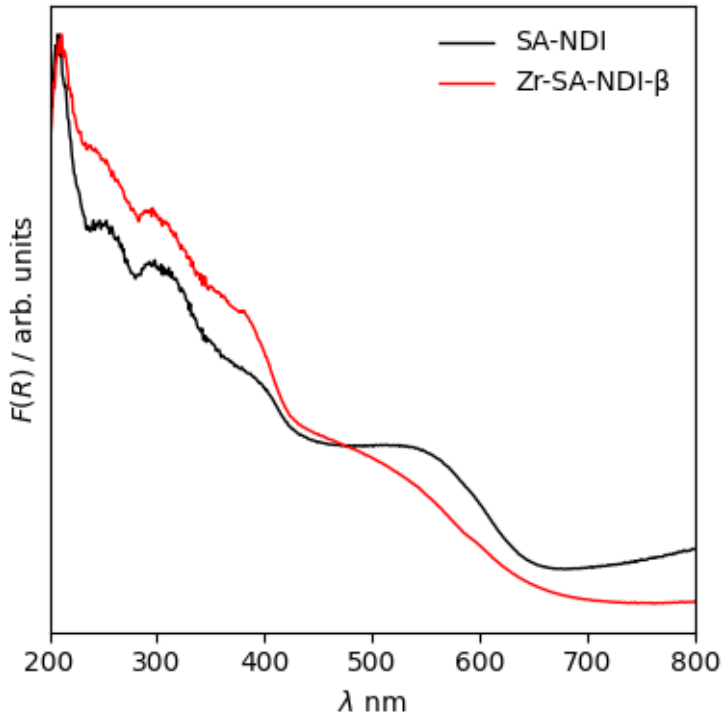

Figure 4.26 – Solid state UV-vis of Zr-SA-NDI-β

The next physical step with this material would be to attempt activation using solvent washing or calcination to try and remove the DEF from the pores. Gas sorption could then be used to determine if the material was porous. Unfortunately, this was not possible in this project due to time constraints.

4.3.8.1 Attempts to solve the structure of Zr-SA-NDI-β

Attempts were made to solve the structure of Zr-SA-NDI-β. Dr Matthew Cliffe and Jem Pitcairn assisted with the work described in this section.

Firstly, indexing of the powder pattern was carried out in TOPAS-Academic (version 4.1) to find the lattice parameters and space group of the structure.[46] The structure was indexed iteratively, starting with high symmetry unit cells before moving to progressively lower symmetry unit cells. The candidate unit cells were assessed by Goodness of Fit (which is calculated by dividing R_{wp} by R_{exp}) and the number of unindexed peaks. A couple of viable results were found and Pawley fitting of the powder pattern against the calculated space groups and lattice parameters from these results was carried out. Through this method a

monoclinic space group ($P2_1/c$) was found to give the best GoF. The lattice parameters (Table 4.3) and Pawley fit (Figure 4.27) are shown below.

Table 4.3 - Lattice parameters and GOF calculated from Pawley fit

Space group	Volume/Å^3	a	b	c	α	β	γ	GOF
$P2_1/c$	10537.607	24.4982	39.7473	15.5535	90.000	135.911	90.000	1.06

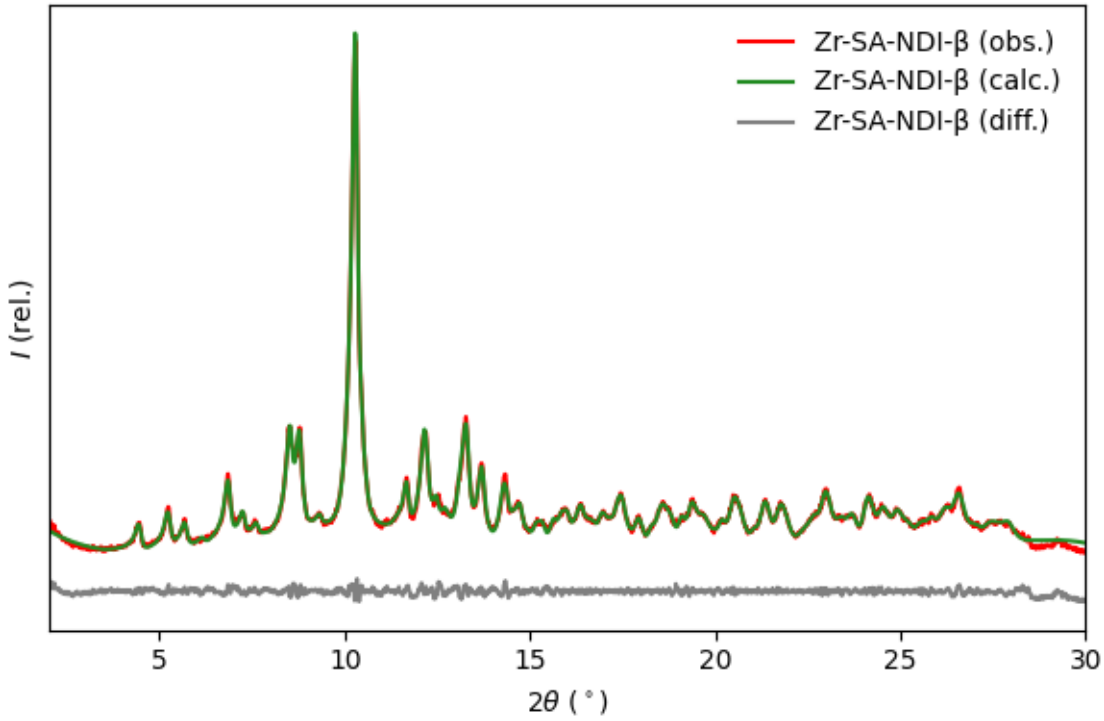

Figure 4.27 – Pawley fitting of Zr-SA-NDI-β to the space group and lattice parameters found through indexing in TOPAS-Academic.[46]

Next, it was assumed that the largest scattering in the Zr-SA-NDI-β was due to the SA-NDI linker and simulated annealing was carried out (in DASH)[47] to see how the structure of SA-NDI fits the unit cell that had been calculated in TOPAS-Academic. The z matrices of SA-NDI were calculated from the SA-NDI HOF crystal structure that is reported in Section 4.4, as this contains the crystal structure of the SA-NDI linker. The NDI core was treated as a rigid unit, whilst the pendant salicylic acid units were allowed to rotate around the NDI core. Zr atoms were omitted as it was assumed that diffraction due to Zr would be relatively weak compared to the diffraction due to the SA-NDI fragments. The space group and lattice parameters of the system and series of SA-NDI z matrices were set up in the DASH software.[47] Several iterations were carried out, with increasing numbers of SA-NDI matrices input as a starting point for the

simulated annealing. The best fits were found when three SA-NDI units were used, and the top five results in this set of structures all had similar structures with similar levels of fit. As this structure (Figure 4.28) made chemical sense, i.e. there were no overlapping bonds, or SA-NDI fragments in too close proximity, a Rietveld refinement of this structure was attempted in TOPAS-Academic.[46] At first, only peak shape was refined and a relatively poor GoF (4.79) was observed (fitting is shown in Figure 4.29).

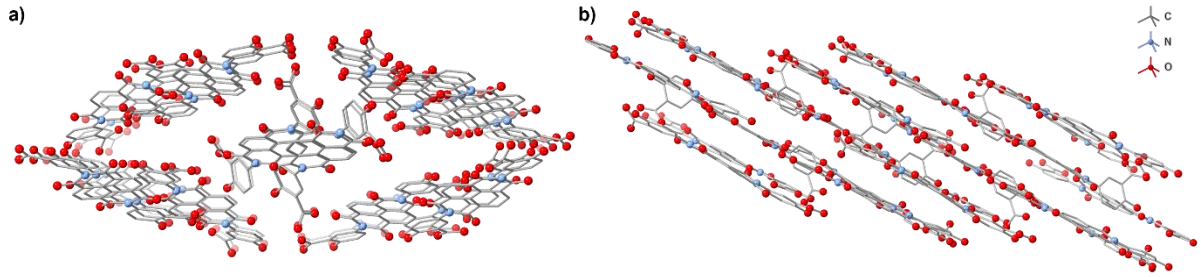

Figure 4.28 – Crystal structure obtained from DASH when three SA-NDI fragments were used in a simulated annealing run on the Zr-SA-NDI-β powder pattern. a) view along *a*-axis and b) vies along *b*-axis. Hydrogens omitted for clarity.[47]

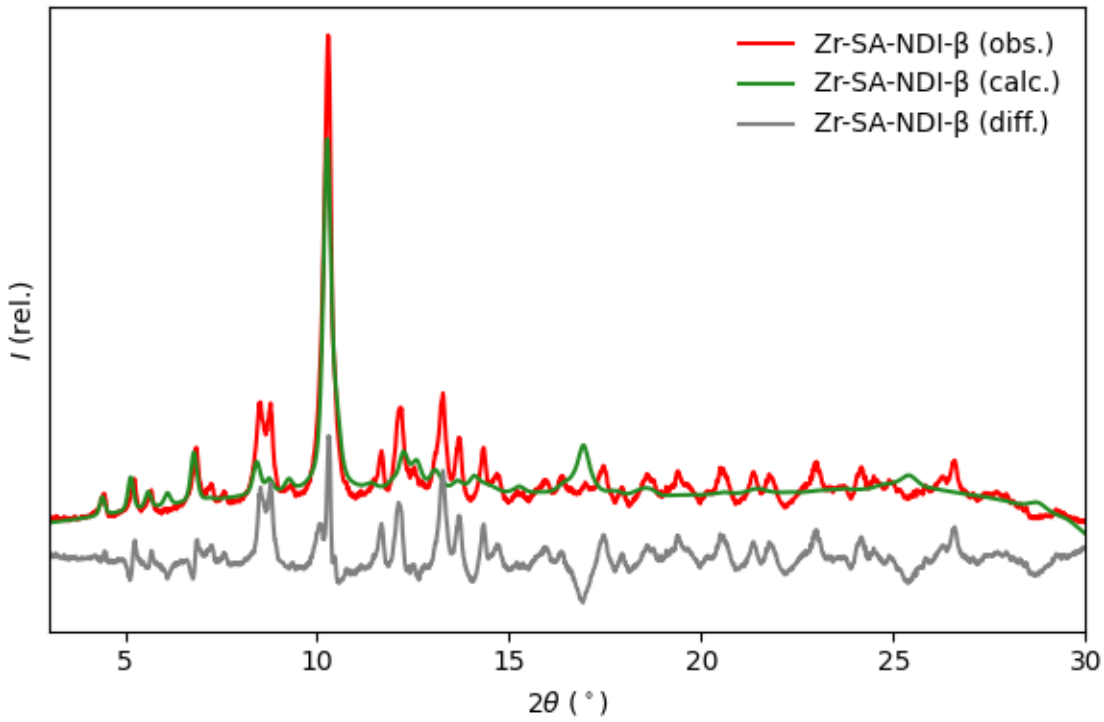

Figure 4.29 – Rietveld refinement of Zr-SA-NDI-β powder pattern against the result of simulated annealing carried out in DASH.[46,47]

Attempts were made to try and refine the structure further. Zr atoms were added at different starting points and simulated annealing of only the Zr atoms was carried out. In each attempt, the Zr moved to positions that made no sense chemically.

Determination of the structure of this compound will require higher quality data, for example, synchrotron powder diffraction, or further characterisation such as collecting electron diffraction data.

4.4 Synthesis of a salicylic acid NDI HOF

Whilst exploring the reaction conditions which led to the formation of Zr-SA-NDI-α and Zr-SA-NDI-β it became clear that crystalline materials had been obtained using DEF, DMF and a DMF/MeCN mix as the solvent, but no reaction had been attempted using a DEF/MeCN mixture as solvent. This reaction was performed in hope that it would lead to a product with enhanced crystallinity.

A 1:6 ratio of metal to linker was used, with 20 equivalents of TFA as the modulator, as this modulator had previously given single crystals that exhibited some diffraction. The reaction was conducted at 100°C in pressure tubes, due to the low boiling point (82°C) of MeCN. The reaction gave yellow needle crystals, and a crystal structure was obtained at DLS. Dr Stephen Argent and Dr Georgia Orton mounted the crystals and carried out the remote data collection. They both assisted with the structure solution using Olex2, with Dr Argent carrying out the final refinements.

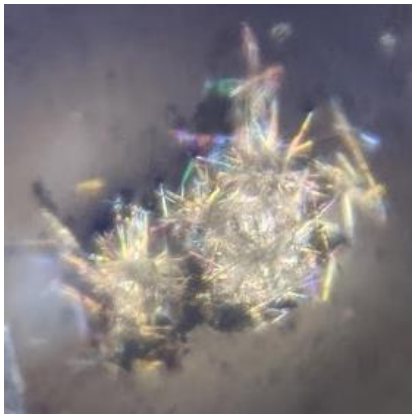

Figure 4.30 – Needle crystals obtained in an attempted SA-NDI Zr reaction, viewed under an optical microscope. Conditions were: 1:6 metal to linker ratio, 20 equivalents of TFA, DEF/MeCN, 100°C, 72 hours.

The crystal structure obtained showed that the material was in fact a hydrogen bonded-framework (HOF), consisting of SA-NDI linkers joined by hydrogen bonding of carboxylate groups in adjacent SA-NDI molecules. (Figure 4.31). The SA groups on each side on the NDI twist in opposite directions, causing a zig-zag connectivity of the linkers, that extends in the *c*-direction (see b, Figure 4.31). The colouring of fragments in Figure 4.31 shows the connectivity of fragments joined by hydrogen bonds extends throughout the material. The view along the *a*-axis (c, Figure 4.31) suggests that the material might be porous.

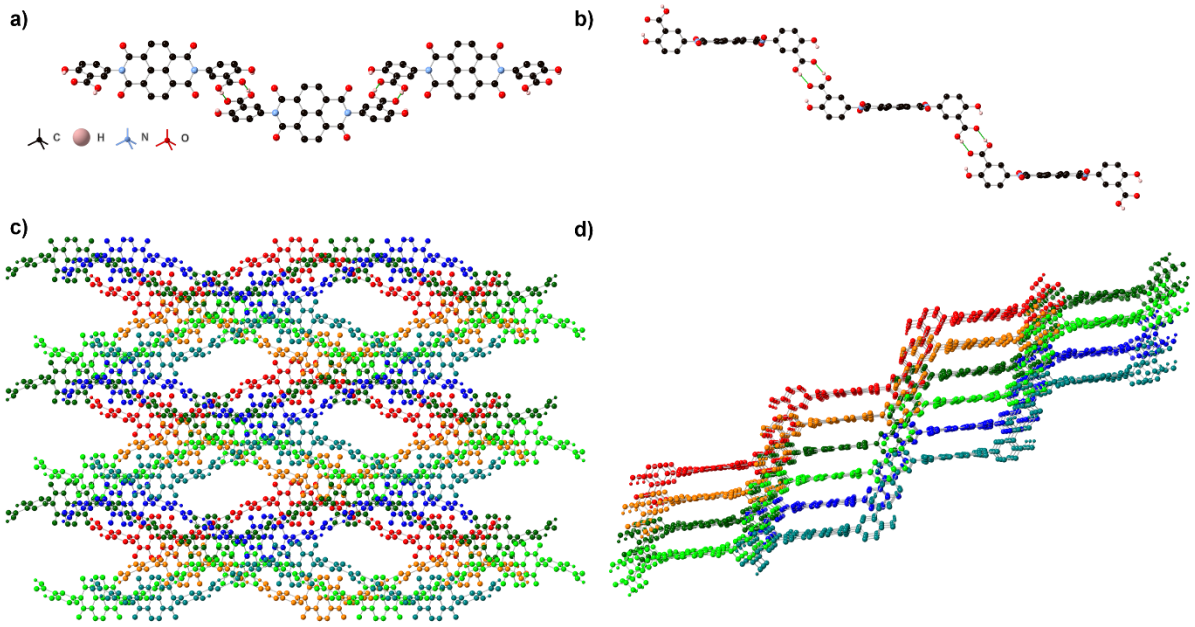

Figure 4.31 – a) Three SA-NDI molecules viewed along the *c*-axis that are joined together by hydrogen bonds between the carboxylate groups of adjacent SA-NDI molecules, b) three SA-NDI units viewed along the *b*-axis to show the twisting of the SA-NDI molecules, c) view along the *a*-axis, and d) chains of connected SA-NDI units have been coloured to show how they zig-zag due to the twisting of SA-NDI molecules, viewed along the *b*-axis. Hydrogen atoms are omitted in all structures for clarity.

Figure 4.32 shows MeCN in the pores of the HOF, these MeCN molecules were omitted from the figures above for clarity, but it was possible to resolve these in the crystal structure solution. The presence of these molecules is not completely unexpected as MeCN was used as a solvent and the molecules are small enough to fit in the pores of the HOF.

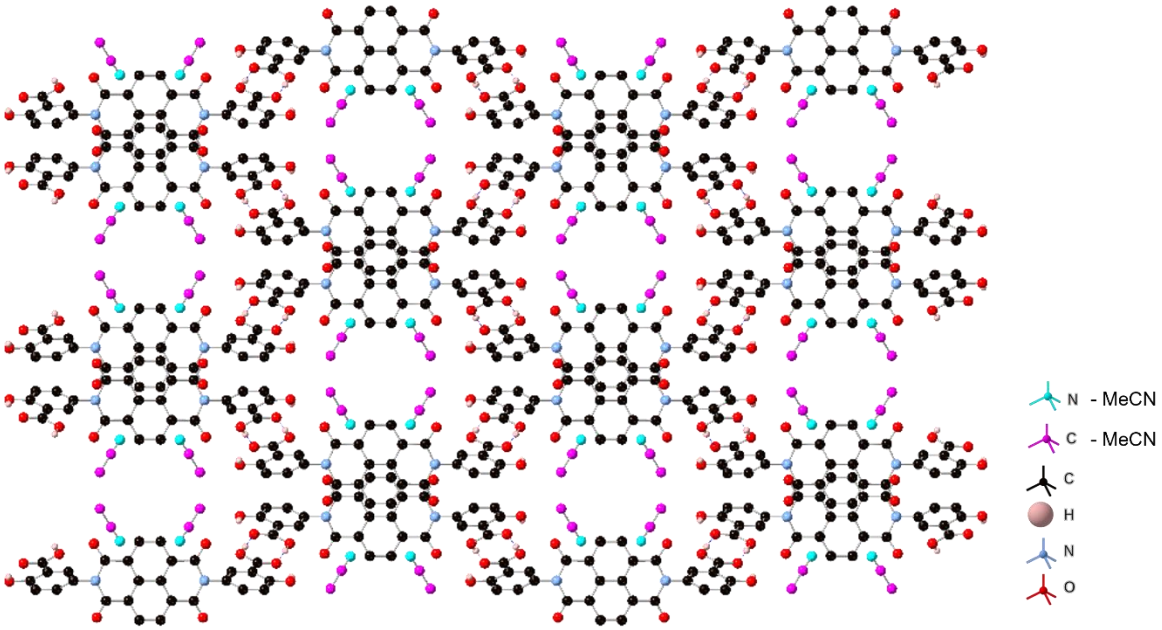

Figure 4.32 – View of SA-NDI HOF along the *c*-axis, showing the presence of MeCN pores of the framework.

The formation of this HOF was unexpected, as $ZrCl_4$ was added to the reaction mixture used to synthesise this material. It seems that under these conditions SA-NDI preferentially forms hydrogen bonds with itself to form a framework, rather than coordinated to the available Zr(IV). On reviewing the SEM-EDX data collected on this sample, it became clear that regions where there are needle shaped particles (Spectrum 7, Figure 4.33) that contain negligible amounts of zirconium and regions of non-uniform smaller particles (Spectrum 10, Figure 4.33) contain zirconium (roughly 1.7 atomic%). These needle particles are the HOF, whilst the other Zr-containing particles might either be $ZrOCl_2$ or another Zr-containing side-products.

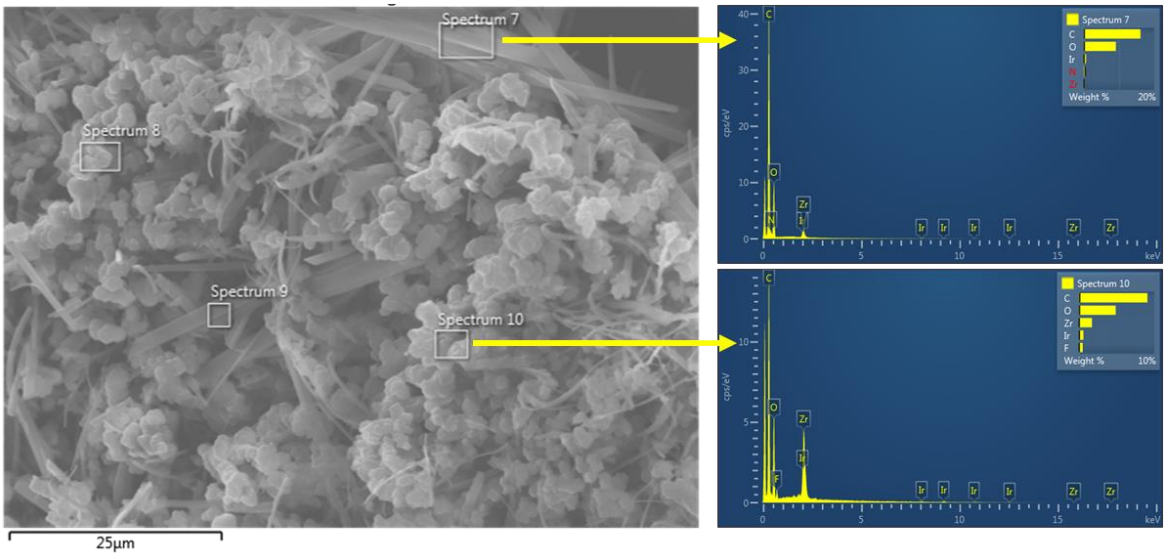

Figure 4.33 – SEM-EDX of a synthesis of attempted SA-NDI Zr reaction that resulted in the formation of SA-NDI HOF as the major phase.

To see if this HOF structure was obtained when there is no metal present in the reaction mixture, the same synthesis was carried out, with the exact same ratio of SA-NDI to TFA to solvent, but with no $ZrCl_4$ added. Once more, yellow needle crystals were obtained. The needles were separated from the reaction solvent by centrifugation and allowed to dry overnight in air and PXRD analysis was carried out to determine if the same phase had been produced.

PXRD (Figure 4.34) shows that the HOF structure is present in sample obtained where no $ZrCl_4$ was added, showing that the other conditions used in the reactions favour the formation of this phase. It appears that there may be some other phases present in the sample, as there are reflections present in the PXRD that are not present in the simulated PXRD of the HOF. In addition, it is noted that the PXRD of the crystals formed when $ZrCl_4$ is present may have been subject to preferred orientation during the analysis, as the pattern lacks several reflections that are present in the simulated pattern. When analysing the *hkl* values of the reflections, it appears that only reflections associated with the *b* direction are present, suggesting that the material's needles grow along the crystallographic *b* direction.

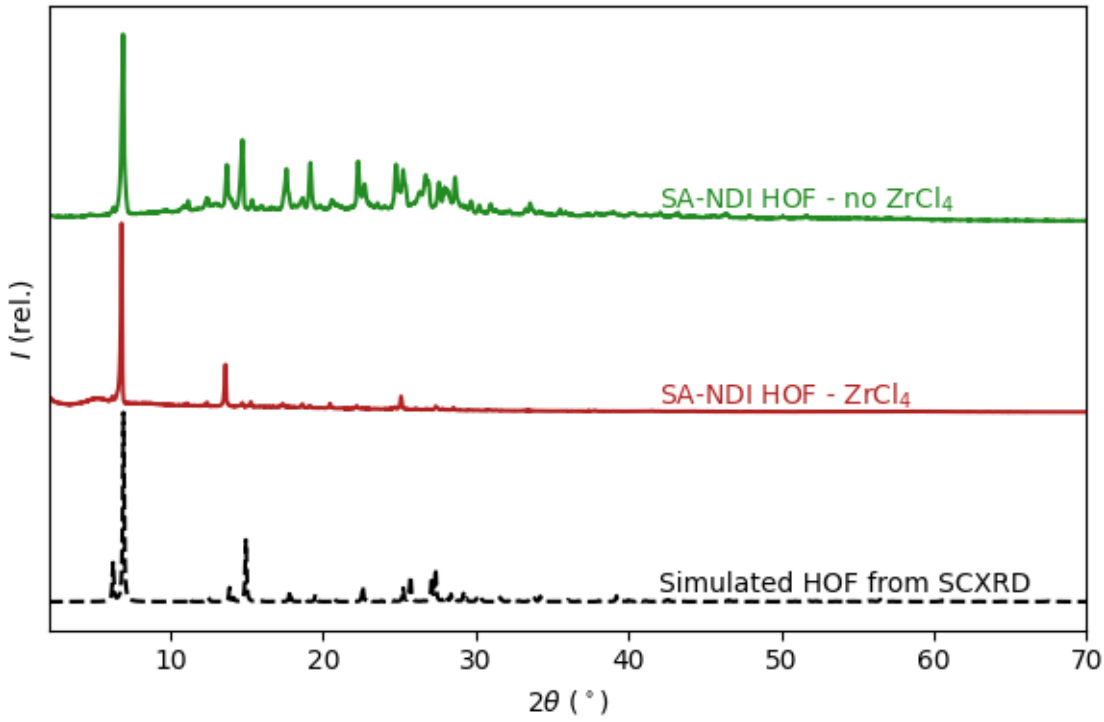

Figure 4.34 – PXRD of materials obtained in HOF-forming reactions with (red) and without $ZrCl_4$ (green), against the simulated pattern of the HOF (black).

Multiple syntheses of the SA-NDI HOF were carried out and the products combined so that further characterisation could be carried out.

TGA (Figure 4.35) shows four distinct decompositions. Firstly, between 70 and 170°C MeCN (20.4%) is assumed to be lost, followed by DEF (11.5%) from 170 to 270 °C, which are both present in the reaction mixture. Between 270 and 400 °C, the loss occurring is predicted to be due to the decarboxylation of the SA-NDI linker. Above this temperature, SA-NDI starts to decompose and completely combusted at 600°C. Overall, this suggests that the HOF structure is only stable up to 270°C because the carboxylate groups are required for the hydrogen bonding that holds the HOF structure together.

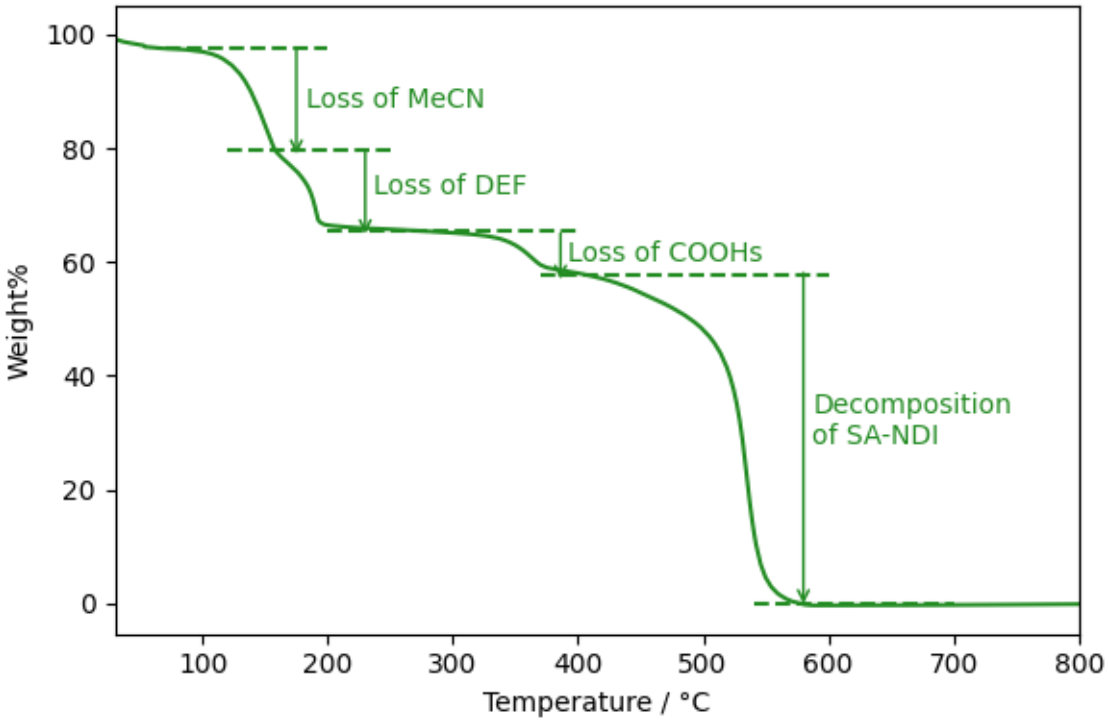

Figure 4.35 – TGA of SA-NDI HOF with labelled decomposition steps.

By using the % mass loss occurring for each step, it is possible to estimate the ratio of each component of the sample (Table 4.4).

Table 4.4 – Ratios of the components in the SA-NDI HOF sample, determined through TGA.

%Loss	Assignment	Molecular weight	Ratios w.r.t. SA-NDI
20.4%	MeCN	41.05	4.06
11.5%	DEF	101.15	0.93
8.5%	COOH	45.01	1.54
65.8%	SA-NDI	538.06	1.00

CHN analysis (Table 4.5) was conducted for the sample. It is noted that no further drying was carried out after centrifuging the reaction mixture, decanting the solvent, and allowing the solid product to dry in air overnight. The oxygen content is calculated under the assumption that this is the only other element present in the sample.

Table 4.5 – CHN results for the SA-NDI HOF. The analysis was repeated once, and an average is taken. The oxygen is content is calculated by assuming there are no other elements present in the sample.

Element	Result 1 / %	Result 2 / %	Average / %
C	55.48	55.33	55.4
H	4.30	4.01	4.2
N	5.82	5.70	5.8
O (calc'd)			34.7

Table 4.6 shows the calculated CHN values, assuming various stoichiometries of the components of the SA-NDI HOF. The nitrogen content in the sample is low compared to what would be expected if the product contained four MeCN and one DEF molecule per SA-NDI, as suggested by the TGA data (Table 4.4). This raises the question whether the decomposition present between 70 and 170°C is due to MeCN or another species. To help to further determine what species are present in the sample FTIR (Figure 4.36) and ^{1}H NMR (Figure 4.37) spectroscopies were carried out.

Table 4.6 – Calculated CHN values for predicted compositions of the SA-NDI HOF.

Element	4 MeCN, 1 DEF, 1 SA-NDI	4 H_2O, 1 DEF, 1 SA-NDI	5 H_2O, 1 DEF, 1 SA-NDI
C	61.3	55.7	54.3
H	4.6	4.7	4.8
N	12.2	5.9	5.8
O	21.9	33.7	35.1

Both analyses show no MeCN present in the sample: the FTIR has no absorbance band between 2260-2222 that could be attributed to the CN triple bond, although the intensity of this band might be too low to be observed. The ^{1}H NMR does not contain any peaks in the region (δ 1.9-2.1) that can be assigned to the methyl protons in MeCN.

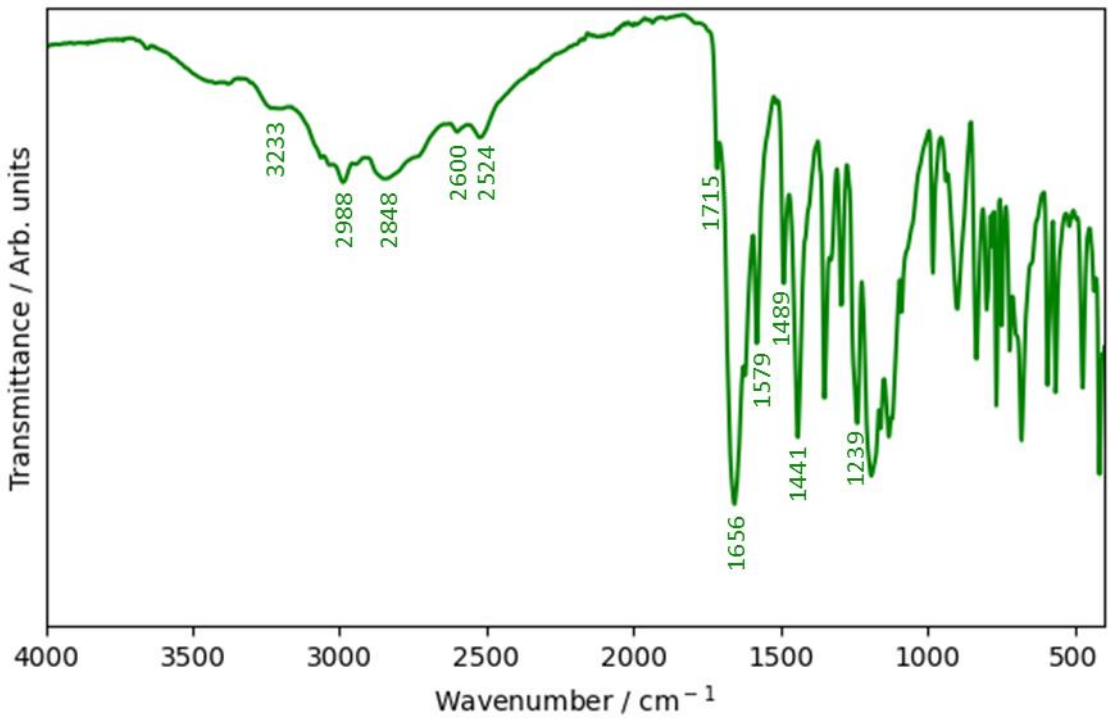

Figure 4.36 – FTIR of SA-NDI HOF. OH in COOH and OH in SA-NDI (2500-3200). Diimide C=O in SA-NDI (1656, 1579), Pendant C=O in SA-NDI (1489, 1441), C-N in SA-NDI (1239).

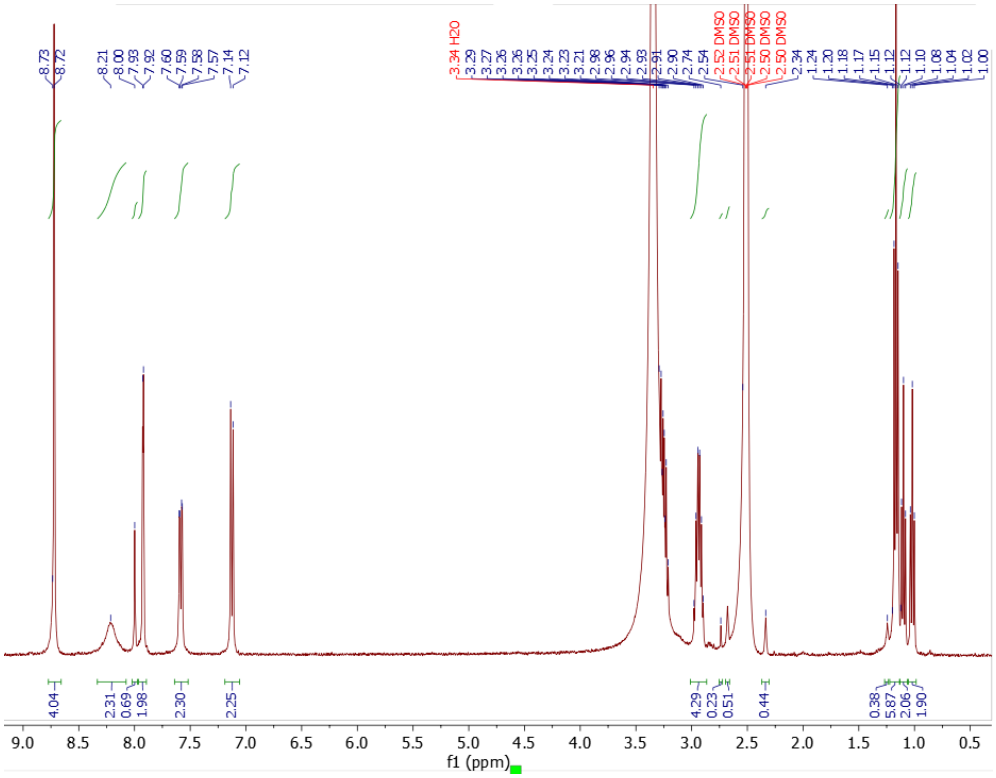

Figure 4.37 – ^{1}H NMR of SA-NDI HOF (400 MHz, DMSO) δ 8.72 (s, 4H_1, , SA-NDI), 8.21 (s, 2H_A, DEF), 8.00 (s, H, DMF), 7.92 (d, J = 2.6 Hz, 2H_2, SA-NDI), 7.58 (dd, J = 8.8, 2.6 Hz, 2H_3, SA-NDI), 7.13 (d, J = 8.7 Hz, 2H_4, SA-NDI), 2.93 (s, 2H_B, DEF), 2.74 (s, 3H, DMF), 2.54 (s, 3H, DMF), 1.17 (s, 6H_C, DEF).

Although the crystal structure of the HOF suggested that there should be MeCN present in the pores, this crystal structure was obtained when a crystal was taken directly from the reaction mixture, which contained MeCN and DEF as co-solvents. As the further analyses were carried out after the samples were left to dry in air, it is possible that the MeCN evaporated and was replaced with H_2O from the atmosphere. The second two columns in Table 4.6 contain the calculated CHN values, assuming that there are four or five H_2O molecules alongside one molecule of SA-NDI and one DEF. These match much more closely with the experimental CHN values, also supporting the possibility of H_2O being present in the dried sample.

Solid state diffuse reflectance UV-vis spectroscopy was performed for both the as-prepared sample of SA-NDI and SA-NDI HOF. The spectrum (Figure 4.38) shows that both the SA-NDI and the SA-NDI HOF absorb light below a wavelength of 500 nm, but that the SA-NDI possesses a further reflectance band at around 550 nm. This extra reflectance band is likely caused by the aggregation of the NDI molecules,[48] due to π-π stacking of the aromatic cores. In the HOF, the hydrogen bonds prevent aggregation as they keep the NDI molecules fixed in

positions that are too far apart to allow intermolecular interactions. Aggregation may also give rise to the difference in colour of the linker and the HOF; SA-NDI is red, and the SA-NDI HOF is yellow.

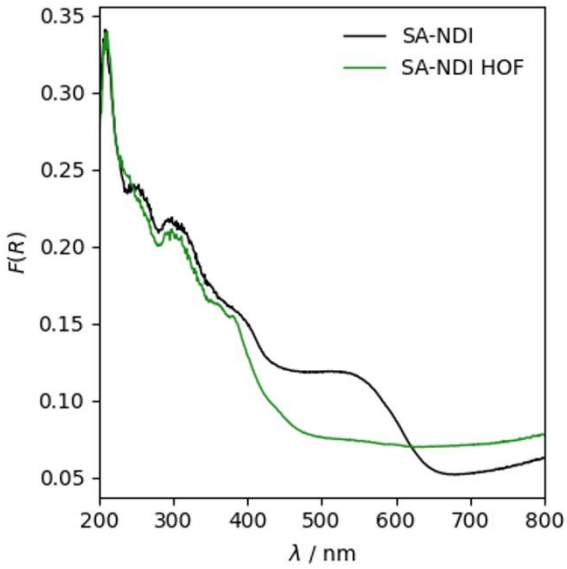

Figure 4.38 – Solid state UV-Vis spectra of SA-NDI and SA-NDI HOF.

4.4.1 Activation of SA-NDI HOF

To try to probe the porosity of the HOF, several activation methods were attempted to try and remove the guest H_2O and DEF from the pores. As the HOF is soluble in DEF, washing to remove the DEF and H_2O was attempted with a variety of less polar and more volatile solvents, including acetone and diethyl ether. In addition, calcination at 200 °C was also carried out as the TGA of the HOF (Figure 4.35) showed that at this temperature, the DEF has been removed but the SA-NDI remains intact.

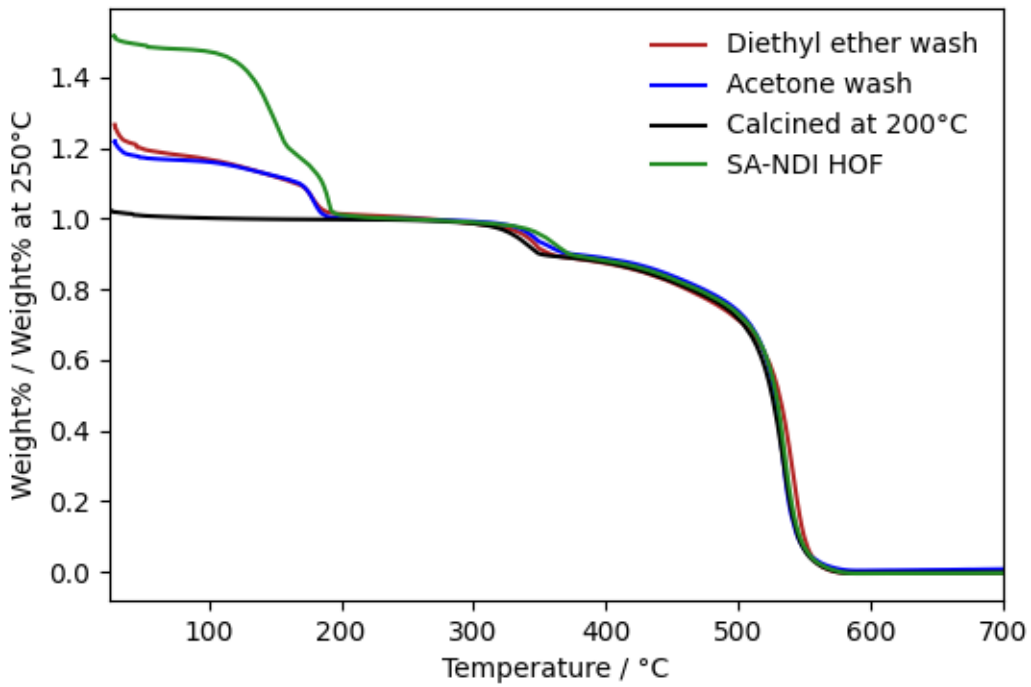

Figure 4.39 - TGA of SA-NDI, SA-NDI HOF, SA-NDI HOF calcined at 200°C for 24 hours, SA-NDI washed in acetone and diethyl ether. To give a more useful representation of the data, each curve has been normalised to its weight% at T = 250°C. This allows the steps before to be compared more easily.

The TGA (Figure 4.39) shows that after calcination, there are no mass losses between 30 and 300°C, suggesting that the solvents have been removed from the pores of the MOF. The mass losses associated with the loss of carboxylate groups and the decomposition of the NDI are still present, indicating that SA-NDI remains intact after calcination. Unfortunately, the PXRD analysis (Figure 4.40) shows that the HOF structure is not stable after calcination at this temperature, as the reflections associated with the HOF are not present in the PXRD pattern. The material has undergone a complete phase transformation. It is likely that the thermal treatment broke the hydrogen bonds, and that the SA-NDI linker is present but in a different polymorph to the synthesised material.

After washing with diethyl ether or acetone, the low boiling point solvent (likely H_2O) has been removed, indicated by the lack of mass loss between 70 and 170°C which is present in the HOF. However, the mass loss occurring between 170 and 270°C suggests that DEF is still present, and that washing has failed to remove this. The PXRD of the samples (Figure 4.40) indicates the HOF is still present, but significant changes have occurred. After diethyl ether washing, a significant loss in crystallinity is observed, indicated by peak broadening and an increase in the background. After acetone washing, only a small number of reflections remain, suggesting that preferential orientation in the *b* direction has occurred. Because of this, it is

hard to confirm whether washing in acetone has influenced the crystallinity of the HOF, but the peaks that are present suggest that the structure remains intact.

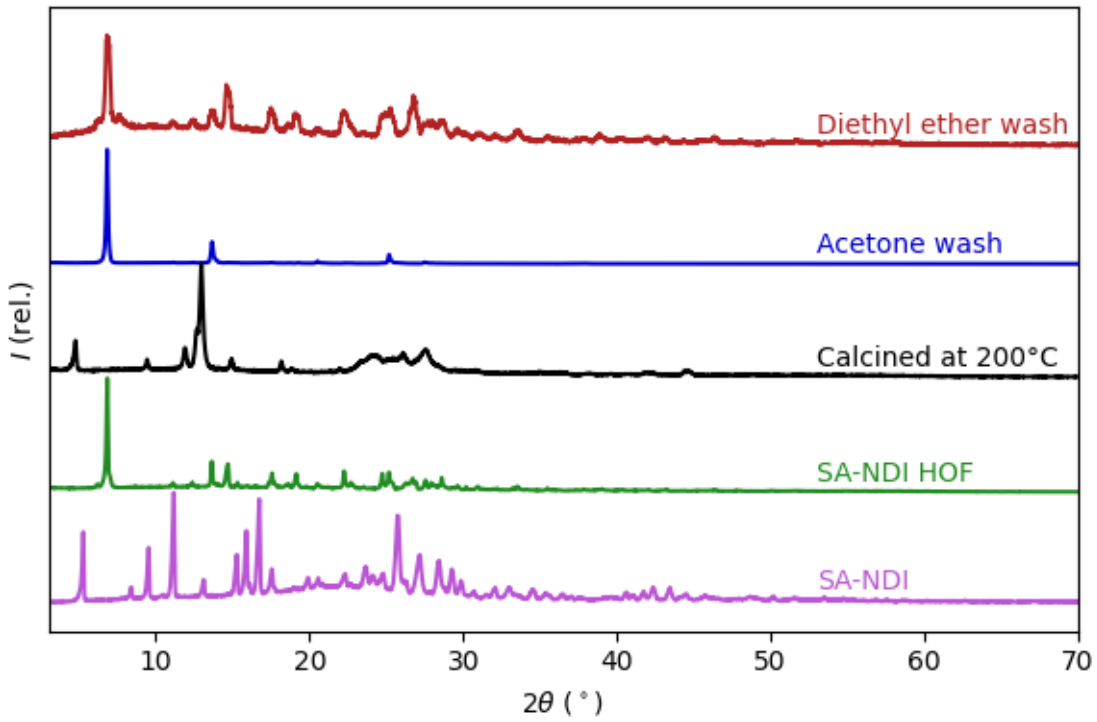

Figure 4.40 – PXRD of SA-NDI, SA-NDI HOF, SA-NDI HOF calcined at 200°C for 24 hours, SA-NDI washed in acetone and diethyl ether.

To understand the phase changes that occur when SA-NDI HOF is heated in air, a temperature dependent PXRD experiment was conducted. The sample was heated in 20°C increments to 400°C and then 50°C increments to 600°C. The peak at 25.37° 2θ is due to the alumina plate on which the sample is mounted.

The data (Figure 4.41) shows that the HOF undergoes a significant phase change between 180 and 200°C, with peak positions changing completely between these two temperature points. This suggests that above 180°C the hydrogen bonds that give rise to the HOF structure are broken, resulting in degradation of the HOF structure. Comparing the sample that has been heated to 200°C to the PXRD pattern for SA-NDI (Figure 4.42) shows that the thermal treatment gives a different phase to the SA-NDI. Although the first reflections are in similar positions, 5.21° 2θ in SA-NDI and 4.68° 2θ in the heated sample, the positions and intensities of the other peaks are not equivalent. It is possible that a new polymorph of SA-NDI is present. The sample that was calcined at 200°C is also shown alongside the heated sample in Figure 4.42, and shows that the PXRD patterns are very similar, showing the same phase is formed

whether the HOF is heated at 200°C in air for 24 hours (calcined) or 5 mins (temperature dependent PXRD). As the crystallinity of the HOF phase is maintained at 180°C, it would be interesting to use this temperature for activation; it might allow the DEF to be removed (the boiling point of DEF is 178.3°C) whilst leaving the HOF structure intact.

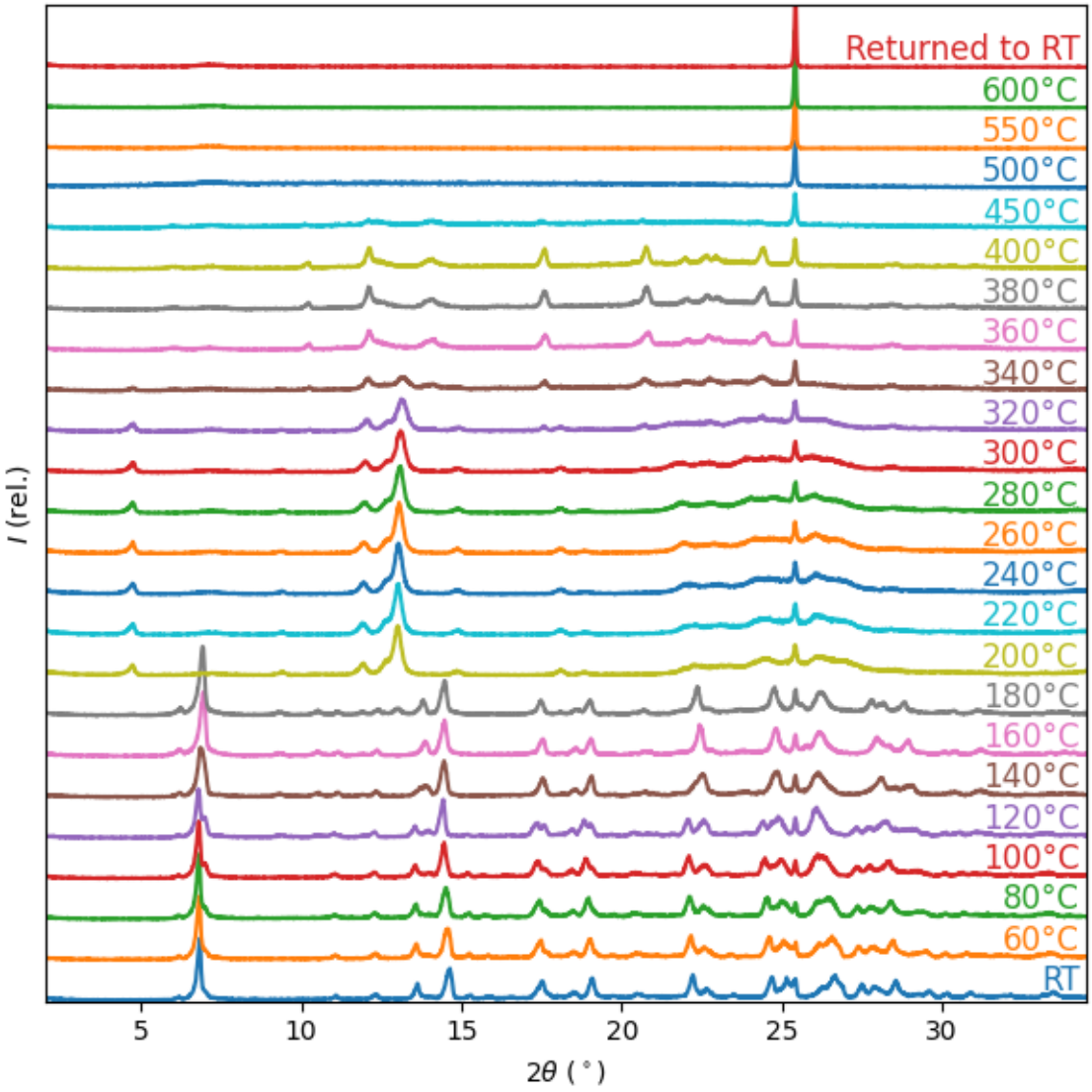

Figure 4.41 – Temperature dependent PXRD of SA-NDI HOF, with heating in 20°C increments to 400°C and then 50°C increments to 600°C. The peak at 25.37° 2θ is just to the alumina plate that the sample was heated in during the experiment.

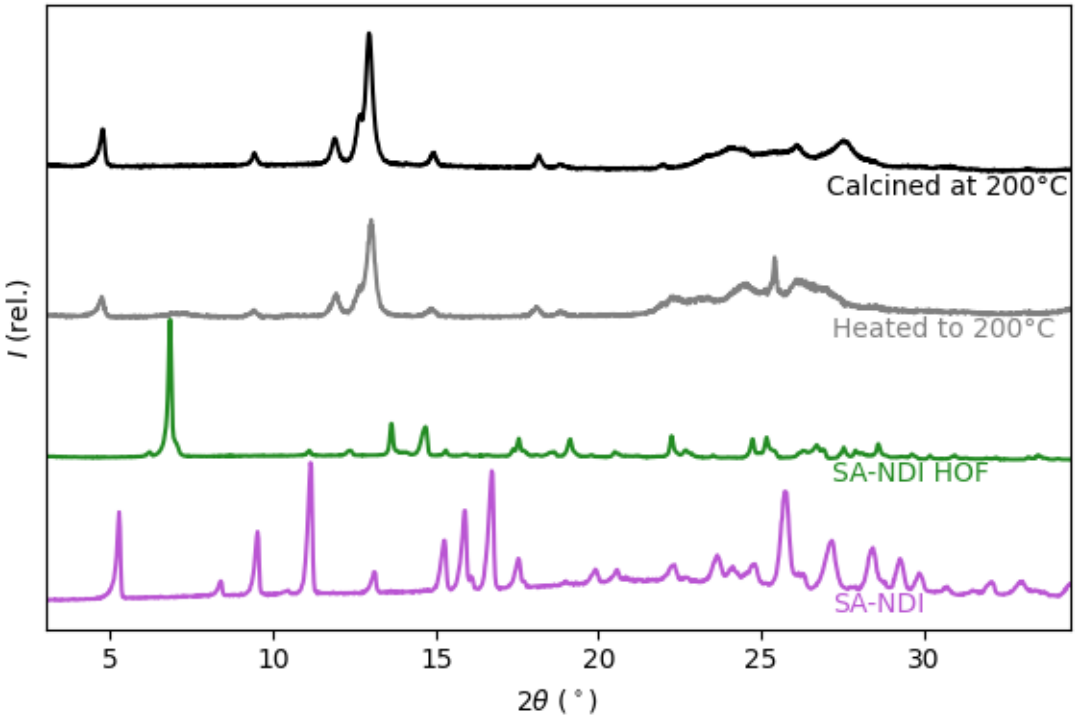

Figure 4.42 – PXRD of SA-NDI, SA-NDI HOF, SA-NDI HOF after heating to 200°C in the temperature dependent PXRD experiment and SA-NDI HOF after calcining at 200°C for 24 hours.

The material undergoes a further change at 340°C, indicated by another set of changes in the peak positions and intensities. According to the TGA of the HOF (Figure 4.35) this is the temperature at which decarboxylation occurs, so a phase change alongside this is expected. The material is completely combusted at 500°C, which also consistent with the TGA results.

Due to the lack of success of activation attempts using calcination or acetone and diethyl ether washes, further work could look at washing with other solvents, such as MeOH, EtOH could be attempted or calcination at lower temperatures for longer times. It is also possible that as the material is only held together through hydrogen bonding, that the solvents present in the pores of the HOF are necessary for the maintenance of the structure. Instead of attempting further activation, gas sorption on the HOF could be carried out to determine if the material is porous and then possible application could be explored.

Although the main aim of this Chapter was to produce Group 4 NDI MOFs, the synthesis of an NDI HOF is a significant result, as the field of HOFs is relatively young.[49] The reaction conditions used to form the HOF are very specific; removing any or changing the ratios of any of the reagents or solvents does not produce the same material. Having said this, the synthesis was also reliable, with repeats forming the same material consistently. Although further investigations using this material were not performed due to time limitations, the

exchange of MeCN with H_2O that was seemingly occurring after synthesis when the material was exposed to air suggests that this material might be porous.

4.5 Synthesis of NDI MOFs using Ti clusters as precursors

The synthesis of Ti MOFs is challenging due to the formation of strong, poorly labile bond Ti-O bonds that lead to high rates of nucleation but prevent crystal growth. Previously, covalent chemistry has been used to overcome these issues, with an example being the synthesis of a Ti MOF by reacting the amine containing metal cluster, $Ti_6O_6(O^iPr)_6(abz)_6$, with a di-aldehyde (see Section 4.1.2.3 in this Chapter for more details). The *in-situ* formation of imide bonds occurs, resulting in the MOF being formed.

Due to these known challenges and the difficulties experienced when attempting to synthesise crystalline Zr NDI MOFs (described throughout this Chapter), the synthesis of Ti NDI MOFs was attempted by using covalent chemistry to form the NDI *in-situ.*

4.5.1 Synthesis of Ti_6 aminobenzoate cluster

The $Ti_6O_6(O^iPr)_6(abz)_6$, where abz = aminobenzoate, was synthesised according to a previously reported procedure (Scheme 4.4).[50] PXRD analysis of the crystalline orange product confirmed that the synthesis was successful, with peak positions and intensities of the product matching the pattern simulated from literature. The cluster will be referred to as Ti(abz) in the following text.

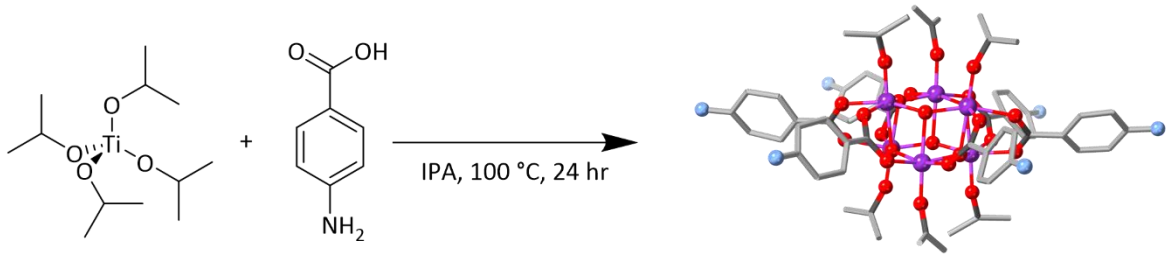

Scheme 4.4 – Synthesis of Ti(abz), including the crystal structure, produced from K. Hong and H. Chun, Inorg. Chem., 2013, 52, 9705–9707, which possesses the formula $Ti_6O_6(O^iPr)_6(abz)_6$.

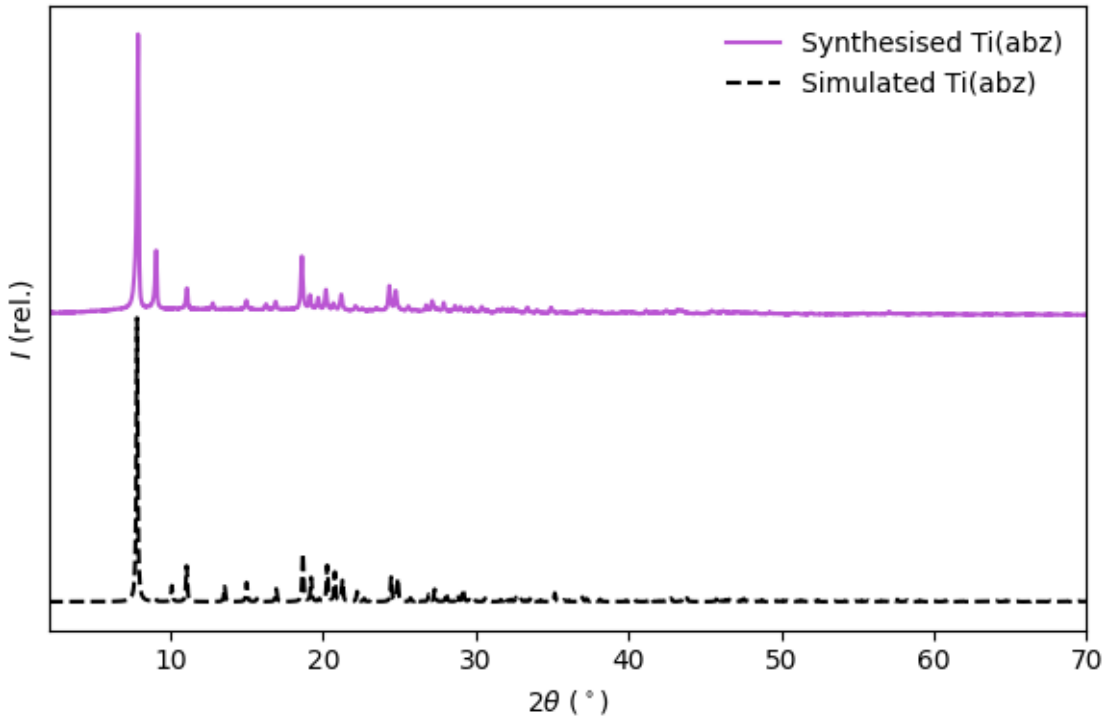

Figure 4.43 – PXRD of synthesised Ti(abz) cluster against data simulated from SCXRD data. CSD code = MINZAM.[50]

The synthesis of a Ti NDI MOF was attempted by trying to carry out the NDI forming reaction between Ti(abz) and 1,4,5,8-naphthalenetetracarboxylic dianhydride (NTCA). This would, potentially, form the NDI and MOF in one-step (Scheme 4.5).

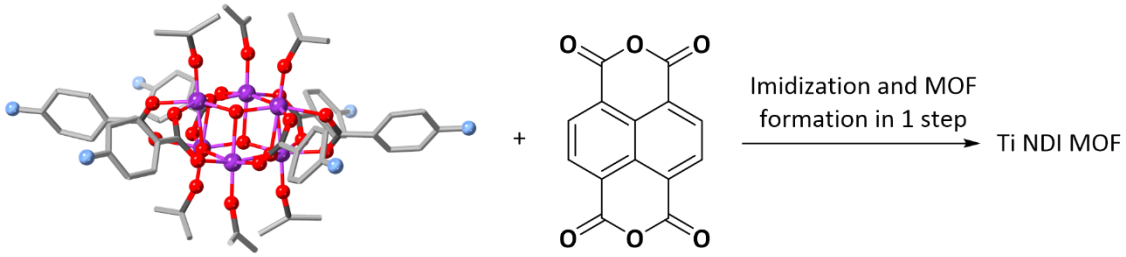

Scheme 4.5 – Suggested preparation for a Ti NDI MOF by carrying an imide-forming reaction between the amino group in the cluster and a dianhydride.

4.5.2 Ti NDI MOF synthesis attempts in DMF and DEF

Attempts to synthesise Ti NDI MOF were first carried out in DMF or DEF, due to DMF being a popular solvent for both MOF and NDI synthesis,[4,32,51] and because of the success with DEF in the formation of Zr-SA-NDI-α, Zr-SA-NDI-β and SA-NDI HOF. Solvothermal reactions were carried out at three temperatures: 80, 100 and 120 °C using a 1:3 ratio of Ti(abz) to NTCA (the

required stoichiometry for complete conversion to the imide to occur). 5 mL of the solvent was used with 50 mg of the cluster and 26 mg of NTCA added in each reaction.

For the reactions carried out in DMF, the reagents readily dissolved before the mixture was placed into the oven, but no precipitate was observed at the end of the reaction. On the other hand, the reagents did not fully dissolve in DEF before heating was carried out. When the reactions conducted in DEF were taken out of the oven, yellow precipitates were obtained (Ti(abz) is yellow-orange and NTCA is off-white), which were washed with DEF and acetone before being allowed to dry in air. The PXRD pattern of the powders (Ti-DEF(5mL)-80, Ti-DEF(5mL)-100 and Ti-DEF(5mL)-120, Figure 4.44) possess a broad peak at low angle (~5° 2θ) which suggests that there was a phase present in the samples which has a large unit cell. However, the lack of diffraction peaks throughout the rest of the patterns and the broadness of the principal reflections suggests that the materials were not very crystalline and/or that the particle size of the materials was very small.

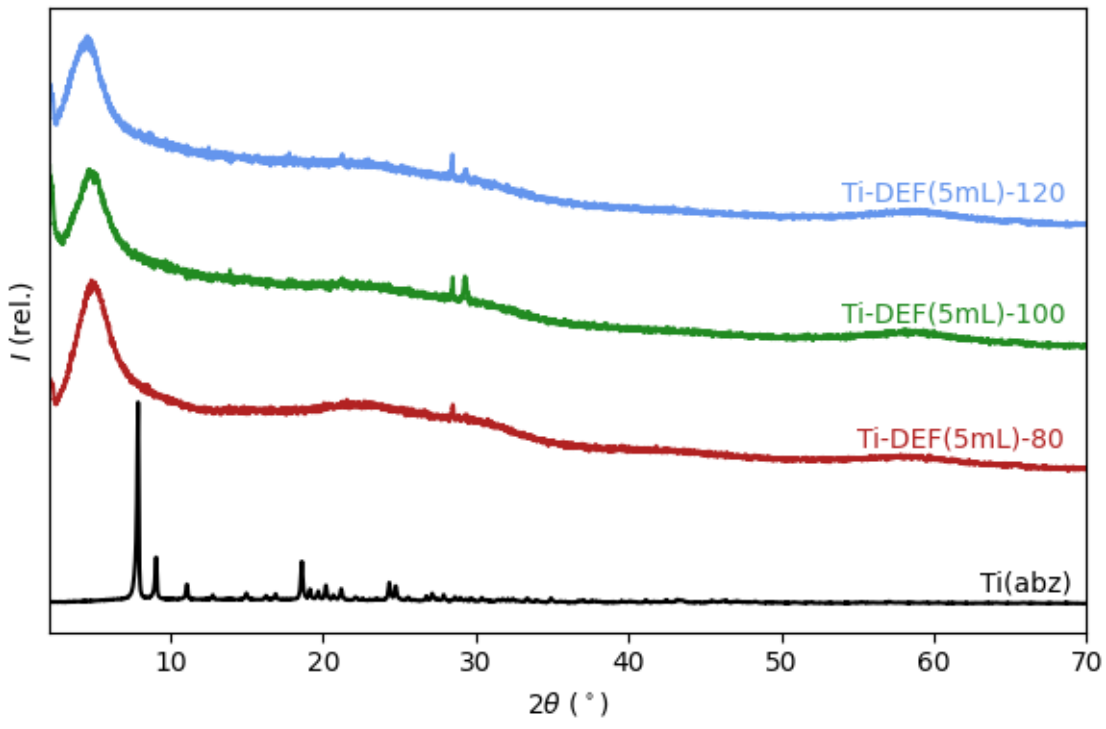

Figure 4.44 – PXRD patterns of black = Ti(abz), red = Ti-DEF(5mL)-80, green = Ti-DEF(5mL)-100 and blue = Ti-DEF(5mL)-120.

FTIR analysis was carried out to try and determine if the bonds associated with an NDI were present in the samples. The carbonyl bond associated with the imide occurs around 1660-1690 cm^{-1} and the C-N bond occurs at 1240-1250 cm^{-1}.[51] The spectra (Figure 4.45) show that

there were no absorption bands in these regions, suggesting that the NDI did not form. Overall, the FTIR spectra of Ti-DEF(5mL)-80, Ti-DEF(5mL)-100 and Ti-DEF(5mL)-120 are similar to the Ti(abz) spectrum, suggesting that the yellow precipitate obtained in these reactions might be Ti(abz), which either did not dissolve in the reaction mixture or re-precipitated from the reaction mixture. The new bands at 1778 and 1735 cm^{-1} are likely due to the imide C=O bonds in DEF that is still present in the samples. Due to the lack of crystallinity in these samples and the FTIR analysis providing no evidence of imidisation, reactions in DEF were discontinued.

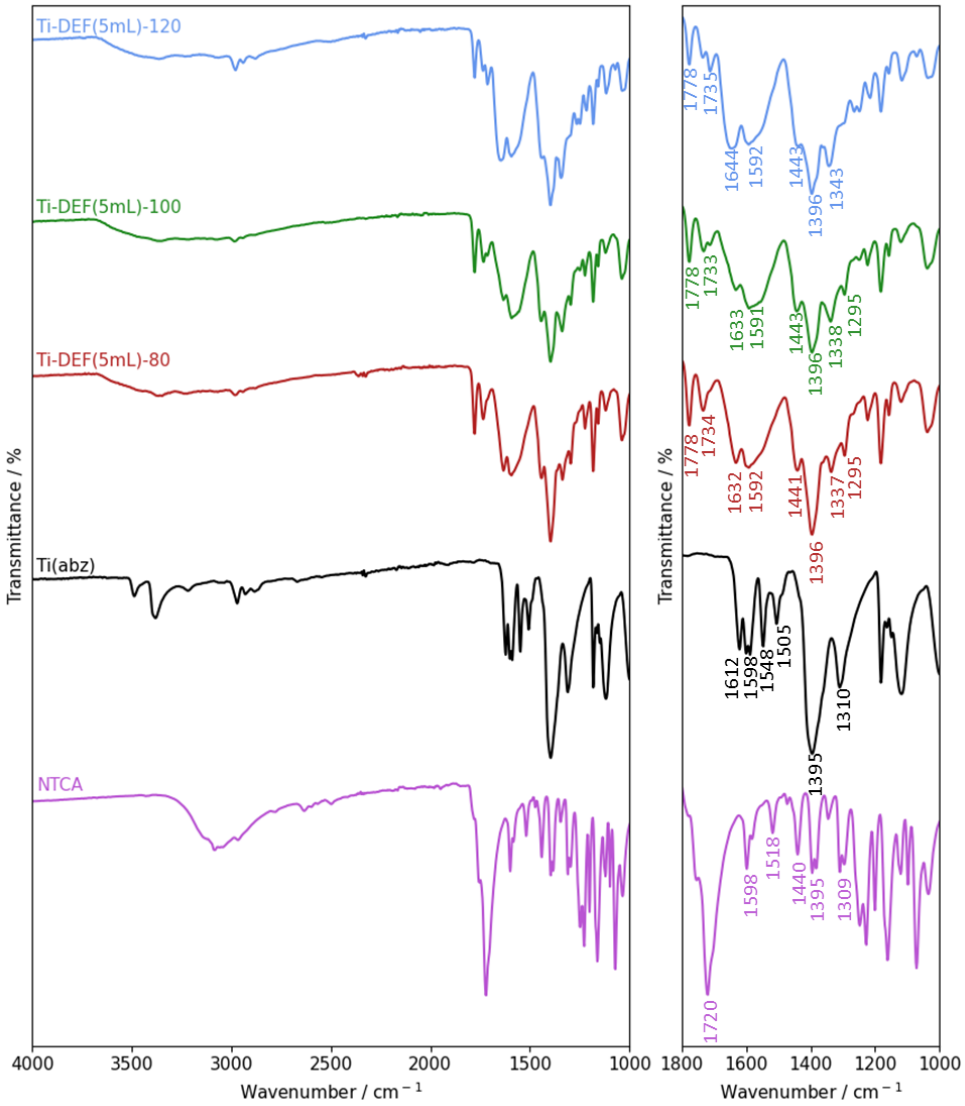

Figure 4.45 - FTIR spectra of purple = NTCA, black = Ti(abz), red = Ti-DEF(5mL)-80, green = Ti-DEF(5mL)-100 and blue = Ti-DEF(5mL)-120. NTCA: anhydride C=O (1720), Ti(abz): NH_2 (3486, 3380), abz C=O (1612, 1598).

4.5.3 Ti NDI MOF synthesis in DMF – varying the volume of solvent and temperature

The next set of reactions were attempted in DMF and the amount of DMF was varied from 1 to 4 mL (all other masses were kept the same) to see if changing the concentration of reagents had any impact on the materials produced. Two sets of reactions were carried out, one at 100 °C and the other at 140 °C. In all reactions, the reagents readily dissolved in the DMF before being heated.

Out of the reactions conducted at 100 °C, only Ti-DMF(1mL)-100 yielded any solid product, a yellow gel-like material. The PXRD (Figure 4.46) carried out directly on the gel (named Ti-DMF(1mL)-100) showed that this material was amorphous. After the gel was allowed to dry for four days in air (named Ti-DMF(1mL)-100-dried) and the PXRD analysis repeated, the PXRD pattern showed some crystallinity, suggesting a new phase might have formed.

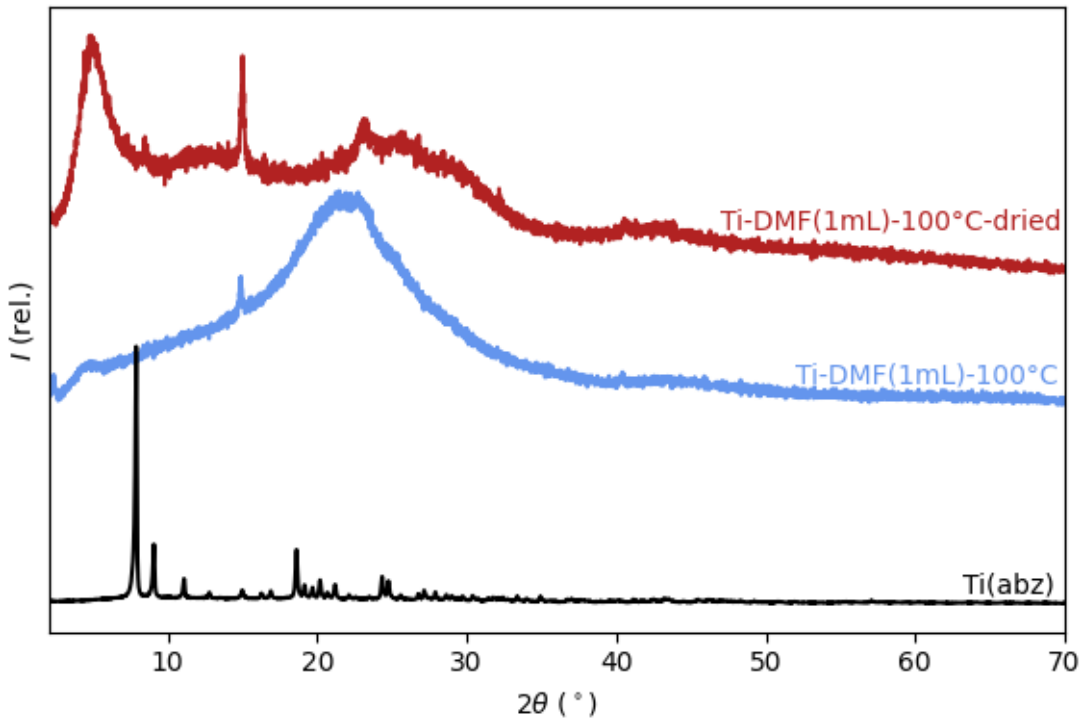

Figure 4.46 – PXRD patterns of black = Ti(abz), blue = Ti-DMF(1mL)-100 and red = Ti-DMF(1mL)-100-dried.

The FTIR spectrum (Figure 4.47) of Ti-DMF(1mL)-100-dried is significantly different to the FTIR spectra of Ti(abz) and NTCA, suggesting that a reaction may have occurred. There is a new absorbance band around 1674 cm^{-1} that may be associated with the C=O group in the imide. This is supported by the band present at 1244 cm^{-1} which indicates the presence of a C-N bond, which would be present if an NDI had formed. The UV-vis spectra (Figure 4.48) of the

Ti(abz) and Ti-DMF(1mL)-100-dried, on the hand, are similar, which is consistent with the fact that both are yellow-orange coloured. Both show broad absorption above 500 nm.

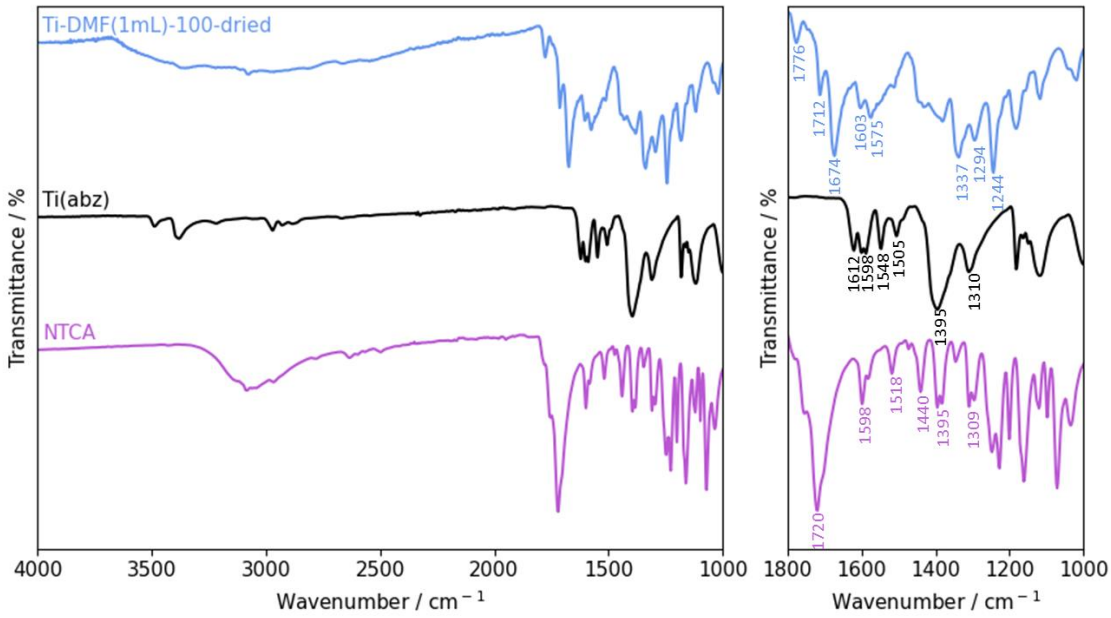

Figure 4.47 - FTIR spectra of purple = NTCA, black = Ti(abz), and blue = Ti-DMF(1mL)-100-dried. The analysis was conducted on the powder formed when the gel-like sample (Ti-DMF(1mL)-100) was placed on a watch glass and allowed to dry in air for 4 days. NTCA: anhydride C=O (1720), Ti(abz): NH_2 (3486, 3380), abz C=O (1612, 1598), Ti-DMF(1mL)-100-dried: imide C=O (1674), imide C-N (1244).

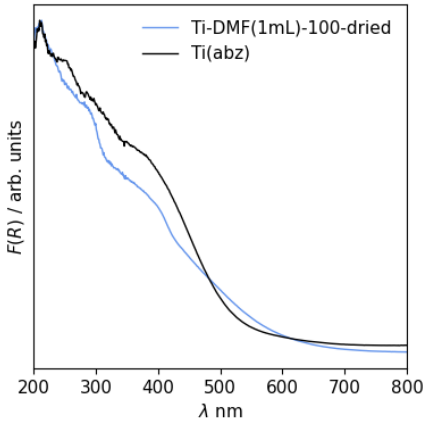

Figure 4.48 – UV-vis spectrum of black = Ti(abz) cluster (black) and blue = Ti-DMF(1mL)-100-dried.

Reactions carried out at 140 °C (Ti-DMF(1mL)-140, Ti-DMF(2mL)-140, Ti-DMF(3mL)-140, and Ti-DMF(4mL)-140) yielded dark brown gel-like materials (Figure 4.49). These materials were placed on a zero-background plate and analysed by PXRD. The PXRD patterns (Figure 4.50) indicated that the gels were amorphous.

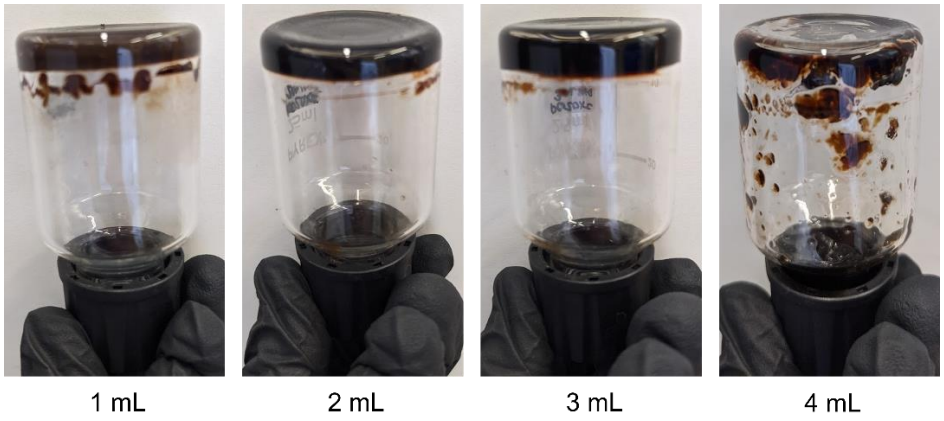

Figure 4.49 – Gel-like materials: Ti-DMF(1mL)-140, Ti-DMF(2mL)-140, Ti-DMF(3mL)-140, and Ti-DMF(4mL)-140.

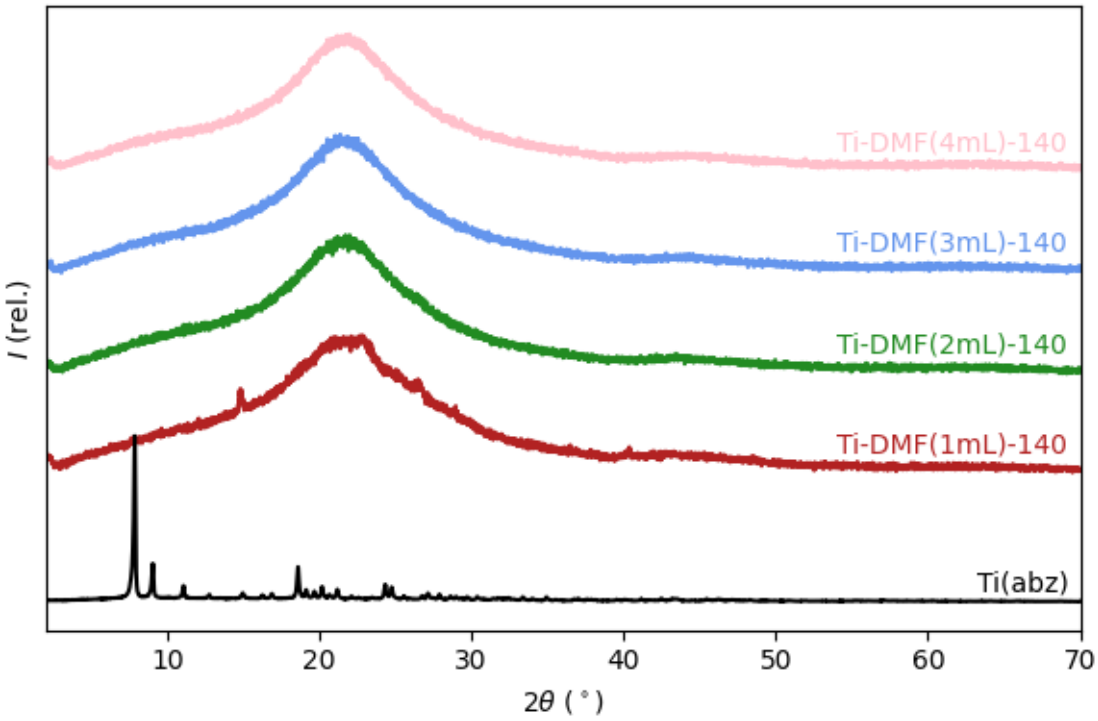

Figure 4.50- PXRD patterns of black = Ti(abz), red = Ti-DMF(1mL)-140, green = Ti-DMF(2mL)-140 and blue = Ti-DMF(3mL)-140, pink = Ti-DMF(4mL)-140. The samples were gel-like and were spread onto a zero-background plate.

As it was expected that the lack of material on the plate (i.e., the use of the unwashed and undried gel) might have prevented some reflections from being recorded, the gel-like material was allowed to dry on a watch glass for four days to give a dark brown powder, before being ground and re-analysed. These PXRD patterns (Figure 4.51) show that the dried samples possess some crystallinity, with some reflections present at low angle.

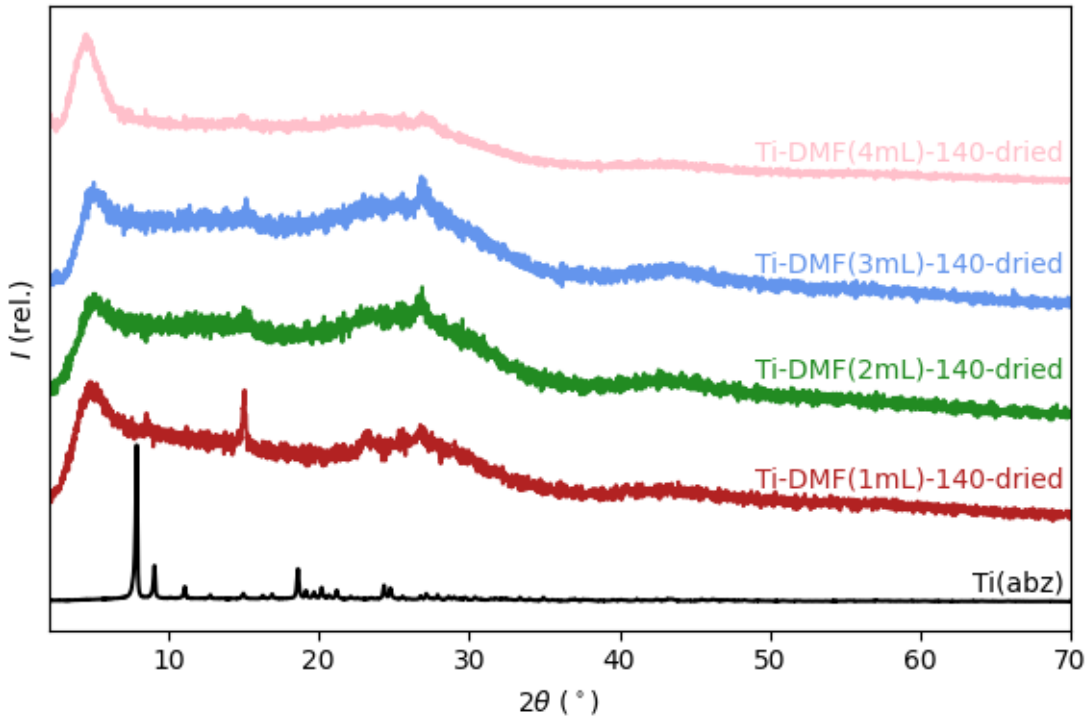

Figure 4.51 - PXRD patterns of black = Ti(abz), red = Ti-DMF(1mL)-140-dried, green = Ti-DMF(2mL)-140-dried and blue = Ti-DMF(3mL)-140-dried, pink = Ti-DMF(4mL)-140-dried. The samples were gel-like and were spread onto a zero-background plate. Gel-like samples were placed on a watch glass and allowed to dry in air for 4 days.

Like Ti-DMF(1mL)-100, the FTIR spectra (Figure 4.52) of these four samples are significantly different to the FTIR spectra of Ti(abz) and NTCA. There is a new absorbance band around 1658-1675 cm^{-1} (the precise value is different across the four samples) that is possibly associated with the C=O group in the imide. This is supported by the band present at 1242-1245 cm^{-1} which indicates the presence of a C-N bond, which would be present if an NDI had formed.

It is worth noting that under the conditions used in these Ti/NDI reactions, the formation of poly(anilines) is possible due the presence of the pendant aniline-like substrate within the Ti cluster that react in a polymerisation reaction with the same substrate in nearby clusters. Having said this, literature suggests that the presence of poly(anilines) is indicated in FTIR by two bands that are around 80-90 cm^{-1} apart at roughly 1580 and 1490 cm^{-1}, that are due to the N-C-N stretch in the quinoid or benzenoid units respectively that occur in poly(anilines).[52–54] As there are no bands present in this region, or at this increment apart, it is unlikely that the formation of poly(anilines) during these reactions is occurring.

The UV-vis spectra (Figure 4.53) of these samples differ that of Ti-DMF(1mL)-100 and from the Ti(abz) in that they have an additional reflectance band, centred around 550 nm, this is consistent with their darker colour. This absorption could be due to a new transition occurring within the Ti NDI MOF that may have formed, for example, ligand-to-metal charge from the NDI to the Ti is possible and has been reported previously.[43,55]

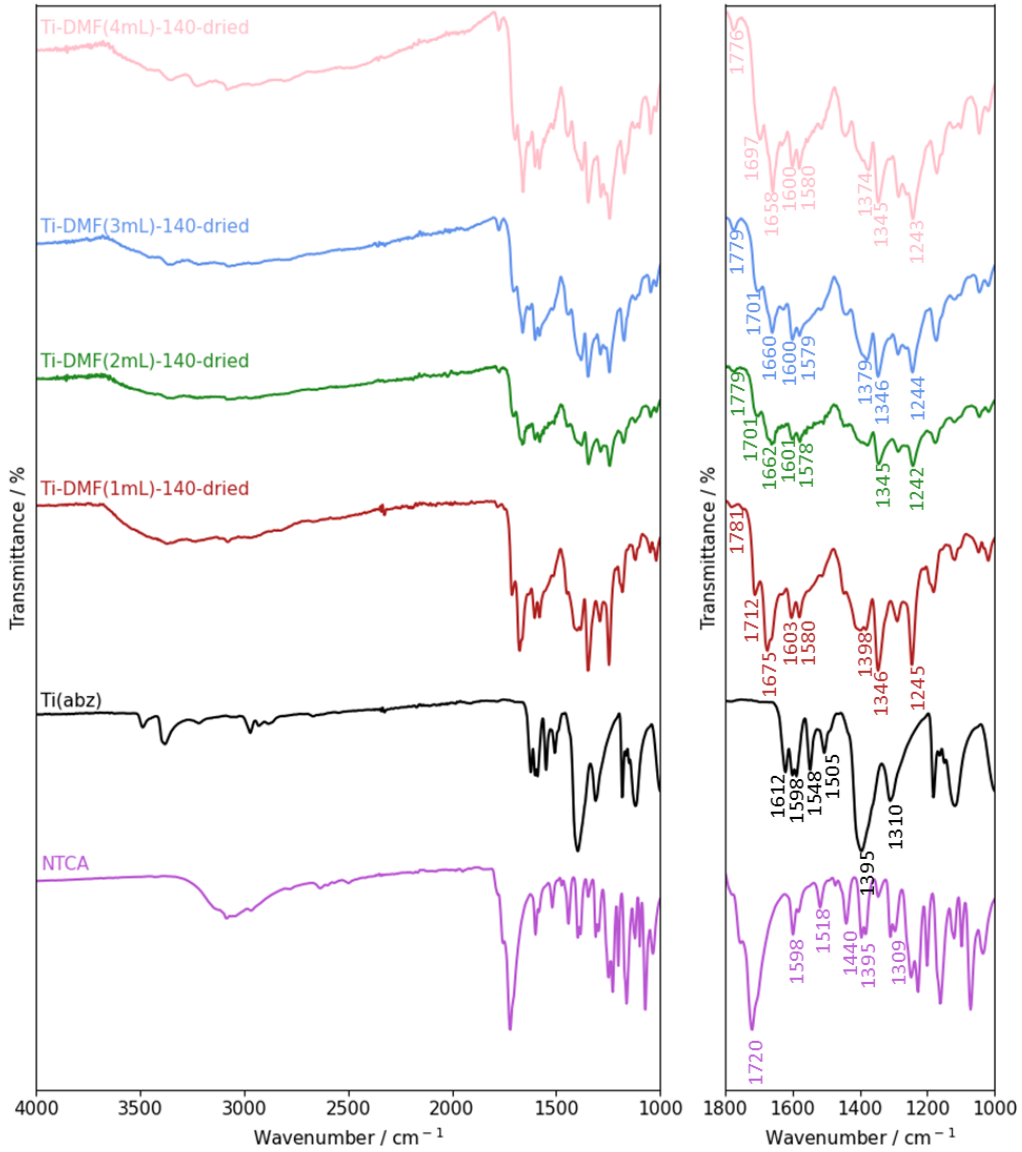

Figure 4.52 – FTIR spectra of purple = NTCA, black = Ti(abz), red = Ti-DMF(1mL)-140-dried, green = Ti-DMF(2mL)-140-dried and blue = Ti-DMF(3mL)-140-dried, pink = Ti-DMF(4mL)-140-dried. The analysis was conducted on the powders formed when the gel-like samples were placed on a watch glass and allowed to dry in air for 4 days. NTCA: anhydride C=O (1720), Ti(abz): NH_2 (3486, 3380), abz C=O (1612, 1598), Ti-DMF(1-4mL)-140-dried: imide C=O (1658-1675), imide C-N (1242-1245).

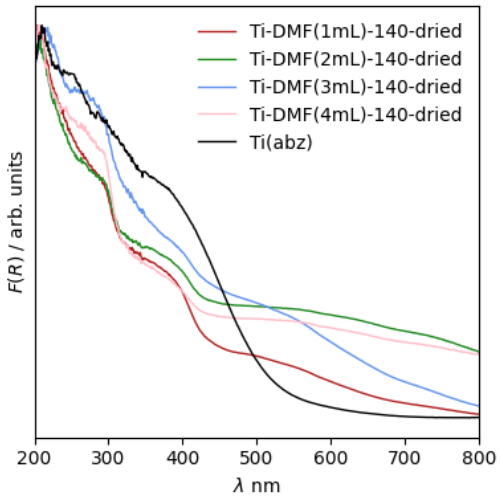

Figure 4.53 – UV-vis spectrum of black = Ti(abz), red = Ti-DMF(1mL)-140-dried, green = Ti-DMF(2mL)-140-dried and blue = Ti-DMF(3mL)-140-dried, pink = Ti-DMF(4mL)-140-dried. The analysis was conducted on the powders formed when the gel-like samples were placed on a watch glass and allowed to dry in air for 4 days.

4.5.4 Ti NDI MOF synthesis – use of modulators

To see if any improvements could be made to the crystallinity of the materials obtained in these attempts to form Ti NDI MOFs, modulators were employed in further reactions. Three monocarboxylic acids (BA = benzoic acid, FA = formic acid, and AA = acetic acid) were added to reactions containing the same loading of Ti(abz) and NTCA, with 2 mL of DMF. Again, two sets of reactions were carried out, one set at 100 °C and the other at 140 °C.

In the reactions carried out at 100 °C, named Ti-DMF(2mL)-100-BA, Ti-DMF(2mL)-100-FA and Ti-DMF(2mL)-100-AA, a yellow precipitate was produced. The PXRD patterns (Figure 4.54) shows that for all three modulators, a crystalline phase was obtained, with sharper reflections than in un-modulated reactions. The positions and intensities of the peaks do not correspond with those of Ti(abz) suggesting that a new phase was formed.

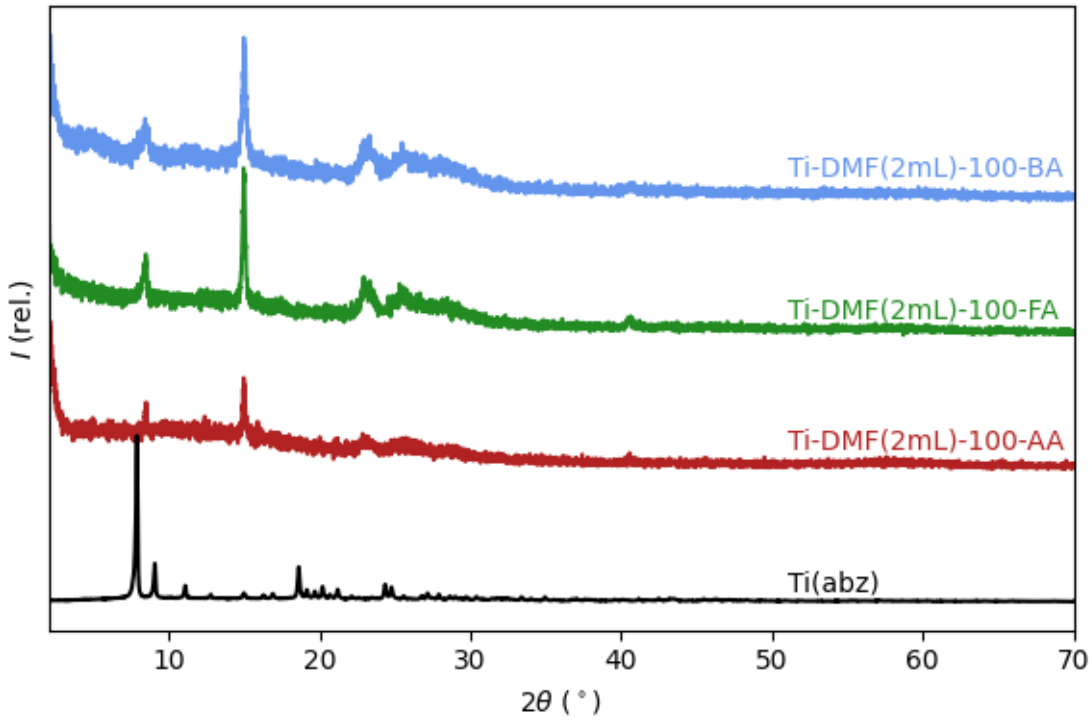

Figure 4.54 - PXRD patterns of black = Ti(abz), red = Ti-DMF(2mL)-100-AA, green = Ti-DMF(2mL)-100-FA and blue = Ti-DMF(2mL)-100-BA.

The FTIR spectra (Figure 4.55) of these samples show similar absorbance bands to the reactions that were carried out with no modulator. As mentioned previously, this could suggest the presence of an NDI in these samples. The UV-vis spectra of these samples (Figure 4.56, excluding Ti-DMF(2mL)-100-AA due to too little powder being available for this analysis) shows that these sample are similar to that of Ti(abz) and Ti-DMF(1mL)-100, with absorbance below 500 nm. This is consistent with these materials being yellow-orange.

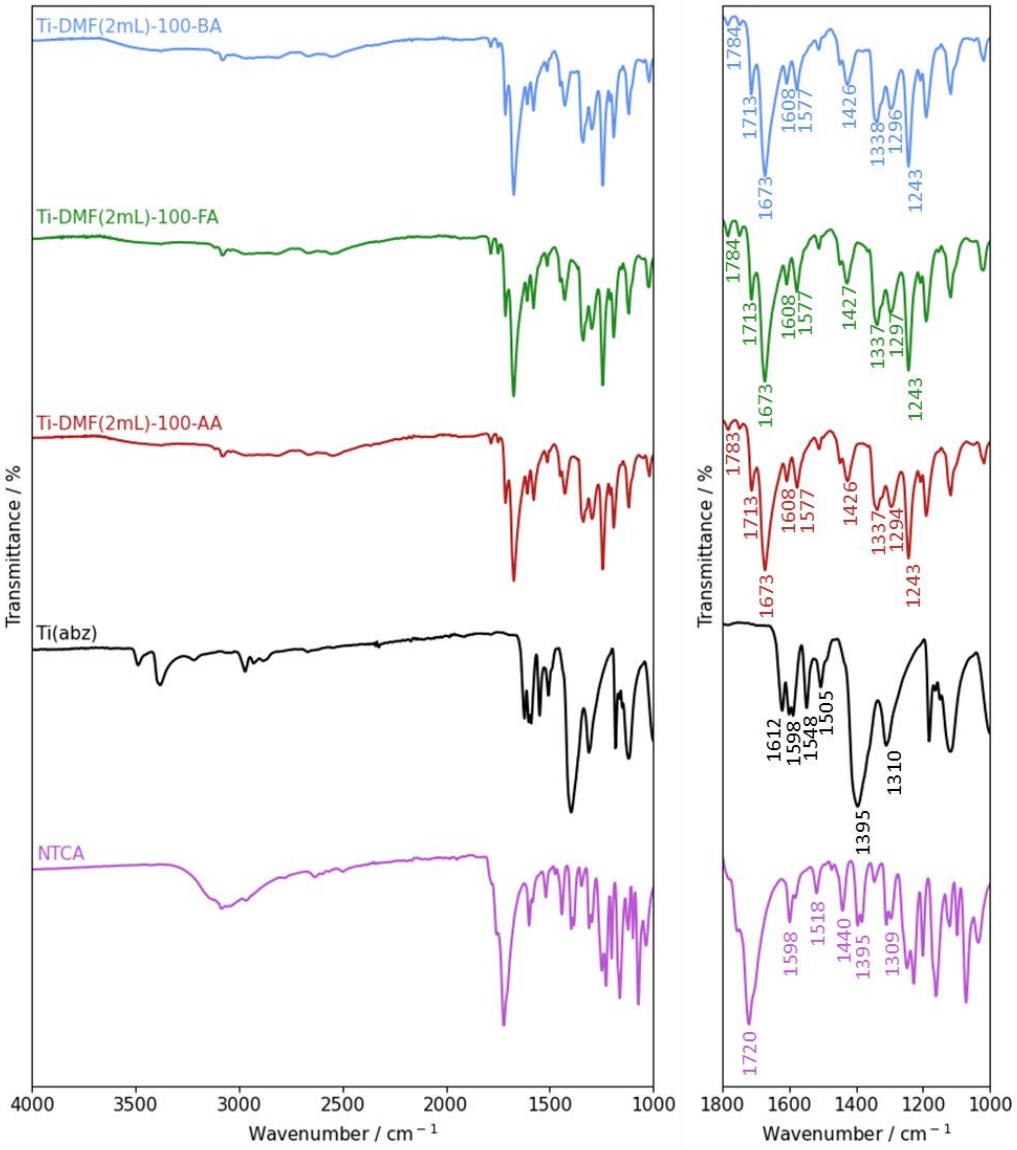

Figure 4.55 - FTIR spectra of purple = NTCA, black = Ti(abz), red = Ti-DMF(2mL)-100-AA, green = Ti-DMF(2mL)-100-FA and blue = Ti-DMF(2mL)-100-BA. Analysis was conducted on the yellow powders. NTCA: anhydride C=O (1720), Ti(abz): NH_2 (3486, 3380), abz C=O (1612, 1598), Ti-DMF(2mL)-100-AA/FA/BA: imide C=O (1673), imide C-N (1243).

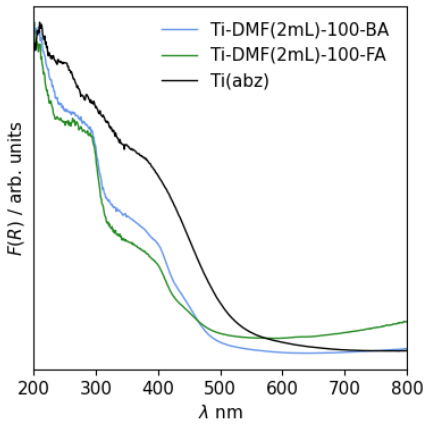

Figure 4.56 - UV-vis spectra of black = Ti(abz), green = Ti-DMF(2mL)-100-FA and blue = Ti-DMF(2mL)-100-BA.

In the reactions carried out at 140 °C, named Ti-DMF(2mL)-140-BA, Ti-DMF(2mL)-140-FA and Ti-DMF(2mL)-140-AA, dark brown gel-like materials were formed, which were placed directly onto a zero-background and analysed by PXRD. Like the modulated reactions conducted at 100 °C, the patterns (samples not labelled with “dried”, Figure 4.57) showed that a crystalline material had been formed, with new peaks that do not correspond to the Ti(abz) phase. This is different to the brown gels that were synthesised at 140 °C with no modulator (see Figure 4.50), which had to be dried before a significant number of reflections could be observed.

The use of benzoic acid (Ti-DMF(2mL)-140-BA, blue curves) produced the most crystalline material, indicated by sharper and stronger reflections in the PXRD pattern. It is possible that the shape, size and chemistry of benzoic acid corresponds well to aminobenzoic acid and therefore reversibly replaces the abz in the Ti(abz), preventing the NDI forming reaction, which in turn slows down the formation of the MOF structure, giving rise to an increase in crystallinity compared to when no or other modulators are used. It is also possible that the reaction conditions provided the correct environment for the formation of a Ti cluster where the aminobenzoate is replaced with benzoate. Unfortunately, the structure of a Ti benzoate cluster has not been reported before, so it is not possible to compare the PXRD pattern to a simulated pattern and determine whether this cluster is present. Indexing of the powder pattern was attempted, but all results had poor fits and a large number of unindexed reflections.

Drying the gels in air for four days gave a brown powder and slight changes in the resulting PXRD (samples labelled with “dried”, Figure 4.57). Reflections became more intense in Ti-DMF(2mL)-140-AA-dried and Ti-DMF(2mL)-140-FA-dried. In DMF(2mL)-140-BA-dried, the intensity of second reflection was significantly reduced, and other reflections at higher angles become more intense. This is likely due to the loss of solvent improving the crystallinity of this sample.

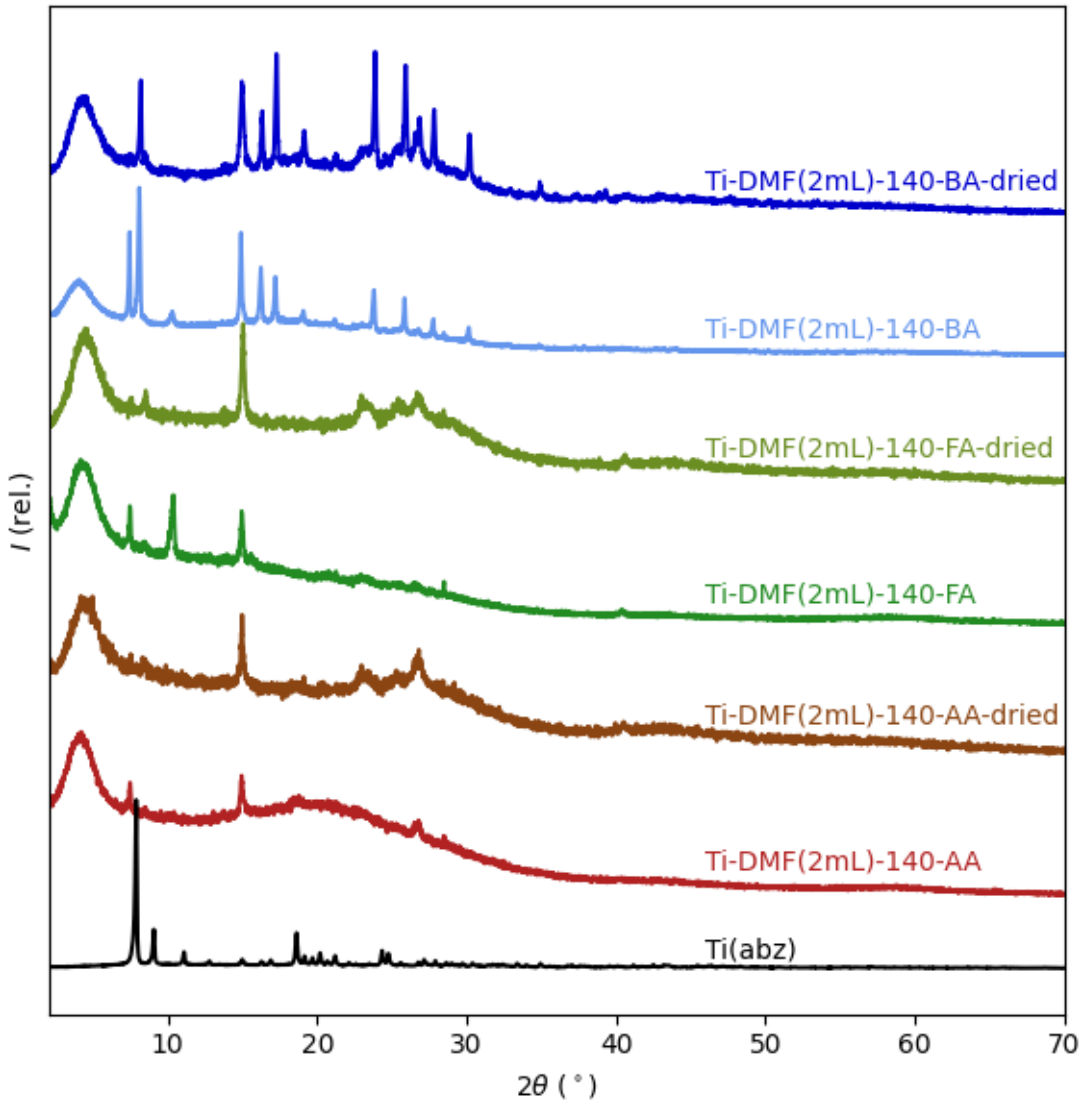

Figure 4.57 - PXRD patterns of black = Ti(abz), red = Ti-DMF(2mL)-140-AA, brown = Ti-DMF(2mL)-140-AA-dried green = Ti-DMF(2mL)-140-FA, olive = Ti-DMF(2mL)-140-FA-dried, light blue = Ti-DMF(2mL)-140-BA, and dark blue = Ti-DMF(2mL)-140-BA -dried. Non-dried samples were gel-like and were spread onto a zero-background. To create the "dried" samples, the gel-like samples were placed on a watch glass and allowed to dry in air for 4 days.

FTIR analysis (Figure 4.58) of the three dried samples shows that the bonds that could be associated with the formation of the NDI (C=O at 1674 cm^{-1} and C-N at 1244 cm^{-1} in imide) were present in the sample. The UV-vis spectra of these samples are consistent with the materials synthesised at 140 °C without modulation; they have an additional absorbance band (compared to Ti(abz)) at around 550 nm.

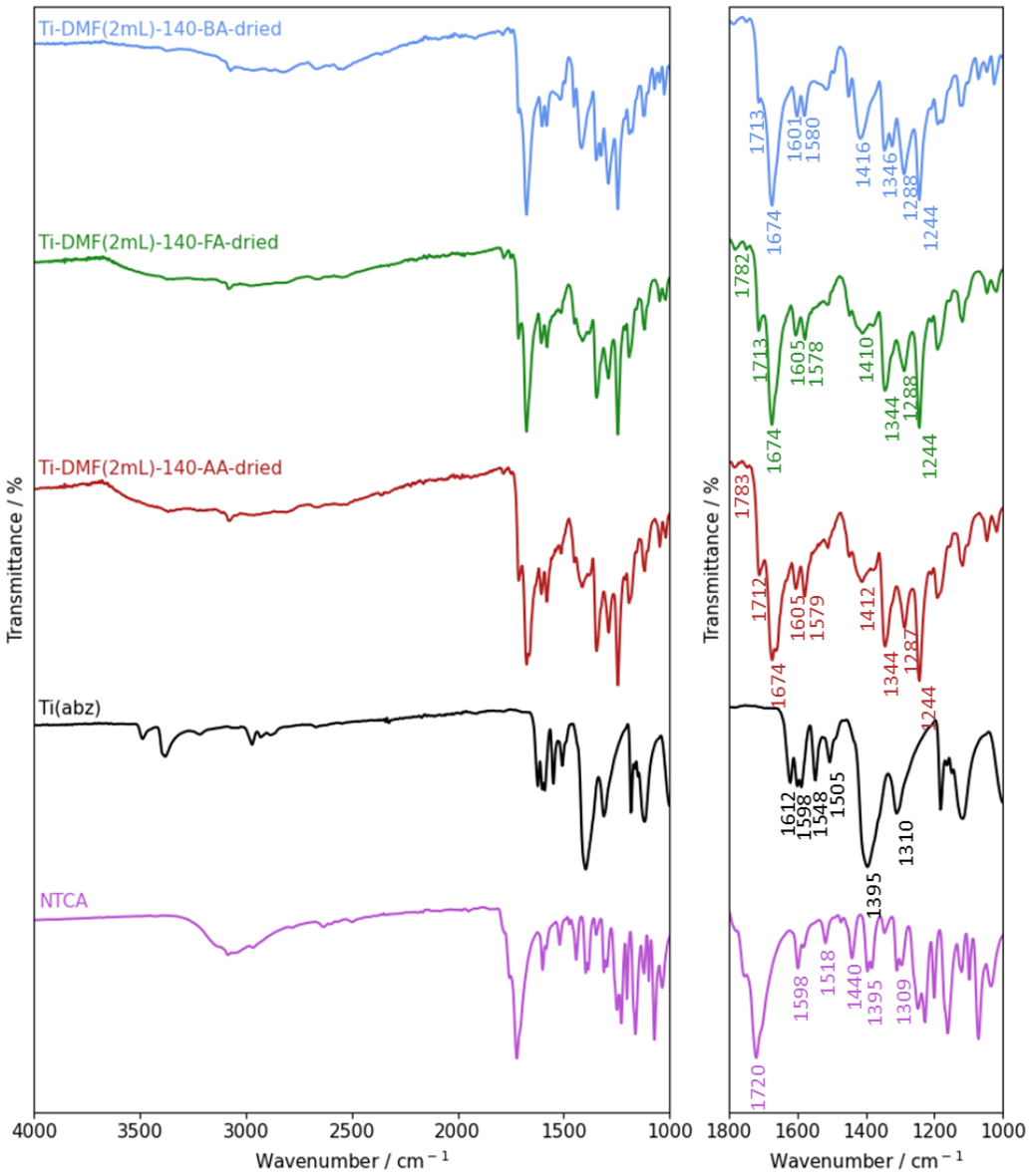

Figure 4.58 – FTIR spectra of purple = NTCA, black = Ti(abz), red = Ti-DMF(2mL)-140-AA-dried, green = Ti-DMF(2mL)-140-FA-dried and blue = Ti-DMF(2mL)-140-BA-dried. Analysis was conducted on the powders formed when the gel-like samples were placed on a watch glass and allowed to dry in air for 4 days. NTCA: anhydride C=O (1720), Ti(abz): NH_2 (3486, 3380), abz C=O (1612, 1598), Ti-DMF(2mL)-140-AA/FA/BA-dried: imide C=O (1674), imide C-N (1244).

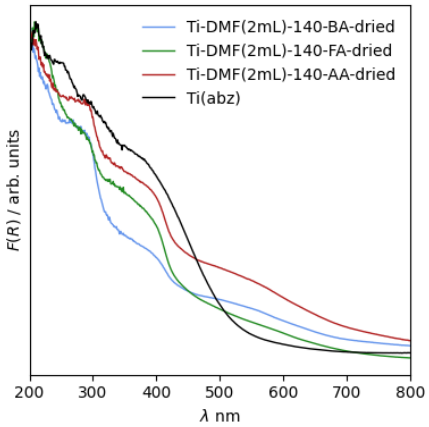

Figure 4.59 - UV-vis spectra of black = Ti(abz), red = Ti-DMF(2mL)-140-AA-dried, green = Ti-DMF(2mL)-140-FA-dried and blue = Ti-DMF(2mL)-140-BA-dried. Analysis was conducted on the powders formed when the gel-like samples were placed on a watch glass and allowed to dry in air for 4 days.

TGA was also conducted on these samples to determine the thermal stability of these materials. Ti-DMF(2mL)-140-BA exhibits an initial mass loss below 120 °C (5%) that is attributed to a low boiling solvent being present in the sample. As this was reaction was conducted was in DMF, this is unexpected, but it is possible that the sample has absorbed some H_2O from the air whilst it was placed on a watch glass to dry. All three samples start to degrade at around 220 °C and are completely degraded at 500 °C. The mass remaining at high temperature is likely due to TiO_2 which would be produced as the samples were burnt in air.

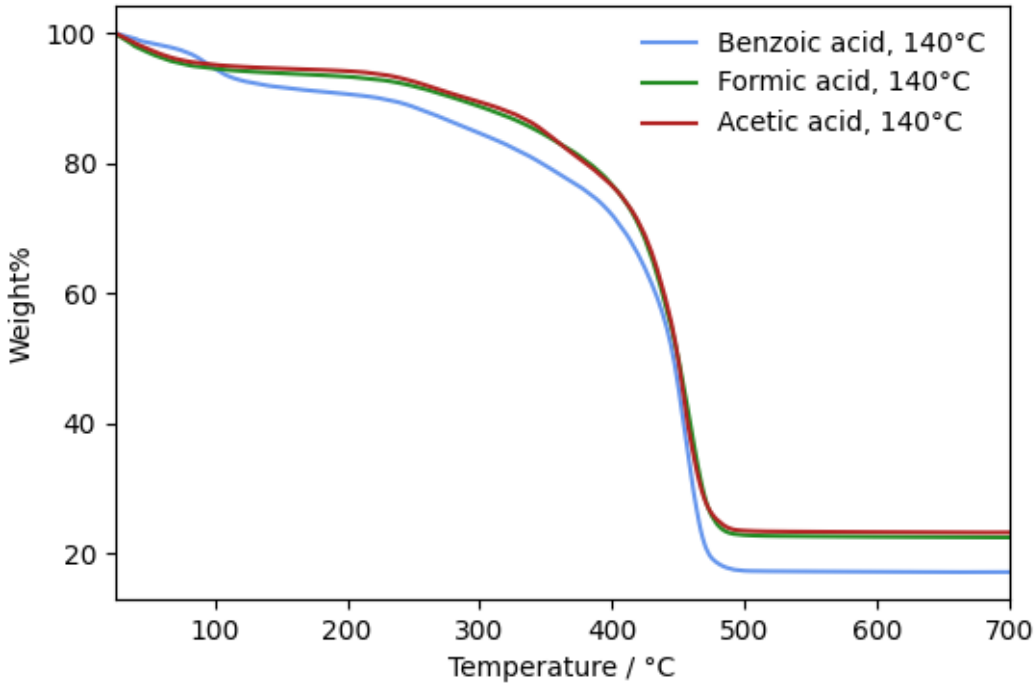

Figure 4.60 – TGA of black = Ti(abz), red = Ti-DMF(2mL)-140-AA-dried, green = Ti-DMF(2mL)-140-FA-dried and blue = Ti-DMF(2mL)-140-BA-dried.

The TGA was used to estimate the ratio of Ti to NDI that might be present in the samples. Assuming that the material left at the end of the thermogram is TiO_2, then the percentage of the material that corresponds to the $Ti_6O_6(O^iPr)_6$ cluster can be determined by finding the percentage of Ti in the sample and dividing this by the molecular weight of 6 Ti atoms (287.202 g mol^{-1}) and multiplying by the molecular weight of the entire cluster (737.736 g mol^{-1}). This percentage can then be taken away from the total weight% of the framework and then the ratios of NDI to cluster can be found by dividing by the molecular weights of each. The calculations (shown in Table 4.7) show that Ti-DMF(2mL)-140-AA and Ti-DMF(2mL)-140-FA both contain fewer NDI than would be expected if a Ti-NDI-NOF has formed (the expected ratio of cluster to NDI is 1:3). This could suggest that these samples may still contain some of the Ti(abz) starting material. The Ti-DMF(2mL)-140-BA contains a higher ratio of NDI, around 2.6, which is closely to the expected value that the MOF may have. This is consistent with the fact that this material is significantly more crystalline than Ti-DMF(2mL)-140-AA and Ti-DMF(2mL)-140-FA.

Table 4.7 – Calculations carried out to estimate the ratio of Ti to NDI in attempted Ti NDI MOF reactions.

	Ti-DMF(2mL)-140-AA	**Ti-DMF(2mL)-140-FA**	**Ti-DMF(2mL)-140-BA**
% remaining (TiO_2)	23.16	22.39	17.08
% Ti % TiO_2 * (MW Ti / MW TiO_2)	13.88	57.57	63.32
% Ti cluster in sample (% Ti / MW of 6Ti) * MW of $Ti_6O_6(O^iPr)_6$	35.66	34.47	26.30
% total framework	71.23	70.99	73.56
% NDI % total framework - % cluster	35.57	36.52	47.26
% cluster / MW cluster	0.048	0.047	0.036
% NDI / MW NDI	0.071	0.072	0.093
Ratio of NDI:Ti	1.46	1.55	2.63

To establish whether the FTIR absorbance bands at approximately 1674 cm^{-1} in these samples could be due to the C=O bond in any remaining DMF present in the powders, the samples were dried in the oven at 200 °C (boiling point of DMF is 153 °C) for four hours. Unfortunately, PXRD analysis (Figure 4.61) shows that a significant reduction in the crystallinity of the samples had occurred, indicated by the broadening of reflections and reductions in their intensities. This indicates that calcination at 200 °C is resulting in degradation of the structure

and is not an effective way of purifying these materials. Despite this, the FTIR spectra (Figure 4.62) of the heat-treated materials shows no significant changes, so although the crystallinity of the material has been impacted, heat treatment does not appear to have changed the functional groups present, at least those that are observed in the FTIR analysis.

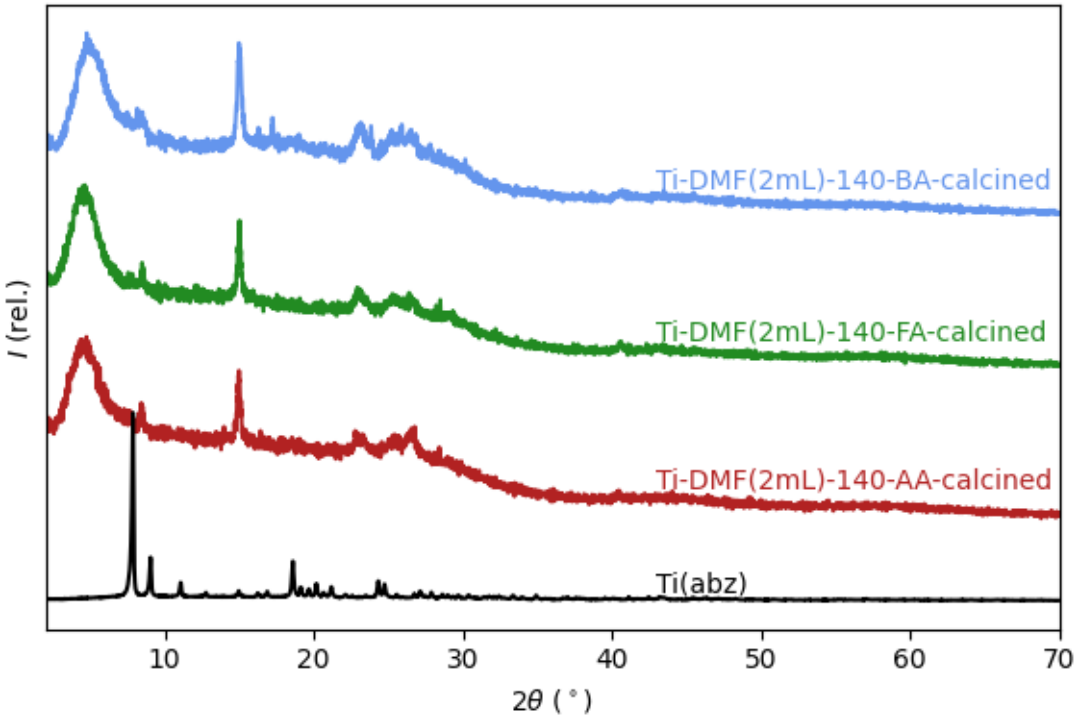

Figure 4.61 - PXRD patterns of black = Ti(abz), red = Ti-DMF(2mL)-140-AA-calcined, green = Ti-DMF(2mL)-140-FA-calcined and blue = Ti-DMF(2mL)-140-BA-calcined. Gel-like samples were placed on a watch glass and allowed to dry in air for 4 days. These samples were then dried in oven at 200°C for 4 hours.

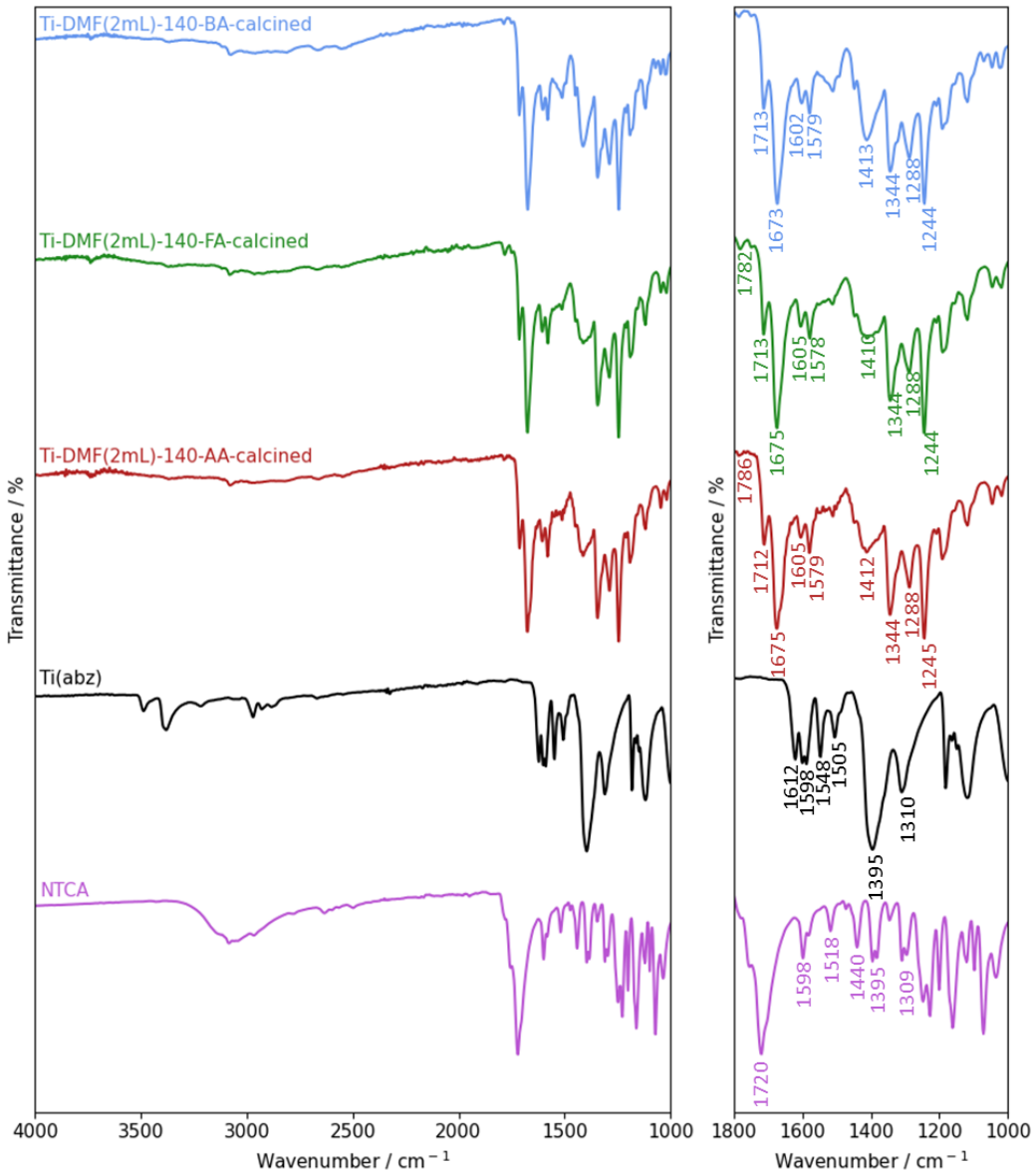

Figure 4.62 - FTIR spectra of purple = NTCA, black = Ti(abz), red = Ti-DMF(2mL)-140-AA-calcined, green = Ti-DMF(2mL)-140-FA-calcined and blue = Ti-DMF(2mL)-140-BA-calcined. The analysis was conducted on the powders formed when the gel-like samples were placed on a watch glass and allowed to dry in air for 4 days, and then placed in the oven at 200°C for 4 hours. NTCA: anhydride C=O (1720), Ti(abz): NH_2 (3486, 3380), abz C=O (1612, 1598), Ti-DMF(2mL)-140-AA/FA/BA-calcined: imide C=O (1673-1675), imide C-N (1244-1245).

Although there was not enough time to make significant progress in making Ti NDI MOFs, the work described here shows that the synthesis of some crystalline materials was achieved, particular where benzoic acid was used as a modulator. PXRD, TGA and UV-vis data suggested that Ti-DMF(2mL)-140-BA could be a Ti-NDI MOF, but further investigations would need to be carried out to properly determine if this is the case and to rule out the formation of a Ti benzoate cluster during this reaction. Ideally, further syntheses would be carried out to produce crystalline materials that could be analysed with SCXRD.

4.6 Synthesis of dimethyl terephthalic acid NDI MOFs

4.6.1 Synthesis of *N,N'*-Di-(2,6-dimethyl-4-benzoic acid)-1,4,5,8-naphthalenetetracarboxydiimide (DM-NDI)

N,N'-Di-(2,6-dimethyl-4-benzoic acid)-1,4,5,8-naphthalenetetracarboxydiimide (DM-NDI) was synthesised according to previously reported procedure,[56] shown in Scheme 4.6, obtaining an off-white powder in 67% yield.

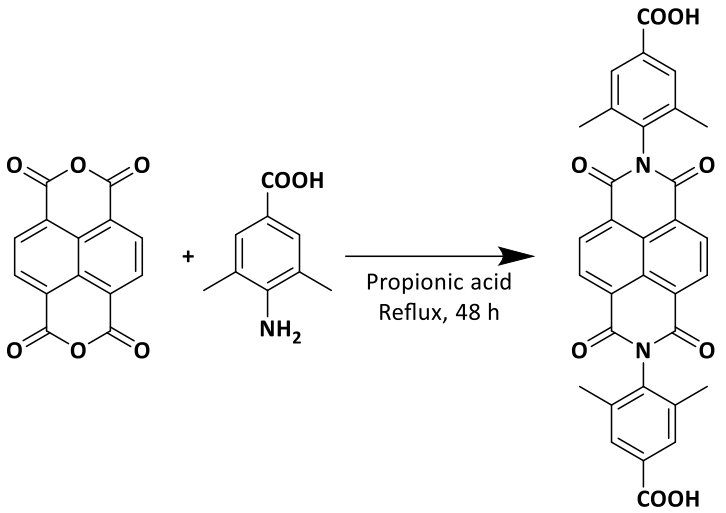

Scheme 4.6 - Synthesis of N,N'-Di-(2,6-dimethyl-4-benzoic acid)-1,4,5,8-naphthalenetetracarboxydiimide.

4.6.2 Synthesis of DM-NDI MOFs

Previously, DM-NDI was used to make a Zr(IV) UiO-type MOF that exhibited promising reductive properties.[21] As such, attempts were made to synthesise this MOF, using Hf(IV) instead of Zr(IV) as the metal ion. The reaction conditions used (Scheme 4.7) were adapted from the previous report of this MOF but a temperature of 120 °C was used here instead of 100 °C, as no crystalline product was observed by PXRD when the reaction was carried out at 100 °C.

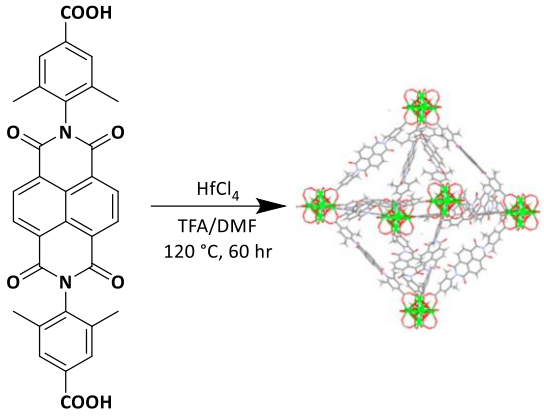

Scheme 4.7 - Reaction conditions used to synthesise DM-NDI-UiO(Hf) MOF. A metal to linker ratio of 1:1 and 20 equivs. of TFA were used. Schematic representation of the octahedron cage of the MOF is adapted with permission from *Chem. Mater*. 2018, **30**, 2488−2492. Copyright 2018 American Chemical Society. Hf = green, O = red, N = blue, C = grey.[35]

The reaction gave a light pink precipitate which was analysed by PXRD. In order to confirm that the desired MOF structure has been formed, a model of the expected structure was developed by modifying a previously reported UiO structure with a linker of similar length.[57] The PXRD pattern of my product (Figure 4.63) is consistent with the simulated pattern and the reflections at low degrees 2θ (2θ = 3.9 and 4.5°) confirming that the fcu-topology that is associated with the UiO family of MOFs is present.[58] The pattern exhibits significant peak broadening, likely due to small crystallite size of the powder, confirmed by SEM, see below.

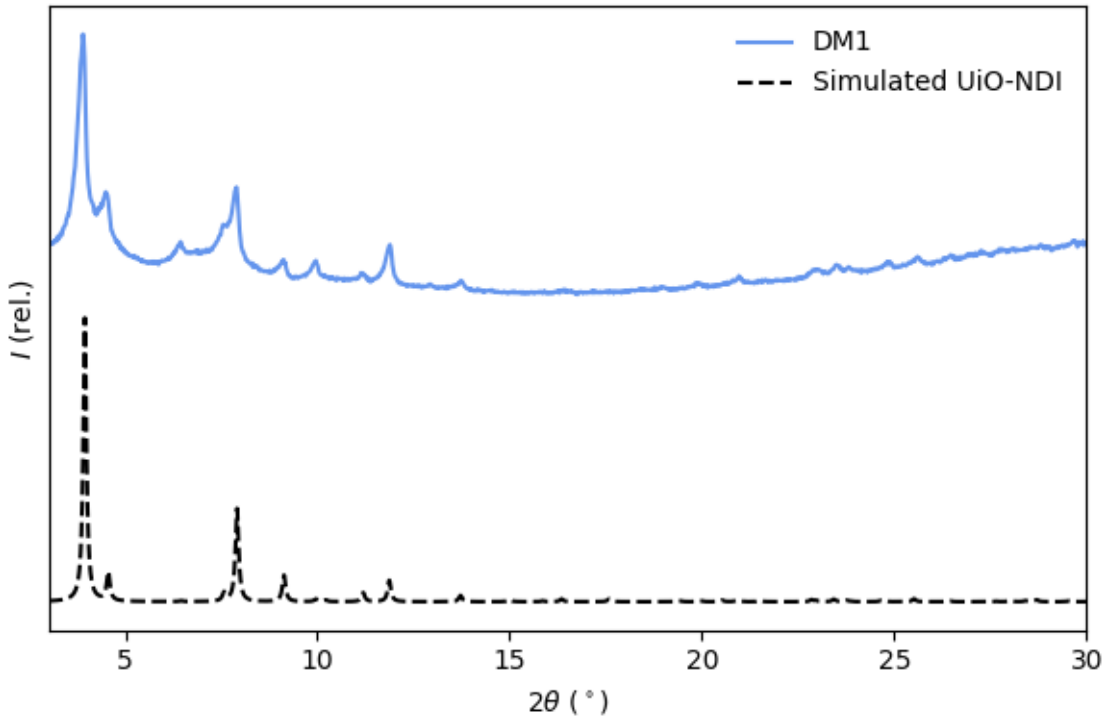

Figure 4.63 - PXRD pattern of DM-NDI-UiO(Hf) MOF, and simulated pattern of the modelled structure. The model structure was developed from a previously reported structure (CSD code RUBYOE).[57]

SEM imaging (Figure 4.64) of the powder also supports the presence of the UiO topology; the typical octahedral crystal (~0.5 – 1 μm) is seen.[21,58]

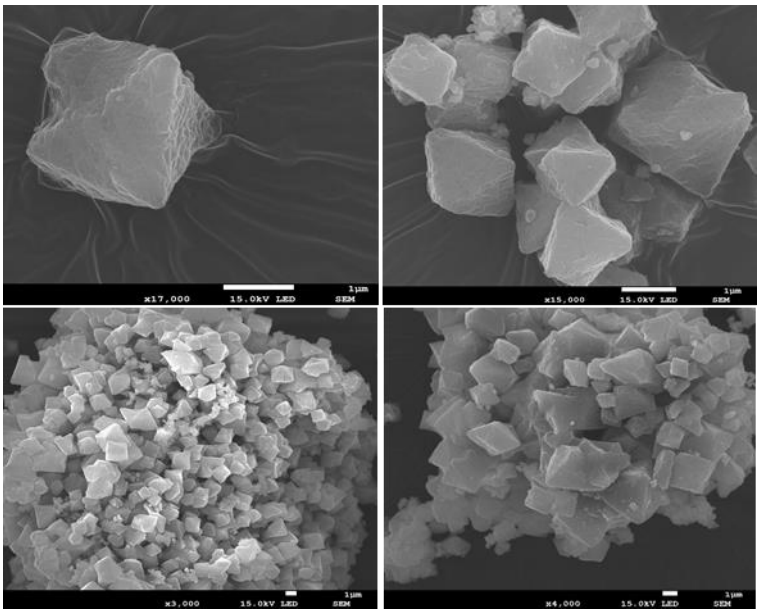

Figure 4.64 - SEM images of DM-NDI-UiO(Hf) MOF. Scale bars: top left = 1 µm, top right = 1 µm, bottom left = 1 µm, bottom right = 1 µm.

In order to obtain enough material to conduct further experiments and analysis, the synthesis of DM-NDI-UiO(Hf) was repeated. Unfortunately, although the same reaction conditions were

used, six repeats (DM2a, DM2b, DM2c, DM2d, DM2e, DM2f; the original successful synthesis is labelled DM1) yielded an amorphous powder, as shown by PXRD (Figure 4.65).

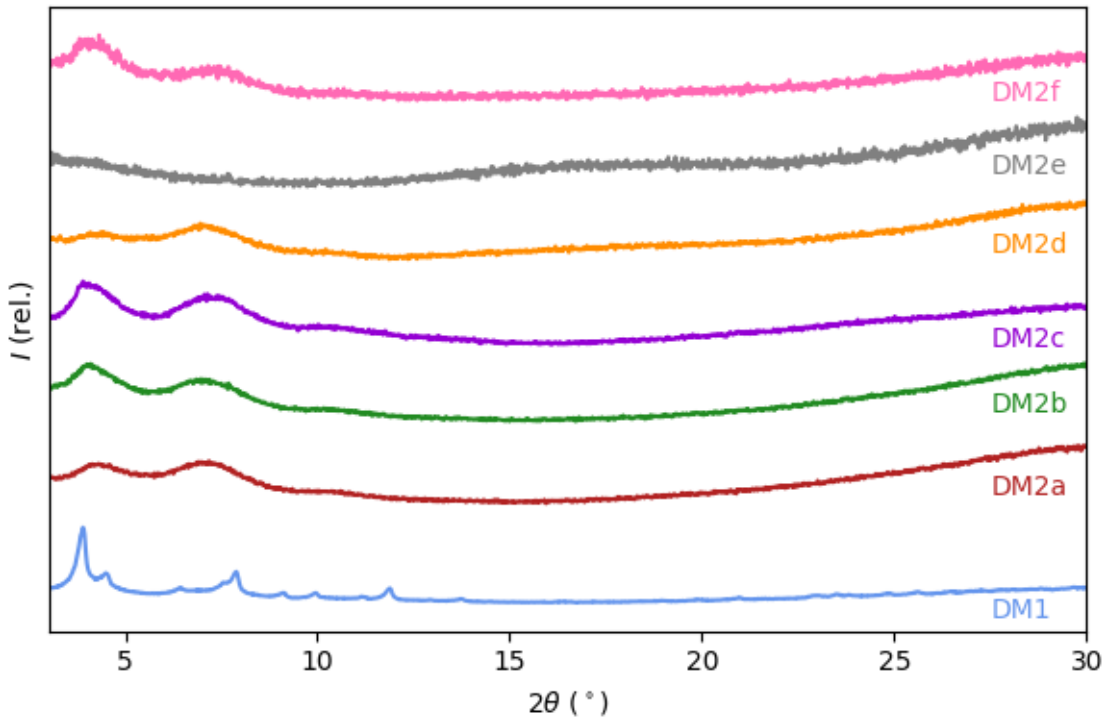

Figure 4.65 – PXRD patterns of DM1, DM2a, DM2b, DM2c, DM2d, DM2e and DM2f.

Further attempts were carried out varying reaction solvent, TFA equivalents, and heating method in attempts to synthesise a crystalline product and to gain an understanding of what might be prohibiting the crystallisation of DM-NDI-UiO(Hf) MOF (Table 4.8).

Table 4.8 - Variables changed in attempted syntheses of DM-NDI-UiO(Hf).

Sample ID	Solvent	Equivalents of TFA	Colour of precipitate
DM1	DMF	19	Pale pink
DM2	DMF	19	Various (brown/grey/pink)
DM3	DMF	10	Pale purple
DM4	DMF	38	Bright pink
DM5	DEF	18	Pale brown
DM6	DMA	19	Dark brown

PXRD analysis (Figure 4.66) shows that for every synthesis where a precipitate was formed, the precipitate is amorphous, with no strong reflections seen in the powder pattern.

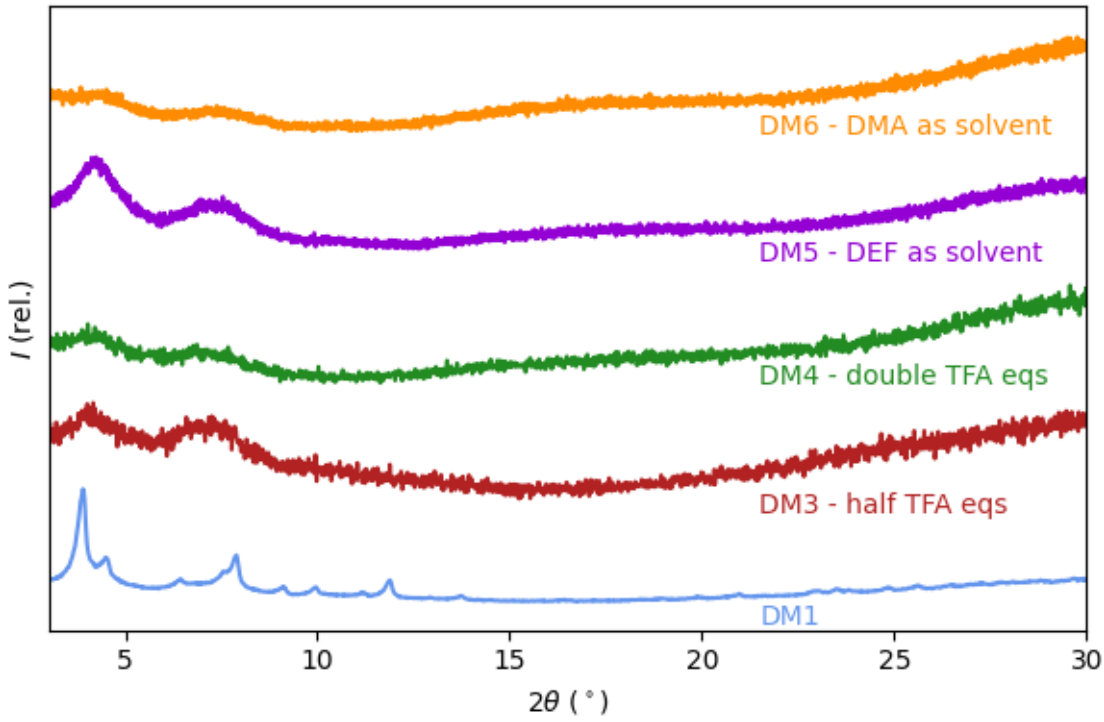

Figure 4.66 – PXRD patterns of DM1, DM3, DM4, DM5 and DM6.

Due to the difficulties encountered in the synthesis of this MOF, further investigations were discontinued.

4.7 Conclusions

Throughout this chapter, the synthesis of Group 4 NDIs MOFs has been explored. Significant detail has been paid to the synthesis conditions required to produce these materials. Changes in conditions such as solvent, reaction temperature, reactant ratios and the use of modulators has been explored in order make incremental improvements to the crystallinity of the materials obtained.

The crystal structure of two new frameworks that contain SA-NDI as a linker were reported. Zr-SA-NDI-α is a Zr containing MOF, where the metal centre interchanges between ZrO_6 and ZrO_7, that are connected through the SA-NDI ligands. The synthesis of this MOF was not repeatable and therefore further characterisation and application of the MOF was not possible. A HOF was also obtained, in which SA-NDI molecules are connected into a framework through hydrogen-bonding between adjacent molecules. This material could only be obtained under very specific conditions, but the reaction was repeatable. Further

characterisation indicated that the HOF could be porous, but full activation of the material was not achieved in the time available.

It is proposed that another Zr-MOF was also obtained, Zr-SA-NDI-β. Unfortunately, the synthesis of single crystals of this phase was not possible but incremental changes to the reaction conditions increased the crystallinity of the powders obtained. Attempts to solve the crystal structure from the powder pattern were made, but an appropriate solution could not be found. It is likely that synchrotron data would be required to solve the structure of this material.

Initial scoping reactions were carried to try and use covalent chemistry to produce crystalline Ti-MOFs. Attempts were made to form an NDI *in-situ* by reacting Ti oxo clusters containing pendant NH_2 groups with 1,4,5,8-naphthalenetetracarboxylic dianhydride. Some crystalline materials were produced and FTIR analysis suggested that bonds associated with NDIs may be present in some of the samples. Further investigations need to be carried to try and produce single crystals and solve the structure of these new materials.

4.8 Experimental

4.8.1 Materials and Chemicals

All chemicals were obtained from commercial sources and used as received unless otherwise stated.

4.8.2 Synthesis of NDIs

4.8.2.1 Synthesis of salicylic acid NDI (SA-NDI)

The synthesis procedure was adapted from literature.[32] 1,4,5,8-tetracarboxylic dianhydride (4.92 g, 18.4 mmol) and 5-amino-2-hydroxybenzoic acid (3.95 g, 25.8 mmol) were combined in anhydrous DMF (40 mL) under nitrogen and heated at 130 °C for 15 minutes. After cooling the product was collected by filtration and washed with DMF (50 mL) and diethyl either (2 x 50 mL) giving a brick red precipitate (7.9 g, 80 % w.r.t 1,4,5,8-tetracarboxylic dianhydride). ^{1}H NMR (400 MHz, DMSO-d_6) δ 8.72 (s, 4H), 7.93 (d, J = 2.6 Hz, 2H), 7.59 (dd, J = 8.8, 2.6 Hz, 2H),

7.13 (d, J = 8.7 Hz, 2H). ESI MS (negative mode) m/z calc'd for [M-H+], $C_{28}H_{14}N_2O_{10}$ 537.1, found 537.1.

4.8.2.2 Synthesis of dimethyl terephthalic acid NDI (DM-NDI)

The synthesis procedure was adapted from literature.[56] 1,4,5,8-tetracarboxylic dianhydride (406 mg, 1.51 mmol) and 4-amino-3,5-dimethyl-benzoic acid (500 mg, 3.03 mmol) were combined in propionic acid (6.5 mL) and refluxed for 48 hrs. After cooling the reaction to room temperature, the product was precipitated with DI water (20 mL), collected by filtration and washed with DMF (50 mL) and diethyl ether (2 x 50 mL). 570 mg (67%) of an off-white precipitate was collected. ^{1}H NMR (400 MHz, DMSO-d_6) δ 8.84 (s, 4H), 7.85 (s, 4H), 2.15 (s, 12H). ESI MS (negative mode) m/z calc'd for [M-H+], $C_{32}H_{23}N_2O_8$ 561.1, found 561.1.

4.8.3 Synthesis of Zr SA-NDI MOFs

4.8.3.1 Initial attempts at synthesising a Zr-SA-NDI MOF using 1:1 or 2:1 ratio of metal to linker

A number of reactions were attempted, as shown in Table 4.12 in the section 4.9.2 of the Appendix. The following procedure was used for these reactions. $ZrCl_4$ and SA-NDI were placed in a 20 mL scintillation vial, followed by the addition of solvent(s) and modulator. The suspension was sonicated for 1 minute, before being place in an oven (temperature and time defined in Table 4.12, Section 4.3.3.). The vial was then removed from the oven and allowed to cool to room temperature. If a solid product was obtained it was collected by centrifugation and washed with DMF (2 x 10 mL) and acetone (2 x 10 mL), before being allowed to dry in air.

4.8.3.2 Varying the metal to linker to modulator ratio to Zr-SA-NDI MOF reactions with BA modulator

$ZrCl_4$ (10 mg, 0.04 mmol), SA-NDI and BA were placed in a 25 mL Schott vial, followed by the addition of solvent(s) (masses and moles and used in the reactions are shown in Table 4.9). The suspension was sonicated for 1 minute, before being place in an oven at 100°C for 72 hours. The vial was then removed from the oven and allowed to cool to room temperature. If a solid product was obtained it was collected by centrifugation and washed with the primary

solvent used in the reaction (2 x 10 mL) and acetone (2 x 10 mL), before being allowed to dry in air.

Table 4.9 – Masses and moles used in Zr SA-NDI MOF reactions where the ratio of metal to linker to benzoic acid was varied. Where DEF was used as the solvent 5 mL was used, where a DMF/MeCN mix was used, 3.5 mL of DMF was used and 1.5 mL of MeCN.

Sample ID	Mass of SA-NDI / mg	Moles of SA-NDI / mmol	Linker: Metal ratio	Eqvs of BA	Solvent	Ppt obtained?
SA-1:6-BA(40)-DEF(100)	139	0.26	6	40	DEF	Y
SA-1:5-BA(40)-DEF(100)	116	0.22	5	40	DEF	Y
SA-1:4-BA(40)-DEF(100)	92	0.17	4	40	DEF	Y
SA-1:3-BA(40)-DEF(100)	69	0.13	3	40	DEF	Y
SA-1:2-BA(40)-DEF(100)	46	0.09	2	40	DEF	N
SA-1:6-BA(20)-DEF(100)	139	0.26	6	20	DEF	Y
SA-1:5-BA(20)-DEF(100)	116	0.22	5	20	DEF	Y
SA-1:4-BA(20)-DEF(100)	92	0.17	4	20	DEF	Y
SA-1:3-BA(20)-DEF(100)	69	0.13	3	20	DEF	Y
SA-1:2-BA(20)-DEF(100)	46	0.09	2	20	DEF	N
SA-1:6-BA(40)-DMF/MeCN(100)	139	0.26	6	40	DMF/MeCN	SA-NDI
SA-1:5-BA(40)-DMF/MeCN(100)	116	0.22	5	40	DMF/MeCN	SA-NDI
SA-1:4-BA(40)-DMF/MeCN(100)	92	0.17	4	40	DMF/MeCN	SA-NDI
SA-1:3-BA(40)-DMF/MeCN(100)	69	0.13	3	40	DMF/MeCN	SA-NDI
SA-1:2-BA(40)-DMF/MeCN(100)	46	0.09	2	40	DMF/MeCN	SA-NDI
SA-1:6-BA(20)-DMF/MeCN(100)	139	0.26	6	20	DMF/MeCN	SA-NDI
SA-1:5-BA(20)-DMF/MeCN(100)	116	0.22	5	20	DMF/MeCN	SA-NDI
SA-1:4-BA(20)-DMF/MeCN(100)	92	0.17	4	20	DMF/MeCN	SA-NDI
SA-1:3-BA(20)-DMF/MeCN(100)	69	0.13	3	20	DMF/MeCN	SA-NDI
SA-1:2-BA(20)-DMF/MeCN(100)	46	0.09	2	20	DMF/MeCN	SA-NDI

4.8.3.3 Varying the temperature of the Zr-SA-NDI MOF synthesis

$ZrCl_4$ (10 mg, 0.043 mmol), SA-NDI (137 mg, 0.255 mmol) and BA (105 mg, 0.86 mmol) were placed in a 25 mL Schott vial, followed by the addition of DEF (5 mL). The suspension was sonicated for 1 minute, before being place in an oven at 80, 100, 120, 140°C for 72 hours. The

vial was then removed from the oven and allowed to cool to room temperature. The orange-red precipitate was collected by centrifugation and washed with the DEF (2 x 10 mL) and acetone (2 x 10 mL), before being allowed to dry in air.

For the reaction conducted at 160°C the same process was used, but a Parr bomb with a Teflon insert was used as the reaction vessel.

4.8.3.4 Varying the modulator of the Zr-SA-NDI MOF synthesis

$ZrCl_4$ (10 mg, 0.043 mmol) and SA-NDI (137 mg, 0.255 mmol) were placed in a 25 mL Schott vial, followed by the addition of DEF (5 mL). 20 equivalents (0.86 mmol) of the required modulator (formic, acetic, salicylic or trifluoroacetic acid) were then added to the mixture. The suspension was sonicated for 1 minute, before being placed in an oven at 100°C for 72 hours. The vial was then removed from the oven and allowed to cool to room temperature. The orange-red precipitate was collected by centrifugation and washed with the DEF (2 x 10 mL) and acetone (2 x 10 mL), before being allowed to dry in air.

4.8.3.5 Zr-SA-NDI-α

$ZrCl_4$ (10.4 mg, 0.045 mmol) and SA-NDI (91.9 mg, 0.171 mmol) were placed in a 25 mL Schott vial, followed by the addition of DEF (4.5 mL) and TFA (98 mg, 0.86 mmol). The suspension was sonicated for 1 minute, before being place in an oven at 100°C for 72 hours. The vial was then removed from the oven and allowed to cool to room temperature. Some orange crystals were collected from the vial and kept in the reaction mixture before being mounted and sent to DLS. Later, the rest of the sample was collected by centrifugation and washed with the DEF (2 x 10 mL) and acetone (2 x 10 mL), before being allowed to dry in air.

4.8.4 Synthesis of SA-NDI HOF

First synthesis of this material: $ZrCl_4$ (10 mg, 0.043 mmol) and SA-NDI (137 mg, 0.255 mmol) were placed in a pressure tube, followed by the addition of DEF (3.5 mL), MeCN (1.5 mL) and then TFA (98 mg, 0.86 mmol). The suspension was sonicated for 1 minute and the pressure tube was place in the oven at 100°C for 72 hours. The tube was then removed from the oven and allowed to cool to room temperature. After the first synthesis of this material, some yellow needle crystals were collected and kept in their reaction mixture before being

mounted and sent to DLS. Afterwards, the remaining crystals were collected by centrifugation and the sample placed on watch glass and allowed to dry overnight.

All following syntheses: SA-NDI (137 mg, 0.255 mmol) was placed in a pressure tube, followed by the addition of DEF (3.5 mL), MeCN (1.5 mL) and then TFA (98 mg, 0.86 mmol). The same process as described above was then carried out, apart from the collection of single crystals.

Reactions were also carried out where either the MeCN or TFA were omitted. Neither reaction yielded a precipitate.

4.8.5 Synthesis of Hf DM-NDI MOF

$HfCl_4$ (22 mg, 0.07 mmol) and DM-NDI (35 mg, 0.06 mmol) were placed in a 20 mL scintillation vial, followed by addition of DMF (8.8 mL) and TFA (88 µL, 1.18 mmol, 19 equivs). The suspension was sonicated for 1 minute, before being placed in an oven at 120 °C for 60 hours. The vial was then removed from the oven and allowed to cool to room temperature. The solid product was collected by centrifugation and washed with DMF (2 x 10 mL) and acetone (2 x 10 mL) to afford a pale pink precipitate which was allowed to dry in air.

Synthesis of samples with IDs DM2 to DM6:

The procedure described above was carried out, but the amounts of reactants and solvent used were varied as shown in Table 4.10.

Table 4.10 – Masses of reactants and solvent used in reactions DM1-6.

Sample ID	Mass of $HfCl_4$ / mg	Mass of DM-NDI / mg	Solvent	Amount of TFA / µL	Eq's of TFA
DM1	21.8	35.0	DMF	88	19
DM2a	19.9	35.9	DMF	88	19
DM2b	20.4	35.7	DMF	88	19
DM2c	21.5	35.4	DMF	88	19
DM2d	20.9	35.0	DMF	88	19
DM2e	20.8	33.5	DMF	88	20
DM2f	21.1	34.7	DMF	88	19
DM3	21.9	34.5	DMF	44	10
DM4	22.4	35.0	DMF	176	38
DM5	21.2	36.9	DEF	88	18
DM6	21.0	35.3	DMA	88	19

4.8.6 Ti NDI MOF synthesis

4.8.6.1 Synthesis of Ti aminobenzoate cluster

The method was adapted from a previously reported procedure.[50] $Ti(O^iPr)_4$ (10 mL, 33.8 mmol) was added dropwise to stirred suspension of 4-aminobenzoic acid (9.2 g, 67.1 mmol) in 2-propanol (100 mL) in a pressure tube. After stirring for 30 mins at RT the orange suspension was refluxed for 24 hours. The orange crystalline product was then collected *via* Buchner filtration and washed with IPA (50 mL), before being dried on a watch glass at 80°C (2.21 g, 25%).

4.8.6.2 Synthesis of Ti NDI MOFs from Ti aminobenzoate cluster

$Ti_6O_6(O^iPr)_6(abz)_6$ (50 mg, 0.032 mmol) was combined with 1,4,5,8-naphthalenetetracarboxylic dianhydride (26 mg, 0.097 mmol) in 25 mL Schott vial. DMF or DEF (volumes defined below in Table 4.11) was added to the same Schott vial, before the mixture was sonicated for two minutes. The Schott vial was placed in the oven at 80, 100 or 120 °C (as defined in Table 4.11) and heated for 24 hours. After this time, the Schott vial was removed from the oven. If a precipitate was present, this was washed twice with the solvent (4 mL) that the reaction was carried out in and twice with acetone (12 mL) before being allowed to dry in air. If a gel was present, this was laid onto a watch glass and the solvent allowed to evaporate to give a powder after 4 days.

Table 4.11 – Details of attempted Ti NDI MOF synthesis from Ti(abz)

Sample ID	Solvent	Volume / mL	Temp / °C	Observation	Mass / mg
Ti-DEF-80	DEF	5	80	Orange ppt	11.5
Ti-DEF-100	DEF	5	100	Orange ppt	9.6
Ti-DEF-120	DEF	5	120	Orange ppt	15
Ti-DMF-80	DMF	5	80	No ppt	-
Ti-DMF-100	DMF	5	100	No ppt	-
Ti-DMF-120	DMF	5	120	No ppt	-
Ti-DMF-1mL -100	DMF	1	100	Yellow gel	45.6
Ti-DMF-2mL -100	DMF	2	100	No ppt	-
Ti-DMF-3mL -100	DMF	3	100	No ppt	-
Ti-DMF-4mL -100	DMF	4	100	No ppt	-
Ti-DMF-1mL -140	DMF	1	140	Brown gel	51.2
Ti-DMF-2mL -140	DMF	2	140	Brown gel	54.6
Ti-DMF-3mL -140	DMF	3	140	Brown gel	54.2
Ti-DMF-4mL -140	DMF	4	140	Brown gel	51.3
Ti-DMF-BA-100	DMF	2	100	Yellow ppt	14.6
Ti-DMF-AA-100	DMF	2	100	Yellow ppt	5.4
Ti-DMF-FA-100	DMF	2	100	Yellow ppt	10.6
Ti-DMF-BA-140	DMF	2	140	Brown gel	68.8
Ti-DMF-AA-140	DMF	2	140	Brown gel	49.4
Ti-DMF-FA-140	DMF	2	140	Brown gel	40.9

4.9 Appendix

4.9.1 Characterisation of NDIs

4.9.1.1 N,N'-Bis(3-carboxy-4-hydroxyphenyl)-1,4,5,8-naphthalenetetracarboxydiimide (SA-NDI)

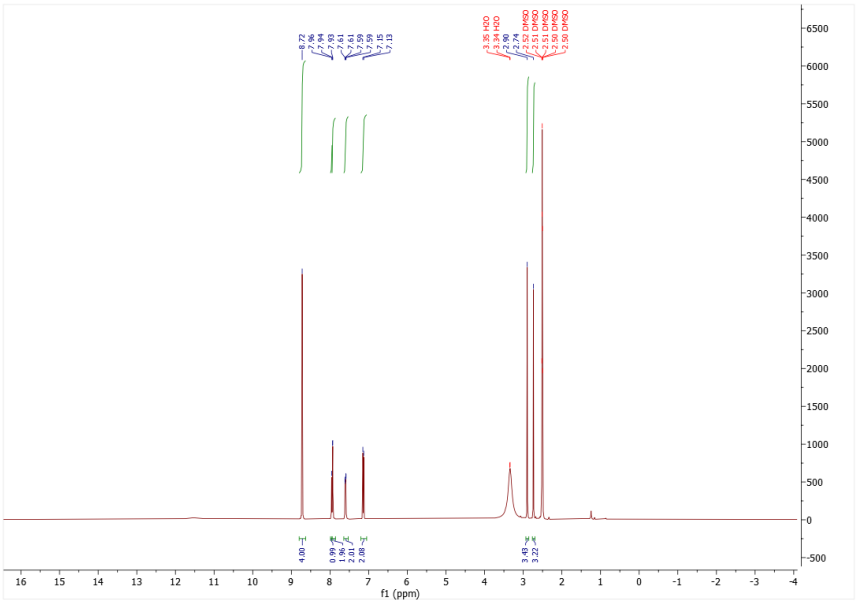

Figure 4.67 - ^{1}H NMR (400 MHz, DMSO-d_6) δ 8.72 (s, 4H), 7.93 (d, J = 2.6 Hz, 2H), 7.59 (dd, J = 8.8, 2.6 Hz, 2H), 7.13 (d, J = 8.7 Hz, 2H). Resonances at δ 7.96, 2.90 and 2.74 are due to DMF.

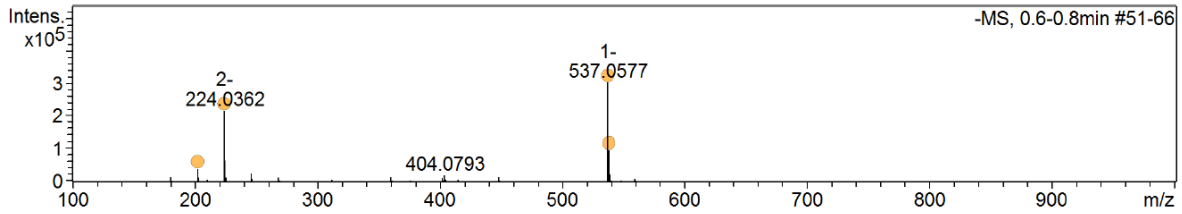

Figure 4.68 - ESI MS (negative mode) for SA-NDI. m/z calc'd for [M-H+], $C_{28}H_{14}N_2O_{10}$ 537.1, found 537.1.

4.9.1.2 *N,N'-Di-(2,6-dimethyl-4-benzoic acid)-1,4,5,8-naphthalenetetracarboxydiimide (DM-NDI)*

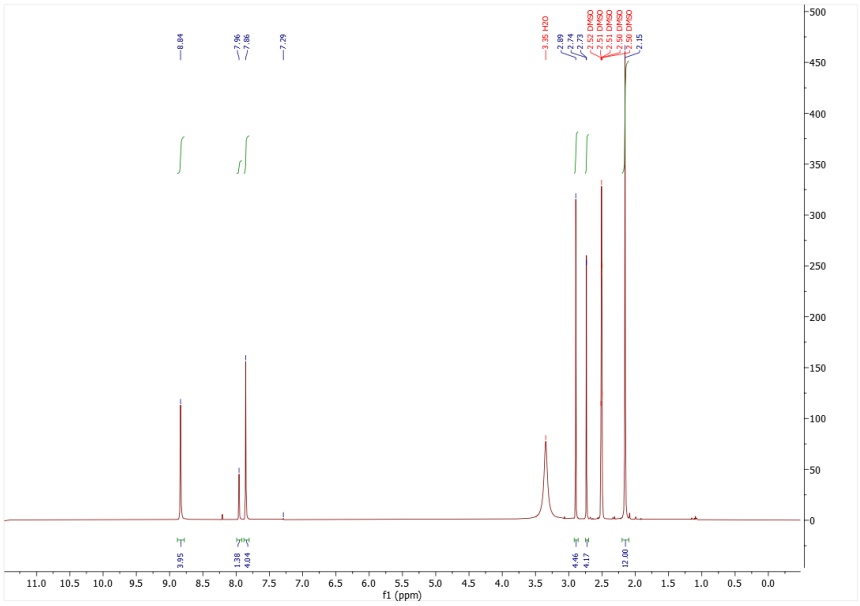

Figure 4.69 - ^{1}H NMR (400 MHz, DMSO-d_6) δ 8.84 (s, 4H), 7.85 (s, 4H), 2.15 (s, 12H). Resonances at δ 7.96, 2.90 and 2.74 are due to DMF.

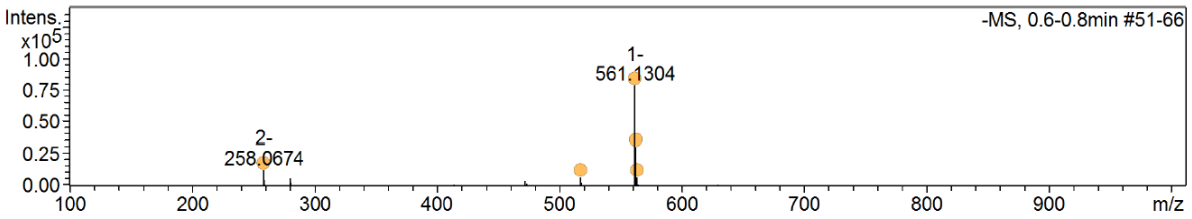

Figure 4.70 - ESI MS (negative mode) for DM-NDI. m/z calc'd for [M-H+], $C_{32}H_{23}N_2O_8$ 561.1, found 561.1.

4.9.2 Synthesis of Zr-SA-NDI MOFs (not included in main discussion)

Before reactions using a metal to linker ratio of 1:4 for were carried out, a range of conditions were explored using a 1:1 or 2:1 ratio of metal to linker, as these are ratios commonly used in MOF synthesis. The temperature, reaction time, modulating agent and solvent used were varied to try and obtain a crystalline product. Unfortunately, none of these reactions yielded a crystalline material. Any precipitates that were formed during the reactions were analysed by PXRD and all were found to be amorphous.

Table 4.12 - Amounts of reagents and conditions used for the attempted synthesis of a MOF composed of Zr(IV) and SA-NDI.

Sample ID	Mass of $ZrCl_4$ / mg	Moles of $ZrCl_4$ / mmol	Mass of SA-NDI / mg	Moles of SA-NDI / mmol	Linker: Metal ratio	Modu-lator	Eqvs	Solvent	Volume of solvent / mL	Temp / °C	Time / h	Ppt obtained?
SA1	5.4	0.023	11.8	0.022	0.97	None	0	DMF	1.5	100	72	Y
SA2	4.0	0.017	10	0.019	1.08	TFA	11	DMF	1.5	100	48	N
SA3	4.0	0.017	10	0.019	1.08	TFA	11	DMF	1.5	120	72	Y
SA4	4.0	0.017	10	0.019	1.08	TFA	11	DMF	3.0	120	72	Y
SA5	8.0	0.034	10	0.019	0.54	TFA	11	DMF	1.5	120	72	Y
SA6	8.0	0.034	10	0.019	0.54	TFA	11	DMF	3.0	120	72	Y
SA7	15.2	0.065	35.8	0.066	1.02	TFA	20	DMF	8.0	120	48	Y
SA8	10.6	0.045	22.3	0.041	0.91	BA	5	DMF	2.5	120	24	N
SA9	10.3	0.044	23.7	0.044	1.00	BA	5	DMF	5.0	120	24	N
SA10	9.8	0.042	23.7	0.044	1.05	AA	5	DMF	2.5	120	24	Y
SA11	11.1	0.046	22.9	0.043	0.89	AA	5	DMF	5.0	120	24	Y
SA12	10.0	0.043	23.2	0.043	1.00	BA	57	DMF	5.0	120	48	N
SA13	10.7	0.046	22.4	0.045	0.91	BA	64	DMF/MeCN	3.5/1.5	120	48	Y
SA14	9.0	0.039	22.0	0.041	1.05	TFA	10	NMP	4.0	120	72	N
SA15	9.7	0.042	22.3	0.041	1.00	TFA	10	NMP	2.0	120	72	N
SA16	21.4	0.092	51.2	0.095	1.04	TFA	20	DMF/EtOH/H_2O	4.0/2.0/2.0	100	72	Y
SA17	22.6	0.097	51.5	0.096	0.99	BA	19	DMF/EtOH/H_2O	4.0/2.0/2.0	100	72	Y
SA18	24.9	0.107	50.5	0.094	0.88	AA	20	DMF/EtOH/H_2O	4.0/2.0/2.0	100	72	Y
SA19	22.5	0.096	53.1	0.099	1.02	TFA	19	DMF/EtOH/H_2O	2.0/1.0/1.0	100	72	Y
SA20	22.7	0.097	51.4	0.095	0.98	BA	21	DMF/EtOH/H_2O	2.0/1.0/1.0	100	72	Y

4.9.3 Crystallographic refinement details

4.9.3.1 Zr-SA-NDI-α

It is noted that the refinement of Zr-SA-NDI-α was extremely challenging. The very thin lath-like crystal diffracted very weakly despite the use of synchrotron radiation. The data used in the refinement was truncated to a resolution limit of 1.20 Å. The asymmetric unit contains two metal sites (modelled as mixed occupancy Zr and Hf) and three SA-NDI ligands. The structure was solved with dual space methods, however, the refinement was very problematic suggesting there is a major unresolved problem with the structure.

All atoms in the structure could only be refined with isotropic displacement parameters and attempts to refine anisotropically resulted in irregular ellipsoids and large numbers of non-positive-definite atoms. The isotropic displacement parameters of both metals and two of the ligands refined to very low values. No missed symmetry for the structure (a common cause of this issue) could be determined with the PLATON routine Addymm. The isotropic displacement parameters of all affected ligand atoms were fixed at values of 0.02. The isotropic displacement parameters of the two Zr atoms were fixed at values of 0.015. The geometries of the ligands were restrained to be similar and where appropriate symmetrical and flat (SAME, SADI, FLAT). The structure contains significant voids that were treated with the Olex2 Solvent Screen routine.

The overall structure refinement is majorly flawed, and no conclusion can be drawn from it other than the identity and connectivity of the ligands involved. The presence of a mixture of metals (for example, Zr and Hf) cannot be ruled out. Although the reaction contained only $ZrCl_4$ as the metal source, $ZrCl_4$ is known to contain trace amounts of Hf.

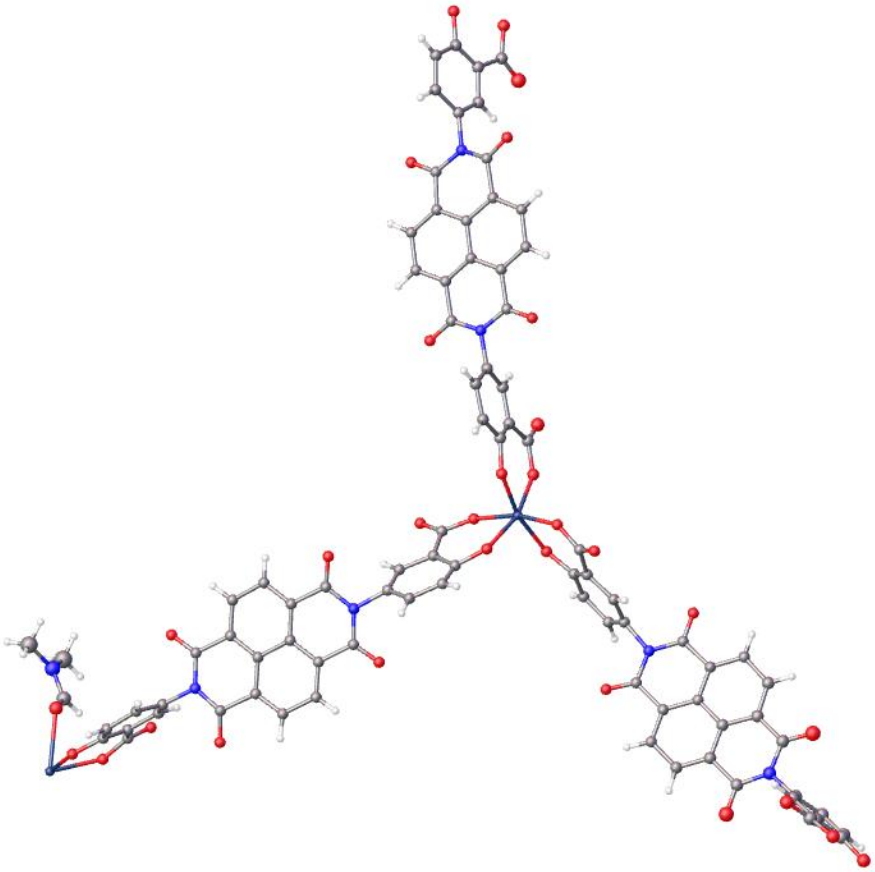

Figure 4.71 - Asymmetric unit of Zr-SA-NDI-α, with all non-hydrogens represented by ellipsoids (zirconium = navy, carbon = grey, oxygen = red, nitrogen = blue, hydrogen = white).

Table 4.13 - Crystal data and structure refinement details for Zr-SA-NDI-α

Empirical formula	$C_{87}H_{37}N_7O_{31}Zr_2$
Formula weight	1858.67
Temperature/K	100(2)
Crystal system	triclinic
Space group	P-1
a/Å	16.111(2)
b/Å	16.526(2)
c/Å	33.106(4)
α/°	76.695(11)
β/°	79.816(11)
γ/°	83.831(13)
Volume/Å^3	8422.3(19)
Z	2
ρ_{calc} g/cm^3	0.733
μ/mm^{-1}	0.156
F(000)	1872.0
Crystal size/mm^3	0.08 × 0.02 × 0.005
Radiation	Synchrotron (λ = 0.6889)
2Θ range for data collection/°	1.24 to 33.36
Index ranges	-13 ≤ h ≤ 13, -13 ≤ k ≤ 13, -27 ≤ l ≤ 27
Reflections collected	31744
Independent reflections	10141 [R_{int} = 0.2231, R_{sigma} = 0.2781]
Data/restraints/parameters	10141/1664/420
Goodness-of-fit on F^2	1.489
Final R indexes [I>=2σ (I)]	R_1 = 0.2304, wR_2 = 0.5090
Final R indexes [all data]	R_1 = 0.2710, wR_2 = 0.5491
Largest diff. peak/hole / e Å^{-3}	3.27/-1.31

4.9.3.2 SA-NDI HOF

The very small needle-like crystals of SA-NDI HOF diffracted very weakly with a low resolution limit despite the use of synchrotron radiation. The data used in the refinement was truncated to a resolution limit of 0.95 Å resulting in a data to parameter ratio of 8.71. Extensive use of restraints and constraints were used to aid refinement of the structure against the weak and truncated data.

Rigid bond and similarity restraints were applied to the anisotropic displacement parameters of all atoms in the structure (RIGU, SIMU). The anisotropic displacement parameters of the three atoms of the acetonitrile residue were constrained to be identical (EADP). Geometric

similarity restraints were applied to all chemically equivalent 1,2 and 1,3 intramolecular distances in the SA-NDI moiety.

The geometry of the acetonitrile residue was refined as a rigid body from atom positions provided by the fragment database in Olex2. The occupancy of the residue was refined before being fixed at a value of 0.5. Residual electron density peaks indicate a further overlapping solvent residue for which a sensible model could not be developed.

No hydrogen atoms were observed in the noisy electron density map. All hydrogen atoms were geometrically placed (taking into account proximate hydrogen bond acceptors in the case of the hydroxy hydrogen atoms) and refined using a riding model.

A solvent mask was calculated which equated to 50 electrons in a volume of 154 Å in 1 void per unit cell. This is consistent with the presence of one acetonitrile per asymmetric unit.

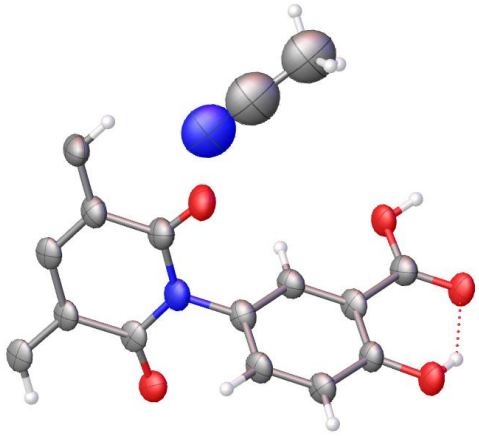

Figure 4.72 – Asymmetric unit of SA-NDI HOF, with all non-hydrogens represented by ellipsoids (carbon = grey, oxygen = red, nitrogen = blue, hydrogen = white).

Table 4.14 – Crystal data and structure refinement details for SA-NDI HOF

Empirical formula	$C_{32}H_{20}N_4O_{10}$
Formula weight	620.52
Temperature/K	100(2)
Crystal system	monoclinic
Space group	C2/c
a/Å	29.8900(19)
b/Å	14.2536(8)
c/Å	6.9617(4)
α/°	90
β/°	109.299(7)
γ/°	90
Volume/Å^3	2799.3(3)
Z	4
ρ_{calc}g/cm^3	1.472
μ/mm^{-1}	0.105
F(000)	1280.0
Radiation	Synchrotron (λ = 0.6889)
2Θ range for data collection/°	3.102 to 42.51
Index ranges	$-31 \leq h \leq 31$, $-14 \leq k \leq 14$, $-7 \leq l \leq 7$
Reflections collected	13190
Independent reflections	1707 [R_{int} = 0.2433, R_{sigma} = 0.1441]
Data/restraints/parameters	1707/317/196
Goodness-of-fit on F^2	1.095
Final R indexes [I>=2σ (I)]	R_1 = 0.1106, wR_2 = 0.2858
Final R indexes [all data]	R_1 = 0.1426, wR_2 = 0.3284
Largest diff. peak/hole / e Å^{-3}	0.75/-0.41

4.9.4 SEM and SEM-EDX of Zr-SA-NDI MOFs

SEM-EDX analysis was carried out on the Zr-SA-NDI materials described throughout this chapter. Samples were ground and then images and EDX spectra were taken of several regions to show the morphologies and elements present in each sample. Due to the samples being mounted on a carbon tab, only qualitative element analysis is possible.

4.9.4.1 *Varying the metal to linker to modulator ratio in Zr-SA-NDI MOF reactions with BA as a modulator*

The SEM-EDX of materials synthesised in a DMF/MeCN solvent mix at 100°C (Figure 4.73) show that there is a negligible amount of zirconium in the sample, suggested that no MOF-forming reaction has occurred and confirmed what was seen in the PXRD, that the sample is primarily linker (Figure 4.12).

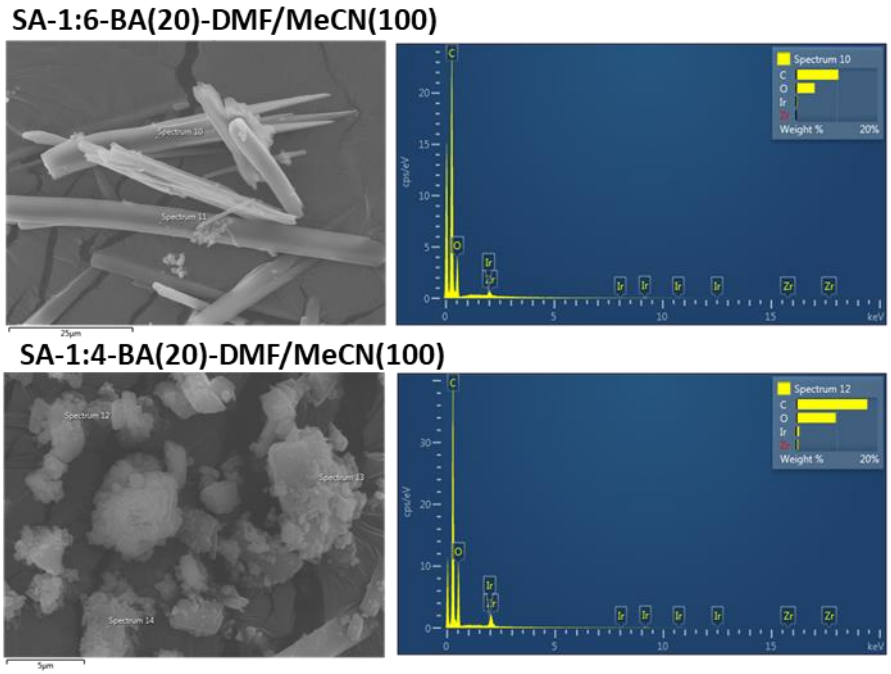

Figure 4.73 – SEM-EDX of materials obtained in attempted Zr-SA-NDI MOF syntheses. Conditions: SA-1:4-BA(20)-DMF/MeCN(100) = 1:4 metal to linker ratio, 20 equivalents of benzoic acid, DMF/MeCN solvent mix, 100°C, 72 hours, SA-1:4-BA(20)-DMF/MeCN(100) = 1:6 metal to linker ratio, 20 equivalents of benzoic acid, DMF/MeCN solvent mix, 100°C, 72 hours.

SEM images of materials obtained whilst varying the metal to linker used in reactions (with 40 equivalents of benzoic acid) to form Zr-SA-NDI materials (Figure 4.74) shows that the morphologies of the particles is relatively non-uniform, with some larger oblong particles mixed in with some smaller irregular circular particles. SEM-EDX (Figure 4.75) shows that all samples contain C, O and Zr. SA-1:3-BA(40)-DEF(100) also contains some chlorine which suggests that some $ZrCl_4$ or $ZrOCl_2$ may be present in the sample.

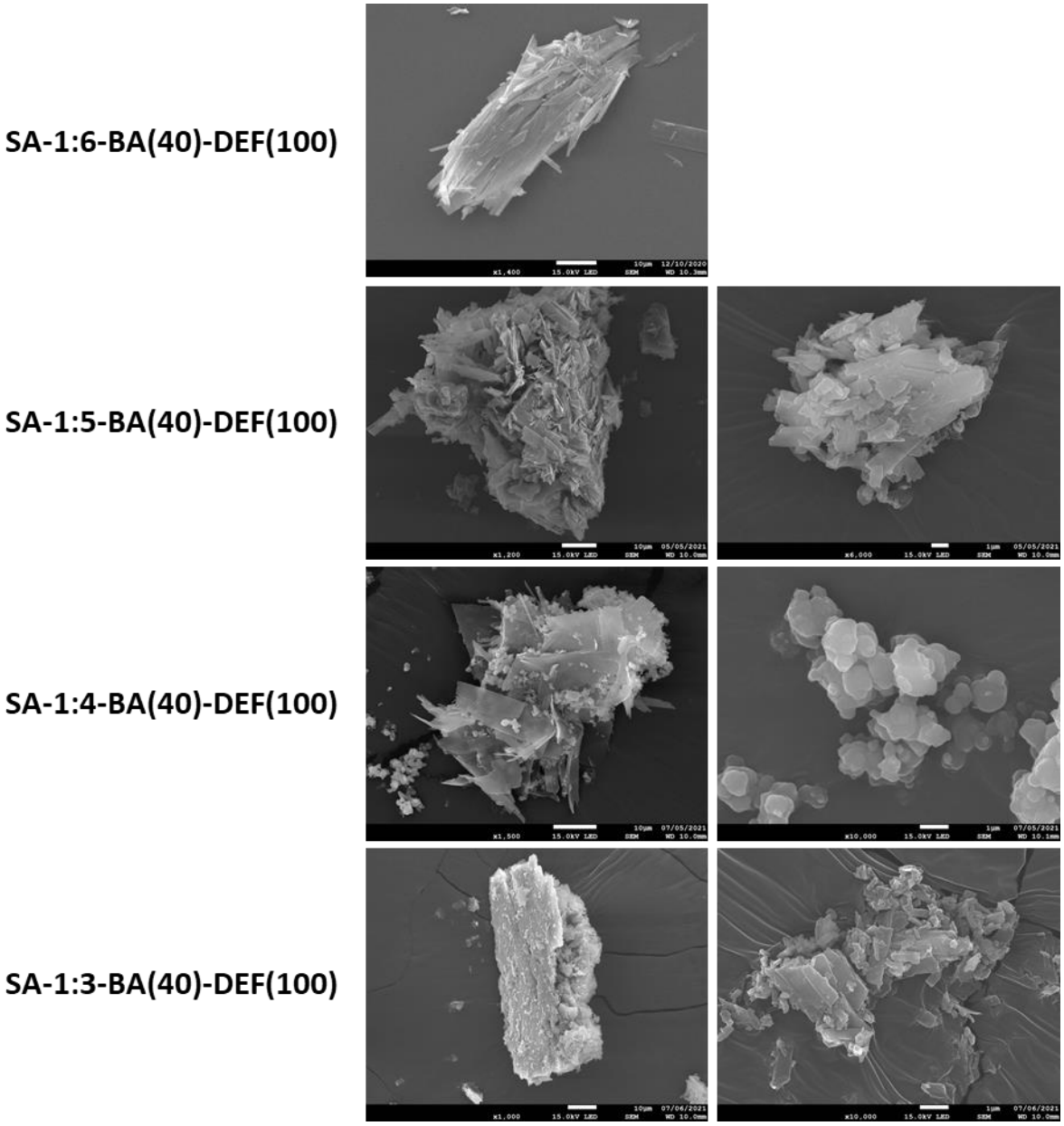

Figure 4.74 – SEM images of Zr-SA-NDI materials. Conditions: SA-1:3-BA(40)-DEF(100) = 1:3 metal to linker ratio, 40 equivalents of benzoic acid, DEF, 100°C, 72 hours, SA-1:4-BA(40)-DEF(100) = 1:4 metal to linker ratio, 40 equivalents of benzoic acid, DEF, 100°C, 72 hours, SA-1:5-BA(40)-DEF(100) = 1:5 metal to linker ratio, 40 equivalents of benzoic acid, DEF, 100°C, 72 hours, SA-1:6-BA(40)-DEF(100) = 1:6 metal to linker ratio, 40 equivalents of benzoic acid, DEF, 100°C, 72 hours. Scale bars: images on left = 10 µm, images on right = 1 µm.

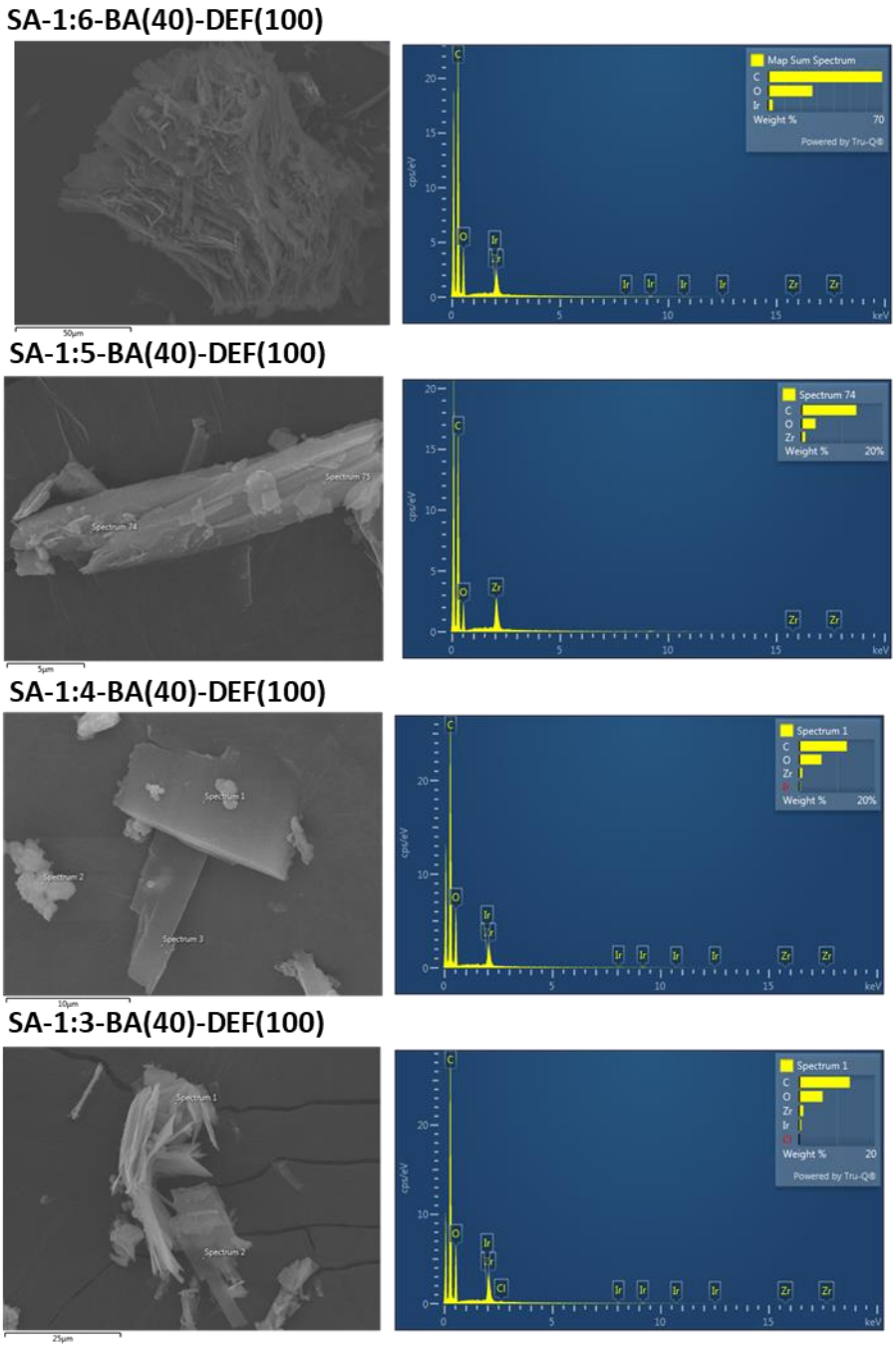

Figure 4.75 - SEM-EDX of Zr-SA-NDI materials. Conditions: SA-1:3-BA(40)-DEF(100) = 1:3 metal to linker ratio, 40 equivalents of benzoic acid, DEF, 100°C, 72 hours, SA-1:4-BA(40)-DEF(100) = 1:4 metal to linker ratio, 40 equivalents of benzoic acid, DEF, 100°C, 72 hours, SA-1:5-BA(40)-DEF(100) = 1:5 metal to linker ratio, 40 equivalents of benzoic acid, DEF, 100°C, 72 hours, SA-1:6-BA(40)-DEF(100) = 1:6 metal to linker ratio, 40 equivalents of benzoic acid, DEF, 100°C, 72 hours.

SEM images of materials obtained whilst varying the metal to linker used in reactions (with 20 equivalents of benzoic acid) to form Zr-SA-NDI materials (Figure 4.76) shows that the morphologies of the particles is relatively non-uniform, with some larger oblong particles mixed in with some smaller irregular circular particles. SEM-EDX (Figure 4.77) shows that all samples contains C, O and Zr.

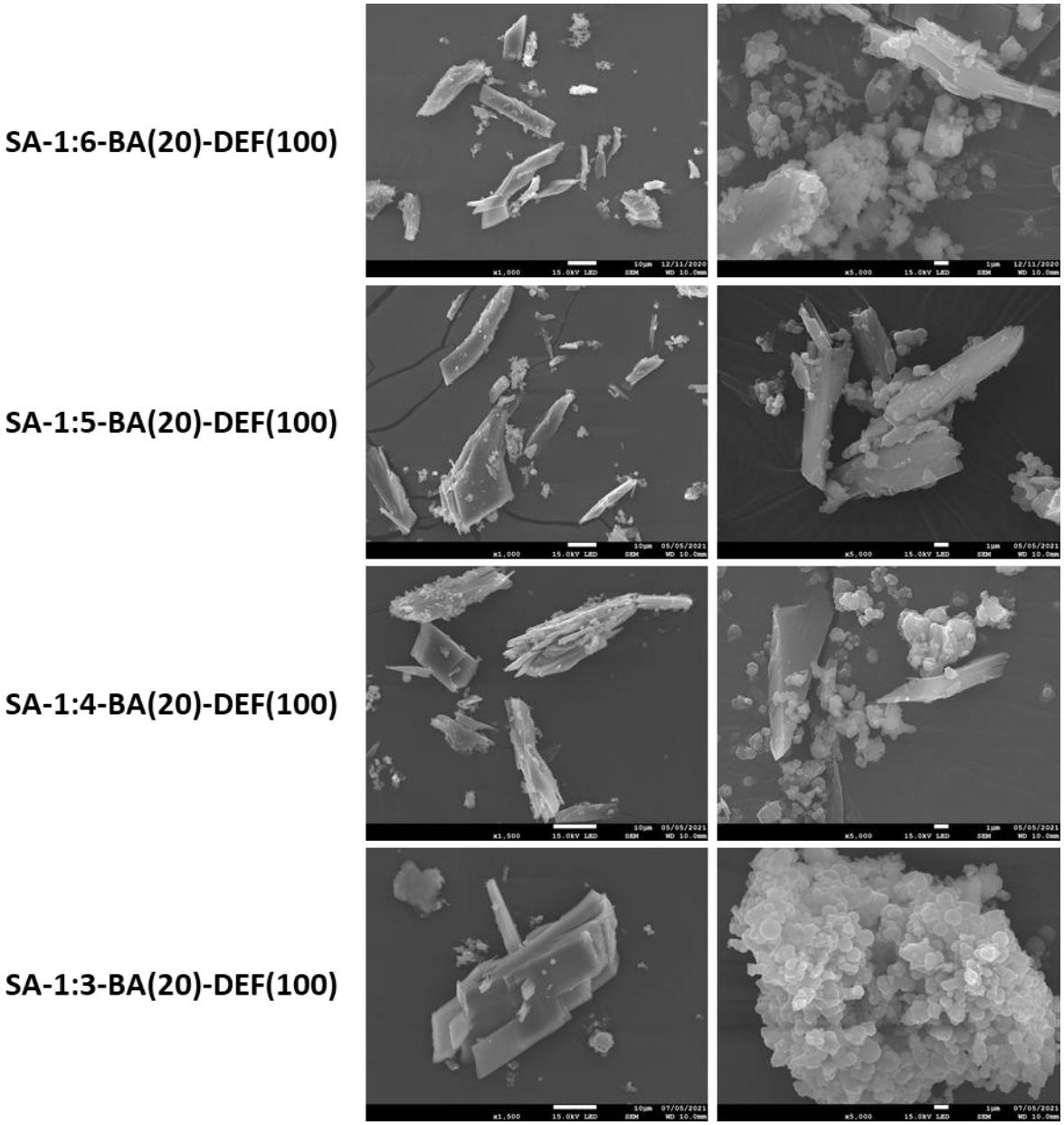

Figure 4.76 - SEM images of Zr-SA-NDI materials. Conditions: SA-1:3-BA(20)-DEF(100) = 1:3 metal to linker ratio, 40 equivalents of benzoic acid, DEF, 100°C, 72 hours, SA-1:4-BA(20)-DEF(100) = 1:4 metal to linker ratio, 40 equivalents of benzoic acid, DEF, 100°C, 72 hours, SA-1:5-BA(20)-DEF(100) = 1:5 metal to linker ratio, 40 equivalents of benzoic acid, DEF, 100°C, 72 hours, SA-1:6-BA(20)-DEF(100) = 1:6 metal to linker ratio, 40 equivalents of benzoic acid, DEF, 100°C, 72 hours. Scale bars: images on left = 10 µm, images on right = 1 µm.

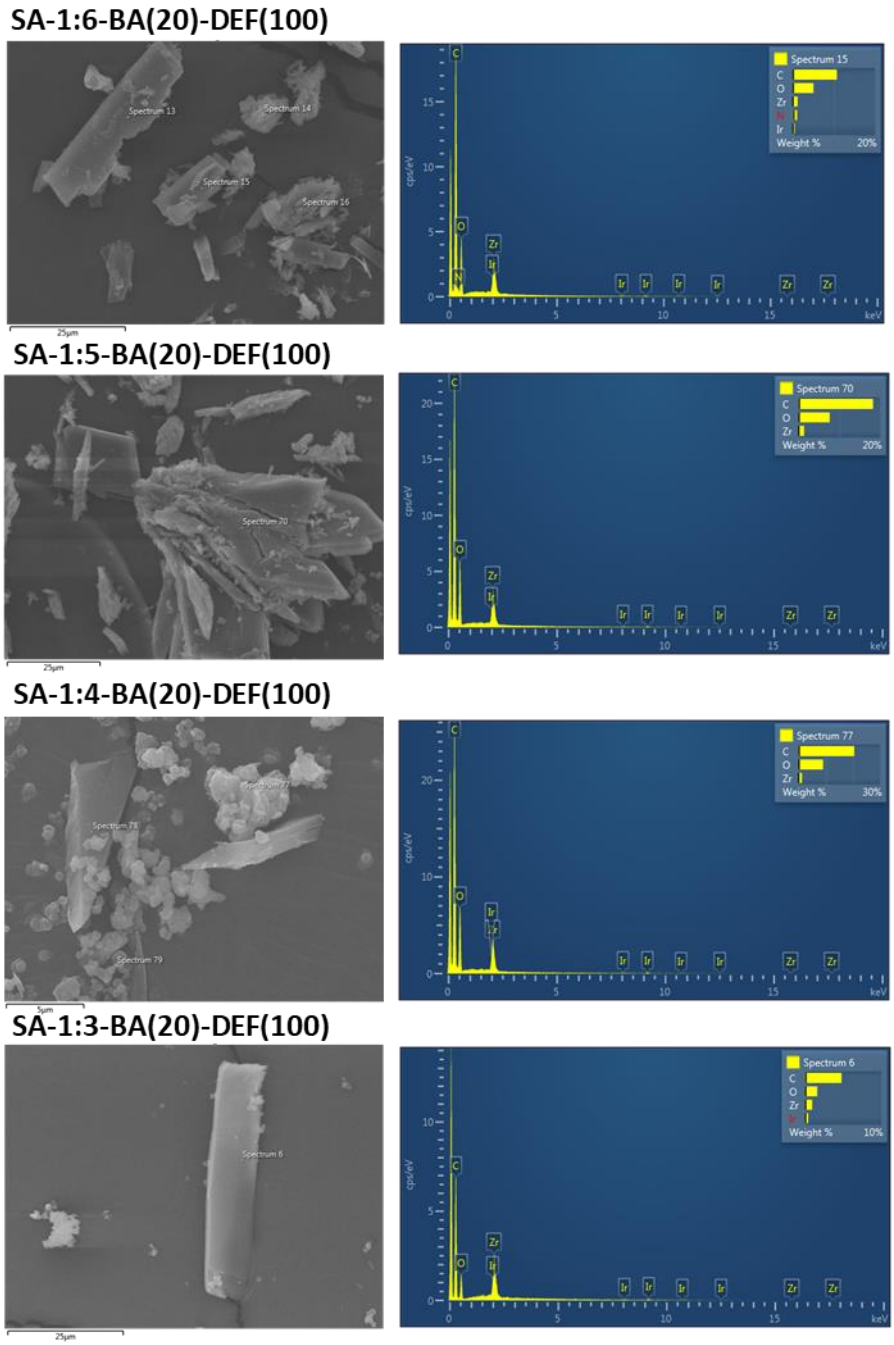

Figure 4.77 - SEM-EDX of Zr-SA-NDI materials. Conditions: SA-1:3-BA(20)-DEF(100) = 1:3 metal to linker ratio, 40 equivalents of benzoic acid, DEF, 100°C, 72 hours, SA-1:4-BA(20)-DEF(100) = 1:4 metal to linker ratio, 40 equivalents of benzoic acid, DEF, 100°C, 72 hours, SA-1:5-BA(20)-DEF(100) = 1:5 metal to linker ratio, 40 equivalents of benzoic acid, DEF, 100°C, 72 hours, SA-1:6-BA(20)-DEF(100) = 1:6 metal to linker ratio, 40 equivalents of benzoic acid, DEF, 100°C, 72 hours.

4.9.4.2 Varying the temperature of the Zr-SA-NDI MOF synthesis

SEM images of materials obtained whilst varying the temperature used to form Zr-SA-NDI materials (Figure 4.78) shows that the morphologies of the particles is relatively non-uniform, with samples synthesised at higher temperatures (SA-1:6-BA(20)-DEF(140) and SA-1:6-

BA(20)-DEF(160)) having a tendency to form large (10-20 µm) flat oblong particles. SEM-EDX (Figure 4.79) shows that all samples contain C, O and Zr.

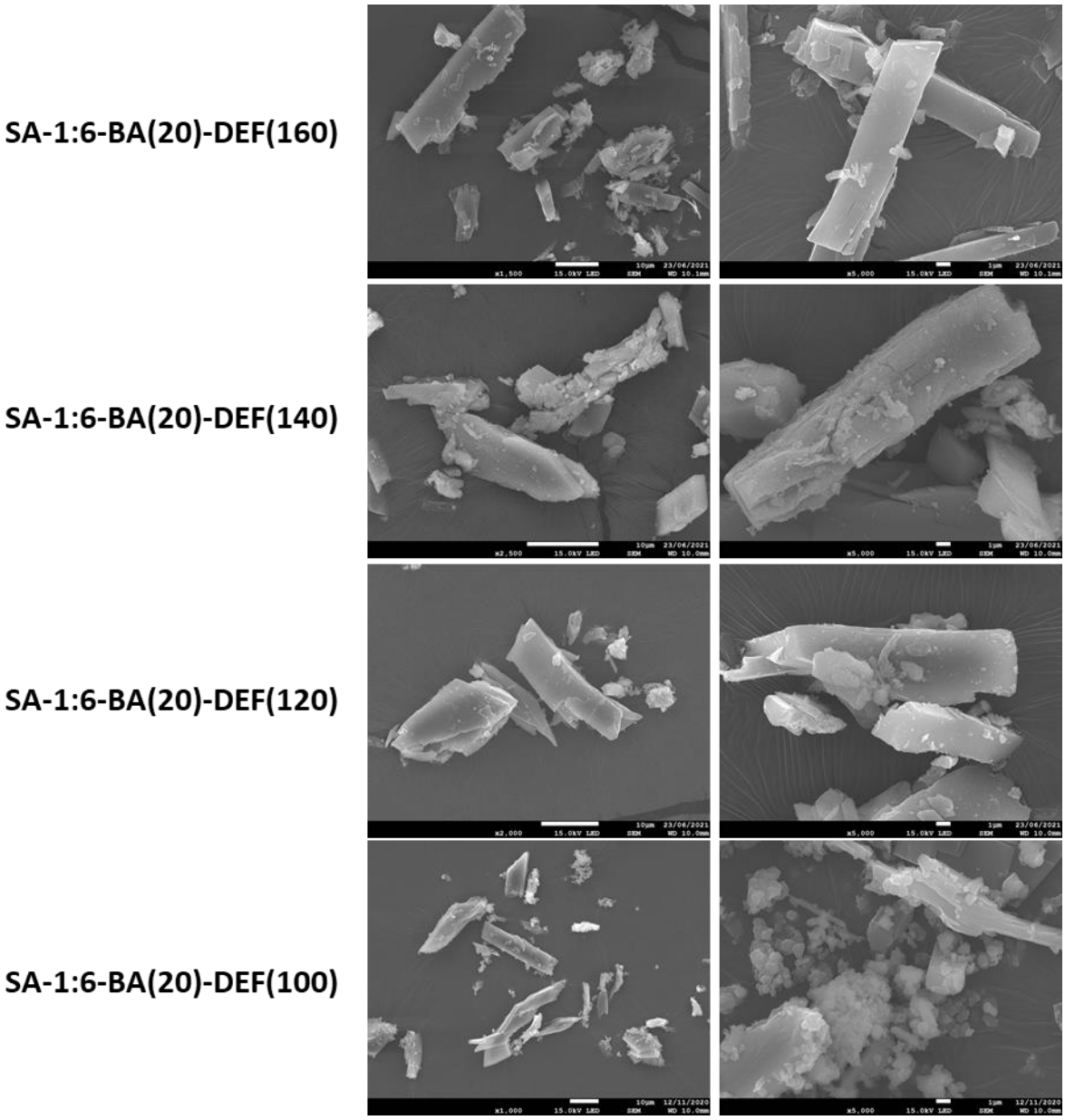

Figure 4.78 - SEM images of Zr-SA-NDI materials. Conditions: SA-1:6-BA(20)-DEF(100) = 1:6 metal to linker ratio, 20 equivalents of benzoic acid, DEF, 100°C, 72 hours, SA-1:6-BA(20)-DEF(120) = 1:6 metal to linker ratio, 20 equivalents of benzoic acid, DEF, 120°C, 72 hours, SA-1:6-BA(20)-DEF(140) = 1:6 metal to linker ratio, 20 equivalents of benzoic acid, DEF, 140°C, 72 hours, SA-1:6-BA(20)-DEF(160) = 1:6 metal to linker ratio, 20 equivalents of benzoic acid, DEF, 160°C, 72 hours. Scale bars: images on left = 10 µm, images on right = 1 µm.

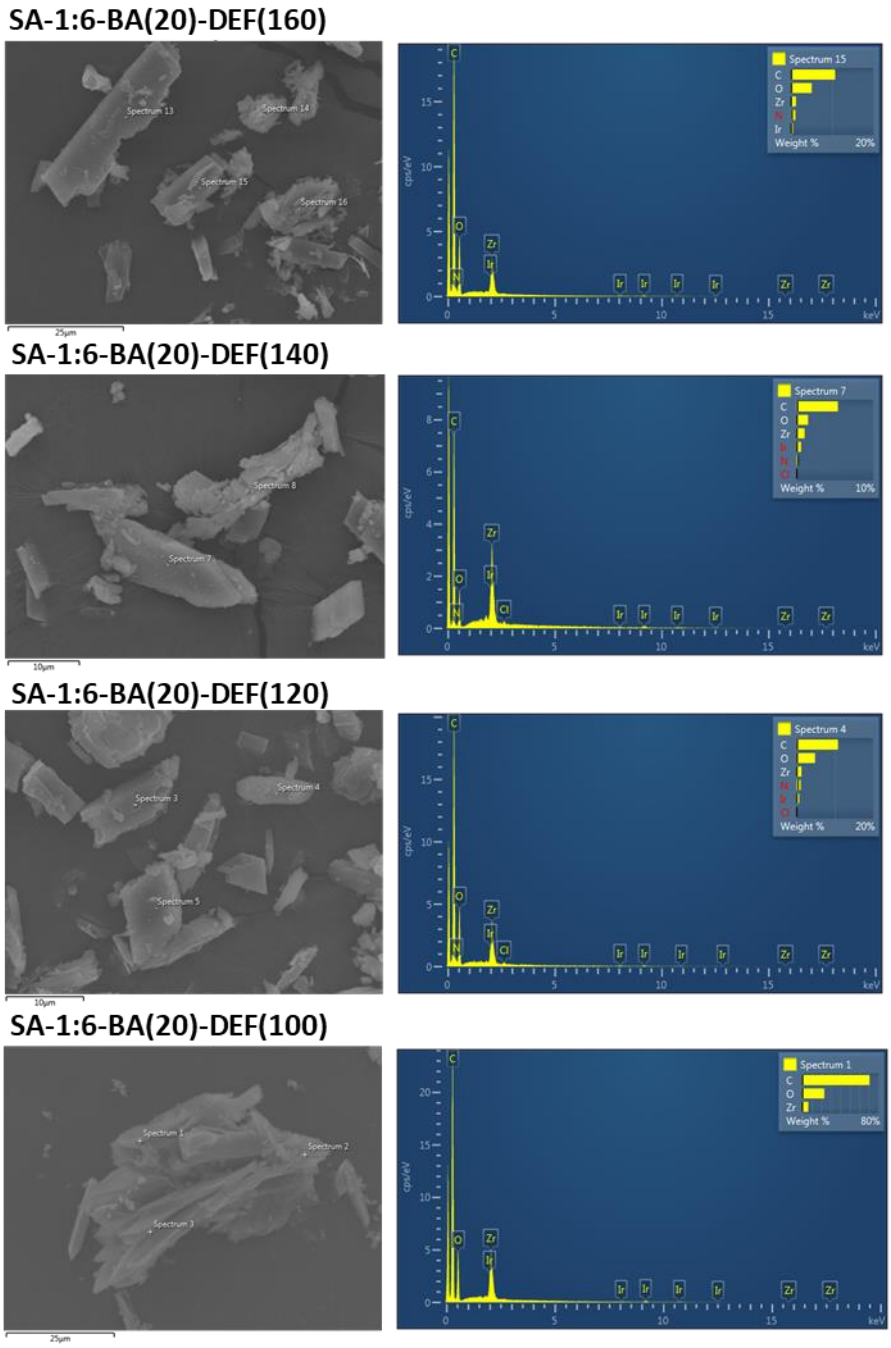

Figure 4.79 – SEM-EDX of Zr-SA-NDI materials. Conditions: SA-1:6-BA(20)-DEF(100) = 1:6 metal to linker ratio, 20 equivalents of benzoic acid, DEF, 100°C, 72 hours, SA-1:6-BA(20)-DEF(120) = 1:6 metal to linker ratio, 20 equivalents of benzoic acid, DEF, 120°C, 72 hours, SA-1:6-BA(20)-DEF(140) = 1:6 metal to linker ratio, 20 equivalents of benzoic acid, DEF, 140°C, 72 hours, SA-1:6-BA(20)-DEF(160) = 1:6 metal to linker ratio, 20 equivalents of benzoic acid, DEF, 160°C, 72 hours

4.9.4.3 Varying the modulator of the Zr-SA-NDI MOF synthesis

SEM images of materials obtained whilst varying the modulator used to form Zr-SA-NDI materials (Figure 4.80) shows that the morphologies of the particles is relatively non-uniform. All samples but SA-1:6-TFA(20)-DEF(100) contain some large (10-20 µm) flat oblong particles,

along with smaller particles which lack definable morphology. SEM-EDX (Figure 4.81) shows that all samples contain C, O and Zr. SA-1:6-FA(20)-DEF(100) and SA-1:6-FA(20)-DEF(100) contain trace amounts of chlorine, which is likely due to the presence of some $ZrOCl_2$ in the sample.

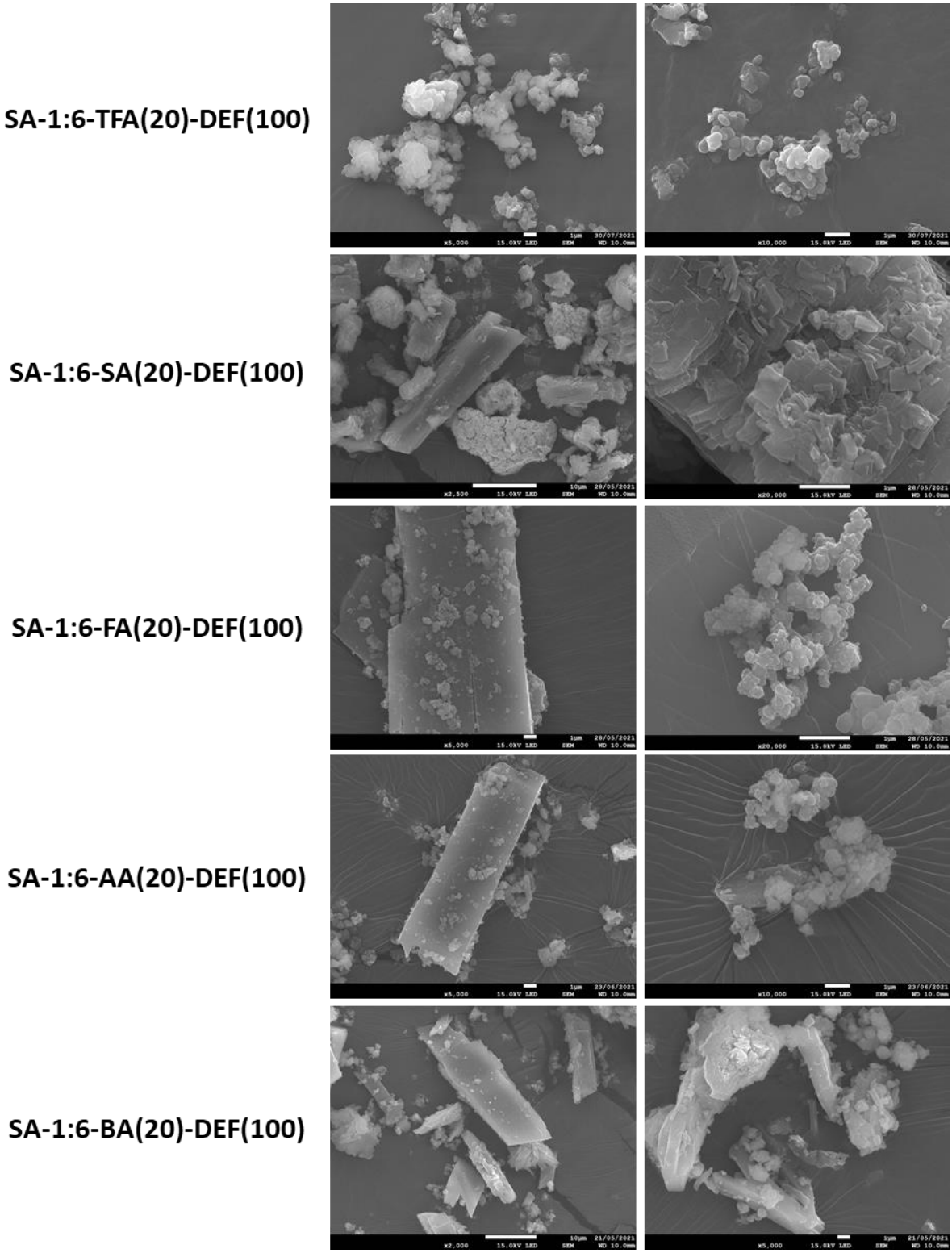

Figure 4.80 - SEM images of Zr-SA-NDI materials. Conditions: SA-1:6-BA(20)-DEF(100) = 1:6 metal to linker ratio, 20 equivalents of benzoic acid, DEF, 100°C, 72 hours, SA-1:6-AA(20)-DEF(100) = 1:6 metal to linker ratio, 20 equivalents of acetic acid, DEF, 100°C, 72 hours, SA-1:6-FA(20)-DEF(100) = 1:6 metal to linker ratio, 20 equivalents of formic acid, DEF, 100°C, 72 hours, SA-1:6-SA(20)-DEF(100) = 1:6 metal to linker ratio, 20 equivalents of salicylic acid, DEF, 100°C, 72 hours, SA-1:6-TFA(20)-DEF(100) = 1:6 metal to linker ratio, 20 equivalents of trifluoroacetic acid, DEF, 100°C, 72 hours. Scale bars: top, third and fourth left = 1 µm, second and fifth left = 10 µm images on right = 1 µm.

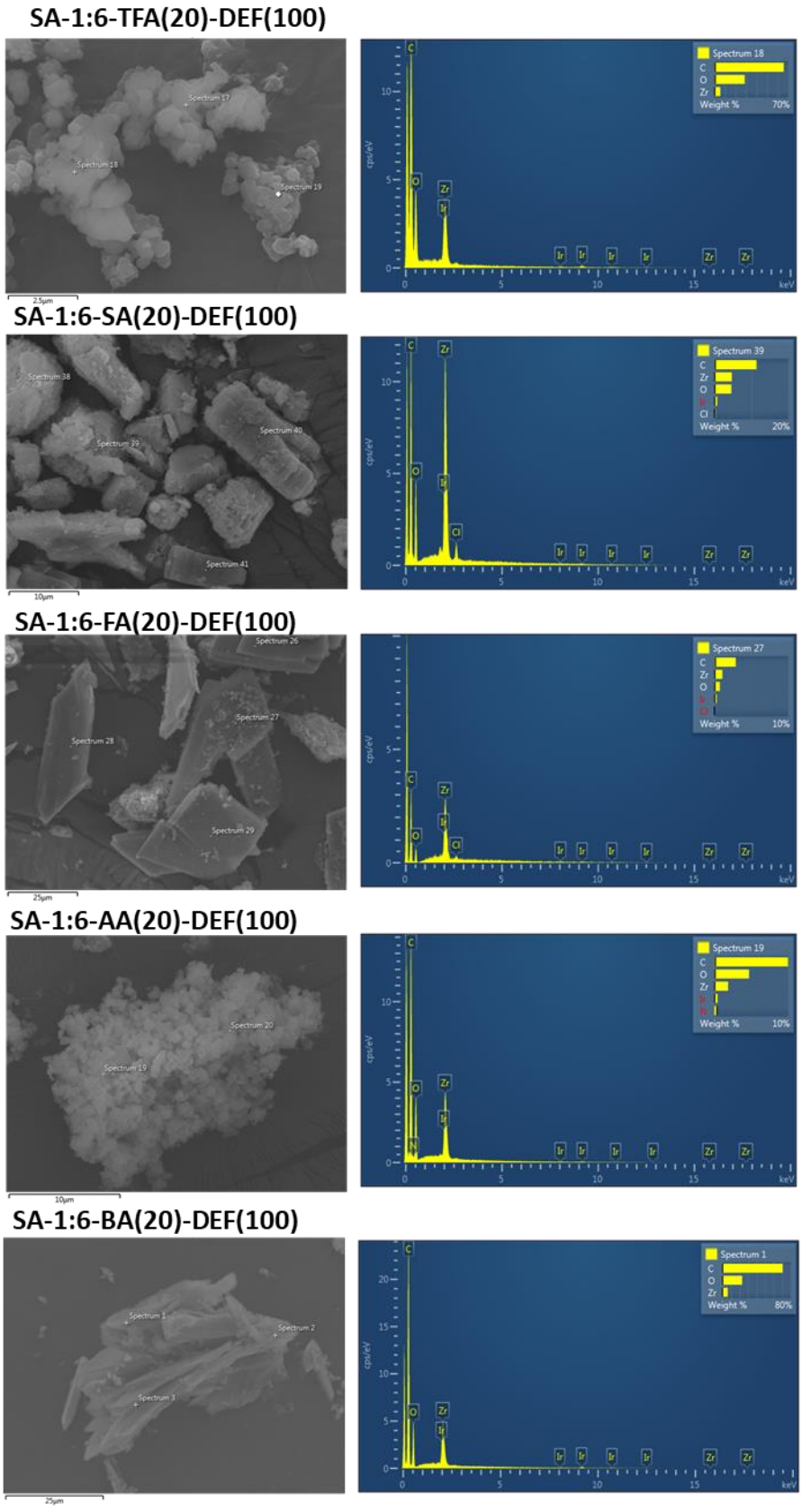

Figure 4.81 – SEM-EDX of Zr-SA-NDI materials. Conditions: SA-1:6-BA(20)-DEF(100) = 1:6 metal to linker ratio, 20 equivalents of benzoic acid, DEF, 100°C, 72 hours, SA-1:6-AA(20)-DEF(100) = 1:6 metal to linker ratio, 20 equivalents of acetic acid, DEF, 100°C, 72 hours, SA-1:6-FA(20)-DEF(100) = 1:6 metal to linker ratio, 20 equivalents of formic acid, DEF, 100°C, 72 hours, SA-1:6-SA(20)-DEF(100) = 1:6 metal to linker ratio, 20

equivalents of salicylic acid, DEF, 100°C, 72 hours, SA-1:6-TFA(20)-DEF(100) = 1:6 metal to linker ratio, 20 equivalents of trifluoroacetic acid, DEF, 100°C, 72 hours.

4.9.4.4 Zr-SA-NDI-β

SEM images (Figure 4.82) of Zr-SA-NDI-β shows that the sample contains very non-uniform particles with no consistent size or shape. EDX (Figure 4.83) confirmed that the only element present are C, O, and Zr. Ir is present due to coating of the sample with this element.

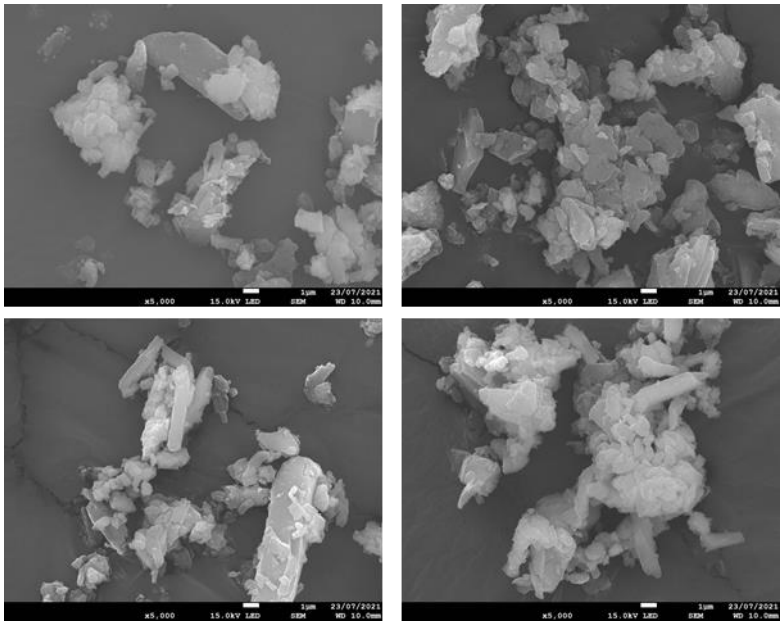

Figure 4.82 – SEM images of Zr-SA-NDI-β. Scale bar = 1 µm.

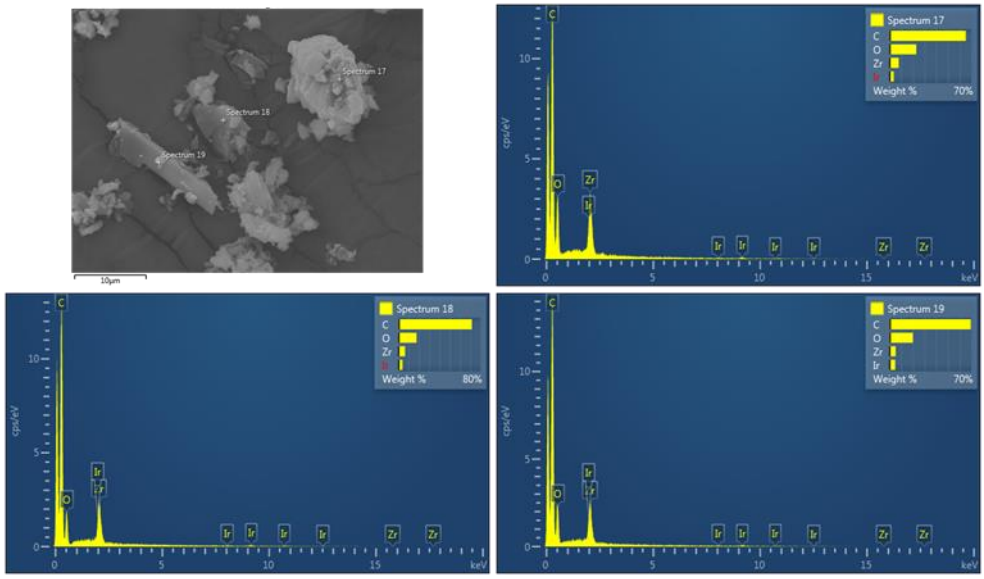

Figure 4.83 – SEM-EDX of Zr-SA-NDI-β.

4.9.5 SEM and SEM-EDX of SA-NDI HOF

SEM images (Figure 4.84) of the SA-NDI HOF confirmed the presence of large single crystals needles throughout the sample. EDX (Figure 4.85) confirmed that the only element present are C and O. Ir is present due to coating of the sample with this element.

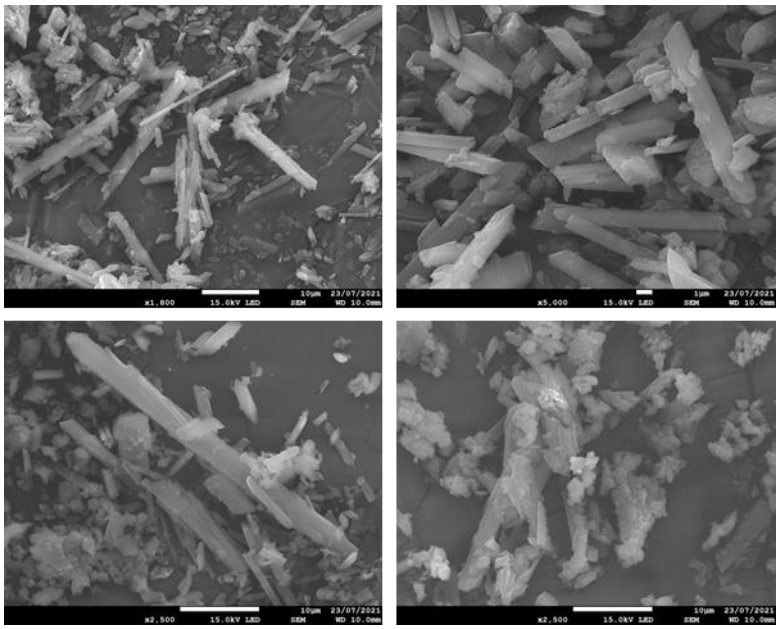

Figure 4.84 – SEM images of SA-NDI HOF. Scale bars: top left = 10 µm, top right = 1 µm, bottom left = 10 µm, bottom right = 10 µm.

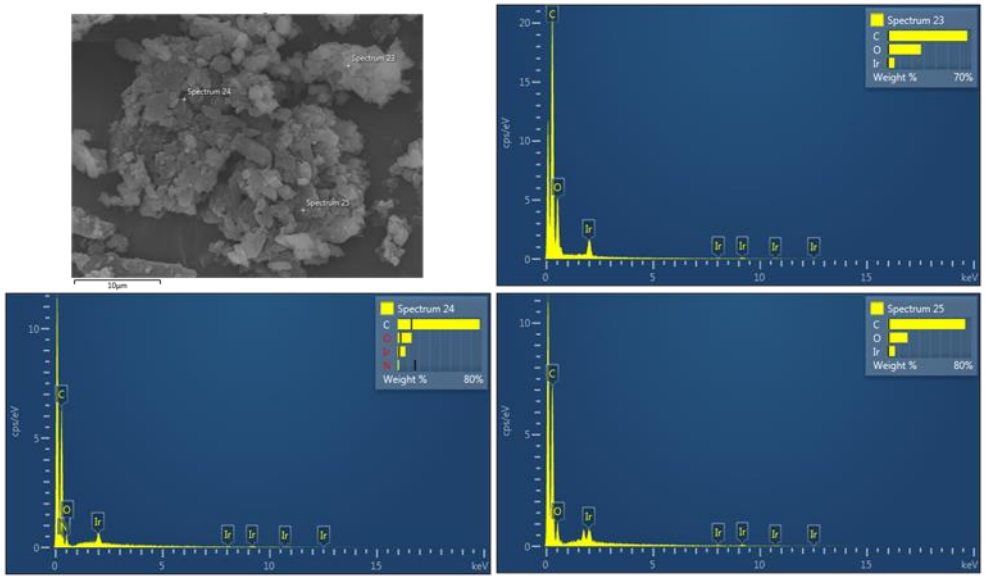

Figure 4.85 – SEM-EDX of SA-NDI HOF.

4.9.6 SEM and SEM-EDX of Ti NDI materials

Due to lack of synthesis material, SEM was only conducted on Ti NDI materials that were synthesised at 100 °C in DMF with modulation. The analysis (Figure 4.86) shows that the particles do not have a distinct and consistent morphology and that they contain C, O and Ti. Ti-DMF(2mL)-100-FA only contains a trace amount of Ti by EDX.

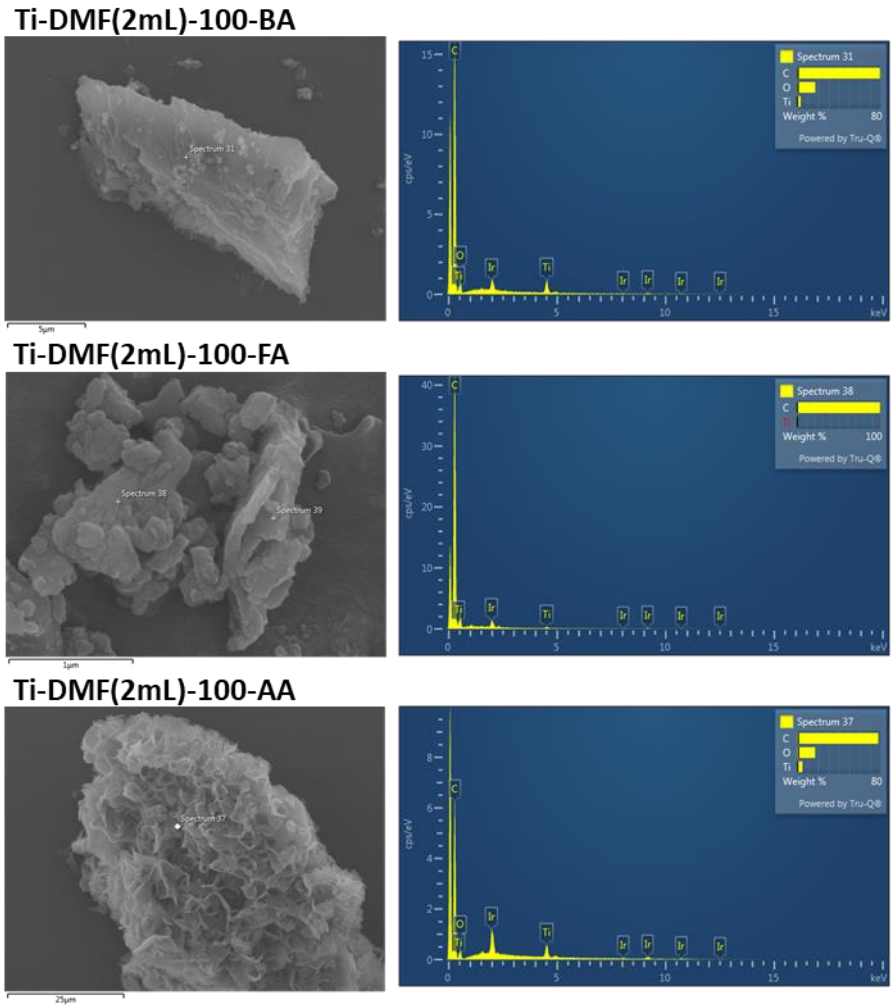

Figure 4.86 – SEM-EDX of Ti-NDI MOF materials.

4.10 References

1 S. V Bhosale, C. H. J. Ab and S. J. Langford, *Chem. Soc. Rev.*, 2008, **37**, 331–342.
2 M. Pan, X. M. Lin, G. B. Li and C. Y. Su, *Coord. Chem. Rev.*, 2011, 255, 1921–1936.
3 S. L. Suraru and F. Würthner, *Angew. Chem. Int. Ed.*, 2014, **53**, 7428–7448.
4 M. Al Kobaisi, S. V Bhosale, K. Latham, A. M. Raynor and S. V Bhosale, *Chem. Rev.*, 2016, **116**, 11685–11796.
5 L. L. Miller, R. G. Duan, Y. Hong and I. Tabakovic, *Chem. Mater*, 1995, **7**, 1552–1557.
6 D. Gosztola, M. P. Niemczyk, W. Svec, A. S. Lukas and M. R. Wasielewski, *J. Phys. Chem. A*, 2000, **104**, 6545–6551.
7 D. Gosztola, M. P. Niemcczyk and M. R. Wasielewski, *J. Am. Chem. Soc.*, 1998, **120**, 5118–5119.
8 H. Shiratori, T. Ohno, K. Nozaki, I. Yamazaki, Y. Nishimura and A. Osuka, *J. Org. Chem.*, 2000, **65**, 8747–8757.
9 B. A. Jones, A. Facchetti, T. J. Marks and M. R. Wasielewski, *Chem. Mater.*, 2007, **19**, 2703–2705.
10 S. Brochsztain, M. A. Rodrigues, G. J. F. Demets and M. J. Politi, *J. Mater. Chem.*, 2002, **12**, 1250–1255.
11 K. D. Johnstone, N. Bampos, J. K. M. Sanders and M. J. Gunter, *New J. Chem.*, 2006, **30**, 861–867.
12 T. Iijima, S. A. Vignon, H. R. Tseng, T. Jarrosson, J. K. M. Sanders, F. Marchioni, M. Venturi, E. Apostoli, V. Balzani and J. F. Stoddart, *Chem. A Eur. J.*, 2004, **10**, 6375–6392.
13 B. Q. Ma, K. L. Mulfort and J. T. Hupp, *Inorg. Chem.*, 2005, **44**, 4912–4914.
14 H. L. Zhang, J. Z. Liao, W. Yang, X. Y. Wu and C. Z. Lu, *Dalton Trans.*, 2017, **46**, 4898–4901.
15 Y. Zhou, L. Qin, M. K. Wu and L. Han, *Cryst. Growth Des.*, 2018, **18**, 5738–5744.
16 C. Fu, H. Y. Wang, G. S. Zhang, L. Li, Y. N. Sun, J. W. Fu and H. Zhang, *CrystEngComm*, 2018, **20**, 4849–4856.
17 C. R. Wade, M. Li and M. Dincă, *Angew. Chem. Int. Ed.*, 2013, **52**, 13377–13381.
18 Y. X. Xie, W. N. Zhao, G. C. Li, P. F. Liu and L. Han, *Inorg. Chem*, 2016, **55**, 549–551.
19 S. Lin, P. M. Usov and A. J. Morris, *Chem. Commun.*, 2018, **54**, 6965–6974.
20 R. Li, K. Li, G. Wang, L. Li, Q. Zhang, J. Yan, Y. Chen, Q. Zhang, C. Hou, Y. Li and H. Wang, *ACS Nano*, 2018, **12**, 3759–3768.
21 S. Goswami, J. N. Nelson, T. Islamoglu, Y.-L. Wu, O. K. Farha and M. R. Wasielewski, *Chem. Mater.*, 2018, **30**, 2488–2492.
22 B. A. Johnson, A. Bhunia, H. Fei, S. M. Cohen and S. Ott, *J. Am. Chem. Soc.*, 2018, **140**, 2985–2994.
23 L. Peng, S. Yang, S. Jawahery, S. M. Moosavi, A. J. Huckaba, M. Asgari, E. Oveisi, M. K. Nazeeruddin, B. Smit and W. L. Queen, *J. Am. Chem. Soc.*, 2019, **141**, 12397–12405.
24 J. Z. Liao, H. L. Zhang, S. S. Wang, J. P. Yong, X. Y. Wu, R. Yu and C. Z. Lu, *Inorg. Chem.*, 2015, **54**, 4345–4350.
25 P. W. Doheny, R. Babarao, C. J. Kepert and D. M. D'Alessandro, *Mater. Adv.*, 2021, **2**, 2112–2119.
26 Y. Ye, Z. Ma, L. Chen, H. Lin, Q. Lin, L. Liu, Z. Li, S. Chen, Z. Zhang and S. Xiang, *J. Mater. Chem. A*, 2018, **6**, 20822–20828.
27 Kirandeep, A. Husain, A. K. Kharwar, R. Kataria and G. Kumar, *Cryst. Growth Des.*, 2019, **19**, 1640–1648.
28 Y. Ye, R. B. Lin, H. Cui, A. Alsalme, W. Zhou, T. Yildirim, Z. Zhang, S. Xiang and B. Chen, *Dalton Trans.*, 2020, **49**, 3658–3661.
29 A. Mallick, H. Liang, O. Shekhah, J. Jia, G. Mouchaham, A. Shkurenko, Y. Belmabkhout, H. N. Alshareef and M. Eddaoudi, *Chem. Commun.*, 2020, **56**, 1883.
30 B. Tian, G. H. Ning, Q. Gao, L. M. Tan, W. Tang, Z. Chen, C. Su and K. P. Loh, *ACS Appl. Mater. Interfaces*, 2016, **8**, 31067–31075.
31 D. K. Panda, K. Maity, A. Palukoshka, F. Ibrahim and S. Saha, *ACS Sustain. Chem. Eng.*, 2019, **7**, 4619–4624.
32 K. AlKaabi, C. R. Wade and M. Dincă, *Chem*, 2016, **1**, 264–272.
33 H. C. Wentz and M. G. Campbell, *Polyhedron*, 2018, **154**, 309–313.
34 Z. Guo, D. K. Panda, M. A. Gordillo, A. Khatun, H. Wu, W. Zhou and S. Saha, *ACS Appl. Mater. Interfaces*, 2017, **9**, 32413–32417.
35 S. Goswami, J. N. Nelson, T. Islamoglu, Y. L. Wu, O. K. Farha and M. R. Wasielewski, *Chem. Mater.*, 2018, **30**, 2488–2492.
36 S. M. Pratik and C. J. Cramer, *J. Phys. Chem. C*, 2019, **123**, 19778–19785.
37 B. A. Johnson, A. Bhunia, H. Fei, S. M. Cohen and S. Ott, *J. Am. Chem. Soc.*, 2018, **140**, 2985–2994.

38 S. Yuan, T.-F. Liu, D. Feng, J. Tian, K. Wang, J. Qin, Q. Zhang, Y.-P. Chen, M. Bosch, L. Zou, S. J. Teat, S. J. Dalgarno and H.-C. Zhou, *Chem. Sci.*, 2015, **6**, 3926–3930.
39 Y. Keum, S. Park, Y.-P. Chen and J. Park, *Angew. Chem.*, 2018, **130**, 15068–15072.
40 H. L. Nguyen, F. Gándara, H. Furukawa, T. L. H. Doan, K. E. Cordova and O. M. Yaghi, *J. Am. Chem. Soc.*, 2016, **138**, 4330–4333.
41 X. J. Kong, T. He, Y. Z. Zhang, X. Q. Wu, S. N. Wang, M. M. Xu, G. R. Si and J. R. Li, *Chem. Sci.*, 2019, **10**, 3949–3955.
42 Y. Zhou and L. Han, *Coord. Chem. Rev.*, 2021, **430**, 213665.
43 J. Gao, J. Miao, P. Z. Li, W. Y. Teng, L. Yang, Y. Zhao, B. Liu and Q. Zhang, *Chem. Commun.*, 2014, **50**, 3786–3788.
44 H. Assi, L. C. Pardo Pérez, G. Mouchaham, F. Ragon, M. Nasalevich, N. Guillou, C. Martineau, H. Chevreau, F. Kapteijn, J. Gascon, P. Fertey, E. Elkaim, C. Serre and T. Devic, *Inorg. Chem.*, 2016, **55**, 7192–7199.
45 H. Chun and D. Moon, *Cryst. Growth Des.*, 2017, **17**, 2140–2146.
46 A. A. Coelho, *TOPAS-Academic, version 4.1 (Computer Software)*, Coelho Software.
47 W. I. F. David, K. Shankland, J. Van De Streek, E. Pidcock, W. D. S. Motherwell and J. C. Cole, *J. Appl. Crystallogr.*, 2006, **39**, 910–915.
48 S. Maniam, H. F. Higginbotham, T. D. M. Bell and S. J. Langford, *Chem. A Eur. J.*, 2019, **25**, 7044–7057.
49 P. Li, M. R. Ryder and J. F. Stoddart, *Accounts Mater. Res.*, 2020, **1**, 77–87.
50 K. Hong and H. Chun, *Inorg. Chem.*, 2013, **52**, 9705–9707.
51 A. Kalita, S. Upadhyaya and N. Sen Sarma, *ChemistrySelect*, 2020, **5**, 12672–12678.
52 M. Trchová, I. Šeděnková, E. Tobolková and J. Stejskal, *Polym. Degrad. Stab.*, 2004, **86**, 179–185.
53 M. Trchová, I. Šeděnková and J. Stejskal, *Synth. Met.*, 2005, **154**, 1–4.
54 A. Yelil Arasi, J. Juliet Latha Jeyakumari, B. Sundaresan, V. Dhanalakshmi and R. Anbarasan, *Spectrochim. Acta - Part A Mol. Biomol. Spectrosc.*, 2009, **74**, 1229–1234.
55 Y. Fu, D. Sun, Y. Chen, R. Huang, Z. Ding, X. Fu and Z. Li, *Angew. Chem. Int. Ed.*, 2012, **51**, 3364–3367.
56 A. P. Nelson, O. K. Farha, K. L. Mulfort and J. T. Hupp, *J. Am. Chem. Soc.*, 2009, **131**, 458–460.
57 K. Manna, T. Zhang, F. X. Greene and W. Lin, *J. Am. Chem. Soc*, 2015, **137**, 15.
58 J. H. Cavka, C. Lamberti, N. Guillou, S. Bordiga, S. Jakobsen, U. Olsbye, N. Guillou, S. Bordiga and K. P. Lillerud, *J. Am. Chem. Soc.*, 2008, **130**, 13850–13851.

Chapter Five: Conclusions and Future Directions

This thesis focused on the synthesis of stable MOFs, with a particular emphasis on improving reaction conditions to increase the crystallinity or yield of the material produced.

The aim of the work described in Chapter 3 was to produce materials that could remove Cu(II) ions from aqueous environments. The MIL-53(Al) series of MOFs was chosen due to their structural stability,[1] and the ability to add pendant groups, such as NH_2 and COOH, within their pores, which are known to enhance the uptake of Cu(II).[2] MIL-53(Al), MIL-53(Al)-NH_2 and MIL-121 were all synthesised and characterised by PXRD, TGA, SEM and surface area measurement from gas sorption data. It was possible to shorten the time taken to produce these MOFs from up to three days to ten minutes by using microwave heating. The breathing effect that MIL-53(Al) and MIL-53(Al)-NH_2 exhibit became a very important feature in the investigation of their synthesis, activation, and the examination of their stability. PXRD data had to be analysed in detail to establish which phases (open, narrow, hydrated, etc.) were present in the samples.

The conditions used to synthesise MIL-53(Al)-NH_2 were investigated, leading to the production of MIL-53(Al)-NH_2 in good yield and with no linker trapped in the pores using a ten minute reaction time. This is a significant improvement on previously reported methods, as the material could be activated by solvent exchange at room temperature, significantly reducing the energy used compared to other methods reported in the literature.

MIL-121 was synthesised *via* microwave heating for the first time in this work but our studies showed that activation of this material is complex. Soxhlet extraction by methanol or DMF did not remove the linker from the pores and calcination resulted in the formation of the dianhydride in the pores of MIL-121 and loss of pendant COOH groups. Further investigations need to be carried out to determine an appropriate activation method that removes the excess linker without blocking the pores. Although solvothermal heating in methanol at 150 °C has been shown to be successful previously,[3–5] it would be interesting to see if a less energy intensive method could be used, such as sonication in a solvent.

Investigations into the stability of MIL-53(Al), MIL-53(Al)-NH_2 and MIL-121 in different aqueous solutions was carried out. Although previous reports indicated that MIL-53(Al) and

MIL-53(Al)-NH_2 are relatively stable, significant changes were seen in the PXRD of these materials after being exposed to a wide range of conditions, suggesting phase changes were occurring or the materials were dissolving. This ultimately showed that if these materials are to be used in industrial applications, such as gas sorption or removal of contaminants from waste streams, special attention needs to be taken to ensure that the material will maintain its structure and/or sorption capabilities under the range of conditions that might be experienced in real-world settings.

On the other hand, MIL-121 maintained its structure under most aqueous conditions (the material began to degrade above pH 10). This could indicate that the extra carboxylate groups improve the stability of this material. Hydrogen bonds are formed between adjacent pendant carboxylate groups in the pores of MIL-121 which could influence the stability of the material, perhaps by increasing the thermodynamic barrier that an attacking species has to overcome to break bonds within the structure.

MIL-53(Al), MIL-53(Al)-NH_2 and MIL-121 exhibited low uptake for Cu(II) under the conditions investigated. It is suspected that this was due to the flexible MOFs (MIL-53(Al) and MIL-53(Al)-NH_2) adopting the narrow pore form or even decomposing in water. In the case of MIL-121, this material had a low surface area due its activation being unsuccessful. For future work in this area, it would be better to choose MOFs that do not exhibit structural flexibility, have larger pores and are stable in aqueous solutions.

Chapter 4 focused on the synthesis of stable NDI MOFs, with the aim of producing new MOFs using Group 4 metals and carboxylate containing NDIs as linkers. The exploration of the conditions required to produce MOFs by combining Zr and salicylic naphthalene diimide (SA-NDI) was a key feature of this chapter. Over fifty reactions were carried out where changes to the solvent mixture, modulator, reactant ratios, reaction temperature and reaction time were made to try and produce a single crystal Zr SA-NDI MOF. The iterations made in these reactions led to a significant improvement in the crystallinity of the materials obtained: Zr-SA-NDI-α, Zr-SA-NDI-β and SA-NDI HOF.

Single crystals of Zr-SA-NDI-α were synthesised and the crystal structure consisted of alternating ZrO_7 and ZrO_6 joined by SA-NDI linkers that coordinate *via* the hydroxyl oxygen

and one carboxylate oxygen. Unfortunately, the synthesis of this material could not be repeated, preventing further characterisation.

Despite many reaction conditions being explored, synthesis of single crystals of Zr-SA-NDI-β was not possible. The crystalline powder was characterised by PXRD, TGA, CHN, FTIR and UV-vis and attempts were made to solve the structure from the powder diffraction data collected. The data gathered indicated that the material was a MOF but further characterisation, such as synchrotron PXRD data or electron diffraction data, would be required to solve the structure of Zr-SA-NDI-β. The TGA data indicated that Zr-SA-NDI-β could be porous, but due to time constraints, activation of Zr-SA-NDI-β was not achieved.

Unexpectedly, a highly repeatable synthesis for an SA-NDI hydrogen bonded-framework (HOF) was also discovered during these experiments. Careful control of choice of modulator, solvents, reactant ratios and temperature led to production of single crystals of SA-NDI HOF, which were not produced when any one of the reactants was omitted from the reaction. The structure solution revealed that MeCN molecules were present in the pores of the HOF and TGA and CHN analysis indicated that the MeCN exchanged with H_2O when the material was left to dry in air. Overall, this suggested that SA-NDI HOF was porous. Activation attempts were unsuccessful, and it was suspected that careful consideration would have to made to the conditions that SA-NDI HOF is subjected to. For example, exposing the material to a large amount of DMF or DEF dissolved the HOF, presumably because these solvents can act as hydrogen bond donors.

Future work with SA-NDI HOF and Zr-SA-NDI-β should focus on activation, followed by further examination of their properties. For example, it would be interesting to see if these materials are redox active and if they could be reduced to produce NDI radical anions, which could be observed through UV-vis analysis. Solid state cyclic voltammetry could also be carried out to observe whether the materials exhibit any interesting electrochemical behaviour. It is hoped that if the properties of this material can be better understood, they could be applied to electro- or photocatalysis. In particular, these HOFs and MOFs could be used to reduce Cu(II) that is found in aqueous waste streams, such as dairy farm waste, to form copper nanoparticles.

The final section of Chapter 4 introduced the use of Ti oxo clusters as a starting material for the synthesis of Ti NDI MOFs using covalent chemistry. The synthesis of crystalline Ti MOFs is known to be challenging, as the formation of strong, poorly labile bonds inhibits crystal growth. Although the work described in this area was relatively underdeveloped, it indicated that there is a potential for the formation of covalent bonds between a cluster and a linker to act as an alternative route to produce crystalline Ti MOFs. Once again, the reaction conditions played a significant role in tailoring the crystallinity of the materials; the most crystalline materials were produced when modulators were employed.

To conclude, this thesis has examined the effect of reaction conditions on the production of Group III and IV MOFs and shown that small changes to conditions can lead to significant changes in crystallinity, yield or even composition of the material produced. Improvements were made to the synthetic requirements used to make three known MOFs and four new framework materials were reported. This work will help aid the design and successful synthesis of MOFs for applications such as metal sorption and electro- and photo-catalysis.

5.1 References

1 M. R. Azhar, H. R. Abid, V. Periasamy, H. Sun, M. O. Tade and S. Wang, *J. Colloid Interface Sci.*, 2017, **500**, 88–95.

2 Y. Zhang, X. Zhao, H. Huang, Z. Li, D. Liu and C. Zhong, *RSC Adv.*, 2015, **5**, 72107–72112.

3 S. Chen, S. Mukherjee, B. E. G. Lucier, Y. Guo, Y. T. A. Wong, V. V. Terskikh, M. J. Zaworotko and Y. Huang, *J. Am. Chem. Soc.*, 2019, **141**, 14257–14271.

4 J. N. Hao and B. Yan, *J. Mater. Chem. A*, 2014, **2**, 18018–18025.

5 S. Chen, B. E. G. Lucier, W. Luo, X. Xie, K. Feng, H. Chan, V. V. Terskikh, X. Sun, T. K. Sham, M. S. Workentin and Y. Huang, *ACS Appl. Mater. Interfaces*, 2018, **10**, 30296–30305.